Final Report

How Far Can We Get?
DSE Group 14

Technische Universiteit Delft

TU Delft

This page is left intentionally blank

Final Report

How Far Can We Get?

by

Emad Adib
Harry Aldridge
Michiel Beyens
Klaas Burger
Hamza El Uamari
Bart (RF) Jacobson
Patrik Kovacik
Timothy van der Duim
Menno van der Toorn

Project duration: April 23, 2018 – July 5, 2018
Tutor: ir. J.A. Melkert
Coaches: ir. V.V. Dighe ir. Y.B. Eisma

Version 2.0

Version	Purpose/changes	Date
1.0	Draft report	27/06/2018
1.1	Implemented tutor feedback	2/07/2018
1.2	Implemented PM/SE lecturers feedback	3/07/2018
2.0	Final report	3/07/2018

Preface

This report continues upon the preliminary design that was layed out in the Midterm Report [1] and the project strategy and design ambition as presented in the Project Plan [2] and the Baseline Report [3]. Moreover, it is the result of eleven weeks of work by the design team. The design team consists of nine Bachelor students in Aerospace Engineering at Delft University of Technology. However, this production wouldn't have been possible without the outstanding help of the Aerospace Engineering faculty personnel. In particular, the team would like to thank the OSSAs, PMSE TAs and the members of the OSCC, who have been part of the organization of this years spring Design Synthesis Exercise. Special thanks go out to our tutor ir. J. A. Melkert and our project coaches ir. V. V. Dighe and ir. Y. B. Eisma. The tutor and coaches have helped the design team in every stage of the project, where their professional insight have proven essential to its success.

DSE Group 14
3^{rd} *of July 2018, Delft*

Contents

List of Symbols

Abbreviations

Symbol	Description	Unit
ADSEE	Aerospace Design and Systems Engineering Elements	[-]
ANOPP	Aircraft Noise Prediction Program	[-]
APU	Auxiliary Power Unit	[-]
BLI	Boundary Layer Ingestion	[-]
BOL	Begin Of Life	[-]
BP	Bypass Ratio	[-]
CFRP	Carbon Fiber Rienforced Polymer	[-]
DOC	Direct operating cost	[$]
DOT	Design option tree	[-]
DSE	Design Synthesis Exercise	[-]
EASA	European Aviation Safety Agency	[-]
ECS	Environmental Control System	[-]
EGTS	Electric Green Taxiing System	[-]
EOL	End Of Life	[-]
EPNL	Effective perceived noise level	[EPNdB]
FB	Functional Breakdown	[-]
FL	Flight Level	[ft/100]
FFD	Functional Flow Diagram	[-]
HLD	High Lift Device	[-]
HLFC	Hybrid Laminar Flow Control	[-]
ICAO	International Civil Aviation Organization	[-]
ISA	International Standard Atmosphere	[-]
MAC	Mean Aerodynamic Chord	[m]
MACW	Mission Adaptive Compliant Wing	[-]
MLW	Maximum landing weight	[kg]
MTOW	Maximum take-off weight	[kg]
LCC	Low Cost Carrier	[-]
LCN	Load Classification Number	[-]
LTO	Landing and Take-off Cycle	[-]
OEW	Operational empty weight	[kg]
OTJ	Oil-to-Jet	[-]
RAMS	Reliability, Availability, Maintainability and Safety	[-]
RAT	Ram Air Turbine	[-]
ROC	Rate of Climb	[ft/min]
ROI	Return on Investment	[-]
SDS	Sustainable Development Strategy	[-]
SF	Safety Factor	[-]
SFC	Specific Fuel Consumption	[kg/s]
SMA	Shape Memory Alloys	[-]
SPL	Sound pressure level	[dB]
TC	Total Cost	[$]
TOP	Take-Off Parameter	[-]
TRL	Technology Readiness Level	[-]
TSFC	Thrust Specific Fuel Consumption	[kg/N/s]
TTCR	Thickness-to-chord ratio	[-]
WBS	Work Breakdown Structure	[-]
WFD	Work Flow Diagram	[-]

Symbols

A	Aspect ratio	[-]
b	Span	[m]
c	Chord length	[m]
c	Ambient speed of sound	[m/s]
c'	Chord length with flaps extended	[m]
C	Cost	[$]
$\bar{c}$	Mean Aerodynamic Chord	[m]
c_j	Fuel consumption	[kg/s]
C_D	Drag coefficient	[-]
C_{D_0}	Zero lift drag coefficient	[-]
C_{f_c}	Flat plate skin friction coefficient	[-]
c_l	Lift coefficient airfoil	[-]
$C_{l_{\delta\alpha}}$	Aileron control derivatives	[-]
C_{l_p}	Roll damping coefficient	[-]
C_L	Lift coefficient aircraft	[-]
$C_{L_{A-h}}$	Lift coefficient aircraft without tail	[-]
C_{L_h}	Lift coefficient tail	[-]
C_{L_0}	Lift coefficient in landing configuration at zero angle of attack	[-]
C_{L_α}	Lift curve slope	[-]
$C_{m_{ac}}$	Moment coefficient around the aerodynamic center	[-]
c_m	Moment coefficient airfoil	[-]
C_P	Pressure coefficient aircraft	[-]
d	Diameter	[m]
D	Drag	[N]
e	Oswald factor	[-]
E	E-modulus	[Pa]
E	Energy density	[MJ/kg]
f	Frequency	[Hz]
F	Force	[N]
F_g	Gross/Static thrust	[N]
F_n	Net thrust	[N]
FF_c	Component form factor	[-]
g	Gravitational acceleration	$[m/s^2]$
h	Height	[m]
I	Area moment of inertia	$[mm^4]$
I	Emission density	[gCO2/MJ]
IF_c	Component interference factor	[-]
K	Column effective length factor	[-]
l	Length	[m]
l_h	Tail arm	[m]
L	Lift	[N]
L/D	Lift over drag ratio	[-]
M	Mach number	[-]
M	Moment	[N/m]
M_F	Fuselage weight divided by MTOW	[-]
M_W	Wing weight divided by MTOW	[-]
n	Load factor	[-]
P	Pressure	[Pa]
P	Roll rate	[rad/s]
P_a	Power available	[N]
P_{cr}	Euler buckling load	[N]
P_r	Power required	[N]
q	Dynamic pressure	[Pa]
r	Radius	[m]

s	Distance	[m]
S	Surface area	$[m^2]$
s_C	Distance to screen height if screen height is **not** exceeded during the transition phase of the take-off run	[m]
s_F	Flare ground distance	[m]
$s_{G_{take-off}}$	Take-off ground roll	[m]
s_S	Distance to screen height if screen height is exceeded during the transition phase of the take-off run	[m]
s_T	Ground distance reached during the transition phase of the take-off run	[m]
t	Time	[s]
t	Thickness	[mm]
T	Thrust	[N]
T	Temperature	[K]
T/W	Thrust loading	[-]
V	Velocity	[m/s]
V_A	Approach speed	$[m/s^2]$
V_F	Average flare speed	$[m/s^2]$
V_h	Horizontal tail velocity	[m/s]
V_{LOF}	Lift off speed	$[m/s^2]$
V_S	Stall speed	$[m/s^2]$
$V_{S_{Landing}}$	Stall speed in the landing configuration	$[m/s^2]$
V_{TD}	Touchdown speed	$[m/s^2]$
V_{TRANS}	Average speed in the transition phase to climb	$[m/s^2]$
w	Width	[m]
W	Weight	[kg]
W/S	Wing loading	$[N/m^2]$
x_{cg}	Longitudinal position of the center of gravity	[m]
X_{LEMAC}	Longitudinal position of leading edge of mean aerodynamic chord	[m]

α	Angle of attack	[deg]
β	Engine bypass ratio	[-]
γ	Specific heat ratio	[-]
γ	Climb angle	[deg]
γ_A	Approach angle	[deg]
δ	Deflection angle	[deg]
ε	Downwash angle	[deg]
θ	Flight path angle	[deg]
λ	Taper ratio	[-]
λ	Bypass ratio	[-]
Λ	Sweep angle	[deg]
μ	Friction coefficient	[-]
ν	Poisson ratio	[-]
ρ	Density	$[kg/m^3]$
σ	Stress	[Pa]
σ	$\frac{\rho_0}{\rho}$	[-]
τ	Aileron effectiveness	[-]
ϕ	Bank angle	[deg]

Executive Overview

Project Objectives

To curb the environmental impact of the aviation sector, the International Civil Aviation Organization (ICAO) and other international bodies have set CO_2 emission targets. These targets are outlined in ICAO Annex 16, Volumes I and II, and include for example, a 2% annual increase in fuel burn efficiency [4]. This demonstrates the need for improved efficiencies in the aviation sector.

A current source of avoidable emissions is the sub-optimal operation of aircraft such as the Airbus A321neo, on short ranges. To comply with ICAO emission targets, an aircraft of comparable capacity, optimized for inter-European operations will be designed. This will be done with an emphasis on the reduction of three key metrics: Emissions, Noise and Direct Operating Cost.

Market Analysis

To follow on from the route analysis, the design range is determined from a set of European flight data[1]. This data set is taken from 12 days between May 2016 and February 2017. For each flight, the distance between each departure and arrival airport is computed. These results are arranged according to frequency, and analyzed. It was concluded that a range of about 1,800 km is required to cover 90% of these flights.

Furthermore, the design shall be performed at a passenger load factor of 94% for the next generation aircraft. This was assumed according to the trends in global load factor: increasing, at a decreasing rate, from 65% in 1990, to 80% in 2016 [5].

To determine airport accessibility for the aircraft, the required take-off length is established. To do this, a list of all paved runways in Europe was obtained from the CIA World Fact Book[2]. Using a take-off distance of 2,000 m, approximately 77% of the airports in Europe are accessible. Comparing this to the Airbus A321-200 and Boeing 737-800 which have a take-off length of 2,280 m and 2,316 m respectively [3], this allows operation on at least 10% more airports than its competitors.

To develop a commercially attractive aircraft, the direct operating cost shall be 10% lower compared to the competitors who's DOCs are summarized in Table 2.

Table 2: Summarized Average Direct Operational Cost of reference aircraft

Aircraft Type	A319	A320	A320neo	A321	B737-900	B737-800 MAX 8	B737-700 MAX 7	B757-200	AVERAGE
Average DOC (USD/h)	3,670	3,788	2,955	4,395	3,438	3,927	4,020	3,475	**3,946**

[1] These data files have been obtained in a previous project during the bachelor, provided by the tutor.
[2] `https://www.cia.gov/library/publications/the-world-factbook/fields/2030.html` [cited 30 April 2018]
[3] `http://booksite.elsevier.com/9780340741528/appendices/data-a/default.htm` [cited 30 April 2018]

Requirements

The relevant users for this project were categorized into the following groups: airlines, authorities, airports, the passengers and the general public. From this list, the stakeholder requirements were derived as shown in Table 3.1. From here the system and subsystem requirements were derived and designed for.

Table 3.1 Summarized list of stakeholder requirements

ID	Stakeholder Requirement
HF-STK-AL-01	The aircraft shall have a range of 1,800 km with a load factor of 94%[4].
HF-STK-AL-02	The aircraft shall be able to carry 240 passengers in single class configuration.
HF-STK-AL-03	The aircraft shall have a maximum cruise speed comparable to current state-of-the-art inter-European airliners.
HF-STK-AL-06	The aircraft shall be able to take off within 2,000 m at ISA conditions at sea level.
HF-STK-AL-08	The aircraft shall be able to cargo at least 10 LD3-45W containers.
HF-STK-AL-09	The direct operating cost of the aircraft shall be at least 10% lower compared to current inter-European state-of-the-art aircraft using an average fuel price of 1.69 USD per gallon [5].
HF-STK-AL-10	The aircraft shall be at least 1 noise class lower compared to current inter-European state-of-the-art aircraft.
HF-STK-AL-11	The aircraft shall be operational within 15 years.
HF-STK-AL-12	The aircraft shall have an emissions reduction of at least 10% compared to current inter-European state-of-the-art aircraft.
HF-STK-AU-01	The aircraft shall comply with CS25 [6].
HF-STK-AU-02	The aircraft shall comply with CS36 [7].

Preliminary Design

Six design were generated and traded-off. The most optimal design was chosen based five trade-off criteria: development cost, emissions, noise, aerodynamic performance and weight. It was found that a circular fuselage was the most optimal fuselage shape for great performance on weight and development cost. Moreover, the ultra-high bypass ratio geared turbofan engine was selected based on its favorable performance on emissions, noise and development cost.

A wing layout with a very high aspect ratio was chosen to be most optimal based on the trade-off criteria. In order to accommodate this slender wing, a strut will be implemented.

Mission Analysis

The aircraft has a design range of 1,800 km. Moreover, the aircraft has a maximum useful range of 3,400 km, a harmonic range of 1,177 km and a ferry range of 6,254 km.

Furthermore, the aircraft has a service ceiling of 12.9 km or 41,900 ft. The service ceiling is defined in CS-25 [6] as the altitude at which the aircraft's maximum rate of climb drops below 500 ft/min.
The TU-ecoliner's ground and logistics operations are comparable to current short-range aircraft like the Boeing 737 and Airbus A320. The ground operation does differ on two critical points though. First, the aircraft will use an electric green taxiing systems (EGTS), which allows the aircraft to taxi using electric motors on the landing gear. In order to provide power to this system without having the engines running, an electric battery cart will be attached to the aircraft when it taxiing. Secondly, the aircraft's APU will be removed, which allows a total of around 600 kg of weight saved. However, it does mean that the aircraft relies heavily on ground based support systems for airconditioning and ground power.

Within the aircraft, all data, information and control inputs will flow through a central flight computer. The computer runs several applications in order to process all data in an adequate manner. The central flight computer is actually a group of three computers. One handles all data for the captain, one handles all data for the first officer and the third computer serves as a redundant back-up solution.

[4] This has been determined in Section 2.3
[5] `https://www.statista.com/statistics/197689/us-airline-fuel-cost-since-2004/` [cited 9 May 2018]

Final Design Characteristics

Class II Weight Estimation

Using the data gathered from the class I weight estimation and additional geometrical parameters, a class II weight estimation was performed. Two methods were used, namely the Roskam and Torenbeek methods. These two methods were separately calculated and averaged to get to the final weight estimation. The results from this can be seen in Table 4.

Table 4: Class II weight estimation in kg

Wing	Fuselage	Landing Gear	Empennage	Propulsion	Nacelle	Equipment & furnishing	OEW/MTOW
7,657	10,203	2,041	1,275	6,385	667	9,916	38,143/68,048

Aerodynamic Characteristics

From the thrust loading and wing loading diagrams, the required wing surface area of 110 m^2 was obtained. With an aspect ratio of 14 and taper ratio of 0.29, the wing planform was established.

After determining the design lift coefficient of the aircraft, a suitable airfoil was selected. Multiple airfoils have been analyzed and compared using aerodynamic software. Based on criteria such as low drag at design lift coefficient and a large maximum lift coefficient, the NASA SC20-612 airfoil was chosen.

The aerodynamic behaviour of the finite wing was analyzed to determine the leading edge sweep angle of 32.9°. The lift slope in cruise conditions was determined to be 5.89 rad^{-1} using the datcom method. In cruise, it reaches a maximum lift coefficient of 0.94 at an angle of attack of 9.4°. The same parameters have been determined at low speed in sea-level conditions.

The drag has been analyzed taking into account the Hybrid Laminar flow control system which enables laminar flow along 65% of the chord. The contribution of different components to the zero-lift drag has been determined using the drag build-up method. In clean configuration, the zero-lift drag coefficient equals 0.0131. The lift induced drag was analyzed in order to obtain the drag polar. Here, the Oswald efficiency factor equals 0.727 and the effective aspect ratio equals 14.75 due to the addition of raked wingtips.

High lift devices have been designed in order to meet the required $C_{L_{max}}$ of 2.2 in take-off and 2.9 in landing. Double slotted fowler flaps and slats where selected. Their size and position was determined. The slats occupy the space between 15% and 69% of the half-span. The flaps are placed between 5% and 66% of the half-span. Their effect on the lift curve and drag increment have been analyzed. Ailerons have been sized and positioned in order to meet the roll rate requirement. They are positioned between 79% and 95% of the half-span and have a maximum deflection of 20°.

Landing Gear Design

Based on the weight of the aircraft, it was determined that two nose wheels and four main gear wheels were required. In order to position the landing gear, several requirements and conditions had to be met. To satisfy longitudinal and lateral stability on the ground, and fulfilling scrapeback (9.5°), tipback (15°) and tipover (63°) angles, the mainlanding gear are placed 21.4 m from the nose, with a track width of 6.5 m. The nose landing gear is positioned 4.5 m from the nose, and satisfies the requirement that the nose gear must sustain between 8% and 14% of the total aircraft mass. The gear struts are long enough to ensure that the bottom of fuselage is 1.5 m off the ground. This height ensures that the gear struts are short enough to fit into the belly fairing, but also that the scrapeback angle requirement is met.

Structural Characteristics

In order to design the structure of the fuselage, first, shear and moment diagrams were made to find the critical loads. The critical load case was determined to be taking off at maximum take-off weight under fatigue load conditions with a pressurized fuselage. As a first approximation, a cylinder with a constant thickness was designed. In a second stage, stringers were added to make the design lighter while keeping the inertia constant. Here, also buckling comes into play. For the CFRP case, which was chosen for the fuselage, this turned out to be more critical then the bending load. Therefore, the fuselage was designed for buckling. This lead to a skin thickness of 1 mm with 87 hat stringers along the skin.

In order to design the wing, the maximum loads experienced by the wing are determined. These occur during take-off at MTOW. The spars, skin and the wing strut of the wing have been optimized for mass under bending, shear and buckling of the spars and skin. Applying CFRP material for the wingbox saved over 21% relative to aluminium material. Additionally, by applying a wing strut, the wing weight decreased by 19% with a drag penalty of only a 5,8% drag penalty during cruise. Due to the nature of the loading on the strut, it will be made from aluminum.

Material Characteristics

In order to choose the right materials for the right parts of the aircraft, first the characteristics of the most used materials have been researched.

After that, the materials for the different designed parts, such as the fuselage skin or stringers and the wingbox, have been chosen. For the fuselage, it was decided to make the entire fuselage out of quasi isotropic CFRP. The same goes for the wingbox. The wing strut however, is going to be made out of 7075-T6 aluminum. The wingbox of the horizontal tail will be made out of 7075-T6 aluminum as well, because here there was not much weight gain and the cost of CFRP was ten times higher.

Finally, with respect to current state-of-the-art composite aircraft, it was decided to make specific parts of the aircraft out of specific materials. For example, heavy duty parts such as the engine pylon and the landing gear will be made out of titanium and all leading edges will be made out of aluminum.

Propulsion System Characteristics

The engines used on the TU-ecoliner will be ultra-high bypass ratio geared turbofan engines with a bypass ratio of 14. In order to size this engine, the method of rubber engine sizing is used, with the Pratt & Whitney PW1000G engine series used as reference. Linearly interpolating between two of these PW1000G series engine and scaling it according to thrust resulted in a fan diameter of 1.87 m, a maximum nacelle diameter of 2.36 m and a total length of 4.76 m. The bypass ratio is however not included in the scaling, since no information was available on the engine core of the new Pratt & Whitney engines. The proper dimensions with the bypass ratio included can be obtained once the full cycle calculations are done.

Stability and Control Characteristics

To design for a stable and controllable aircraft, you first need to know the location of the aircraft center of gravity at operational empty weight. In Table 6.22, an overview showing all main aircraft components and their respective center of gravity location is presented.

Table 6.22: Longitudinal c.g. positions of components.

	Mass [kg]	$\mathbf{x_{cg}}$ [m]	**M** [kg·m]
Wing	7,657	20.39	156,125
Horizontal stabilizer	319	41.82	13,337
Vertical stabilizer	957	41.93	40,114
Fuselage	10,203	19.20	195,890
Nacelles	667	17.44	11,626
Nose landing gear	204	4.50	919
Main landing gear	1,837	21.40	39,314
Engines	6,385	17.77	113,428
Fixed equipment	9,916	18.75	185,918
Operational Empty Weight	38,143	20.10	766,680

Using these values for the center of gravity at the operational empty weight of the aircraft as a base, the loading diagram of the aircraft was constructed. This showed a most forward center of gravity location of 0.25 MAC and a most aft center of gravity location of 0.67 MAC, which leads to a center of gravity range of 1.29 m. A scissor plot has been constructed showing the regions of center of gravity in which the aircraft is stable and controllable. Showing the center of gravity ranges for varying wing positions in a plot shows how much the center of gravity shifts with a changing wing position. Overlapping this plot with the scissor plot shows for which wing position the center of gravity range is within the limits of controllablility and stability of the aircraft, making it possible to ascertain a horizontal tail surface.

The final longitudinal wing position and horizontal tail area over wing area ratio is shown in Figure 6.23. The analysis led to a wing leading edge MAC positioned at 42.5% of the fuselage, or 18.75 m measured from the nose. Furthermore, the required horizontal stabilizer surface area was found to be 23.1 m^2.

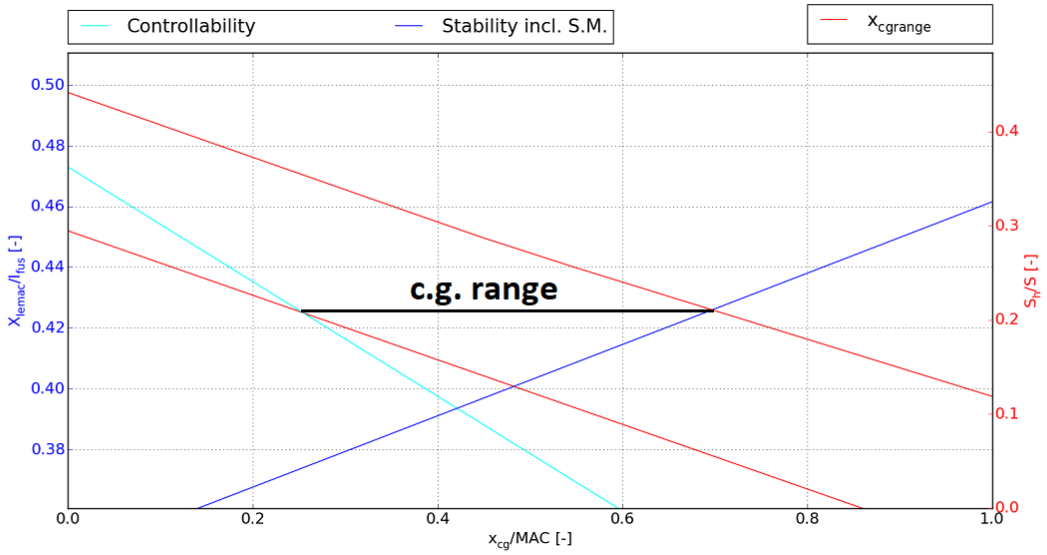

Figure 6.23: Match of scissor plot and c.g. range plot.

Empennage Design

The TU-ecoliner will feature a conventional tail design with a horizontal and a vertical tail surface. The horzontal tail will have a surface area of 23.1 m^2, a taper of 0.33 and an aspect ratio of 4. This brings the span to 9.61 m. The mean aerodynamic chord is determined to be 2.61 m.

The vertical tail will have a surface area of 21.6 m^2, a taper of 0.34 and an aspect ratio of 1.8. The total span of the vertical tail is 6.23 m and the mean aerodynamic chord equals 3.74 m.

Summary of Design Characteristics

Table 5 gives a summary of all relevant parameters and characteristics of the design.

Table 5: Summary of design characteristics

Symbol	Value	Unit	Symbol	Value	Unit	Symbol	Value	Unit
Fuselage planform			*Structures: fuselage*			*Landing gear*		
d_{ext}	4.00	m	material	QI CFRP	-	x_{LG_n}	4.5	m
d_{int}	3.68	m	t_{skin}	1.0	mm	x_{LG_m}	21.4	m
h_{cabin}	2.19	m	n_{string}	83	-	track width	6.49	m
w_{cabin}	3.61	m	*Structures: wing*			height	1.50	m
l_{cabin}	34.40	m	material	QI CFRP	-	tipback angle	15.0	deg
w_{cargo}	2.50	m	t_{spar}	10	mm	scrapeback angle	9.5	deg
h_{cargo}	1.20	m	t_{skin}	27	mm	lateral tipover	63.0	deg
l_{fus}	44.13	m	*Structures: strut*			*Weights*		
Wing planform			material	7075-T6 aluminum	-	$fuel_{max}$	12,161	kg
S	110	m^2	l_{strut}	7.27	m	$payload_{max}$	21,600	kg
A	14	-	t/c	21	%	crew	694	kg
lambda	0.29	-	c	45.1	mm	OEW	38,143	kg
b	39.24	m	*Structures: hor. tail*			MTOW	68,048	kg
c_r	4.34	m	material	7075-T6 aluminum	-	MLW	62,366	kg
c_t	1.26	m	t_{skin}	1.0	mm			
MAC	3.08	m	t_{spar}	6.0	mm			

System Analysis

Multiple subsystems for the aircraft have been designed and analyzed. A detailed design and redundancy philosophy has been presented for the cabin environmental control system, the fuel system, the hydraulic system and the electrical system.

The cabin environmental control system provides a safe and comfortable place to accommodate the passengers and crew. The cabin will be pressurized to a cabin altitude of 8,000 ft, in order to provide a sufficient level of passenger comfort while saving weight. Moreover, the airconditioning will be designed to provide a comfortable cabin temperature when outside temperatures drop to about −56° C. Since the APU will be removed, the aircraft relies on external airconditioning equipment while stationed at the gate.

The fuel system has the main job of providing fuel to the two engines. The aircraft features a total of nine fuel tanks, four in each of the wings and a trim tank in the horizontal tail plane. All the tanks combined can store a total of 15,013 L of Jet A-1 fuel, 7,250 L in each wing and 513 L in the trim tank. Moreover, the fuel system features three fully redundant systems for supplying fuel to the engines.

The hydraulic system provides primary and secondary power to the primary flight controls. It also provides power for deploying and retracting the landing gear, flaps, slats and spoilers. The total system comprises three separate systems, the right, center and left system. These systems provide two levels of redundancy to the hydraulically powered subsystems. The hydraulic power will be provided by electrically driven hydraulic generators.

Since the aircraft is designed to be a more-electric aircraft, meaning that most systems will be powered using electric power, an extensive electrical system is crucial. The electric power will be generated by four engine mounted generators. In case of emergency, electricity can be sourced from one of the two batteries or using the ram air turbine. Power will be distributed using two central power distribution busses, a forward one and a center one. Moreover, the system will be fully redundant and will supply power to electric actuators on the primary flight controls in order to provide two additional layers of redundancy. The removal of the APU means that the aircraft will be more dependent on auxiliary ground power supply. Therefore, two external power connectors are incorporated into the system. Moreover, the aircraft will be connected to a battery in order to provide power for the EGTS.

Final Design Analysis

The final design analysis has been split-up into seven parts. These parts are performance, noise, emissions, RAMS characteristics, cost, risk and budget breakdown analysis. All parts will be covered hereafter.

Performance Analysis

The take-off and landing performance of the TU-ecoliner are assessed using a method as described in Jenkinson [8]. This analysis resulted in a take-off distance of 1,673 m and a landing distance of 1,554 m. The TU-ecoliner needs 35% less runway length for take-off compared to the Airbus A321neo. The speeds associated with the take-off and landing performance are tabulated in Tables 8.1 and 8.5, respectively.

8.1: Speeds as defined in the take-off performance

Speed	Determined from	Value [kts]
$V_{S_{to}}$ (stall speed)	-	131
V_{LOF} (Lift off speed)	$1.1 \cdot V_{S_{to}}$	144
V_2	$1.2 \cdot V_{S_{to}}$	157

Table 8.5: Speeds as defined in the landing performance

Speed	Determined from	Value [kts]
$V_{S_{land}}$ (stall speed)	-	109
V_A (Approach speed)	$1.3 \cdot V_{S_{land}}$	141
V_F (Average Flare speed)	$(1.15 + 1.3) \cdot V_{S_{land}} / 2$	133
V_{TD} (Touch-down speed)	$1.15 \cdot V_{S_{land}}$	125

Furthermore, the second segment climb with one engine inoperative is assessed. The CS25 regulations (CS25.121) specify a minimum climb gradient of 0.024 to be obtained in the second segment climb. The TU-ecoliner reaches a climb gradient of 0.055, which means that this requirement is met.

The climb performance of the TU-ecoliner is depicted in Figure 8.12. This climb performance results in a theoretical service ceiling of 43,100 ft. The discontinuity in the rate of climb graph is due to an empirical relation which is used to take into account the effect of altitude and speed on the thrust. This relation changes after Mach 0.4 and hence the line shows this kink. This relation and an explanation can be found in Section 8.1.5.

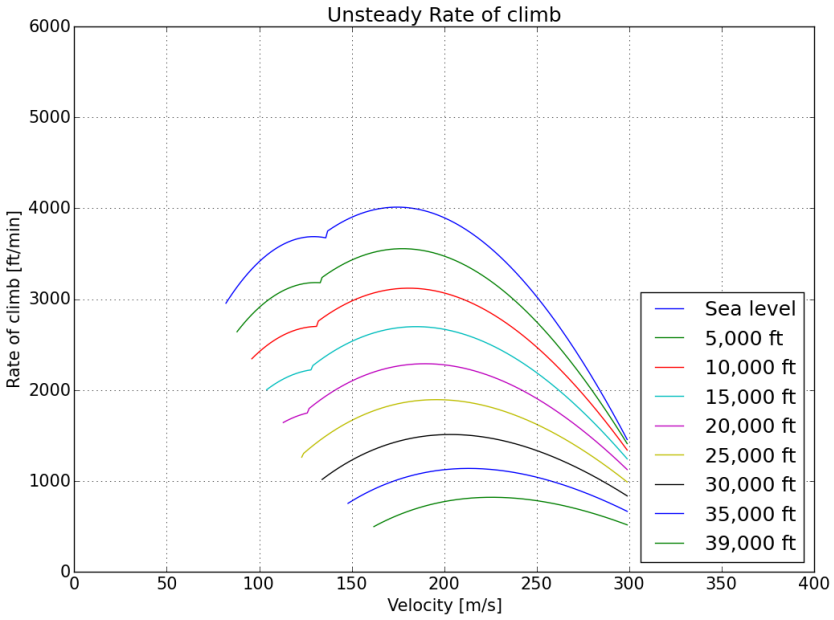

Figure 8.12: Unsteady rate of climb

Noise

In order for a next-generation aircraft to pass certification, it has to pass Chapter 14 noise requirements set by ICAO. The noise of the aircraft can be divided into 2 groups, the airframe noise and the engine noise. The airframe noise of the TU-ecoliner is assessed using NASA's ANOPP noise prediction method, which takes into account the noise generated by the wing, the tailplanes, flaps, slats, landing gear and landing gear strut.

To assess the engine noise using the ANOPP method, detailed engine characteristics are necessary and could not be obtained within the limited time frame. Therefore, the engine noise during the approach phase of the flight is assessed based on a PhD thesis by Lothar [9], in which the assumption is made that during approach the engine noise and airframe noise are comparable. During take-off, the engine noise is estimated assuming that the acoustic power of the jet is proportional to the eighth power of the average engine exit velocity.

Since the ANOPP method does not fully represent the airframe noise of the aircraft, the results of this method can not be compared to actual measured data. Therefore, to have an estimation of the noise emissions of the TU-ecoliner compared to a current aircraft, the aircraft characteristics of the Boeing 737 MAX 8 were used as input in the self-written code. From this comparison, which can be seen Figure 8.23, it follows that during approach after approximately 900 Hz, the Sound Pressure Level (SPL) of the TU-ecoliner is higher than the Boeing 737 MAX 8. However, the noise reduction technologies which will be implemented on the aircraft can not be assessed with this ANOPP method and the code showed some deficiencies. Therefore, the decision has been made to assess the noise of the TU-ecoliner qualitatively bases on the noise reduction technologies. With these noise reduction technologies it is expected that the aircraft will comply with the Chapter 14 noise requirements.

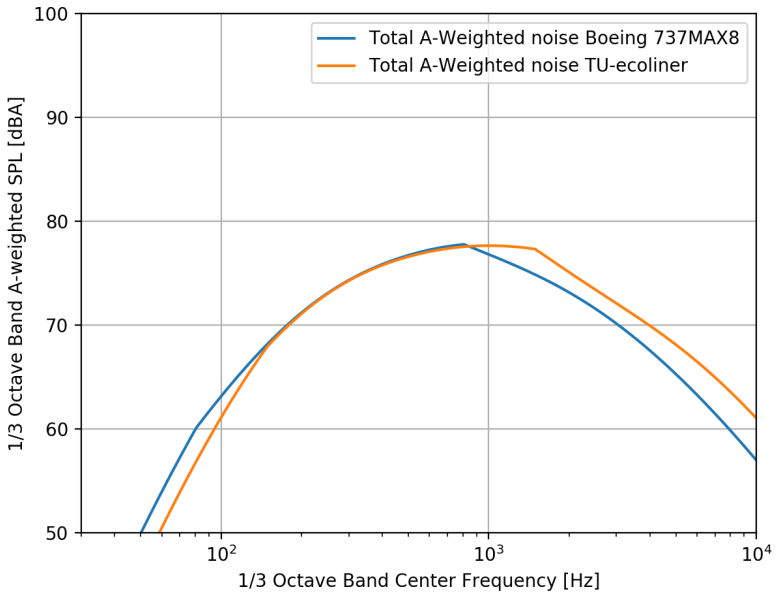

Figure 8.23: Comparison between Boeing 737 MAX 8 and TU-ecoliner in approach conditions

Emissions

Using a database from EASA containing over 500 turbofan engines, a statistical analysis is done on the thrust specific fuel consumption (TSFC) during climb. Looking at the relation between the bypass ratio and TSFC, a regression line was obtained with an R^2 of 0.8872. From extrapolation a TSFC during climb of 6.692 mg/N/s was found[6], which led to a $c_{j_{TO}}$ of 1.425 kg/s. Using fuel consumption ratios statistically obtained for a thrust output of $\frac{213}{2} = 106.5$ kN, a $c_{j_{CR}}$ of 1.171 kg/s and a $c_{j_{AP}}$ of 0.412 kg/s was found.

From the obtained engine fuel consumption the CO_2 emissions of the aircraft could be determined using the fuel consumption, emission index and the time spent in a flight phase. For a flight of 1806 km, 30,657 kg of CO_2 is emitted by the TU-ecoliner. This is a reduction of 17% compared to the Airbus A321neo.

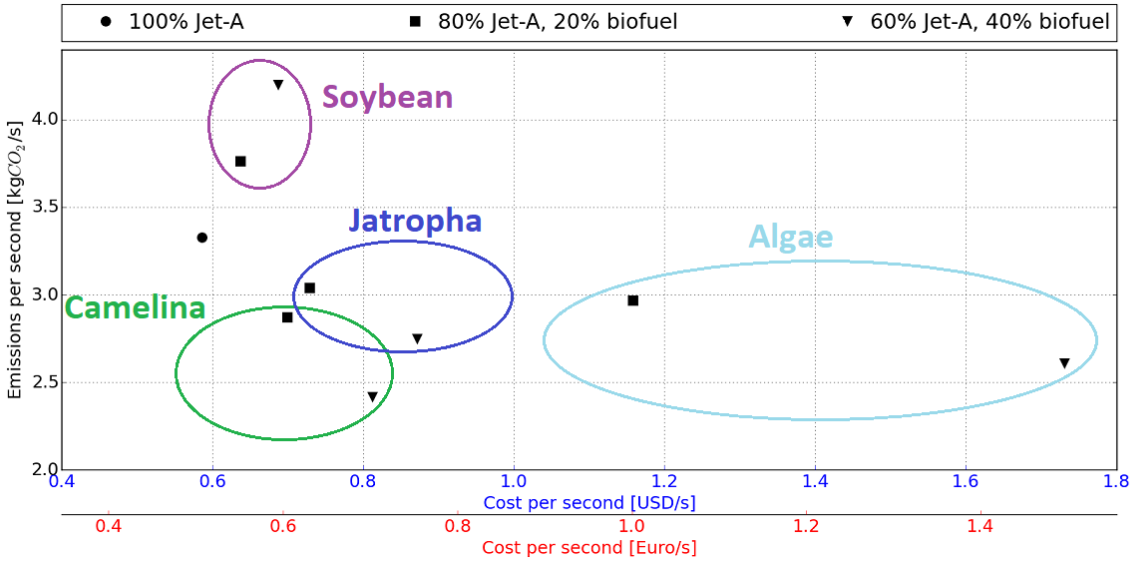

Figure 8.31: Fuel cost per second vs fuel consumption per second for different fuel blends.

[6]This number had been confirmed by looking at the trend of TSFC over time.

Furthermore, the implementation of biofuels is assessed. Different types of biofuels were mixed in a blend of 80% of Jet-A fuel and 20% biofuel and a blend of 60% of Jet-A fuel and 40% biofuel. The results of this assessment are depicted in Figure 8.31. It shows the cost per second and the emissions per second for the different biofuel/conventional fuel combinations.

A blend of kerosene with 40% of e.g. camelina would lead to a decrease in emissions of more than 8 tons compared to when only kerosene is used, leading to 21.7t CO_2 emitted in a flight of 1,806 km.

RAMS Characteristics

The TU-ecoliner is designed to be a highly reliable and safe aircraft. Overall, the reliability of the aircraft is expected to be on par with the current state-of-the art inter-European aircraft like the Airbus A321neo. Reliability might be reduced somewhat by the hybrid laminar flow control system as this is a complex and sensitive subsystem. The engines will also incorporate several new technologies which might be more sensitive to reliability issues. However, the aircraft will be fitted with a state-of-the-art aircraft monitoring system, which allows problems to be communicated at an early stage and maintenance to be properly planned.

A high level of safety will be realized by fully complying with the requirements set by CS-25 [6]. Furthermore, a comprehensive list of safety critical items has been compiled. The items on this list have been heavily Incorporated in the redundancy philosophy, which provides four levels of redundancy to the primary flight controls and three levels of redundancy to the engine fuel supply.

Cost Analysis

The cost analysis was done using statistical methods. The estimated market price of the TU-ecoliner is 85.2 million US dollars. The total production and development costs add up to 33.3 billion US dollars.

Following from the market analysis and estimated market share of single aisle aircraft, it was estimated that 960 TU-ecoliners will be produced over a 30 year production period. The resulting return on investment for the manufacturer is 145.8%. This is approximately 5% per year, which is approximately 3% above the forecast inflation rate.

The direct operating cost has been determined considering fuel, maintenance, crew, depreciation, and insurance cost. The total DOC of the aircraft is 4004 dollars per block hour.

Risk Assessment

The most severe risks that have to be accounted for in the design are:

- R.A.1: An incorrect assumption has been made
- R.A.2: The code does not calculate the intended outcome
- R.A.3: The design fails to comply with CS-25
- R.A.4: Requirements have not been met
- R.M.1: The electric actuators on primary flight controls have not been implemented yet

In order to minimize these risks, mitigation strategies have been decided on. These have to do with for example verification and validation, making good assumptions, keeping track of requirements or creating redundant systems.

Design Rationale

In the design rationale, the requirement compliance matrix and the sustainable developement strategy have been covered.

Requirement Compliance Matrix

During the design process, a requirement compliance matrix has been assembled in order to check if all requirements have been met. All stakeholder and product requirements have been met and almost all system and subsystem requirements have been met. A few requirements are still unknown and only requirement HF-SYS-LG-05 which states that the nose landing gear carries more than 8% of the aircraft weight has not been met.

Sustainable Development Strategy

A sound sustainable development strategy is crucial to the successful design of the TU-ecoliner. Environmental sustainability has mainly been implemented by reducing noise, fuel consumption and emissions. Moreover, a strong emphasis has been put on designing the aircraft to be highly recyclable at its end-of-life. The design team will also work in accordance with AFRA and BMP [10] in order to increase the value of recycled parts to provide a financial incentive for recycling.

Economic and social sustainability will be realized for all stakeholders. This will mainly be achieved by lowering the noise and emissions, and fully complying with all regulations. Moreover, it will be realized by implementing a solid reliability and maintainability strategy.

Outlook

Considering the post-DSE phase of the project, a manufacturing, assembly and integration plan, a project design and development logic and a Gantt chart have been made. The manufacturing, assembly and integration plan gives an overview of the different stages that make up the manufacturing and assembly process. It starts with manufacturing and buying of parts and subsystems, goes through sub-sub assemblies, sub assemblies, the final assembly and painting all the way to flight testing and delivering the aircraft.

The project design and development logic gives an overview of the phases the project goes through after the DSE. It starts with further refining the preliminary design and making a detailed design, next the certification process must be gone trough. After that, the aircraft has to be manufactured, assembled and test flown before it can be delivered to the customer.

The DSE Gantt chart contains all tasks that need to be performed after the DSE in order to deliver the aircraft to the customer. It has a timeline of 15 years, which is the deadline for delivery, starting right after the DSE. Each task has been assigned an approximate duration. The planning is finished in 14 years, which means there is a one year contingency for delays along the way.

Conclusion and Recommendation

The TU-ecoliner presents a convincing response to the environmental challenges facing the future of the aviation industry. With a high strutted wing configuration, an aspect ratio of 14 is attained. The result is a smaller, more efficient wing, that is 19% lighter than a cantilever wing of equivalent aspect ratio and surface area. Implementing a gearbox between the fan and compressor stages allows the turbine and fan to run at their respective optimum speeds, enabling ultra-high bypass ratios to be achieved. Moreover, a geared turbofan presents potential for weight saving, as less compressor and turbine stages are required. Achieving a bypass ratio of 14, the average exhaust velocity is reduced, reducing jet noise and lowering specific fuel consumption by 17%. Finally, with the emphasis on a more electric aircraft, the TU-ecoliner is EGTS compatible, completely eliminating noise and emissions at airports. Furthermore, the removal of the APU, and adoption of electric actuators in place of pneumatic actuators results in weight savings and a bleedless aircraft, increasing engine efficiency.

Taking all technological advancements into account, the TU-ecoliner promises 17% reductions in CO_2 emissions, while reducing DOC by 24% compared to the A321neo, while meeting ICAO Chapter 14 noise regulations. The result is a cleaner, cheaper aircraft, optimized for the typical inter-European range, capable of transporting 240 passengers on over 90% of all European routes, and able to service 10% more airports than the current competition.

Considering all improvements in design and performance, there are still opportunities to further refine the design. With the future of aviation specifically concerned with emissions, noise and migrating to fully electric aircraft, further detailed design iterations can be performed with emphasis on these key aspects. The full performance potential of the aircraft can be realized through a fully detailed design of the engines and wing profile. Finally, a detailed operational analysis will establish the TU-ecoliner as a truly viable option for the future of clean flying.

1

Project Objectives

Nowadays, the International Civil Aviation Organization (ICAO) and other international bodies set CO_2 emission targets in order to lower the impact that the aviation industry has on the environment. This means there is an apparent need for improved efficiencies in the civil air transport sector.

The goal of this project is to design an aircraft for 240 passengers for the inter-European market. The current generation of aircraft that are used on this market result in increasing and avoidable emissions due to their over designed wings and engines. This sub-optimal operation of aircraft is shown in Figure 1.1 [11].

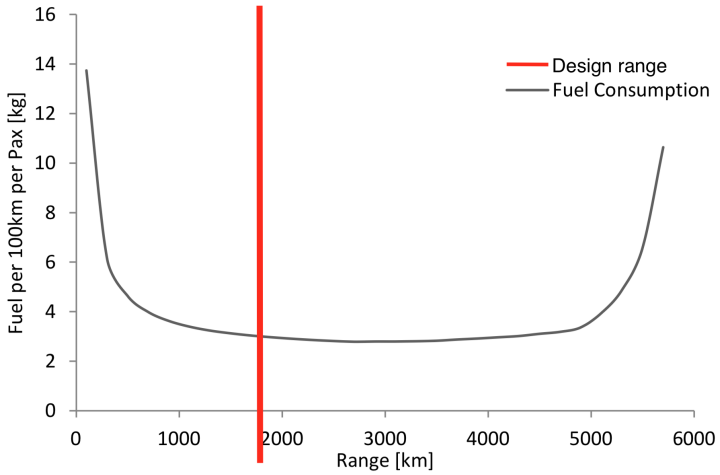

Figure 1.1: Range-fuel consumption diagram of an A320

Reducing Emissions

The main focus during the design is on decreasing its environmental impact by reducing emissions as much as possible. This is where the title of the project "How Far Can We Get?" comes from. It will be visible throughout the project that major design choices will be strongly based on this criterion.

Reducing Noise

Besides the reduction of emissions, also noise reduction is a major objective. Requirement HF-STK-AL-10 states: "The aircraft shall be at least 1 noise class lower compared to current inter-European state-of-the-art aircraft." Aircraft noise can be divided into two categories: airframe noise and engine noise. A reduction in the combination of these two will be the objective.

Reducing Direct Operating Cost

A third objective is optimizing the direct operating cost. For this, requirement HF-STK-AL-09 says: "The direct operating cost of the aircraft shall be at least 10% lower compared to current inter-European state-of-the-art aircraft." The direct operating cost of an aircraft includes fuel, crew, maintenance and owning cost. Lowering any of these will lower the total direct operating cost.

2

Market Analysis

An analysis of the current and future markets has been performed to determine stakeholder demands, and to forecast the areas of growth for the next generation of aircraft. Specific attention will be payed to inter-European routes. Identifying these demands will allow for the development of an aircraft that will be well positioned in the market, and more attractive than the current competition. Specific metrics such as passenger capacity, range, take-off length and direct operating costs will be determined, and stakeholders will be identified to develop a series of aircraft requirements in Chapter 3.

2.1. High Demand Routes

A significant area of interest in the current market is the identification of the routes with high demand. These routes give a general indication of the needs and demands of passengers, airlines and airports, with respect to range and capacity. Furthermore, the competition can be identified.

The average distance flown by low cost carriers (LCCs) in Europe is 1,150 km, with passenger capacity increasing 12% in the years between 2002 to 2016 [5]. To further determine high demand routes in Europe, lists of high demand airport pairs[1] and country pairs [2] have been analyzed. From the list of airport pairs it can be seen that the most high-demand routes are relatively short distances. The longest route in the list (Paris-Nice) is not even 700 km and the shortest route in the top ten (Barcelona-Palma de Mallorca) is 200 km.

From a more recent study of the 20 busiest air travel routes globally, two inter-European routes are present in the list [12]. These are the Dublin-London Heathrow (DUB-LRH) and Amsterdam-London Heathrow (AMS-LHR) routes. Both saw the transport of approximately 1.8 million passengers in 2017. The DUB-LHR route involves an average stage length of 449 km and the average stage length of the AMS-LHR route is 365 km.
A large competitor for the really short range market of routes up to 1,000 km is high speed rail. On certain routes in Europe high speed rail offers a strong alternative to aircraft. On the route London to Paris the high speed train has a market share of 80% [3] operating 15 trains a day. Furthermore there are several other connections between city pairs in Europe but many cities remain unconnected to the high speed rail network and it will take much loner than one generation of aircraft to connect these. Also when there is a proper connection such as Berlin-Munich there is still a high demand for air travel so rail does not necessarily pose a significant commercial threat to short range air travel.

2.2. Market Forecast

The demand for global aviation is expected to more than double over the next twenty years [5, 13]. The domestic and inter-regional European market is expected to have an annual growth rate of 2.9% [5]. This growth is driven by a demand for approximately 5,500 single aisle aircraft to be delivered in Europe alone, over the next two decades [5, 13]. Approximately 45% of the regional single aisle aircraft will be large single aisle aircraft [14]. Single aisle aircraft are forecast to occupy 71% of total global aircraft deliveries in this timespan [13]. This data clearly demonstrates the significant demand for this aircraft type in the future.

[1] `http://ec.europa.eu/eurostat/statistics-explained/index.php?title=File:Top_10_airport_pairs_within_the_EU28_2016.jpg` [cited 8 May 2018]

[2] `http://ec.europa.eu/eurostat/statistics-explained/index.php?title=File:Intra-EU_traffic_at_country_level_Top-10_country_pairs_represent_40_%25_of_2016_intra-EU_traffic.png` [cited 8 May 2018]

[3] `https://www.theguardian.com/commentisfree/2016/oct/28/eurostar-exile-europe-brexit-britain-relationship_france` [cited 8 May 2018]

With the smallest members of the A320 and 737 families only accounting for 2% of deliveries [15], it is an apparent trend that larger single aisle aircraft like the A321neo are in high demand [16]. The market forecast analysis identified that European carriers, especially LCCs, are increasing the seat capacity on their flights [5]. Carriers such as EasyJet have upgraded their orders for 30 of the A320neo, to the larger A321neo in order to increase route capacity [4]. Therefore it is concluded, that a seating capacity of 240 passengers in a single class configuration is found to be desirable for the market.

The increase in single-aisle aircraft capacity is a response to the increasing number of passengers who travel due to lower cost tickets. This requires LCCs to focus on greater aircraft and operation efficiencies, in order to yield sufficient revenues [5]. This trend is also in line with the increasing emphasis on sustainability, due to the targets set by government bodies such as ICAO. One of these targets is a 2% annual increase in fuel burn efficiency [4]. This goal is a response to the UN 2030 Agenda for Sustainable Development.

2.3. Aircraft Range

For the range determination, a data set[5] of twelve different days was used, with each day containing a list of every flight within Europe on that day. This data set ranges from May 2016 to February 2017. As all days are in a different period of the year, this gives a reasonable estimate for the daily traffic throughout the year. The ranges of 20,000 flights a day were plotted in a histogram, resulting in a 12 day average. As can be seen in Figure 2.1, the histogram is heavily skewed to the left, indicating that short range routes are flown most frequently, supporting the findings of Section 2.1. From the data set, it can be deduced that in order to cover 90% of flights, on average[6] a range of around 1,800 km is needed.

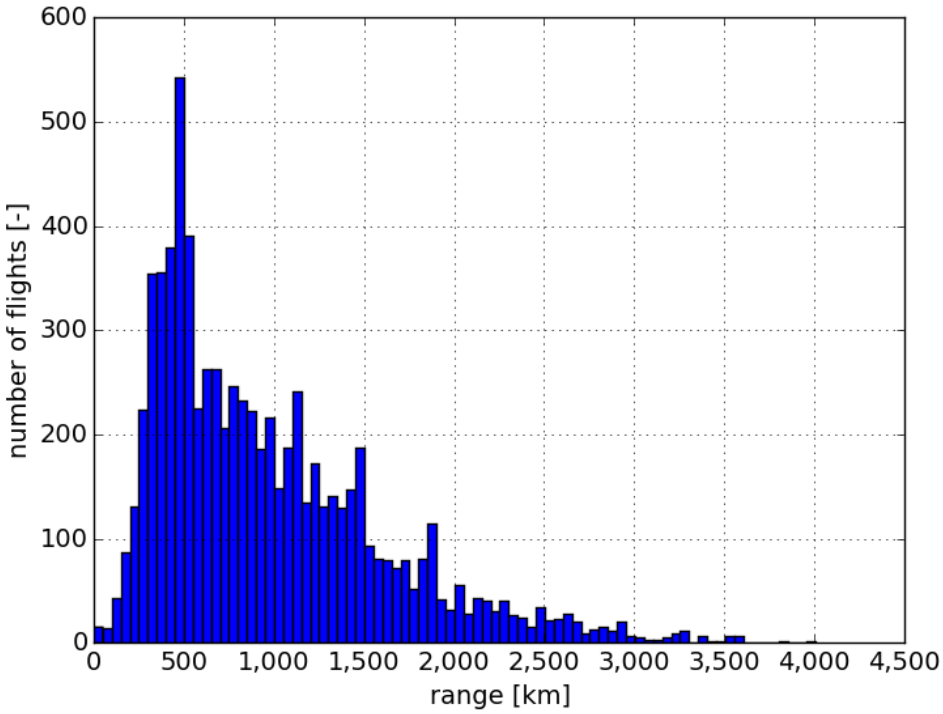

Figure 2.1: Range distribution functions of inter-European flights during twelve different days.

Finally, the passenger load factor must be determined. According to the Airbus Global Market Forecast [5], the global load factor in 2016 was around 80%, compared to 65% in 1990. Recently however, the load factor is seen to be increasing at a slower rate. Therefore, a load factor of 94% is assumed for the next generation aircraft and hence the aircraft has to perform the design range with a load factor of 94%.

[4] `http://corporate.easyjet.com/corporate-responsibility/environment` [cited 30 April 2018]
[5] These data files have been obtained in a previous project during the bachelor, provided by the tutor.
[6] The data of twelve different days have been compared for a 90% flight coverage.

2.4. Aircraft Required Take-off Length

A preliminary requirement was set regarding the required take-off length of 2,000 m [17]. To determine what impact this has on the operation of the aircraft, a list of all paved runways in Europe is obtained from the CIA World Fact Book[7] and summarized in a graph as can be seen in Figure 2.2. From this graph it can be seen that if the aircraft requires a take-off distance of 2,000 m, it can use approximately 77% of the airports in Europe. Reference aircraft such as the Airbus A321-200 and Boeing 737-800 have a required take-off length of 2,280 m and 2316 m[8] respectively, as indicated in Figure 2.2. This makes approximately 67% of Europe's airports accessible. Thus, designing for a maximum take-off length of 2000 m, allows the aircraft to operate at least 10% more airports than its competitors.

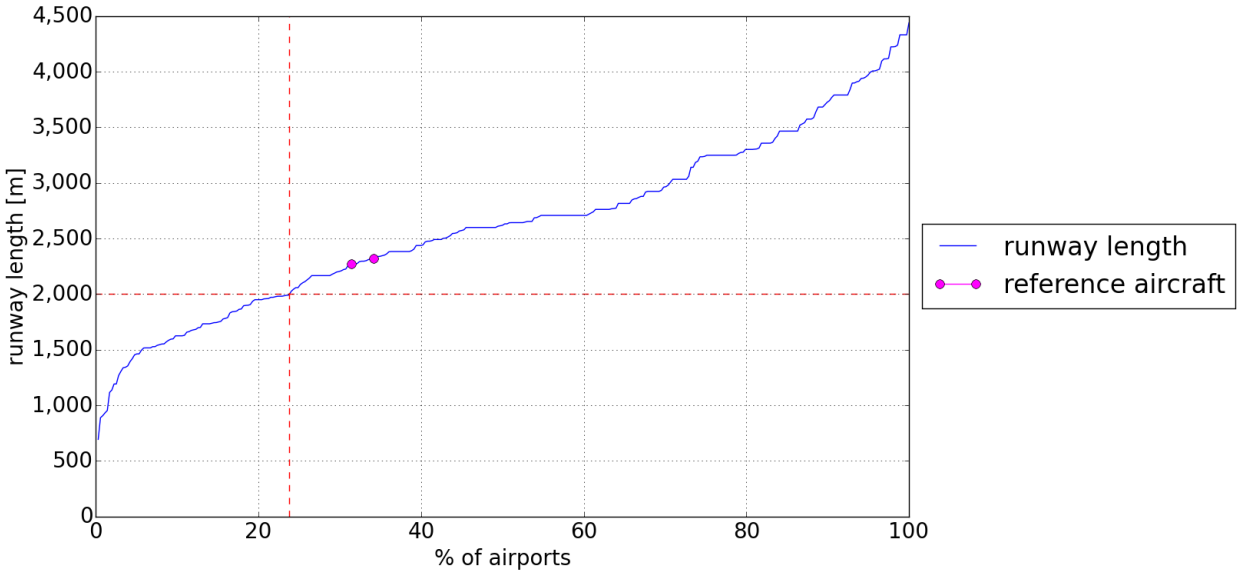

Figure 2.2: Runway distribution function of paved European runways.

2.5. Aircraft Direct Operating Costs

In order to make the aircraft more attractive to costumers, it should be cheaper to operate compared to its competitors. Therefore, the aircraft should have at least 10% lower direct operating cost (DOC), where the DOC consists of maintenance costs, crew costs, ownership costs and fuel costs[9]. However, crude oil prices are expected to increase from 63$ a barrel to around 85$ a barrel in 2025[10]. Therefore, comparing the DOC of the designed aircraft in 2025 with the aircraft nowadays is not legitimate. So, to have a proper comparison of the DOC, the fuel and oil costs will be kept fixed at the 2017 value.

An indication of comparable aircraft DOC was obtained using data from the Bureau of Transportation Statistics. Table 2.1 indicates the operating costs in dollars per flying hour for comparable sized aircraft. Where flying hour is the time between take-off and landing[11]. From this table it can be seen that operating costs of the new generation aircraft such as the A320neo and the Boeing 737 MAX 8 are lower than those for the older generation, which is predominantly caused by the lower maintenance costs. However, this conclusion is questionable, since the amount of data points (flying hours) is insufficient.

[7] `https://www.cia.gov/library/publications/the-world-factbook/fields/2030.html` [cited 30 April 2018]
[8] `http://booksite.elsevier.com/9780340741528/appendices/data-a/default.htm` [cited 30 April 2018]
[9] `https://www.icao.int/MID/Documents/2017/Aviation%20Data%20and%20Analysis%20Seminar/PPT3%20-%20Airlines%20Operating%20costs%20and%20productivity.pdf` [cited 1 May 2018]
[10] `https://www.thebalance.com/oil-price-forecast-3306219` [cited 8 May 2018]
[11] `https://www.transtats.bts.gov/Fields.asp` [cited 9 May 2018]

Table 2.1: Direct operating cost distribution of 9 reference aircraft of 2017

Aircraft	Cost per flying hour (USD/h)								Flying hours (h)
	Fuel & Oil	Maintenance	Crew	Depreciation	Rental	Insurance	Other	TOTAL	
A319	1,495	841	990	334	306	4.88	5.37	**3,670**	951
A320	1,568	915	971	319	312	4.56	9.52	**3,788**	1,706
A320neo	1,651	395	678	226	944	2.46	2.93	**2,955**	28
A321	1,828	971	1,267	327	429	0.57	1.32	**4,395**	1,109
B737-900	1,433	583	1,079	341	16	1.83	1.27	**3,438**	630
B737-800	1,599	810	1,179	331	283	5.17	2.62	**3,927**	2,510
B737-700 MAX 7	1,625	900	1,195	291	174	9.51	0.05	**4,020**	1,828
B737 MAX 8	1,683	214	1,155	413	20	10.10	0.00	**3,475**	10
B757-200	2,010	1,599	1,509	702	192	7.02	19.96	**5,847**	863
AVERAGE	**1,655**	**803**	**1,114**	**365**	**298**	**5.12**	**4.78**	**3,946**	

2.6. Technical SWOT Analysis

In this section the technical SWOT analysis is performed, and presented in Figure 2.2. A technical SWOT analysis is a useful tool to analyze the product, in this case the aircraft, on multiple aspects. The internal strengths and weaknesses are assessed. This includes researching what the aircraft in itself is good at and how it performs compared to competitors. The external factors are assessed under opportunities and threats. These include factors like market trends or regulatory actions, things that the aircraft has no influence on but do have an influence on its commercial performance and operations.

Table 2.2: Technical SWOT analysis

	Helpful	Harmful
Internal	**Strengths** - Fuel saving because of lower design range - Lower direct operating cost - Lower emissions - Higher payload capacity than average inter-European flights	**Weaknesses** - Small range (so less flexibility) - Required take-off length - Required airport analysis
External	**Opportunities** - Growing aviation market - Need to make aviation more sustainable - Increased inter-European migration flows (international labor market)	**Threats** -Lot of knowledge and facilities in hands of current oligopoly market making semi-homogeneous products → difficult to compete - Stronger (environmental) regulations - Increased aviation taxes/charges

2.7. Target Cost

To ensure a competitive aircraft is designed, it is necessary to have a target cost that ensures the aircraft performs well on the market. To find a competitive price for the aircraft, comparable aircraft prices were referenced. The main competitor for this aircraft is the A321neo, which has a list price of 129.5 million USD[12]. As the aircraft will not enter service for another 15 years the aircraft price will be expressed in fiscal year 2018. This enables the sales team to take inflation into account in the price in 15 years time. As cost of ownership is a large part of the direct operating cost of an aircraft, the aimed price of the aircraft will be 10% lower than that of the A321neo. Therefore the target selling price of the aircraft will be 116.55 million USD.

[12] `http://www.airbus.com/newsroom/press-releases/en/2018/01/airbus-2018-price-list-press-release.html` [cited 1 May 2018]

2.8. Stakeholders

The following five groups have been identified as stakeholders due to their interest or involvement in this aircraft's development program. Each stakeholder has requirements which must be defined and ultimately complied with. The stakeholder requirements are summarized in the breakdown chart in Figure 2.3.

2.8.1. Airlines

Airlines are seen as a primary stakeholder as they are often the primary customer, i.e. they purchase the final product. They (may) have different interests that flow down into requirements, generally putting constraints on the design. The interests and considerations of airlines may be summarized as follows[13].

- The range (in combination with payload) should be such that the airline can operate on its desired routes with a desired payload capacity.
- The Direct Operating Cost (DOC) should be low for airlines as their primary purpose is to make profit.
- The internal fuselage arrangement, which results in a passenger capacity, is also of major importance for airlines. It has a big influence on the profit an airline can make.
- One of the primary goals of (air) transport is to bring the passengers as quickly as possible to their destinations. Therefore aircraft parameters as cruise speed (V_{cruise}) have a high priority for airlines.
- For an airline, the environmental impact of its fleet is important. Airports charge landing charges which contain noise and emissions charges, depending on the noise and emissions level of the aircraft[14].
- The general flight performance of aircraft is of interest to the operating airline, as this determines the efficiency of the aircraft and passenger comfort, among others. A special category within flight performance is the take-off and landing performance, flowing down into a required take-off and landing distance. This distance is an important parameter as it determines on which airports the aircraft can land and therefore determines the possible network. For now this stakeholder requirement has been set such that it corresponds to the findings in Section 2.4.

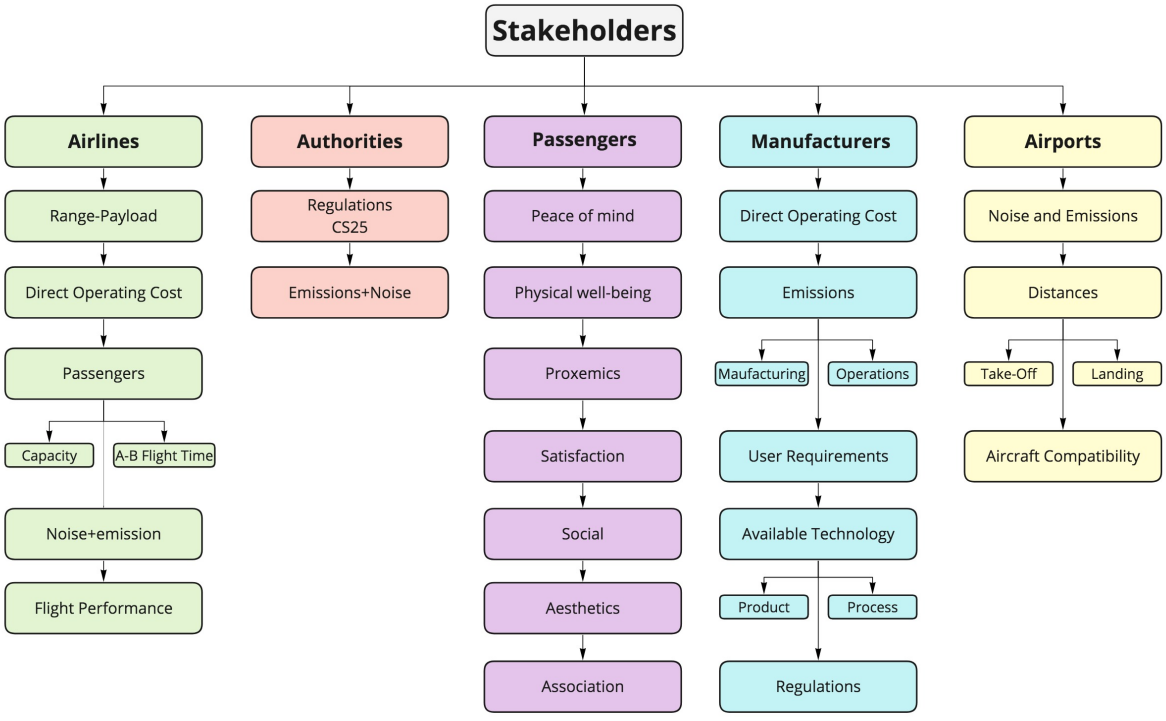

Figure 2.3: Stakeholder Requirement Breakdown

[13] Note: these are not yet formulated as requirements.

[14] `https://www.easa.europa.eu/eaer/topics/market-based-measures/airport-charging-schemes` [cited 2 May 2018]

2.8.2. Authorities

The design of the aircraft has to be such that it complies with the regulations set by authorities. If not, the aircraft will not receive certification and has to be redesigned, hence authorities are important stakeholders. This regulatory function is performed by the European Aviation Safety Agency (EASA)[15]. This agency has multiple certification specifications, where CS-25 is specifically for large aircraft.

From a noise perspective, the aircraft must comply with the CS-36 noise regulations [7]. These are prescribed by ICAO in Annex 16 to the Convention on International Civil Aviation, Volume I [18]. Certification requirements on engine emissions are also specified by ICAO in Volume II of this Annex [19]. These emissions are: unburned hydrocarbons (HC), carbon monoxide (CO), oxides of hydrogen (NO_x) and smoke. Reference times and thrust settings are defined during which emissions are measured. They are based on the operating modes of the landing and take-off (LTO) cycle: take-off, climb, approach, taxi/ground idle.

2.8.3. Passengers

The entire aircraft development program essentially is a direct response to passenger travel needs and requirements. Passengers have considerable influence on the design of the aircraft, and should be treated as stakeholders. Passenger concerns can be broken down into eight distinct factors [20], each describing one aspect of flight experience. The first factor: 'peace of mind' implicates a state of psychological ease and corresponds to concerns for security, tranquility and relief. The second factor: 'Physical well being' indicates the physical aspect of comfort concerning bodily support and energy. Factor number three: 'Proxemics' relates to the amount of autonomy, control and privacy passengers can achieve within the limits of their seat. Factor number four: 'Satisfaction' represents an experience of gratitude as soon as the concerns or accessibility, adequacy and quality of design are fulfilled. Factor number five: 'Pleasure' represents the joyful experience on board and the extent to which the anticipations of the passenger are exceeded. The sixth factor: 'Social' is the interaction between passengers on board the aircraft and the extent to which they tolerate each others' behaviour. Factor number seven: 'Aesthetics' refers to the neatness and style the passenger experiences. The eighth and final factor: 'Association' involves evoking familiar memories and symbolism.

2.8.4. Manufacturers

The manufacturer is defined as the company that designs and assembles the aircraft. Even though the manufacturing team and design team often fall within the same company, they have separate roles within the company. Thus, 'manufacturers' can be seen as an individual stakeholder that should be taken into account by the design team when designing the aircraft. The manufacturer requirements are mainly composed to ensure the manufacturer is able and allowed to sell the aircraft once it has been designed and built. Therefore, the manufacturer requirements concern customer related points such as direct operating cost and operational emissions of the aircraft, but also manufacturing aspects such as emissions due to manufacturing.

2.8.5. Airports

Airports are also considered major stakeholders in the development of new aircraft, as almost all aircraft operations after delivery take place in and between airports. As such, the regulations and requirements that airports enforce shall be taken into consideration. To accommodate new aircraft, airports are specifically concerned with the compatibility of aircraft with existing equipment; as such the aircraft's dimensions are constrained by airport taxiway and gate clearances. Lastly, the aircraft must be compatible with existing ground support equipment. This includes jet bridges, stair trucks, refuelers, tugs and ground power units.

Furthermore, airports require that aircraft comply with their noise and emission mitigation initiatives, which vary per airport. Airports with a certified environmental or quality management system manage approximately 80% of European air traffic [16]. Most of these measures aim to reduce the aircraft's reliance on consuming jet fuel on the ground with initiatives such as 'green taxiing' and the adoption of electrically powered ground support equipment.

2.8.6. General Public

As final important stakeholder there is the general public. As aircraft are still polluting the environment and creating noise around airports. The most important sub group of this general public are the people living in the vicinity of the airports. They suffer the most from noise and emissions pollution. The current trend that more and more restrictions are put on airport operations and operating hours is due to complaints of their neighbours. This puts a restriction on the growth of the industry. If quieter and less polluting aircraft are designed, maybe these restrictions can be reversed.

[15] `https://www.easa.europa.eu/the-agency/the-agency` [cited 2 May 2018]
[16] `https://www.easa.europa.eu/eaer/topics/airports` [cited 3 May 2018]

3
Requirements

The requirements chapter shall firstly present the user requirements. Thereafter, the user requirements that are not specified in enough technical detail are further specified in Section 3.2. Requirements for the aircraft as a whole are referred to as product requirements. These requirements for the aircraft are then broken down to system and subsystem requirements.

3.1. User Requirements

The users for this project were identified as the airlines, authorities, airports and of course the passengers. The requirements of each of the aforementioned categories were determined in the baseline report [3] and are presented below in Table 3.1.

Table 3.1: List of all user requirements

ID	Requirement
Airlines	
HF-STK-AL-01	The aircraft shall have a range of 1,800 km with a load factor of 94%[1].
HF-STK-AL-02	The aircraft shall be able to carry 240 passengers in single class configuration.
HF-STK-AL-03	The aircraft shall have a maximum cruise speed comparable to current state-of-the-art inter-European airliners.
HF-STK-AL-04	The aircraft shall have a service ceiling of 12 km.
HF-STK-AL-06	The aircraft shall be able to take off within 2,000 m at ISA conditions at sea level.
HF-STK-AL-07	The aircraft shall be able to land within 2,000 m at ISA conditions at sea level.
HF-STK-AL-08	The aircraft shall be able to carry at least 10 LD3-45W cargo containers.
HF-STK-AL-09	The direct operating cost of the aircraft shall be at least 10% lower compared to current inter-European state-of-the-art aircraft using an average fuel price of 1.69 USD per gallon [2].
HF-STK-AL-10	The aircraft shall be at least 1 noise class lower compared to current inter-European state-of-the-art aircraft.
HF-STK-AL-11	The aircraft shall be operational within 15 years.
HF-STK-AL-12	The aircraft shall have an emissions reduction of at least 10% compared to current inter-European state-of-the-art aircraft.
HF-STK-AL-13	The aircraft shall have a operational life of at least 30 years.
Authorities	
HF-STK-AU-01	The aircraft shall comply with CS25 [6].
HF-STK-AU-02	The aircraft shall comply with CS36 [7].
HF-STK-AU-03	The aircraft shall comply with the emission requirements prescribed in Annex 16 to the Convention on International Civil Aviation, Volume II [19].
Airports	
HF-STK-AP-01	The aircraft shall satisfy taxiway clearances.
HF-STK-AP-02	The aircraft shall satisfy gate clearances.
HF-STK-AP-03	The aircraft shall be compatible with existing airport ground support equipment.
Passengers	
HF-STK-PS-01	The cabin shall be able to store the carry-on luggage taken on board by passengers.
HF-STK-PS-02	The seating area shall have enough legroom to sit comfortably.
HF-STK-PS-03	The passengers shall be able to make use of all passenger intended areas.

[1] This has been determined in Section 2.3

[2] `https://www.statista.com/statistics/197689/us-airline-fuel-cost-since-2004/` [cited 9 May 2018]

3.2. Specified Product,System and Subsystem Requirements

Following from the user requirements, the product (complete aircraft) requirements are specified in technical terms and further specified for each system and subsystem. These requirements are presented in Table 3.2

Table 3.2: List of all product, system and subsystem requirements

ID	Requirement
Product Requirements	
Pre-flight operations system requirements	
HF-PROD-PFOPS-01	The center of gravity shall not shift beyond the safety limits, when loading the cargo.
HF-PROD-PFOPS-02	The center of gravity shall not shift beyond the safety limits, when loading the passengers.
HF-PROD-PFOPS-03	The aircraft shall be compatible with modern communication technology.
Ground operations requirements	
HF-PROD-GO-1	The aircraft shall not tip over during taxiing.
Flight requirements	
HF-PROD-FLT-01	The center of gravity of the aircraft shall stay between 25 and 65 %MAC during all operations of the aircraft.
HF-PROD-FLT-02	The aircraft shall be statically stable along all axes.
HF-PROD-FLT-03	The aircraft shall be dynamically stable along all axis.
HF-PROD-FLT-04	The aircraft shall have a scrapeback angle of 9.5 degrees.
HF-PROD-FLT-05	The aircraft shall be controllable within the flight envelope.
HF-PROD-FLT-06	The aircraft shall have a climb rate of at least 2000 ft/min.
HF-PROD-FLT-07	The maximum mach operating number shall be 0.82 M.
HF-PROD-FLT-08	The aircraft shall be able to loiter for 30 minutes.
HF-PROD-FLT-09	Passengers shall be able to safely disembark from the aircraft.
HF-PROD-FLT-10	The aircraft shall be able to operate on an airport with an LCN of 50.
HF-PROD-FLT-11	The aircraft shall be able to cruise at 0.79 M.
System and Subsystem Requirements	
Wing	
HF-SYS-WING-01	The wing loading (W/S) shall be at least 6000 N/m^2.
HF-SYS-WING-02	The optimum C_L at clean configuration shall be at least 0.73.
HF-SYS-WING-03	The critical mach number shall be at least 0.79.
HF-SYS-WING-04	The drag divergence mach number shall be at least 0.82.
HF-SYS-WING-05	The incidence angle of the wing shall be 3.3 degrees.
Wingbox	
HF-SYS-WING-BOX-1	The wingbox shall not yield in bending at any point along the span due to a pull-up manuever at MTOW.
HF-SYS-WING-BOX-2	The wingbox shall not yield in shear at any point along the span due to a pull-up maneuver at a load factor of 2.5 at MTOW.
HF-SYS-WING-BOX-3	The The von Mises stress shall not exceed the effective yield strength of the wingbox material at any point due to a pull-up maneuver at a load factor of 2.5 at MTOW.
HLD's	
HF-SYS-WING-HLD-1	The HLD's shall be able to provide a $\Delta C_{L_{max}}$ of 1.55 at 50 degrees deflection.
HF-SYS-WING-HLD-2	The margin between the beginning of the flaps and fuselage along the wing span shall be at at least 5 cm.
HF-SYS-WING-HLD-3	The margin between the beginning of the slats and the fuselage along the wing span shall be 2 m.
Aileron	
HF-SYS-WING-AIL-1	The aileron shall be able to roll the aircraft by 45 degrees within 1.4 seconds.
HF-SYS-WING-AIL-2	The position of the aileron shall not hinder the operation of other wing devices or systems during operation.

Propulsion	
HF-SYS-PROP-01	The thrust loading (T/W) shall be less than 0.32.
HF-SYS-PROP-02	The engine shall deliver a maximum static thrust of 213 kN at sea level.
HF-SYS-PROP-03	The engine shall have a ground clearance of at least 0.5 m.
Fuel system	
HF-SYS-PROP-FUE-01	The fuel system shall provide three levels of redundancy in fuel supply to the engines.
HF-SYS-PROP-FUE-02	The fuel tanks shall be able to carry 12,161 kg of Jet A-1 fuel.
HF-SYS-PROP-FUE-03	The left and right wing fuel tanks shall be able to store 7,250 L each.
HF-SYS-PROP-FUE-04	The empennage fuel tank shall be able to store stored 510 L.
Landing gear	
HF-SYS-LG-01	The pressure on the wheel braking systems shall not exceed those specified by the brake manufacturer.
HF-SYS-LG-02	The angle between the lateral landing gear position and the cg about the z-axis shall be at most 63 degrees [21].
HF-SYS-LG-03	The angle between the longitudinal landing gear position and the cg about the z-axis shall be at least 15 degrees [21].
HF-SYS-LG-04	All landing gears shall be able to be fully stored within the fuselage after take-off.
HF-SYS-LG-05	The nose landing gear shall not carry less than 8% of the aircraft weight.
HF-SYS-LG-06	The nose landing gear shall not carry more than 14% of the aircraft weight.
Braking system	
HF-SYS-LG-BS-01	The Braking system shall be able to provide a friction reaction coefficient of 0.4.
Fuselage structure	
HF-SYS-FUS-01	The cabin shall maintain a pressure equivalent to 2,438 m altitude at ISA conditions under normal operating condition.
HF-SYS-FUS-02	The fuselage skin shall not buckle during take-off.
HF-SYS-FUS-03	The fuselage structure shall not yield in bending during take-off at a load factor of 2.5.
HF-SYS-FUS-04	The fuselage structure shall not yield in shear during take-off at a load factor of 2.5.
HF-SYS-FUS-05	The fuselage structure shall not yield in bending during landing at a load factor of 2.5.
HF-SYS-FUS-06	The fuselage structure shall not yield in shear during landing at a load factor of 2.5.
Cabin Layout	
HF-SYS-FS-CL-01	The seat pitch shall be at least 28 in.
HF-SYS-FS-CL-02	The head-space height shall be at least 65 in.
HF-SYS-FS-CL-03	The aisle width shall be at least 19 in.
Floor	
HF-SYS-FS-FL-01	The cabin floor shall be level during cruise.
HF-SYS-FS-FL-0l'	The cabin floor shall not yield at 100% loading at a load factor of 2.5.
Stringers	
HF-SYS-FS-ST-01	The stringers installed on the fuselage shall not overlap one another
HF-SYS-FS-ST-02	The stringers shall not fail due to crippling stress.
HF-SYS-FS-ST-03	The stringers shall not fail due to maximum bending stress experienced during operations.
Horizontal tail	
HF-SYS-TAL-01	The horizontal tail shall be placed at least 0.5 m above the engine thrust direction.
Horizontal tail wingbox	
HF-SYS-TAL-BOX-1	The horizontal tail wingbox shall not yield in bending at any point along the span during landing at most forward cg position.
HF-SYS-TAL-BOX-2	The horizontal tail wingbox shall not yield in shear at any point along the span during landing at most forward cg position.
HF-SYS-TAL-BOX-3	The von Mises stress shall not exceed the effective yield strength of the horizontal tail wingbox material at any point of the span during landing at most forward cg position.

Hydraulic and electric system	
HF-SYS-HYS-1	The hydraulic system shall be able to deliver the primary power to flight controls.
HF-SYS-HYS-2	The hydraulic system shall have two levels of redundancy.
HF-SYS-ECS-1	The electric system shall be able to provide two additional levels of redundancy to the flight control system.
HF-SYS-ECS-2	The electric system shall have three levels of redundancy for the power supply.

3.3. Constraints

Several types of constraints can be identified. The constraints are divided into technical and non-technical constraints. These constrains are presented in Table 3.3.

Table 3.3: List of technical and non-technical constraints

Type	Constraints
Technical	
Materials	A certain combination of specific strength, specific weight, fatigue resistance and elasticity constrains the material selection.
Fuel type	The fuel specific energy, mass density, amount of net CO_2 emissions produced due to fuel production and burn per MJ and the cost.
Engine technology	The maximum thrust, specific fuel consumption, noise and fan size.
Non-technical	
Resources	A justified conceptual design shall be finished by 9 team members of 5 8 hour working days per week.
Schedule	A conceptual design shall be finished within 10 weeks.
Cost	Follows from HF-STK-AL-09
Legal	The aircraft shall comply with CS25 [6], CS36 [7] and emission requirements prescribed in Annex 16 to the Convention on International Civil Aviation, Volume II [19].

4

Preliminary Design

4.1. Design concepts and Trade-off

The following section will start by describing the design concepts that have been formed in Subsection 4.1.1. Followed by the trade-off criteria in Subsection 4.1.2 The results of the trade-off are discussed in 4.1.3 along with a sensitivity analysis in Section 4.2. Finally, the recommended design will be described in Section 4.3.

4.1.1. Design Concepts

In the first phase of the project six design concepts were formed based on a performed technology assessment. Each concept was build around a single major design choice, to ensure a set of six coherent concepts. The different concepts are depicted in Figures 4.1 to 4.6. A short description of the characteristics of the concepts can be found in the captions of each design.

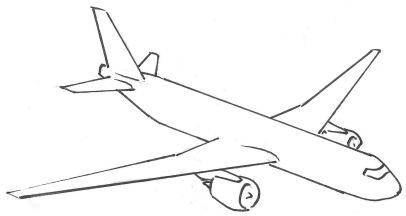

Figure 4.1: Concept 1 - Baseline design with geared turbofan engines

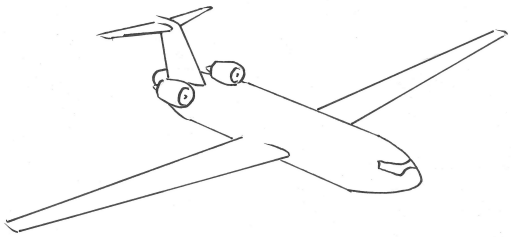

Figure 4.2: Concept 2 - Double-bubble fuselage with ultra high bypass ratio engines

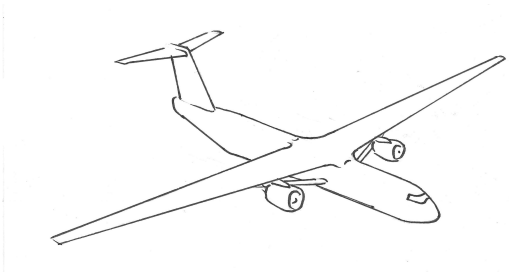

Figure 4.3: Concept 3 - High aspect ratio, strutted wing with circular fuselage and intercooled turbofan engines

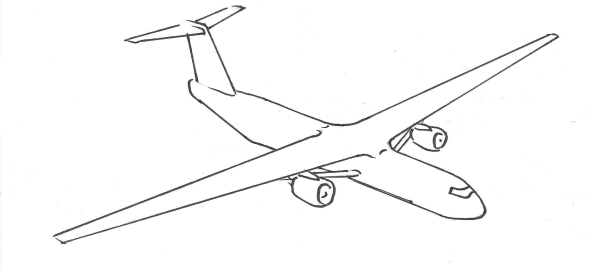

Figure 4.4: Concept 4 - High aspect ratio, strutted wing with non-circular flattened bottom fuselage and ultra high bypass ratio engines

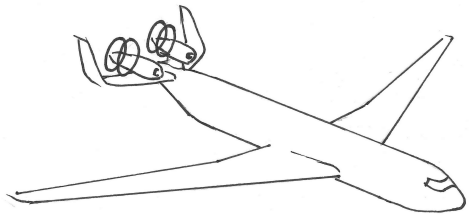

Figure 4.5: Concept 5 - High aspect ratio wing with circular fuselage and propfan engines shielded by a U-tail

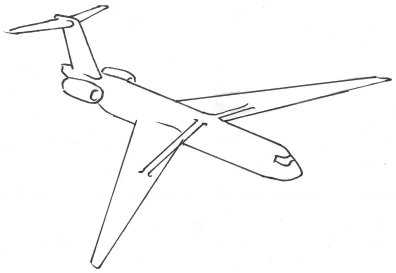

Figure 4.6: Concept 6 - High aspect ratio, forward swept, strutted wing circular fuselage and geared turbofan engines

4.1.2. Trade-off Criteria

The design team has identified five main trade-off criteria upon which each of the six recommended designs will be judged. The specified trade-off criteria are explained below. The weights of the different criteria and their sensitivity range are summarized and depicted in Table 4.1.

Table 4.1: Trade-off criteria with weights and sensitivity

Criteria	Min	Weight	Max
Development Cost		**7**	8
Emissions	8	**9**	10
Noise	5	**6**	8
Weight	6	**7**	8
Aerodynamic Performance		**8**	9

- **Development cost:** Development cost is a measure of the amount of work and cost involved in developing the incorporated technologies from each design into a final product. It is primarily based of the technology readiness level (TRL), as specified by NASA[1].
- **Emissions:** Emissions will be scored on the fuel efficiency of the engines. It is evident that if the engines are more fuel efficient, they consume less fuel and therefore emit less pollutants.
- **Noise:** Noise is an important objective for the new aircraft, as is stated in Section 1. Therefore, it will be included in the trade-off with a weight of 6.
- **Weight:** One of the most important parameters in the design of an aircraft is weight. As a rule of thumb it can be stated that a higher operational empty weight (OEW) results in a less fuel efficient aircraft. Since a lower fuel efficiency leads to higher emissions, lowering the weight is of key importance to the effective design of the aircraft.
- **Aerodynamic performance:** As a rule of thumb, higher aerodynamic performance leads to increased fuel efficiency and lower overall emissions. As the aerodynamic performance directly influences the emissions and fuel consumption of the aircraft it will be weighted with 8.

4.1.3. Trade-off Results

Each design is scored points between 1 and 10 for each criterion. Table 4.2 presents the trade-of results and keywords upon which the score is based.

From the trade-off, it can be seen that Design 4 performs best. This is the result of good aerodynamic performance, low emissions and desirable noise characteristics. Design 3 is second best, because of its aerodynamic performance, relatively low development cost and low weight.

The final scores of the trade-off are depicted in Figure 4.7. The blue bars represent the outcome of the original trade-off. The choice for the concepts that will be used in the detailed design phase, will not only be based on the trade-off, but rather on an in-depth analysis of the strengths and weaknesses of the designs. This will be discussed in Section 4.2.

[1] `https://www.nasa.gov/directorates/heo/scan/engineering/technology/txt_accordion1.html` [cited 22 May 2018]

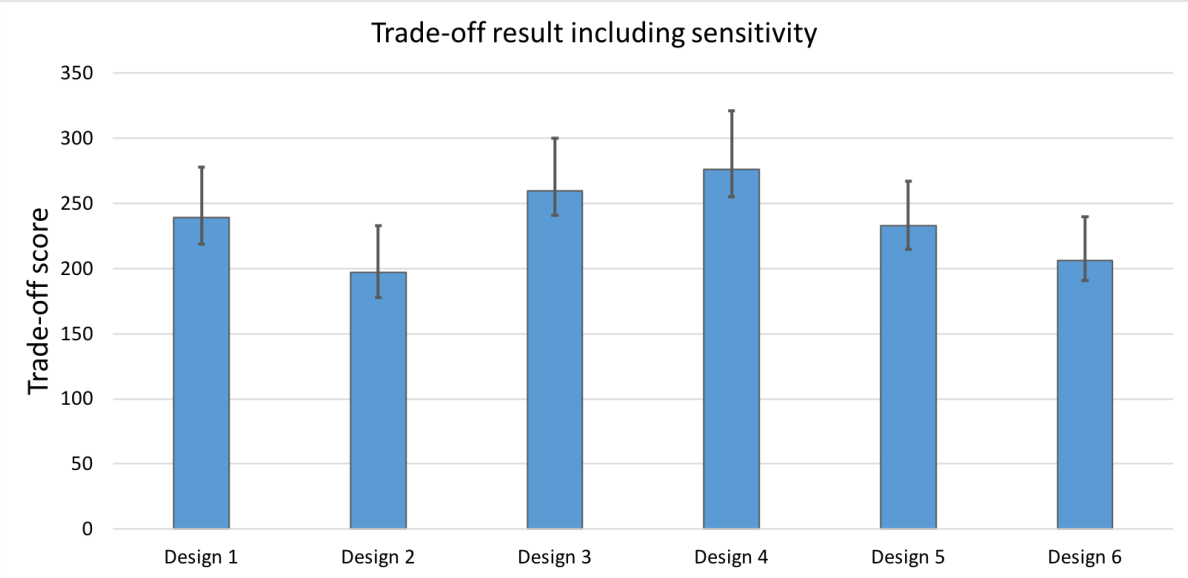

Figure 4.7: Results from the trade-off including the sensitivity bars

4.2. Sensitivity Analysis

To evaluate the sensitivity of a design, the weighting factors are varied over a specified range. The exact range is specified in Table 4.1. This is done in order to determine whether the winning design has been chosen objectively. Figure 4.7 presents the outcome of the original trade-off by the blue bars and adds the sensitivity range with the black bars. From these bars it can be determined that at the extreme weighting factors Design 4 is still the most optimal. However, with certain weighting factors Design 1, 3 and 4 might overlap and Design 1 or 3 might even be the best design. Moreover, it can be found that Designs 2 and 6 are very close in the final trade-off scores.

From these conclusions it is evident that no clear winning design can be appointed. The results from the trade-off and the sensitivity analysis do not show significant differences between certain designs. Therefore, there is no single best design. Instead, a combination of designs will be investigated from which a recommended design will be set up.

4.3. Recommended Design

From Table 4.2 it can be seen that Design 1 has the lowest development cost and the lowest weight. This is mainly caused by the use of a circular fuselage design. Design 5 performs best on emissions, because of its propfan engine. However, the propfan performs worst with respect to noise. Since there is a strict requirement on noise, it is chosen not to implement a propfan in the design. Instead, a high bypass ratio engine will be used, because of the reduction in fuel usage. This will reduce the emissions and noise, as can be seen from the performance of Designs 2 and 4.

Designs 3 to 5 have the best aerodynamic performance, caused by the high aspect ratio high wing configuration. In order to keep the structural weight low, a strutted wing will be used. These designs perform very well on weight. Thus, it is chosen to implement this on the recommended design.

The following design is recommended: a high wing aircraft with a high aspect ratio supported by struts. A circular fuselage will be implemented along with high bypass ratio engines which are placed below the wing.

Table 4.2: Trade-off table

	Development cost (7)	**Emissions (9)**	**Noise (6)**	**Weight (7)**	**Aerodynamic performance (8)**	**Total (including weights)**
Design 1	9: low development cost. Iteration on current aircraft.	5: geared turbofan and medium aspect ratio	6: regular geared turbofan	9: small tail, medium aspect ratio	4: medium aspect ratio, low wing	239
Design 2	5: new fuselage and new engine option	7: ultra high bypass ratio but large frontal area	9: ultra high bypass ratio, no HLD's, low wing so short landing gear	3: large tail, non-circular fuselage, T-tail, medium aspect ratio	3: medium aspect ratio, large frontal area, T-tail	206
Design 3	8: only new engine to be developed	6: intercooled turbofan	5: no gearing in the engine	8: circular fuselage, high aspect ratio but strutted wing	8: slender fuselage, high aspect ratio, T-tail	269
Design 4	7: new non-circular fuselage	8: ultra high bypass ratio and slender fuselage	8: ultra high bypass ratio engine but fairing required for landing gear	5: non-circular fuselage, high aspect ratio but strutted wing	9: high aspect ratio, high wing, slight smaller frontal area. than circular fuselage	276
Design 5	5: very new engine option still to be developed	10: propfan engine	4: open blades	4: cantilevered high aspect ratio wing	7: high aspect ratio, U-tail, low wing, fuselage mounted engines	233
Design 6	7: forward sweep and struts in compression	5: geared turbofan with a high aspect ratio	6: large HLD's	4: forward sweep, high aspect ratio, strut loaded in compression	6: high aspect ratio, low wing, strut on top of the wing, T-tail	206

5
Mission Analysis

In this chapter, first the mission profile will be given in Section 5.1. Secondly, the functional breakdown will be explained in Section 5.2 after with the functional flow will be given in Section 5.3. In Section 5.4, the operations and logistics will be explained. Finally, in Section 5.5 the communication flow will be elaborated on.

5.1. Mission profile

This section first shows the flight profile diagram of the mission. Next, the payload range diagram is given. Finally, the service ceiling of the aircraft is elaborated on.

5.1.1. Flight Profile Diagram

The flight profile diagram of the aircraft is depicted in Figure 5.1. The figure presents all expected flight phases during normal operation of the aircraft and should be read from left to right. A typical mission starts with taxiing using the EGTS. Upon arrival at the runway, the engines are started. The aircraft takes off and climbs to an initial flight level, 1,500 ft in this case. It then climbs out further to a flight level of 10,000 ft and holds for a short while. It continues to climb to the cruise altitude of 39,000 ft (FL390). It then cruises at this altitude for around 1,400 km.

After cruise, the descend 1 phase is started. This has the aircraft descend to sea-level. In case of an aversion, the aircraft climbs from sea-level back to cruise altitude and cruises to an alternative airport at most 250 km away. Here, it descends to 1,500 ft and loiters for 30 minutes. Finally, it descends back to sea-level and lands The aircraft, shuts down its engines and taxis back to the gate using the EGTS.

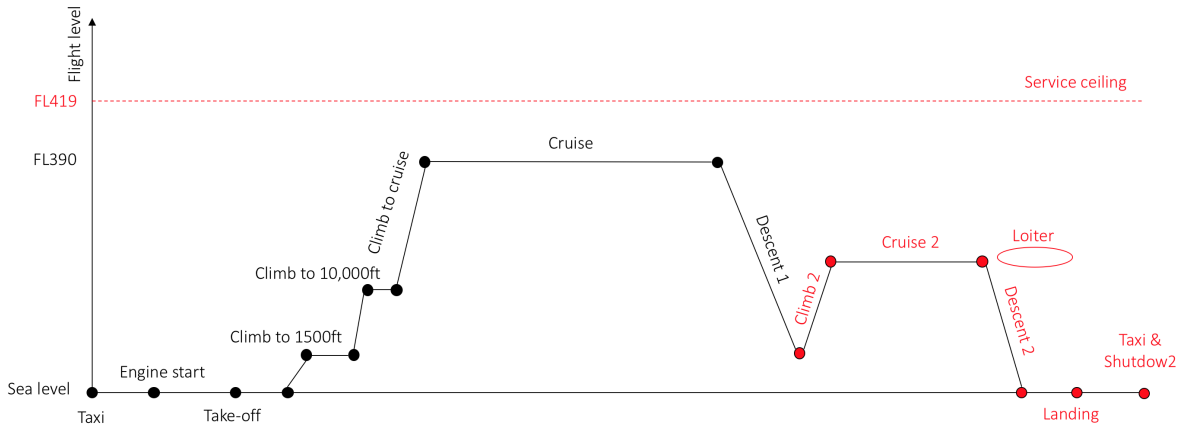

Figure 5.1: Flight profile diagram

5.1.2. Payload-Range Diagram

The payload-range diagram is presented in Figure 5.2. It depicts five main points, A, B, C, D and X. Point A is the zero-fuel point. Here, the range is 0 km and the full payload capacity of 21,600 km is utilized. Point B represents the maximum range at maximum payload, or harmonic range, this range equals 1,177 km. Point X is the design point. The aircraft will be optimized for this combination of payload and range. The design range equals 1,800 km at 20,375 kg of payload, or a loadfactor of 94%. Point C is the maximum useful range, it equals 3,400 km at a payload weight of 18,047 kg. Finally, point D represents the ferry range. At this range no payload is carried and the aircraft is fully fueled. The range at this point equals 6,254 km.

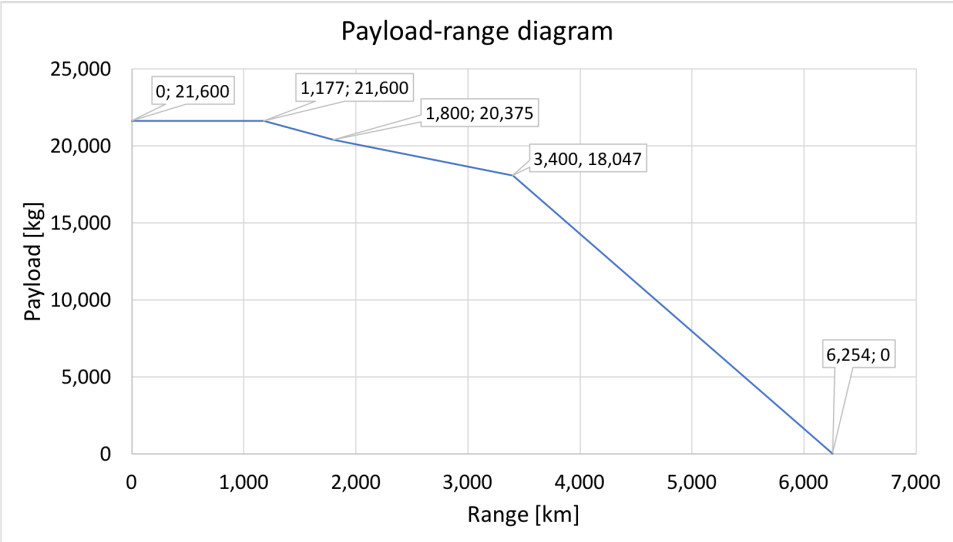

Figure 5.2: Payload-range diagram

5.1.3. Service Ceiling

As prescribed by CS25 [6] the service ceiling is defined as the altitude at which the aircraft is not able to climb with at least a rate of climb of 500 ft/min. In the simulation of the rate of climb as discussed in Subsection 8.1.5 an iteration was performed in order to obtain the theoretical service ceiling of the aircraft. From this a theoretical service ceiling at 43,100 ft is obtained. The climb performance at this altitude can be seen in Figure 5.3, from which it is clear that at the cruise speed a maximum service ceiling of 500 ft/min can be reached. The discontinuity in the rate of climb graph is due to an empirical relation which is used to take into account the effect of altitude and speed on the thrust. This relation changes after Mach 0.4 and hence the line shows this kink. This relation and an explanation can be found in Section 8.1.5.

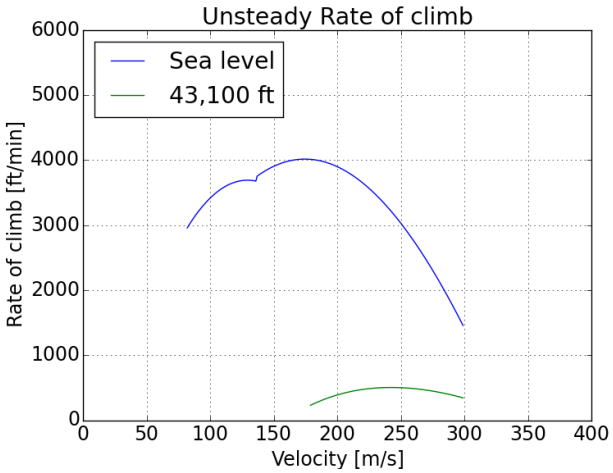

Figure 5.3: Unsteady rate of climb performance at sea level and the theoretical service ceiling

5.2. Functional Breakdown

The Functional Breakdown (FB) outlines all the functions that the aircraft as a system needs to perform. The diagram can be found in Figure 5.4. The FB breaks down the aircraft's top level functions, and details functions at a lower level. This effectively illustrates the hierarchy of the different function levels. This is further demonstrated by the identification numbering system. Top level functions are designated a one digit number, while two digits separated by a full stop are indicative of a second level function, and three digits indicate a third level function. Each level is also assigned a colour, to easily visualize.

It was decided that the total functions would be divided into two operations; aircraft operations and auxiliary operations. The aircraft operations outline all of the functions that the aircraft must be capable of performing in a normal flight cycle. This includes everything from pre-flight preparations to post-flight activities.
The auxiliary operations encompasses functions that are not necessary for a typical flight cycle, but must be performed in atypical circumstances. This includes emergency situations and maintenance operations. The maintenance routine consists of aircraft checks and repairs and is further detailed in Subsection 8.4.2. The emergency operations consist of fuel dumping, emergency landing and evacuation of passengers.

Having outlined and broken down the basic functions of the aircraft, it is possible to determine the systems and subsystems required to perform these functions. For example, the high lift devices (flaps and slats) can be analyzed and sized. Furthermore, the flight performance analysis in Chapter 8 ensures that all functions outlined in the Functional Breakdown are addressed and are effectively integrated into the total system.

5.3. Functional Flow

The Functional Flow Diagram (FFD) presents the chronological ordering of the functions that the aircraft must perform from the start to the end of a typical flight cycle. These functions are consistent with those present in the FB. Top and second level operations are presented in Figure 5.5, while some second level operations are further detailed in Figure 5.6. In green, denoted by a single digit, are the highest level functions, which essentially outline the different phases of a flight cycle. In yellow, denoted by two digits separated by a full stop, the functions performed in each phase of the flight cycle are shown. Finally, the third and most detailed function level describes how a function from the second level is executed. The identification numbering system and colours used are again consistent with the FB.

Some functions are separated by 'and' and 'or' junctions. At an 'and' junction, two or more functions are to be performed. At an 'or' junction, only one of the listed functions is to be performed. An 'or' junction is used where decisions are made. It is used either because only one function can be performed at a time (ie. loading cargo from front to back or back to front), or due to an atypical circumstance (ie. Avert or Land). These decisions are made according to the circumstance, and thus the aircraft must be designed to adequately accommodate both situations.

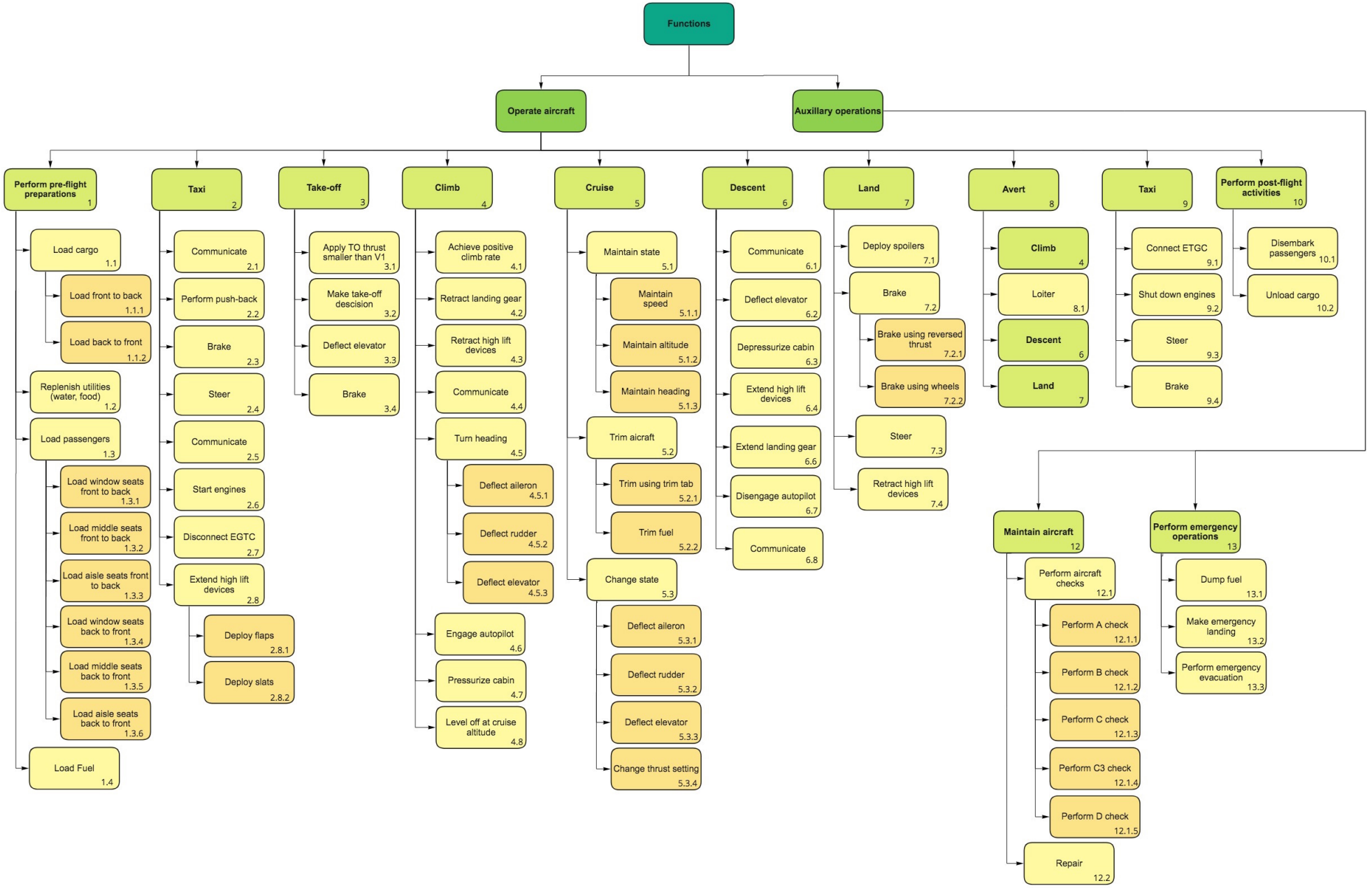

Figure 5.4: Functional Breakdown

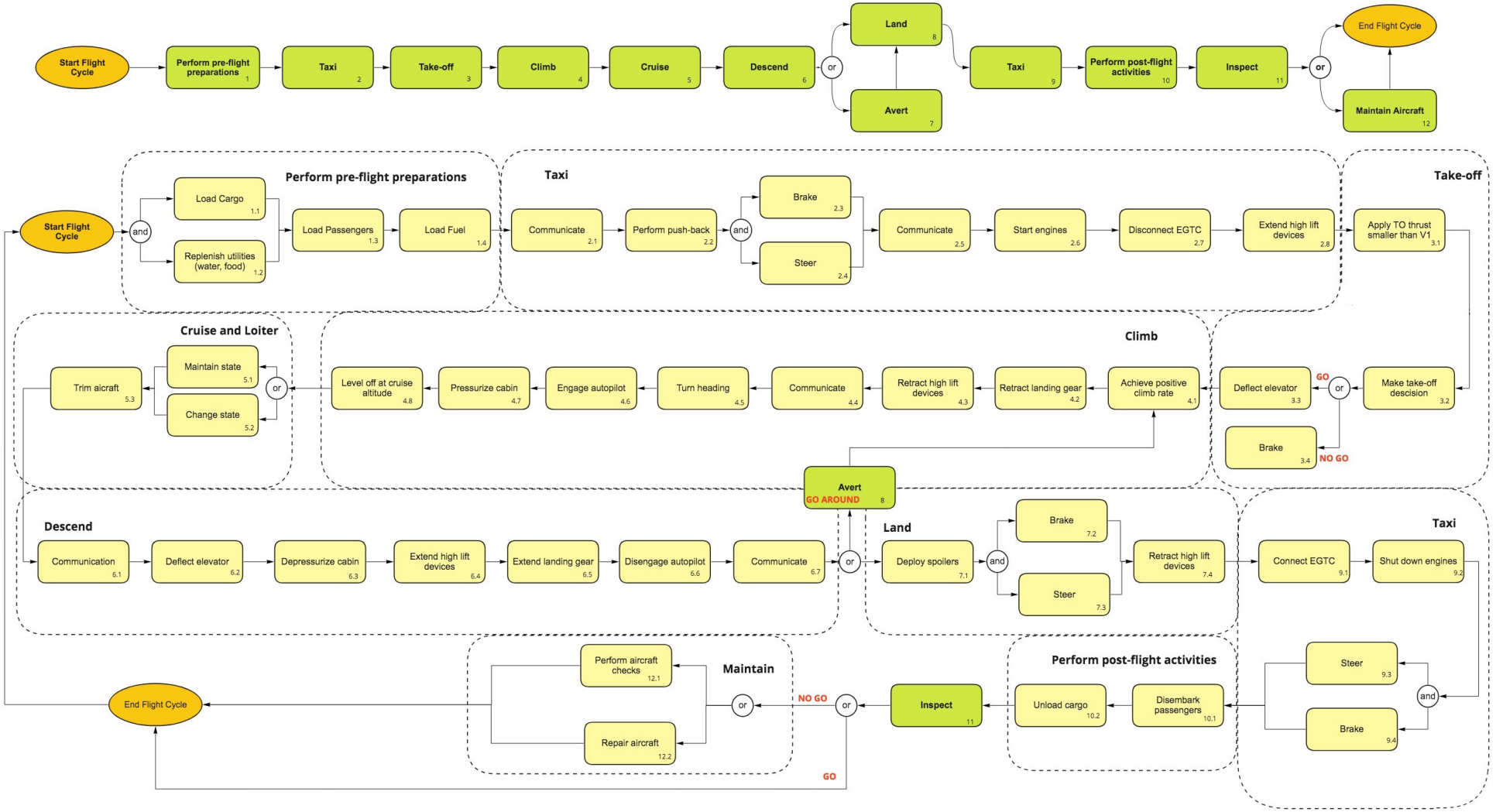

Figure 5.5: Functional Flow Diagram

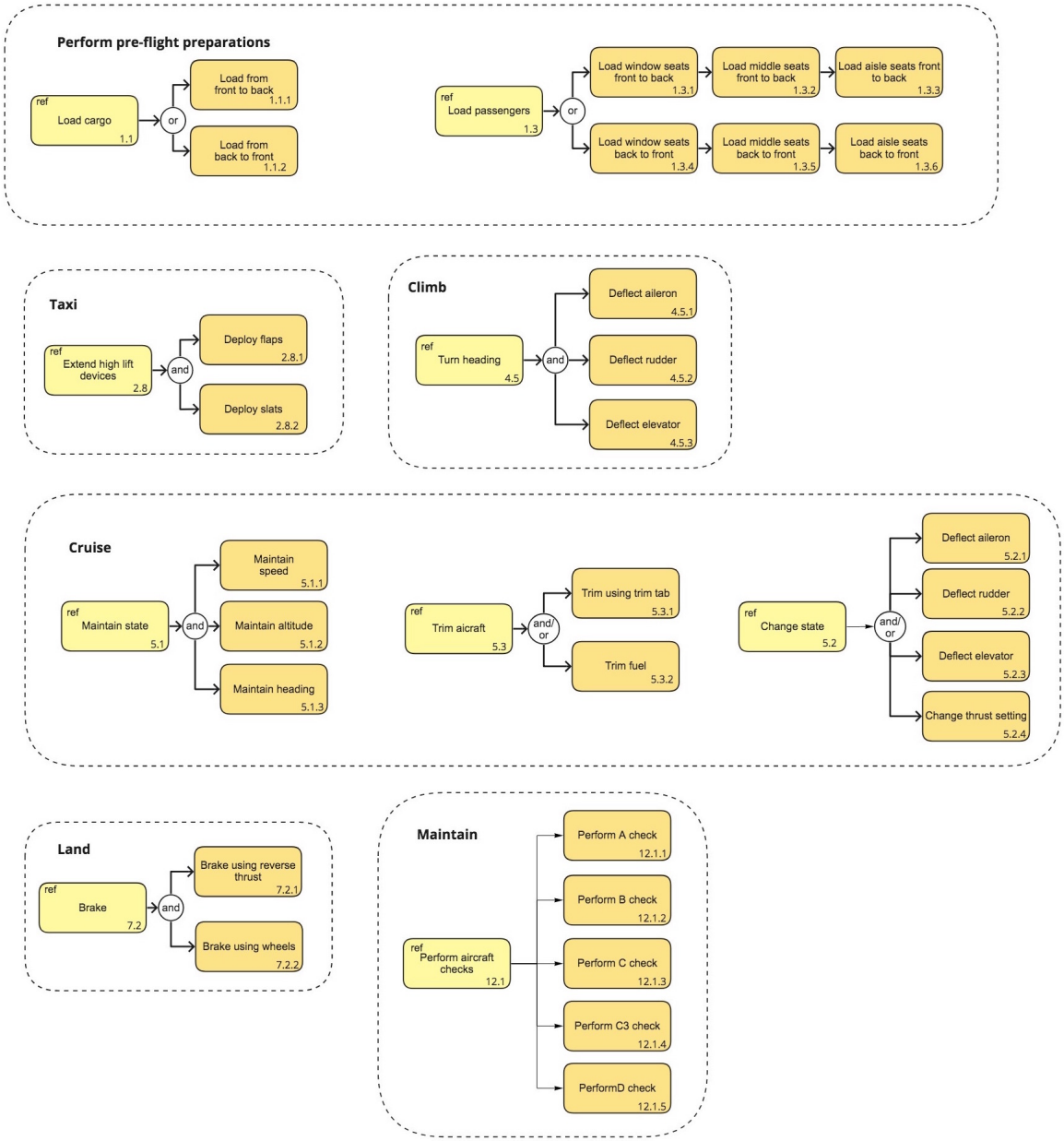

Figure 5.6: Functional Flow Diagram (low level)

5.4. Operations and Logistics

Figure 5.8 presents the typical ground operations that the aircraft undergoes during a typical flight. It starts with the landing and ends at take-off. For the most part, the ground operations are similar to those performed for a typical inter-European flight operated today. The operations do vary on two critical points.

First, the aircraft will use an electric green taxiing system (EGTS)[1] [2] [3], which allows the aircraft to taxi without having the engines running. However, the EGTS does require additional power which will be provided by means of an electric cart to be connected when exiting the runway. Moreover, when the aircraft reaches the gate, it is connected to the auxiliary ground power. This will also charge the electric cart. When the aircraft leaves the gate, ground power is disconnected and power to the aircraft and the EGTS will be provided by the electric cart again. Just before take-off, the engines are started and the cart is disconnected. The aircraft then takes off using its regular engine power.

Secondly, due to the removal of the APU, the aircraft relies heavily on the ground power and air supply. It is therefore critical that these are connected at all times when the aircraft is at the gate. These tasks have also been included in Figure 5.8.

5.5. Communication Flow

In the communication flow diagram, the flow of data through the system and the environment is shown. From Figure 5.9 it can be seen that all systems are connected and communicate via the computers. For example, the pilot operates the flight controls, but these are not directly linked to the control surfaces. First a signal goes to the computer, which in turn moves the actuator. Furthermore, the aircraft entails 3 individual systems as can be seen in Figure 5.7, each containing the computers from Figure 5.9. The captain and first officer both have their own system with own input in case a complete failure occurs on one of the systems or in case the input data from a measurement device, such as the Pitot tube for example, is wrong. This way, each system gets data from their own measurement device. There also is a third redundant system in case of complete failure of system 1 and 2. In case of an error, the pilot can also press the reset button and restart the system, while the other systems are still operational. Moreover, Figure 5.9 makes a distinction between hardware and software systems. Hardware systems are indicated by a red box while software is indicated using a green box.

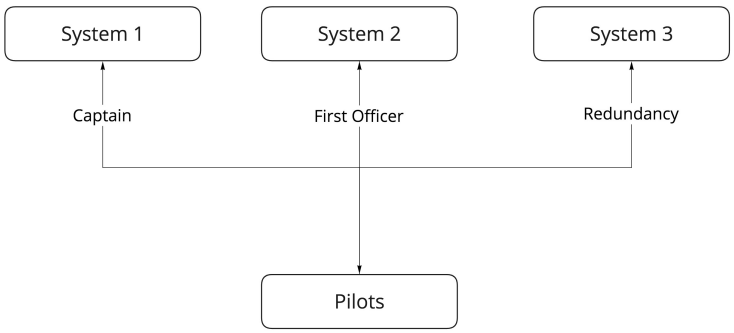

Figure 5.7: General Computer System with redundancy

[1] https://www.safran-Dgroup.com/media/20120209_easyjet%2Dfirst%2Dairline%2Dtrial%2Delectric%2Dgreen%2Dtaxiing%2Dsystem%2Dsafran%2Dand%2Dhoneywell [cited 16 May 2018]

[2] https://www.flightglobal.com/news/articles/farnborough-honeywell-and-safran-halt-electric-tax-427400/ [cited 16 May 2018]

[3] https://www.ainonline.com/aviation-news/air%2Dtransport/2013%2D06%2D18/honeywell%2Dsafran%2Ddemo%2Delectric%2Dtaxiing%2Dsystem%2Dairlines [cited 17 May 2018]

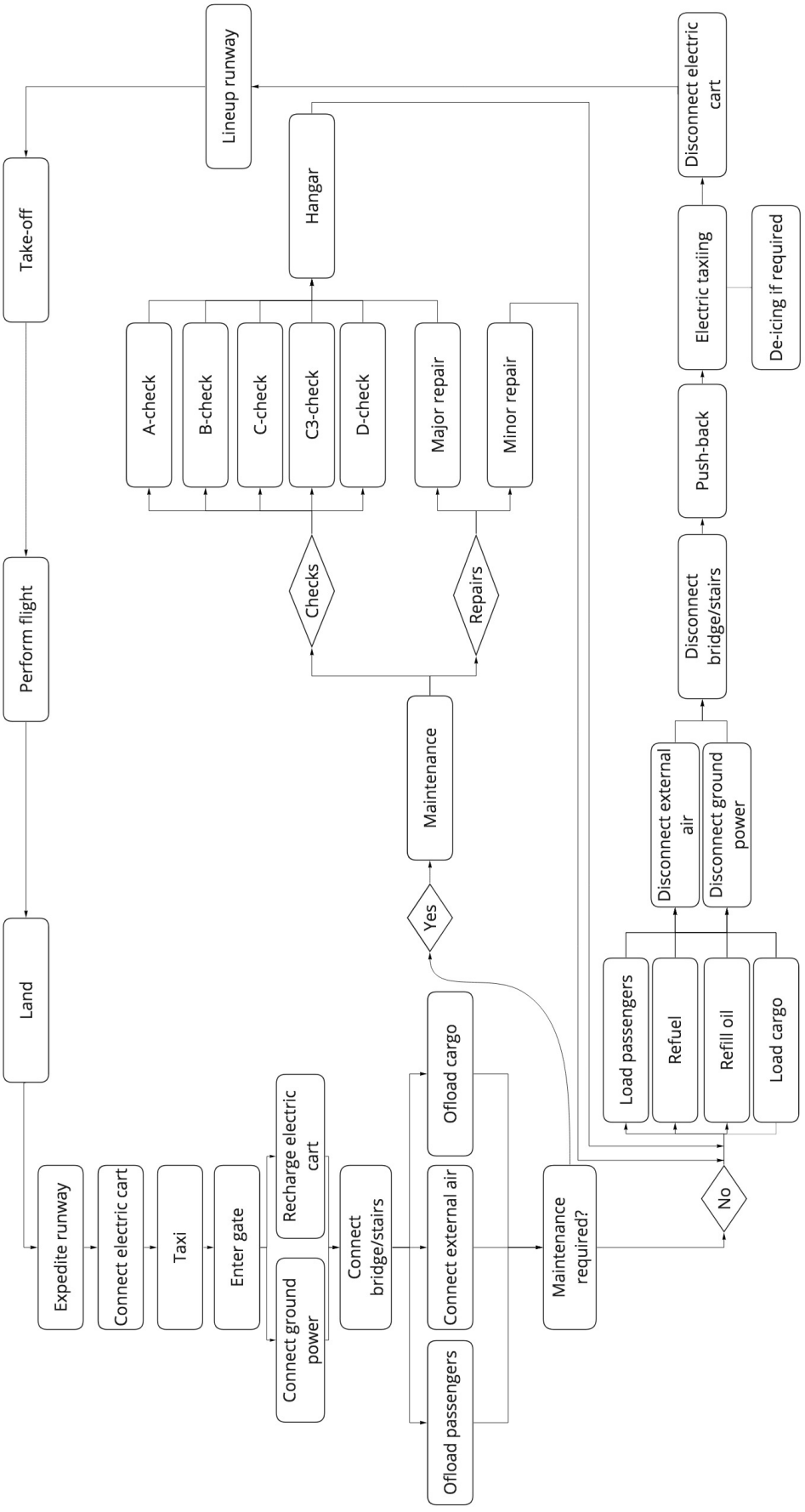

Figure 5.8: Operations and logistics diagram

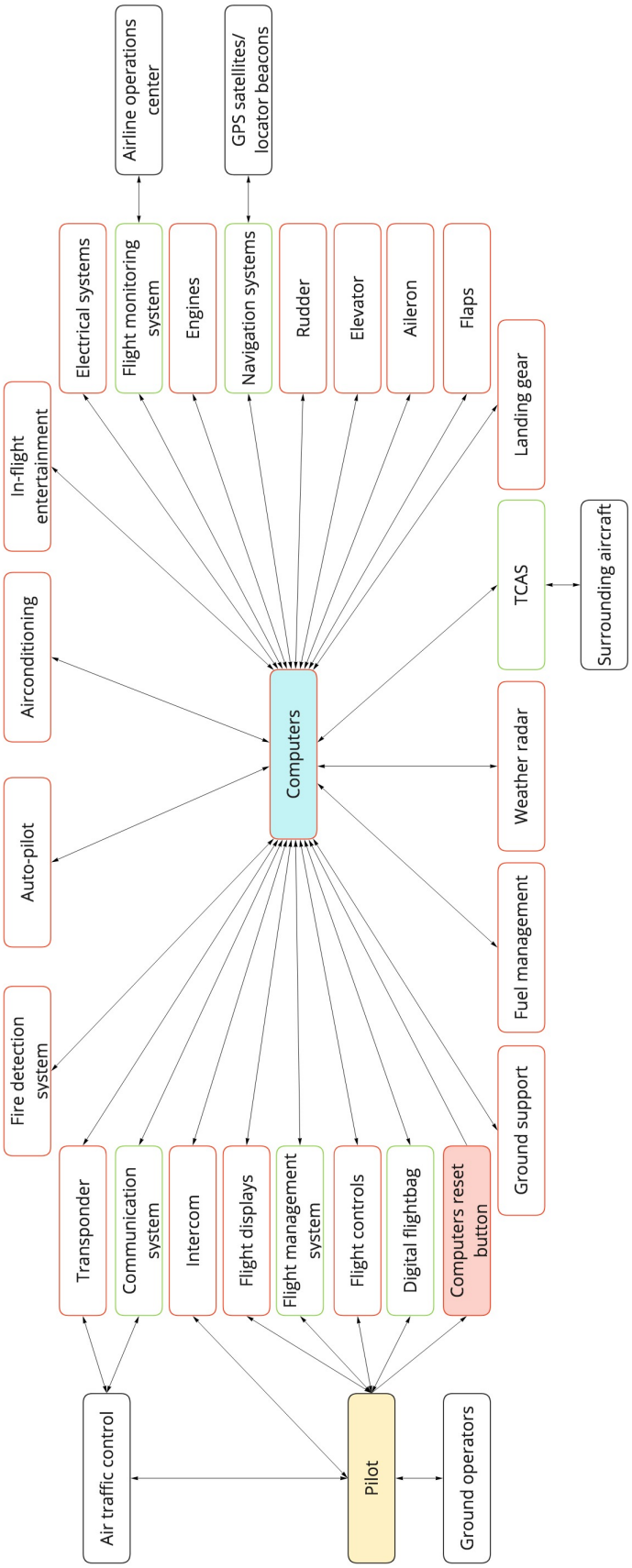

Figure 5.9: Communication flow diagram (hardware is red, software is green)

6

Final Design Characteristics

This chapter focuses on presenting all aspects of the final design. It has been subdivided into ten sections. First, Section 6.1 will present the Class II weight estimation. Next, Section 6.2 will focus on the aerodynamic design and analysis of the aircraft. Section 6.3 is dedicated to the design and positioning of the landing gear. Moreover, Section 6.4 presents the structural layout of the aircraft, while Section 6.5 explains the material choices for the aircraft. The propulsion system is presented in Section 6.6, followed by the stability and control analysis in Section 6.7. The empennage design will be discussed in Section 6.8. The internal configuration is layed out in Section 6.9. Finally, a summary and overview of the final design is presented in Section 6.10.

6.1. Class II Weight Estimation

In this section, the Class II weight estimation will be elaborated on. First, the methods used will be explained. Later, the results will be provided. Finally, the methods that were used and the results that have been found will be verified and validated.

6.1.1. Methodology

To perform the Class II weight estimation, two methods were used. The first method that was used was the method by Torenbeek [22]. This method splits the aircraft weight in 13 groups: 'wing', 'fuselage', 'landing gear', 'empennage', 'propulsion', 'nacelle', 'flight controls', 'instruments', 'hydraulics and pneumatics', 'electrics', 'avionics', 'equipment and furnishing' and 'air conditioning and anti icing'. Each of the groups has a specific formula to calculate the group weight based mainly on statistical data and simple geometry. These formulae were implemented into a python tool in order to compute the weight for each group.These results were summed to calculate the OEW. This was added up with the fuel weight and payload to compute the MTOW.

Later on, also the method of Roskam [23] was computed. This method splits the aircraft into seven component groups: 'wing', 'fuselage', 'landing gear', 'propulsion', 'nacelle' and 'equipment and furnishing'. Because both methods have different groups, a good comparison is not possible. Therefore, the groups that Torenbeek defines as 'flight controls', 'instruments', 'hydraulics and pneumatics', 'electrics', 'avionics', 'equipment and furnishing' and 'air conditioning and anti icing' are all summed into the goup 'equipment and furnishing' in order to make a comparison possible. The formulae for the different groups were implemented into a python tool and the weights were computed and summed to form the OEW. From this also the MTOW was calculated.

6.1.2. Results and Comparison

In Table 6.1 the results of both methods can be seen. It can be seen that the two methods that are used differ quite significantly. Comparing the values for the MTOW to the value from the Class I weight estimation (69,176kg) it can be seen that the method by Torenbeek [22] is larger than this value and the method by Roskam [23] is smaller than this value. The question that must be asked is where this difference comes from. It can be observed that for all groups, the Torenbeek value is bigger than the Roskam value except for the 'equipment & furnishing' group. An explanation for this could be that the method from Torenbeek is a bit older than the method from Roskam. Over the last decades, significant innovation has been made in the aviation field. Therefore, older methods can yield heavier structures. The biggest difference in weights is the fuselage group. This could be explained by the fact that different aspects have been taken into account. Below, Equation 6.1 is used in the Roskam method, while equations 6.2 and 6.3 are used in the Torenbeek method.

$$W_f = 10.43 \cdot K_{inl}^{1.42} \left(\frac{\bar{q_D}}{100}\right)^{0.283} \left(\frac{W_{TO}}{1000}\right)^{0.95} \left(\frac{l_f}{h_f}\right)^{0.71} \tag{6.1}$$

$$S_g = \pi d_{fus} l_{fus} \left(1 - \frac{F_{NC}}{3F} - \frac{F_{TC}}{2F}\right) \tag{6.2}$$

$$W_f = k_{fus} S_g^{1.2} \sqrt{V_D \frac{l_h}{b_{fus} + h_{fus}}} \tag{6.3}$$

As can be seen from Equation 6.1, the Roskam method does not take into account the tail or nose cone. It is merely a function of basic fuselage dimensions, dive pressure, a scaling factor for fuselage podded engines and a factor of the maximum take-off weight. The equations Torenbeek uses are more detailed and are in function of tail and nosecone fineness, dive speed, a scaling factor and a bit more detailed fuselage dimensions. After the structural designing had been performed, it is seen that the Torenbeek method is closest to the actual value for an aluminum fuselage. This will be further explained in Section 6.4.

Because the different methods take into account different parameters and factors that are all relevant to the design, it was decided to take the two methods and average them. This gives a reasonable average because one of the methods has the tendency to be larger and the other has the tendency to be smaller. This average is also presented in 6.1. It has to be noted that the two different methods have some different component groups. The Roskam method has a group 'equipment and furnishing' which corresponds to the Torenbeek component groups 'flight controls', 'instruments', 'hydraulics and pneumatics', 'electrics', 'avionics', 'equipment and furnishing' and 'air conditioning and anti icing'. To calculate the average, these are all added up and taken as the 'equipment and furnishing group'. With adding up all the groups, the operational empty weight can be calculated. Summing this with the maximum payload weight of 20,375 kg and the fuel weight of 9,530 kg gives the maximum take-off weight. Finally, it should be noted that the OEW includes a crew of 2 pilots and 5 cabin crew.

Table 6.1: Class II weight estimation component group weights in kg

Method	Wing	Fuselage	Landing gear	Empennage	Propulsion	Nacelle	Flight controls
Torenbeek	8,745	13,287	1,857	1,333	7,414	999	793
Roskam	6,569	7,118	2,225	1,218	5,355	334	/
Average	7,657	10,203	2,041	1,275	6,385	667	/
Method	**Instruments**	**Hydraulics & pneumatics**	**Electrics**	**Avionics**	**Equipment & furnishing**	**Air conditioning & anti icing**	**OEW / MTOW**
Torenbeek	228	402	907	1,020	4,357	666	42,008/71,914
Roskam	/	/	/	/	11,458	/	34,278/64,182
Average	/	/	/	/	9,916	/	38,143/68,048

6.1.3. Verification and Validation

In order to verify the tool used for the Class II weight estimation, two programs were made separate from each other. In the end, the two were compared and the differences analyzed. With this, the mistakes were corrected until they had the same outcome.

The Class II weight estimation is performed using two of the most established weight estimation methods in the industry, namely by Roskam [23] and Torenbeek [22]. Therefore, validating these methods is not really necessary. However, because the two methods yielded different results, investigation into this was performed. Mr. Torenbeek was consulted to discuss the results and he referred to a phd thesis [24] where the method was used to perform a Class II weight estimation and where also the actual data of the airplane is presented. The errors of this method are also discussed and seven out of nine component groups have errors within 6%. Therefore the method is considered to be valid.

6.2. Aerodynamic Characteristics

The aerodynamic characteristics are layed out in the upcoming eight subsections. The wing planform will be presented in Subsection 6.2.1. The airfoil selection is presented in Subsection 6.2.2. The airfoil selection is then transformed into a finite wing and analyzed in Subsection 6.2.3. A full overview of the hybrid laminar flow control system is provide in Subsection 6.2.4. Subsection 6.2.5 explains the drag analysis. The aerodynamic moment is determined in Subsection 6.2.6. Furthermore, the design of the high lift devices is elaborated upon in Subsection 6.2.7. Finally, the aileron design is presented in Subsection 6.2.8.

6.2.1. Wing Planform Design

The preliminary wing surface area will be determined using the T/W-W/S diagram as presented in Figure 6.1. In this figure the design is indicated by the black triangle, reference aircraft are indicated by the pink dots. It was decided to aim for a $C_{L_{take-off}}$ of 2.0 and a $C_{L_{land}}$ of 2.2, in order to limit the size, weight and complexity of the high lift devices. Using these constraints and the respective design point, the wing surface area was determined to be 128 m^2.

After careful consideration of the design and the landing and take-off performance, as presented in Section 8.1, it was decided to further optimize the wing surface area and maximum lift coefficients in landing and take-off configuration. As further explained in Section 8.1, a design iteration was performed. This iteration resulted in a $C_{L_{max,take-off}}$ of 2.2, a $C_{L_{max,landing}}$ of 2.9 and a reduced wing surface area of 110 m^2. The increased maximum lift coefficients in landing and take-off do result in more complex and heavier high lift devices, however the wing surface area has been reduced with 18 m^2. This has also resulted in a higher wing loading of 6,049.6 N/m^2, which is more in line with the reference aircraft presented in the plot.

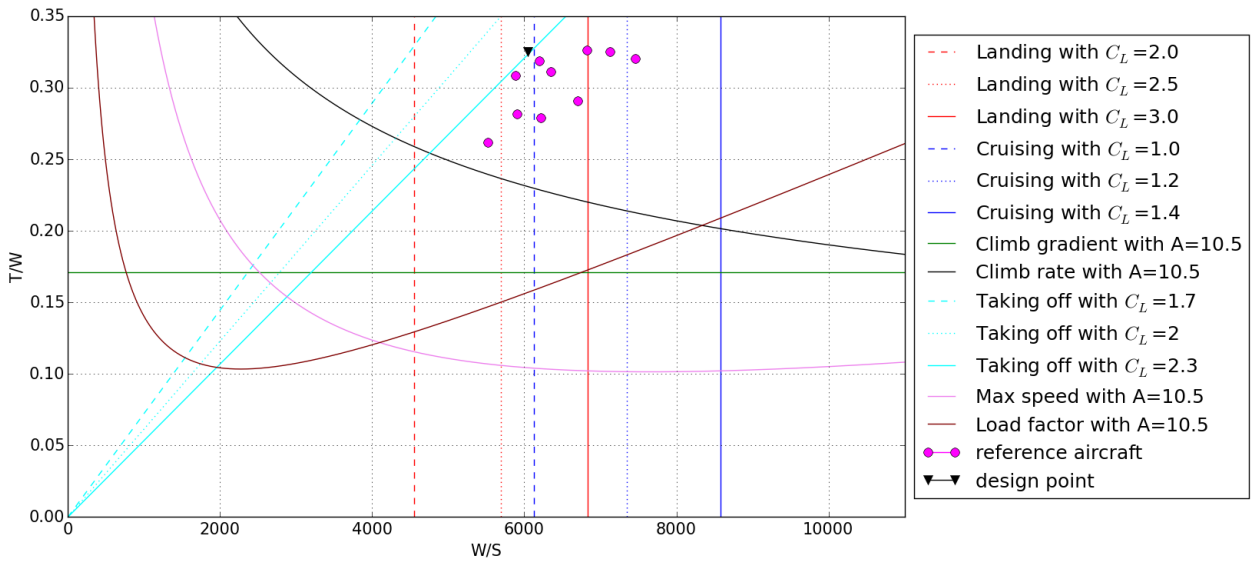

Figure 6.1: Thrust loading and wing loading diagram

In the Midterm Report [1], an aspect ratio of 14 was chosen for the recommended design. This is one of the key drivers in this design for greater fuel efficiency. Furthermore, the aircraft will feature a straight tapered wing design with a taper ratio of 0.29 in order to approximate the optimal elliptical lift distribution to the greatest extend possible. This also takes the difficulty of manufacturing into account. A taper ratio of 0.29 is in line with reference aircraft.

With the wing surface area, aspect ratio and taper ratio determined, the full straight tapered wing planfrom can be developed using Equations 6.4 to 6.7 for the trapezoidal wing. The results of which are presented in Table 6.2.

$$b_w = \sqrt{S \cdot A} \tag{6.4}$$

$$c_r = \frac{2S}{(1+\lambda)b_w} \tag{6.5}$$

$$c_t = c_r \cdot \lambda \tag{6.6}$$

$$MAC = \frac{2}{3} \cdot c_r \cdot \frac{1+\lambda+\lambda^2}{1+\lambda} \tag{6.7}$$

Table 6.2: Wing planfrom parameters

Parameter	Symbol	Value	Unit
Wing surface area	S	110	m^2
Aspect ratio	A	14	-
Taper ratio	λ	0.29	-
Span	b_w	39.24	m
Root chord	c_r	4.34	m
Tip chord	c_t	1.26	m
Mean aerodynamic chord	MAC	3.08	m

6.2.2. Airfoil Selection

The airfoil used for the cross-sectional shape of the wing is chosen based mainly on the required lift coefficient during cruise conditions. The drag of the airfoil should be as low as possible in this condition. The design lift coefficient of the wing is calculated using Equation 6.8 [25]. This equation averages the weight at the start and end of cruise to take into account the effect of fuel burn.

$$C_{L_{des_{wing}}} = 1.1 \frac{1}{q} \left(0.5 \left[\left(\frac{W}{S} \right)_{startcruise} + \left(\frac{W}{S} \right)_{endcruise} \right] \right) \tag{6.8}$$

The factor 1.1 is used to compensate for the negative lift generated by the tail. This resulted in a $C_{L_{des_{wing}}}$ of 0.73. And a $C_{L_{des}}$ of 0.66 for the entire aircraft. Taking into account the effect of wing sweep, the design lift coefficient of the airfoil can then be determined using Equation 6.9. Because the final sweep angle can only be determined after the airfoil is chosen, the sweep angle Λ used in this equation is only an initial estimate calculated using the wing planform parameters of Table 6.2.

$$c_{l_{des}} = \frac{C_{L_{des_{wing}}}}{cos(\Lambda)^2} \tag{6.9}$$

Note that this value is calculated for a Mach number of 0.79. Airfoil data is usually obtained at low Mach numbers. In order to select an airfoil, the design lift coefficient must be known for a low Mach number. This can be estimated using the Prandtl-Glauert compressiblity corrections given by Equation 6.10.

$$c_{l_{des,M=0}} = c_{l_{des}} \sqrt{1 - M_{cr}^2} \tag{6.10}$$

This resulted in a design airfoil lift coefficient of 0.6. Several airfoils have been selected that have low drag at c_l = 0.6. They have been compared based on the following criteria:

- The airfoil shall have minimum drag at $c_{l_{des}}$.
- The airfoil shall have a wide drag bucket around $c_{l_{des}}$.
- The airfoil shall have the largest possible $c_{l_{max}}$.
- The airfoil shall not have a sharp drop in c_l after stall.
- The critical Mach number shall be as high as possible.
- The c_m at $c_{l_{des}}$ shall be as low as possible.

The airfoils have been analyzed using the panel method software XFLR5. This tool plots the lift curve, drag polar, pitching moment curve, and pressure distribution of an airfoil using the Reynolds number as input. The Reynolds number during cruise was determined to be 13,500,000 using Equation 6.11. The resulting lift curve and pitching moment curve of the analyzed airfoils are shown in Figures 6.2 and 6.3. Due to limitations of XFLR5 in viscous flow, the results at high angles of attack may be inaccurate and overestimate the $c_{l_{max}}$. However it can still be used to analyze how the airfoils behave compared to each other.

The critical Mach number is determined using Equation 6.12 and Equation 6.13 [26]. In Equation 6.12, $C_{p,0}$ is the pressure coefficient at the point of minimum pressure at zero Mach number. This equation calculates the pressure coefficient at Mach numbers in the subsonic range. Equation 6.13 yields the critical pressure coefficient as function of critical Mach number. Using these equations two lines of pressure coefficients against Mach number can be plotted. The point of intersection determines the value of the critical Mach number. The results of the analysis are presented in Table 6.3. It contains three NACA 6-digit series airfoils and six NASA supercritical airfoils.

$$Re = \frac{V cos(\Lambda) \rho \bar{c}}{\mu} \tag{6.11}$$

$$C_p = \frac{C_{p,0}}{\sqrt{1 - M_\infty^2}} \tag{6.12}$$

$$C_{p_{cr}} = \frac{2}{\gamma M_{crit}^2} \left[\left(\frac{1 + \frac{\gamma - 1}{2} M_{crit}^2}{1 + \frac{\gamma - 1}{2}} \right)^{\frac{\gamma}{\gamma - 1}} - 1 \right] \tag{6.13}$$

Table 6.3: Airfoil data from XFLR5 analysis at Re = 13,500,000

Airfoil name	**NACA 643618**	**NACA 633618**	**NACA 632615**	**SC 20612**	**SC 20614**	**SC 20610**	**SC 20712**	**SC 20714**	**SC 20710**
t/c	0.18	0.18	0.15	0.12	0.10	0.10	0.12	0.14	0.10
$\mathbf{c_{l_{des}}}$	0.6	0.6	0.6	0.6	0.6	0.6	0.7	0.7	0.7
$\alpha_{\mathbf{des}}$ [deg]	0.121	0.24	0.36	0.678	0.475	0.908	-0.117	-0.38	0.051
Wide drag bucket	No	No	No	Yes	Yes	Yes	Yes	Yes	Yes
$\mathbf{c_d @ c_{l_{des}}}$	0.005	0.006	0.007	0.006	0.006	0.006	0.006	0.007	0.006
$\mathbf{c_{l_{max}}}$	1.67	1.64	1.76	2.36	2.4	2.34	2.38	2.43	2.36
$\mathbf{c_{d_{min}}}$	0.005	0.005	0.005	0.006	0.006	0.006	0.006	0.007	0.006
$\mathbf{c_m @ \alpha_{des}}$	0.119	0.116	0.115	0.116	0.121	0.110	0.131	0.143	0.128
Sharp drop in c_l after stall	No	No	No	No	Yes	Yes	No	No	Yes
$\mathbf{M_{crit}}$	0.687	0.688	0.687	0.663	0.665	0.639	0.677	0.680	0.675
$\mathbf{C_{p_{min}} @ \alpha_{des}}$	-1.000	-0.990	-1.000	-1.177	-1.163	-1.358	-1.073	-1.043	-1.087

From the Table 6.3 it is clear that the supercritical airfoils all have better $c_{l_{max}}$ values than the NACA airfoils. The NACA airfoils have lower minimum drag coefficients, but they do not have a wide drag bucket around $c_{l_{des}}$. Comparing the supercritical airfoils, the SC20-614, SC20-610, and SC20-710 have a sharp drop in lift coefficient after stall. Therefore, these airfoils were discarded from the trade-off. Of the remaining three airfoils, SC20-714 was discarded, because it has the highest drag coefficient at $c_{l_{des}}$. Finally it was decided that SC20-612 has the most favourable characteristics in terms of drag, maximum lift, and moment coefficient, although the critical Mach number is slightly lower than for the SC20-712. Thus, SC20-612 was selected to use as airfoil in further wing analysis. The SC20-612 is shown in Figure 6.4 with the pressure distribution at the angle of attack at $c_{l_{des}}$. The curves corresponding to this airfoil are marked in red in Figures 6.2 and 6.3.

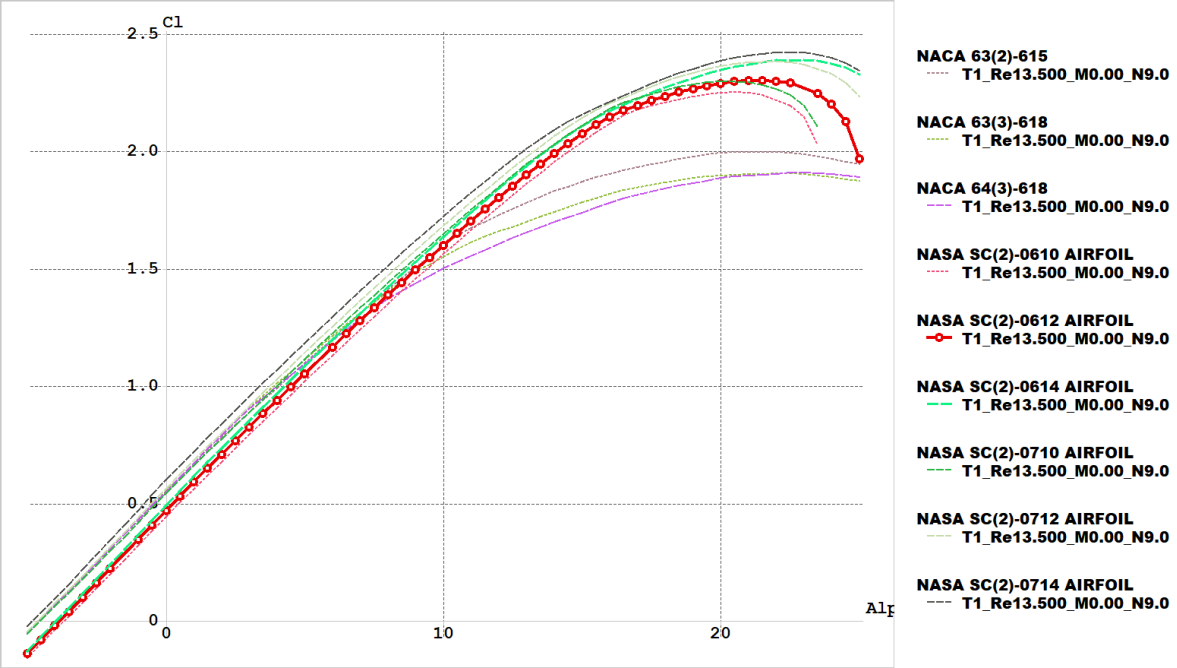

Figure 6.2: Lift slope curve $c_l - \alpha$ comparison of airfoils, Re = 13,500,000, M = 0

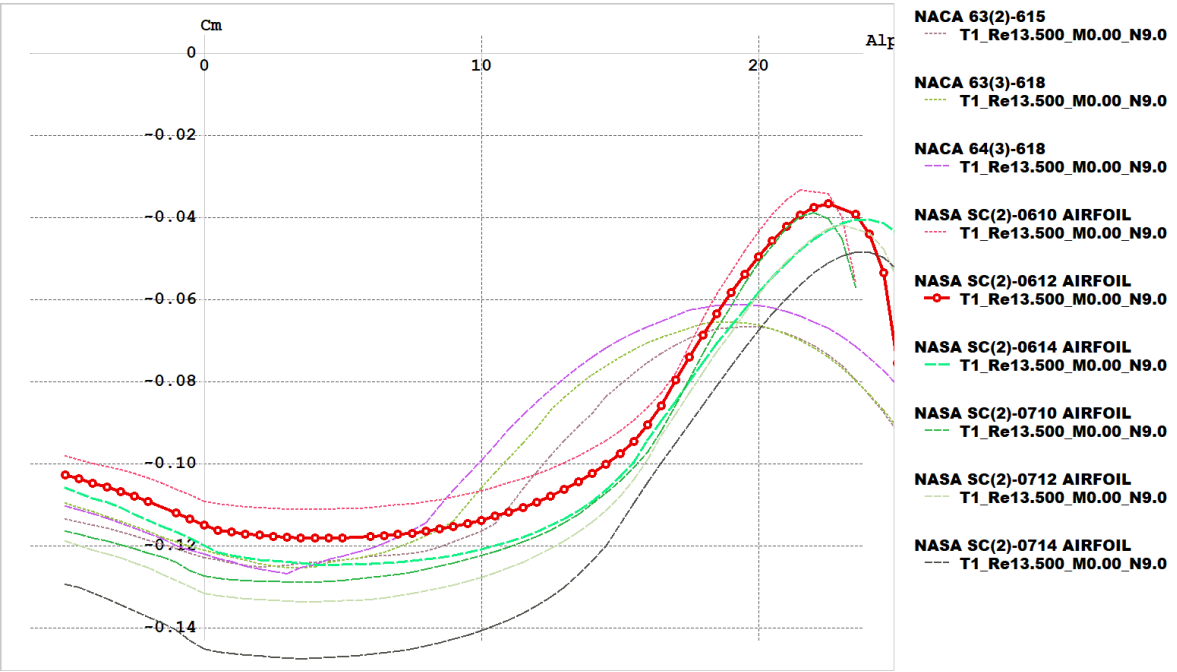

Figure 6.3: Pitching moment curve $c_m - \alpha$ comparison of airfoils, Re = 13,500,000, M = 0

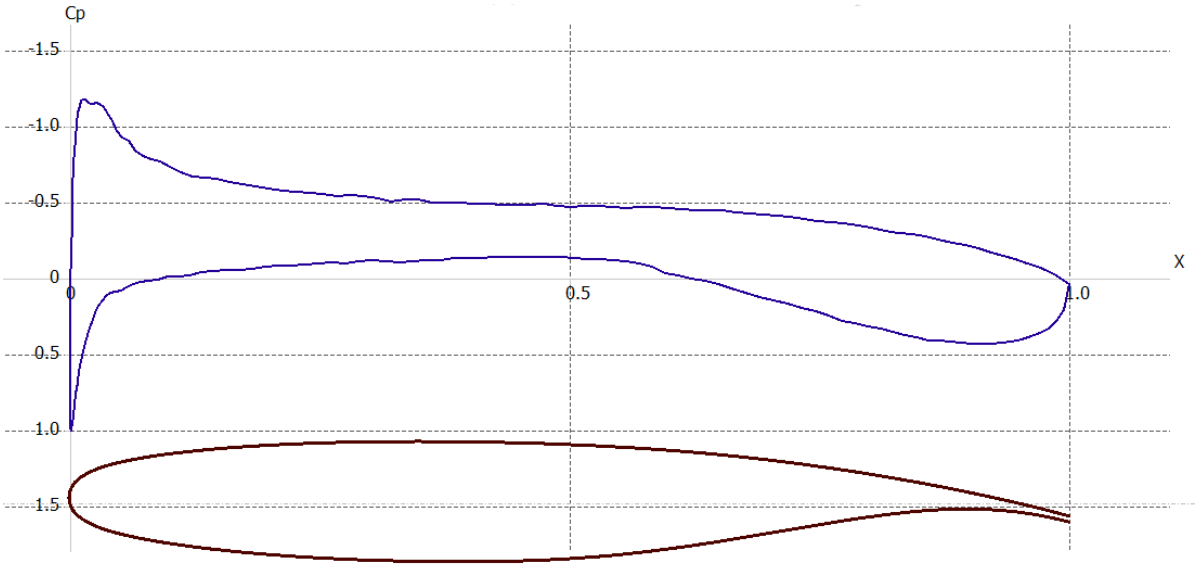

Figure 6.4: Pressure distribution of the SC20-612 airfoil at α = 0.678 °, Re = 13,500,000, M = 0

In reality, the wing will have different types of airfoils at different sections of the span. This is because each section requires specific airfoil characteristics for optimal performance. For example, at the root a thicker airfoil is needed for high torsional stiffness and at the tip the airfoil should have gradual stall characteristics. Therefore, the selected airfoil is the average shape of the continuously changing airfoil along the span.

6.2.3. Finite Wing Analysis

Now that the NASA SC20-612 airfoil has been selected, it can be further developed into a full wing with the parameters specified in Table 6.2. This section will focus on determining the sweep angle and lift-curves. As stated in Table 3.1, the aircraft shall be able to cruise at Mach 0.79 and the maximum operating speed shall be Mach 0.82. However, the SC20-612 airfoil has a critical Mach number of just 0.663. Consequently, a sweep angle is required in order to bring our critical Mach number to 0.79. Assuming that the drag divergence Mach number (M_{DD}) is 4% higher than the critical Mach, the M_{DD} will equal 0.821. This means that the aircraft complies with both requirements. In order to achieve a M_{crit} of 0.79 a leading edge sweep angle of 32.9° is required. This was determined using Equation 6.14. The value for quarter chord sweep can be obtained using Equation 6.15 and is calculated to be 31.3°.

$$\Lambda_{LE} = cos^{-1}\left(\frac{M_{crit,airfoil}}{M_{cr}}\right) = cos^{-1}\left(\frac{0.663}{0.79}\right) \tag{6.14}$$

$$\Lambda_{0.25C} = tan^{-1}\left(tan(\Lambda_{LE} - \frac{4}{A}\left[0.25 \cdot \frac{1-\lambda}{1+\lambda}\right]\right) \tag{6.15}$$

The lift curves for the wing are determined in two different regimes. First, the lift curve slope will be analyzed in cruise condition with a clean configuration. Hereafter, the lift will be analyzed at sea level conditions with a Mach number of 0.2 in clean configuration. The effect of high lift devices and/or the landing gear will be analyzed in Subsection 6.2.7. The value of C_{L_α} was evaluated using Equation 6.16, based on the Datcom method [27]. Where β is the Prandtl-Glauert compressibility correction factor given by Equation 6.17 and $\Lambda_{0.5C}$ is the half-chord sweep angle given by Equation 6.18. Moreover, the airfoil efficiency factor, κ, is approximated using Equation 6.19 [27] at 0.911.

$$\frac{dC_L}{d\alpha} = C_{L_\alpha} = \frac{2\pi A}{2 + \sqrt{4 + \left(\frac{A \cdot \beta}{\kappa}\right) \cdot \left(1 + \frac{tan^2 \Lambda_{0.5C}}{\beta^2}\right)}} \tag{6.16}$$

$$\beta = \sqrt{1 - M_\infty^2} \tag{6.17}$$

$$\Lambda_{0.5C} = tan^{-1}\left(tan(\Lambda_{LE} - \frac{4}{A}\left[0.5 \cdot \frac{1-\lambda}{1+\lambda}\right]\right) \tag{6.18}$$

$$\kappa = \frac{c_{l_\alpha}}{2\pi} \tag{6.19}$$

Using these equations, the lift curve slope in cruise conditions with a clean configuration is estimated to be 5.89 rad^{-1}. This value is very close to the theoretical maximum value of 2π or 6.28. Therefore, it can be concluded that the designed wing is very efficient. In sea level conditions with an airspeed of 0.2M and a clean configuration, the lift curve slope is estimated to equal 4.69 rad^{-1}. Using the C_{L_α} values, the lift coefficient at any arbitrary angle of attack can be calculated using Equation 6.20 [28]. Where, α_{0L} is the zero lift angle of attack which is the same for the full 3-D wing as for the airfoil, -3.82°.

$$C_L = C_{L_\alpha}(\alpha - \alpha_{0L}) \tag{6.20}$$

Using the slope of the lift curve, the trim angle of attack in cruise can be calculated using Equation 6.21 [28]. The average trim angle during cruise is estimated to be 3.3°. In order to increase passenger comfort and have the aircraft fly level as much as possible, the wing will be placed at an incidence angle equal to the trim angle in cruise. The incidence angle will therefore also equal 3.3° set between the cabin floor and the wing chord line.

$$\alpha_{trim} = \frac{C_{L_{des}}}{C_{L_\alpha}} + \alpha_{0L} \tag{6.21}$$

The maximum lift coefficient for the wing is determined using Equation 6.22 [28]. The values for $\left[\frac{C_{L_{max}}}{C_{l_{max}}}\right]$ and $\Delta C_{L_{max}}$ are obtained from [29]. $C_{l_{max}}$ is the maximum lift coefficient for the NASA SC20-612 airfoil as presented in Subsection 6.2.2. This yields an estimated maximum wing lift coefficient of 1.04 in cruise conditions and clean configuration. $C_{L_{max}}$ for the entire aircraft is statistically estimated to be 10% lower due to the negative lift being generated by the horizontal tail to trim the aircraft [25]. This brings the maximum lift coefficient for the aircraft in cruise conditions and clean configuration to 0.94. The maximum lift coefficient at sea-level conditions and a Mach number of 0.2 is obtained in a similar way. The $C_{L_{max}}$ for the wing in these conditions was calculated to be 1.45. For the full aircraft this would reduce to 1.32.

$$C_{L_{max}} = \left[\frac{C_{L_{max}}}{c_{l_{max}}}\right] \cdot c_{l_{max}} + \Delta C_{L_{max}} = 0.52 \cdot c_{l_{max}} - 0.19 \tag{6.22}$$

The stall angle of attack can be determined using Equation 6.23 [29]. Where, the value for $\Delta\alpha_{C_{L_{max}}}$ is obtained to be 3.1° [29]. For cruise condition and clean configuration this results in a stall angle of attack of 9.4°. At sea-level conditions while flying at a Mach number of 0.2 in clean configuration, the wing will stall at an angle of attack of 17.0°.

$$\alpha_{stall} = \frac{C_{L_{max}}}{C_{L_\alpha}} + \alpha_{0L} + \Delta\alpha_{C_{L_{max}}} \tag{6.23}$$

The most important lift parameters for the finite 3-dimensional wing have now been determined for both cruise conditions and sea-level conditions at a Mach number of 0.2 for a clean configuration. Subsection 6.2.5 will present the drag analysis and Subsection 6.2.7 will provide the design and analysis of the high lift devices.

6.2.4. Hybrid Laminar Flow Control

As mentioned in the Midterm Report [1], the aircraft will feature an active hybrid laminar flow control (HLFC) system. The system actively sucks air from the boundary layer into the wing near the leading edge. Using this technology, it is possible to have laminar flow along 65% of the wing chord [30] [31], providing a significant reduction in drag. In order to use this drag reduction to its maximum potential, active HLFC will be implemented along the full leading edge of the main wing from 5% to 20% of the total chord. The hardware for the system will be housed in the leading edge in front of the front spar. The system will be powered by two electrically driven generators housed in the fuselage of the aircraft.

Since the system sucks in air from the boundary layer through tiny holes in the wing skin, it is very sensitive to getting blocked by tiny particles in the air. These particles could include small insects, pollen or ice crystals. In order to protect the system as much as possible, it will feature three protection systems. First, the slats will be deployed when flying at low altitudes. This should divert most particles away from HLFC holes. Secondly, the system will feature an anti-icing system. The holes will be surrounded by heating mats which can be heated in order to melt accumulated ice crystals. Finally, when the aircraft is on the ground, the airflow through the holes can be reversed in order to blow out any possible contaminants.

6.2.5. Drag Analysis

The drag experienced by an aircraft is the sum of many different drag components. The general expression for the drag polar is stated in Equation 6.24. From the drag polar it is evident that there are two main components to drag, C_{D_0} or the zero lift drag and the lift induced drag [32]. The zero lift drag will be analyzed first, followed by the lift induced drag component.

$$C_D = C_{D_0} + \frac{C_L^2}{\pi A e} \tag{6.24}$$

Zero Lift Drag

The zero lift drag has been evaluated with the component drag build-up method [32] [29]. The general expression for this method is presented in Equation 6.25. Here, S_{ref} is the aircraft's reference area which is equal the wing surface area.

$$C_{D_0} = \frac{1}{S_{ref}} \sum_c C_{f_c} \cdot FF_c \cdot IF_c \cdot S_{wet_c} + C_{D_{misc}} \tag{6.25}$$

C_{f_c} is the flat plate skin friction coefficient, it estimates the friction drag induced by a component. The value of the skin friction coefficient is highly dependent the type of flow encountered by the component [32]. Due to the aircraft's active hybrid laminar flow control system (HLFC), laminar flow along 65% of the wing chord is achievable [30] [31]. The same is true for the horizontal and vertical tail surfaces. This greatly reduces the drag induced by these components. For laminar flow, C_{f_c} is given by Equation 6.26 [32] [29]. For turbulent flow, C_{f_c} is given by Equation 6.27 [32] [29]. The total skin friction coefficient for each of the surfaces is obtained by combining the values for laminar and turbulent flow in the respective ratio for that component. For example, 65% laminar and 35% turbulent flow for the wing.

$$C_{f_c} = \frac{1.328}{\sqrt{Re}}, \qquad Re = min\left(\frac{\rho V l}{\mu}, \quad 44.62(l/k)^{1.053} M^{1.16}\right) \tag{6.26}$$

$$C_{f_c} = \frac{0.455}{(\log_{10} Re)^{2.58}(1+0.144M^2)^{0.65}}, \qquad Re = min\left(\frac{\rho V l}{\mu}, \quad 44.62(l/k)^{1.053} M^{1.16}\right) \tag{6.27}$$

The component form factor, FF_c, estimates the pressure drag due to viscous separation [32] [29]. It has been evaluated for several components, which have a significant contribution to the total zero lift drag, such as the fuselage, wing, tail, struts and pylons. The equations to calculate the component form factor are lengthy and lie beyond the scope of this report.

The component interference factor, IF_c, estimates the influence on the total zero lift drag induced by the drag interference between different components. It was obtained using statistical values as presented in [32].

Due to the unconventional addition of a strut to the aircraft, special attention will be given the drag calculation for it. The drag has also been determined using the drag build-up method [32] [29]. The $C_{f_{strut}}$ has been determined using Equations 6.26 and 6.27. Where, 'l' equals the strut chord length as mentioned in Subsection 6.4.2. For the value 'k', it has been assumed that the strut will be made of aluminum and covered with smooth paint. The component form factor for the strut has been calculated using Equation 6.28. The strut will use the NASA 16-021 symmetric airfoil, which has a maximum thickness-to-chord ratio of 0.21 and a maximum thickness located at 50% of the chord. Furthermore, an interference factor of 1.1 has been obtained for the strut [32]. Finally, the wetted area has been calculated using Equation 6.29, where the strut length and chord are presented in Subsection 6.4.3. The total drag increment induced by the two struts is calculate using Equation 6.30. The total $\Delta C_{D_{0_{strut}}}$ equals 0.000778.

$$FF_{strut} = \left[1 + \frac{0.6}{(x/c)}\left(\frac{t}{c}\right) + 100\left(\frac{t}{c}\right)^4\right] \cdot 1.34M^{0.18} \tag{6.28}$$

$$S_{wet_{strut}} = l_{strut} \cdot c_{strut} \cdot 2 \tag{6.29}$$

$$\Delta C_{D_{0_{strut}}} = 2 \cdot C_{f_{strut}} \cdot FF_{strut} \cdot IF_{strut} \cdot S_{wet_{strut}} \tag{6.30}$$

The $C_{D_{misc}}$ term in Equation 6.25 accounts for the addition of miscellaneous drag induced by several factors. First of all, the term accounts for the additional drag induced by the extension of the landing gear and flaps during take-off and landing. Moreover, it accounts for the drag induced by the fuselage upsweep. It also accounts for the fuselage base drag component, which is a specific pressure drag contribution attributed to a blunt afterbody [32]. Since the TU-ecoliner does not have an APU, it is possible to make the afterbody completely pointy. Thereby, there is no blunt afterbody and the fuselage base drag is equal to 0. Finally, the $C_{D_{misc}}$ term also accounts for the excrescence drag caused by different protrusions from the aircraft's smooth body, such as antennas and probes. This contribution is often small, about 2% - 5% of the total C_{D_0} for jet transport aircraft [32].

Accounting for all these forms of drag and summing them together according to Equation 6.25 provides the total zero lift drag in clean configuration of 0.0131. The contributions to the zero lift drag of all components are presented in Table 6.4. This table also includes the zero-lift drag contributions for the flaps, slats and landing gear which have been calculated in Subsection 6.2.7 and Section 6.3, respectively.

Using the values for drag as specified in Table 6.4 the C_{D_0} during different flight phases can be determined. During take-off, with the landing gear extended, the C_{D_0} equals 0.0346. The C_{D_0} for the climb-out after take-off, with the flaps still in take-off position but the landing gear retracted, equals 0.0302. During landing, with the flaps in landing position and the gear down, the C_{D_0} equals 0.0974. The relative drag contribution of the components in the respective flight configurations is given in Table 6.4. In order to determine the full drag polar, the lift induced drag will be estimated next.

Table 6.4: Drag contribution breakdown

Component	**C_{D_0}**	**% of total C_{D_0}**	**Component**	**ΔC_{D_0}**
Wing	0.00267	20.4	Landing gear	+0.00439
Horizontal tail	0.000760	5.8	Flaps landing	+0.0684
Vertical tail	0.000684	5.2	Flaps take-off	+0.00171
Fuselage	0.00566	43.1	Slats landing	+0.0115
Strut	0.000758	5.8	Slats takeoff	+0.00306
Fuselage upsweep	0.00221	16.8		
Excrescence	0.000383	2.9		
Total	**0.0131**	**100**		

The breakdown of the zero-lift drag for the aircraft in clean configuration is visualized in Figure 6.5. From this figure, it is evident that the fuselage is the biggest contributor to the zero-lift drag. Moreover, it can be noted that the struts contribute only 5.8% to the zero-lift drag.

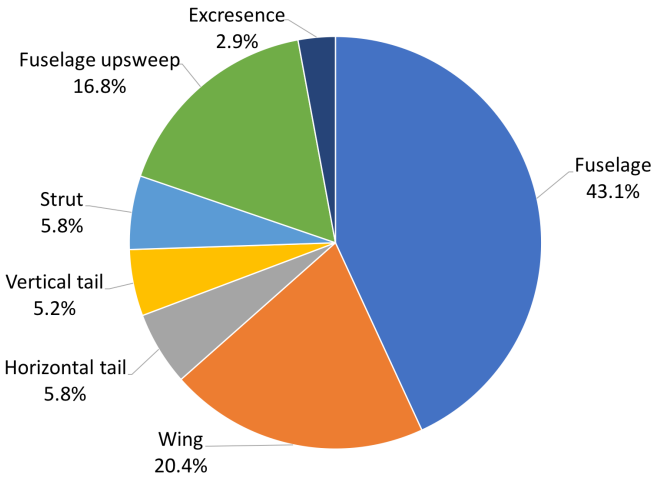

Figure 6.5: Zero-lift drag breakdown

Lift Induced Drag

As can be seen from Equation 6.24, there are two main contributions to the total drag coefficient of an aircraft, the zero lift drag and the lift induced drag. The lift induced drag will be discussed here.

Lift induced drag is given by Equation 6.31 [32]. Where, 'C$_L$' is the aircraft lift coefficient, 'A' is the effective aspect ratio and 'e' is the Oswald span efficiency factor.

$$C_{D_{lift-induced}} = \frac{C_L^2}{\pi A e} \tag{6.31}$$

The effective aspect ratio of the wing is obtained by accounting for the type of wingtip specified on the aircraft. The aircraft will feature raked wingtips, which increase the effective aspect ratio by 0.5 - 1.5 [32]. Raked wingtips are selected as they provide a greater percentage of drag reduction at cruise, with the smallest percentage increase in vertical and horizontal wing span [33]. For the specific wingtips to be equipped on the TU-ecoliner, an increase of 0.75 to the 'normal' aspect ratio has been assumed. As stated in Table 6.2, the wing will have an aspect ratio of 14. Accounting for the positive effect of the raked wingtips, the effective aspect ratio will equal 14.75.

The Oswald span efficiency factor, 'e' in Equation 6.31, was obtained using the Obert method [33]. The Obert method is presented in Equation 6.32. Using this method, an Oswald efficiency factor of 0.727 was calculated. This is in line with reference aircraft as presented by [34].

$$e = \frac{1}{1.05 + 0.07\pi A} \tag{6.32}$$

Combining the values obtained for the effective aspect ratio and the Oswald span efficiency factor with the C$_{D_0}$ obtained earlier, yields the drag polar presented in Equation 6.33 for the full aircraft in clean configuration.

$$C_D = 0.0131 + 0.0297 C_L^2 \tag{6.33}$$

6.2.6. Moment Coefficient Around Aerodynamic Center

Below, in Equation 6.34 till Equation 6.38 is shown how the moment coefficient around the aerodynamic center was calculated, using the method described in [35]. The moment coefficient around the aerodynamic center is indifferent for variations in angle of attack, and is the sum of the moment coefficient of the aerodynamic center of the wing, fuselage, HLDs and nacelles. b_f, h_f and l_f are geometrical properties for which the definition can be found in [35]. From the analysis C$_{m_{ac}}$ was found to be -1.00911.

$$C_{m_{ac}} = C_{m_{ac_w}} + \Delta_f C_{m_{ac}} + \Delta_{fus} C_{m_{ac}} + \Delta_{nac} C_{m_{ac}} \tag{6.34}$$

$$C_{m_{ac_w}} \approx C_{m_{0_{airfoil}}} \left(\frac{A \cos \Lambda^2}{A + 2\cos \Lambda} \right) \tag{6.35}$$

$$\Delta_f C_{m_{ac}} = \mu_2 \cdot (-\mu_1 \cdot \Delta C_{l_{max}} \cdot \frac{c'}{c} - (C_{L_{A-h}} + \Delta C_{l_{max}} \cdot (1 - \frac{S_{wf}}{S}) \frac{1}{8} \frac{c'}{c} (\frac{c'}{c} - 1)) + 0.7 \cdot \frac{A}{1 + \frac{2}{A}} \cdot \mu_3 \cdot \Delta C_{l_{max}} \cdot \tan(\Lambda_{0.25_w}) - C_{L_{A-h}} \cdot (0.25 - \bar{x}_{ac}) \tag{6.36}$$

$$\Delta_{nac} C_{m_{ac}} \approx \begin{cases} 0.2 & \text{fuselage-mounted engines, full flaps} \\ -0.05 & \text{wing-mounted engines, full flaps} \end{cases} \tag{6.37}$$

$$\Delta_{fus} C_{m_{ac}} = 1.8 \left(1 - \frac{2.5 b_f}{l_f}\right) \frac{\pi b_f h_f l_f}{4 S \bar{c}} \frac{C_{L_0}}{C_{L_{\alpha_{A-h}}}} \tag{6.38}$$

6.2.7. High Lift Devices

As explained in Section 6.2.1, the aircraft needs a $C_{L_{max,take-off}}$ of 2.2 and a $C_{L_{max,landing}}$ of 2.9 in order to meet the take-off and landing requirements. However, the $C_{L_{max}}$ at low speed in clean configuration is 1.45. Therefore, in order to increase the lift during take-off and landing while keeping a small wing surface area during cruise, the wing needs high lift devices.

Sizing of HLDs

Both leading edge and trailing edge devices will be used. The trailing edge devices mainly increase the $C_{L_{max}}$ and leading edge devices avoid flow separation at higher angles of attack. Single slotted fowler flaps will be considered for the first iteration of the flap sizing. They are more efficient than plain slotted flaps, but less complex and heavy than double or triple slotted flaps. Slats will be used as leading edge devices, because of their effectiveness in combination with the hybrid laminar flow control system.

The required reference wing flapped surface area can be determined as function of the required $\Delta C_{L_{max}}$ using Equation 6.39 from [29]. This is the portion of the total wing surface that is under the effect of high lift devices. The equation can be used to calculate both the area affected by flaps and slats. It is assumed that the trailing edge flaps contribute to 86% of the $\Delta C_{L_{max}}$ and the leading edge devices 14%.

$$\frac{S_{wf}}{S} = \frac{\Delta C_{L_{max}}}{0.9 \Delta C_{l_{max}} cos(\Lambda_{hingeline})} \tag{6.39}$$

Since the $\Delta C_{L_{max}}$ is the largest for landing, this value is used for the calculation of the flapped area. A margin of 0.1 is added to decrease the risk of stalling. The increase in $C_{L_{max}}$ is thus:

$$\Delta C_{L_{max,land}} = C_{L_{max,landing}} - C_{L_{max_clean}} = 2.9 - 1.45 + 0.1 = 1.55 \tag{6.40}$$

In Equation 6.39 $\Delta C_{l_{max}}$ is the increase in lift coefficient of the flapped airfoil. The value of $\Delta C_{l_{max}}$ depends on the type of flap, the deflection angle δ_f, and flap chord length c_f. These parameters were adjusted in order to obtain acceptable values for the spanwise position of the high lift devices. The value of $\Lambda_{hingeline}$ is the sweep angle of the wing rear spar, where the flap is attached. After the first iteration, it turned out that the the flapped area would be too high. Therefore, instead of single flotted flaps, double slotted flaps are used. In case doubleslotted fowler flaps are used, $\Delta C_{l_{max}}$ is given by Equation 6.41, with the values for the final iteration inserted. A flap deflection angle of 20° is used during take-off and 50° during landing. A similar calculation was performed for the slats.

$$\Delta C_{l_{max,land}} = 1.3 \frac{c'}{c} = 1.3 \frac{c + \Delta c}{c} = 1.6 \frac{c + c_f \frac{\Delta c}{c_f}}{c} = 1.3 (1 + \frac{c_f}{c} \frac{\Delta c}{c_f}) = 1.3 (1 + 0.35 \cdot 0.89) = 2.1 \tag{6.41}$$

Using the calculated values of the reference flapped surface, the spanwise placement of the high lift devices can be determined. The slats shall be placed at least 2 m away from the fuselage intersection, to ensure that stall occurs close to the root first. The flaps can be placed starting at 5 cm from the fuselage intersection. A margin of 5 cm is taken between the flaps and the fuselage along the wingspan. This is included in order for the flaps to extend with sufficient margin for manufacturing and installation tolerances. The flaps should not take up too much space of the outboard portion of the span, in order to leave space for the ailerons. The position as fraction of the half-span is calculated using the known wing geometry. The resulting dimensions of the high lift devices are presented in Table 6.5.

Table 6.5: Dimensions and positioning of high lift devices

Parameter	Symbol	Flaps	Slats
Reference flapped surface	S_{wf}/S	0.66	0.69
Inboard position along halfspan	$b_i/(b/2)$	0.05	0.15
Outboard position along halfspan	$b_o/(b/2)$	0.70	0.96
Landing deflection angle [deg]	δ_{land}	50	25
Take-off deflection angle [deg]	δ_{to}	20	14

Lift Slope

The application of high lift devices increases the slope of the lift curve and also shifts it to the left. The approximate shift in zero lift angle of attack is given by Equation 6.42. The lift curve slope of the flapped aircraft is calculated using Equation 6.43.

$$\Delta\alpha_{0L} = (\Delta\alpha_{0l})_{airfoil}\frac{Swf}{S}cos(\Lambda_{hingline}) \tag{6.42}$$

$$C_{L_{\alpha,flapped}} = \frac{S'}{S}C_{L_{alpha,clean}} \tag{6.43}$$

Here, S is the area of the wing when the flaps are extended. For $\Delta\alpha_{0l_{airfoil}}$ $-15°$ is used for landing, and $-10°$ for take-off. Using these equations, the linear part of the lift curve of the flapped wing during take-off and landing could be plotted. These curves are presented in Figure 6.6. The points of $C_{L_{max}}$ with corresponding stall angle of attack are indicated, as calculated using Equation 6.23. From these plots, the C_L at zero angle of attack during take-off and landing can be determined. For take-off, $C_{L0_{takeoff}} = 1.1$ and for landing, $C_{L0_{landing}} = 1.4$

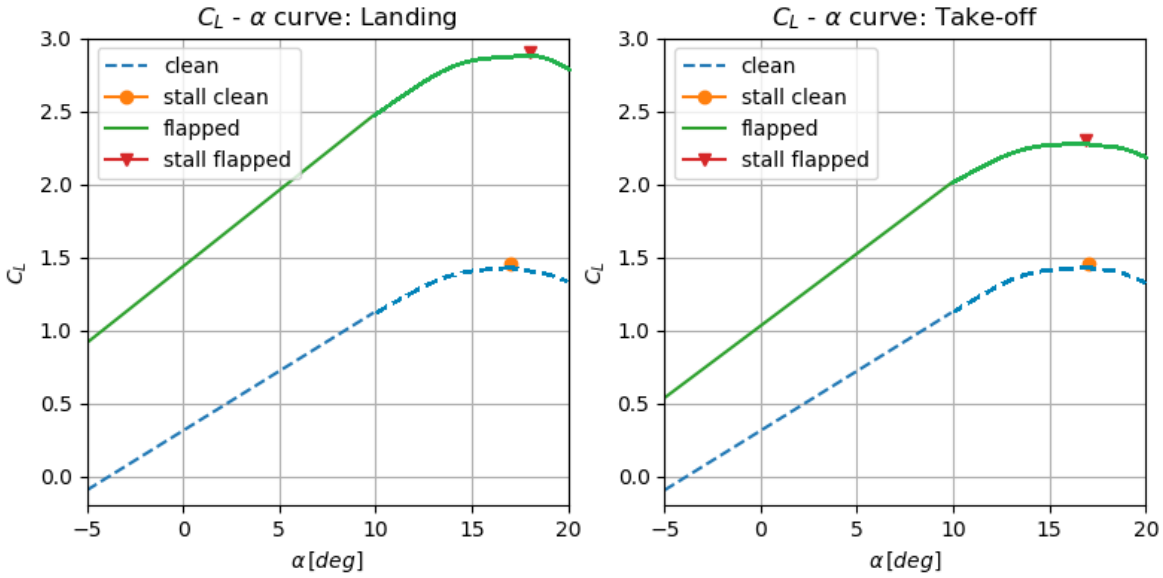

Figure 6.6: C_L - α curves of the clean and flapped aircraft

Drag Increment due to HLD's

Extending the high lift devices will increase the drag significantly. The drag of the flaps and the slats will be calculated separately using the drag estimation method presented in Equation 6.44 obtained from [29]. For single slotted flaps, F_{flap} equals 0.0074 [29]. Using the parameters as obtained above, the total $\Delta C_{D_{0_{flap}}}$ can be calculated to be 0.0082 in take-off setting and 0.0492 in landing setting.

$$\Delta C_{D_{0_{flap}}} = F_{flap}\cdot\frac{C_f}{C}\cdot\frac{S_{flapped}}{S_{ref}}\cdot(\delta_{flap}-10) = 0.0074\cdot0.35\cdot0.66\cdot(\delta_{flap}-10) \tag{6.44}$$

In order to calculate the drag for the slats the same method [29] will be used. The relation used for obtaining the drag increment due to the deployment of the slats is presented in Equation 6.45. The total drag increment due to the deflection angle of 25° of the slats in landing equals 0.0127. When the slats are deflected 14° during take-off the drag increment will equal 0.0034.

$$\Delta C_{D_{0_{slat}}} = F_{slat} \cdot \frac{C_{slat}}{C} \cdot \frac{S_{slatted}}{S_{ref}} \cdot (\delta_{slat} - 10) = 0.0074 \cdot 0.15 \cdot 0.69 \cdot (\delta_{flap} - 10) \tag{6.45}$$

These drag increments will be added to the C_{D_0} for the aircraft in clean configuration as calculated in Subsection 6.2.5. All final values will be presented in Section 6.10.

6.2.8. Aileron Design

The ailerons have to be designed in order to meet the roll rate requirements of weight class II aircraft. This means that the aircraft must be able to achieve a roll angle of 45° in 1.4 seconds. The time needed to perform a certain bank angle is related to the roll rate. The roll rate during cruise with maximum aileron deflection is calculated using Equation 6.46, assuming steady state roll.

$$P = -\frac{C_{l_{\delta a}}}{C_{l_p}} \delta a_{max} \left(\frac{2V}{b}\right) \tag{6.46}$$

Its value depends on the aileron control derivative $C_{l_{\delta\alpha}}$ and roll damping coefficient C_{l_p}. These parameters are calculated using Equations 6.47 and 6.48. They are a function of the wing, aileron, and airfoil geometry. The parameters associated with the aileron geometry are the spanwise location of the aileron, $b_{i,a}$ and $b_{o,a}$ and the aileron effectiveness τ. The value of τ is related to the chord length of the aileron.

$$C_{l_{\delta\alpha}} = \frac{2c_{l\alpha}\tau}{S_{ref}b} \int_{b_{i,a}}^{b_{o,a}} c(y)y\,dy \tag{6.47}$$

$$C_{l_P} = -\frac{4(c_{l\alpha} + c_{d_0})}{S_{ref}b^2} \int_0^{b/2} y^2 c(y)\,dy \tag{6.48}$$

By varying the geometric dimensions of the ailerons, the roll rate can be varied. This was done until the required Δt, calculated using Equation 6.49, became smaller than 1.4 s, with a $\Delta\phi$ of 45°. Here it was also taken account that the inboard position cannot be less than 63% of the halfspan, in order to avoid interference with the flaps. The obtained aileron geometry is presented in Table 6.6.

$$\Delta t = \frac{\Delta\phi}{P} = \frac{45}{0.5637}\frac{\pi}{180} = 1.39s \tag{6.49}$$

Table 6.6: Aileron geometry

Parameter	Symbol	Value
Maximum aileron deflection [deg]	δa_{max}	20
Inboard position along the halfspan	$b_{i,a}/(b/2)$	0.79
Outboard position along the halfspan	$b_{o,a}/(b/2)$	0.95
Ratio aileron chord/wing chord	c_a/c	0.2
Aileron effectiveness	τ	0.4

6.3. Landing Gear Design

The landing gear is a vital part of the aircraft. It serves its main purpose during take-off and landing. The undercarriage has six main functions [36]:

- Absorb shocks during landing
- Absorb shocks during taxiing
- Provide the ability for ground manoeuvring
- Provide braking capability
- Allow for towing of the aircraft
- Protect the ground surface

6.3.1. Landing Gear Positioning

The number of wheels required for the landing gear is obtained from statistical relations for CS25 aircraft [36]. These relations are given by Equation 6.50 and 6.51 for the nose and main landing respectively. In these equations all weight are given in Newtons. From the relations, the number of nose landing gear wheels is determined to be 2. Furthermore, 4 main landing gear wheels are required. This means that the aircraft will have two main landing gear struts and a nose gear strut, with two wheels per strut [36].

$$N_{nw} = 2 \tag{6.50}$$

$$N_{mw} = \frac{f \cdot MTOW}{210,000}, \qquad f = \frac{W_{max,land}}{MTOW} \tag{6.51}$$

The exact positioning of the landing gear is crucial to provide support and stability in all conditions while the aircraft is on the ground. To provide stability along the length of the aircraft, the main landing gear had to be positioned such that the aircraft does not exceed a scrapeback andle of 9.5°. This mitigates the risk of tailstrike, which is high for such a long fuselage. This value for the scrapeback angle is consistent with the scrapeback angle for the A321neo, which has a fuselage of similar length. The tailcone had to be elongated to accomdate this scrapeback angle.

Furthermore, to prevent the aircraft from tipping back during loading, the main landing gear also have to be sufficiently far behind the most aft centre of gravity. To ensure this, the tipback angle has to be greater than the scrapeback angle. A tipback angle of 15° was used. A larger angle is preferable, which would place the gear further back, providing greater stability margins, however the positioning of the nose gear is very sensitive to the longitudinal position of the main gear. Placing the main gear as close to the most aft centre of gravity as possible, and ensuring that the force on the nose gear is within 8%(for steering) and 14% of the total aircraft mass, results in a favourable position of the nose gear. The nose gear is 4.5 m from the nose (under the cockpit), and the main landing gear is 1.1 m behind the most aft centre of gravity (21.4 m from the nose). With the main landing gear any further aft, the nose landing gear would need to be in front of the nose.

In order to prevent the aircraft from lateral tipover, a sufficiently wide gear track is determined based on the angle between the outer gear and the vertical height of the centre of gravity. This angle is 63° and is within requirements. The length from the bottom of the fuselage to the ground is 1.5 m, as the track width is sensitive to the height of the aircraft's centre of gravity off the ground. This is the lowest, reasonable value for the height off the ground of the aircraft, that would satisfy all angles (scrapeback, tipback and tipover), while producing favourable gear positioning.

As there was no option to put the gear in the high wings, the gear has to be integrated into the fuselage through a fairing, which will also support the strut-fuselage integration. Accounting for these factors, the gear track is determined to be 6.49 m wide, which is wide enough to provide lateral stability, and is the narrowest possible, to be able to fit into the belly fairing. This fairing increases the overall drag. Minimizing the track-width allows designers to minimize the size of this fairing and, therefore, its induced drag.

From the positioning of the landing gear and the loading diagram as presented in Figure 6.21 the maximum loads of the gears can be calculated. The nose landing gear has to sustain a maximum load of 67,689 N, which can occur during the loading of passengers on the aircraft. This comes down to 3,450 kg per wheel for the nose gear. The main landing has to sustain a maximum load of 608,220 N , which occurs for the fully loaded aircraft. This comes down to 15,500 kg per wheel.

As the TU-ecoliner is designed to operate on airports with properly paved runways, a high load classification number (LCN) has been chosen. The LCN provides a measure for the maximum load that can be sustained by the runway surface and determines the maximum tire pressure to be used. Based on the LCN for reference aircraft provided by [21], a LCN of 50 was specified for the aircraft.

Using the maximum load per wheel for the main and nose landing gear, and the LCN for the aircraft, the tire pressure for the wheels can be determined using statistical relations from [22]. For the nose landing gear wheels the tire pressure equals 8.5 kg/cm^2. The main landing gear wheels will be pumped up to a pressure of 10.5 kg/cm^2.

Using [22], the wheels for the landing gear can now be selected. The nose wheels, with a maximum load of 3,450 kg and a tire pressure of 8.5 kg/cm^2, will be 26 x 6.6 inch tires. Meaning they will have a diameter of 66.0 cm and a width of 16.8 cm. The main landing gear wheels, with a maximum load of 15,500kg and a tire pressure of 10.5 kg/cm^2, will feature 45 x 15.75 inch tires. Which means they will feature a diameter of 114.3 cm and a width of 40.0 cm.

6.3.2. Landing Gear Drag

An extended landing provides a significant source of additional drag. The drag of the landing gear is estimated using a method presented by Raymer [29]. The method is based on statistics from reference aircraft and presents values for the drag with a unit of $\frac{\text{D/q}}{\text{landing gear frontal area}}$. For a streamlined wheel and tire a value of 0.18 is presented, a streamlined strut has a value of 0.05. Consequently, the C_{D_0} increment due to the landing gear can be determined using Equation 6.52. The frontal area of the wheel equals the wheel diameter multiplied with the wheel width. This equals 0.111 m^2 for the nose wheels and 0.457 m^2 for the main gear wheels. The length of a landing strut is determined to be 1.5 m and its width is 0.15 m. Therefore, the strut's frontal area equals 0.225 m^2. This brings the total drag increment for a main landing gear bogey to $12.36 \cdot 10^{-4}$. For the nose gear the drag increment equals $6.595 \cdot 10^{-4}$. The total landing gear drag increment should be multiplied by 1.2 [29], bringing the total $\Delta C_{D_{0_{\text{Landinggear}}}}$ to 0.00439. This increment will be added to the C_{D_0} value calculated in Subsection 6.2.5 for the aircraft in clean configuration.

$$\Delta C_{D_{0_{Landinggear}}} = \frac{2 \cdot 0.18 \cdot A_{wheel} + 0.05 \cdot A_{strut}}{S_{ref}} \tag{6.52}$$

6.4. Structural Characteristics

In this section, the structural build-up of the TU-ecoliner will be presented. For all parts that are designed, both a quasi isotropic CFRP and 7075-T6 aluminum will be considered. Later on, in Section 6.5 a trade-off will be provided on which material to use. The aircraft coordinate system that will be used is defined in figure 6.7.

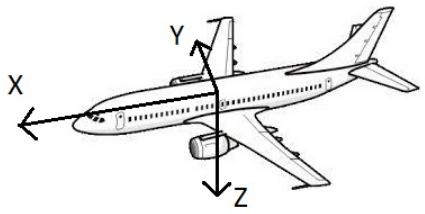

Figure 6.7: Coordinate System of the Aircraft (body oriented)

6.4.1. Fuselage Design

The fuselage shall be sized for the maximum bending moments, torques and shear stresses that occur during the nominal mission. Assuming a uniform distribution of the weight, the maximum loads on the fuselage structure are summarized below in Table 6.7. The internal shear and moment diagrams for take-off and landing are presented in Figures 6.8 and 6.9. Also the loads for pressurizing the cabin have to be taken into account. The pressure difference between the pressure inside the fuselage, which is kept at the pressure level of 8,000 ft, and the outside pressure at the surface ceiling of 42,000 ft.

The internal shear diagram seen in Figure 6.8 shows two jumps in shear force in the take-off diagram. These are the wing loading and tail loading respectively. The internal shear diagram in landing shows four jumps in shear force. These respectively account for the front landing gear, main landing gear, wing loading and tail loading. The internal moment diagram shown in Figure 6.9 shows two kinks in the landing diagram. These are the reaction forces of the nose and main landing gear respectively.

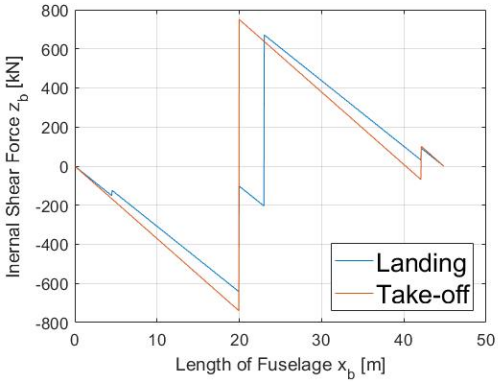

Figure 6.8: Internal shear force diagram

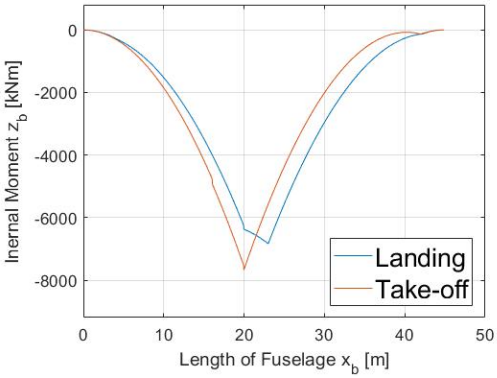

Figure 6.9: Internal Moment M_y diagram

Table 6.7: Loads on the fuselage

Load	**Take-off**	**Landing**
Vertical Shear [kN]	767.0	671.0
Moment M_y [MN]	7.669	6.833
Torque [MNm]	NA	4.43
Pressure difference [Pa]	58,227[1]	NA

As a first estimation, the fuselage is approximated as a cylinder with a constant thickness. It is then sized for all different load cases. It was found that the critical load case was the bending moment about the y_b axis during take-off combined with the pressurization of the cabin at fatigue conditions. Note that at this point in the design, buckling is not yet accounted for. For this, the thickness was calculated using Equation 6.53 and found to be 4.7 mm using a quasi isotropic CFRP material and 7.0 mm using 7075-T6 Aluminum.

$$t = \frac{M \cdot y + \Delta P \cdot R^4 \cdot \pi}{\frac{\sigma_y}{SF} \cdot \pi \cdot R^3} \tag{6.53}$$

From this simple approximation, designed not to fail under the given loads, the inertia required to withstand the loads can be derived. This was calculated to be 0.1004 m^4 for CFRP and 0.1514 m^4 for Aluminum. In a first iteration, the thickness of the skin is replaced by stringers. When doing this, the inertia calculated with the simple estimation must be kept in order to still withstand the loads. The result of this can be found in Table 6.8. The chosen stringer is a hat stringer with dimensions given in Figure 6.10.

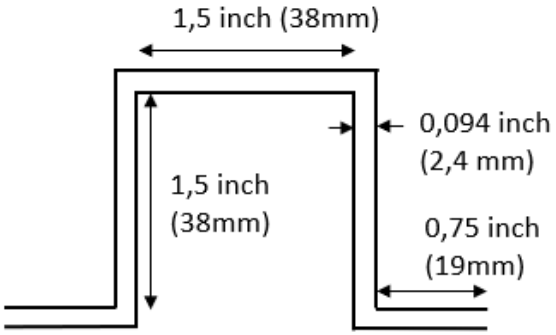

Figure 6.10: Stringer dimensions

[1] Pressure forces are added to the take-off conditions to account for the phase when the aircraft just reached its cruise altitude

Table 6.8: Details on fuselage sizing for bending

Material	**Required interia** [m^4]	**Inertia** [m^4]	**Number of stringers**	**Skin thickness** [mm]
QI CFRP	0.1004	0.1013	70	1.0
7075-T6 aluminum	0.1514	0.1521	99	1.8

However, now also buckling comes into play. The sizing of a stiffened panel for buckling is split up into three steps [37]. First, the critical buckling stress of the skin panel is calculated with Equation 6.54. Secondly, the crippling stress of the stringer is found using Equation 6.55. Thirdly, using Equation 6.56, the critical stress of the stiffened panel is found. The effective sheet width is calculated using Equation 6.57.

$$\sigma_{cr} = C\frac{\pi^2 \cdot E}{12\left(1-\nu^2\right)}\left(\frac{t}{b}\right)^2 \tag{6.54}$$

$$\frac{\sigma_{cc}}{\sigma_y} = \alpha\left(\frac{C}{\sigma_y}\frac{\pi^2 \cdot E}{12\left(1-\nu^2\right)}\left(\frac{t}{b}\right)^2\right)^{1-n} \tag{6.55}$$

$$(\sigma_{cc})_{panel} = \frac{\sum \sigma_{cc}^{(i)} \cdot A_i}{\sum A_i} \tag{6.56}$$

$$2 \cdot w_e = t\sqrt{\frac{C \cdot \pi^2}{12\left(1-\nu^2\right)}}\sqrt{\frac{E}{\sigma_{cc_{stiff}}}} \tag{6.57}$$

Equation 6.56 gives the critical stress of the stiffened panel, which means that this is the maximum stress the panel can take before local buckling takes place. This is compared by the actual stress on the panel calculated using the flexure formula as given by Equation 6.58. This has to be smaller than the critical stress for the panel not to fail.

$$\sigma_{bend} = \frac{M_{max} \cdot y_{max}}{I} \tag{6.58}$$

The results of this analysis can be found in Table 6.9. It can be seen that for CFRP, the inertia provided by the configuration of skin thickness and amount of stringers is still enough to satisfy the bending case. For the aluminum however, it can be seen that when sized for buckling only, the inertia needed for bending is not met. This means that for an aluminum fuselage, bending is the critical load case and it should be sized for that. During the design process, the structure was optimized for the lowest weight. This was done for example by implementing stringers instead of skin when possible. Stringers add less weight for the same inertia then skin does.

Table 6.9: Details on fuselage sizing for buckling

Material	$\sigma_{\mathbf{cr}}$ [MPa]	$\sigma_{\mathbf{bend}}$ [MPa]	$\Delta\sigma$ [MPa]	**Number of stringers**	**Skin thickness** [mm]	**Inertia** [m^4]
QI CFRP	121.80	120.40	1.40	87	1.0	0.1210
7075-T6 aluminum	97.96	97.94	0.04	98	1.7	0.1488

Verification and Validation

To verify the program used for the sizing of the fuselage, Calculations were performed by hand as much as possible. Also, at regular intervals fellow students were consulted with. When problems were encountered, professors were consulted with to make sure the calculations stay on point. Also, plugging in characteristics of materials given in reference books [38], the program was verified.

To validate the results, and thus the method used, reference values for existing aircraft [38] were looked into. However, because the aircraft is designed to be made out of a quasi isotropic CFRP material reference aircraft are not entirely representative. It is good however, to get an approximate idea. As mentioned before, also characteristics of reference materials are used to check with reference aircraft.

6.4.2. Wing Design

The maximum lift force that the wing and tail produce, was determined by computing the maximum required forces during landing and take-off for 3 situations; take-off at MTOW, take-off at maximum aft cg position, and take-off with maximum forward cg position. The maximum forces are summarized in Table 6.10.

Table 6.10: Design Forces for wing and tail

Maximum Tail Force [kN]	47.48	Occurs at MTOW
Maximum Wing Force [MN]	1.68	Occurs at $x_{aft_{max}}$ at take-off

The wing loads are simplified to the weight of the wing, the lift, the fuel stored in the wing, the weight of the engine, and the reaction force of the strut. These load distributions were simplified to model the internal moment, shear and torques. The lift was assumed proportional to the surface area using Equation 6.59. The wing and fuel weight were assumed proportional to the surface area. This assumption leads to a larger bending moment compared to reality.

$$L(y)\int_0^y C_L \cdot q_{TO} \cdot S(y)\,dy = C_L \cdot q \int_0^y \left[c_r - \frac{c_r - c_t}{L} \cdot y\right] dy \tag{6.59}$$

The internal torque has two contributions; the engine thrust and the lift. The thrust is assumed to be a point load through the center of the engine. The fairing height of 13cm is included in the moment arm.

$$T_{wing}(y) = \int_0^y 0.25 \cdot c(y) \cdot L(y)\,dy \tag{6.60}$$

The shear, moment and torsion diagrams of the wing during take-off are shown below.

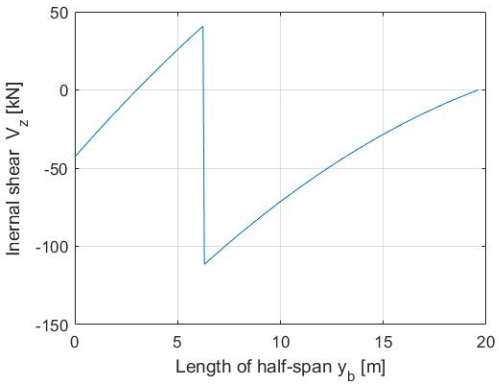

Figure 6.11: Internal wing shear in z_b

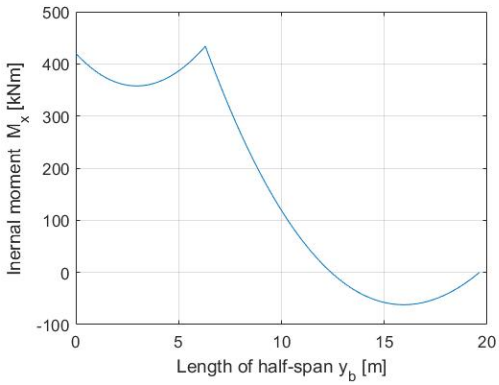

Figure 6.12: Internal wing moment about x_b axis

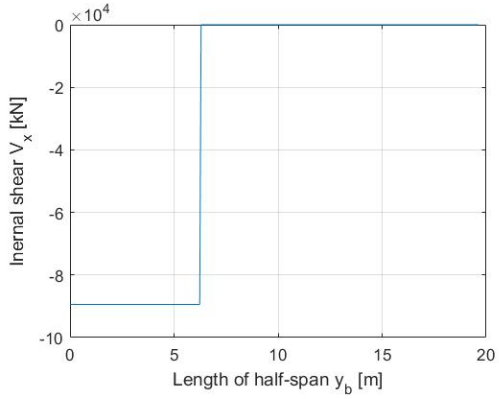

Figure 6.13: Internal wing shear in x_b

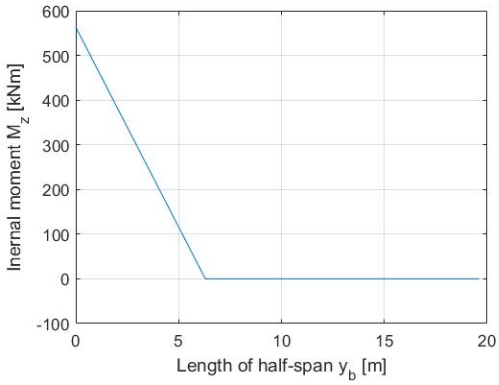

Figure 6.14: Internal wing moment about z_b axis

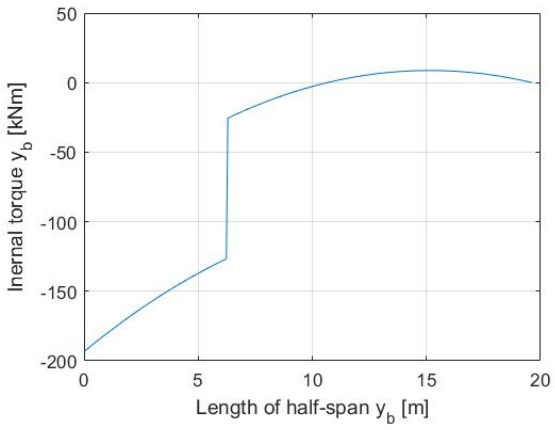

Figure 6.15: Internal Torque in wing about y_b axis

Despite many verification and re-coding efforts to solve the strut force properly using indeterminate beam equations, the force of the strut is assumed as 30% of the maximum lift of a single wing. This is done to solve the unreliable results. The maximum shear flow from all 25 rib positions was measured to be 293 N/mm for the 7075-T6 Aluminum option and 370 N/mm for the QI CFRP option. Assuming ribs from the aforementioned 7075-T6 material and addding appropiate fatigue (FF) and load safety factors (SF), the minimum rib thickness is calculated using Equation 6.61. The rib thickness is rounded to 3 mm in both designs.

$$t_{min} = \frac{q}{\tau_{max}\frac{FF}{SF}} = \frac{370 \cdot 10^3}{331 \cdot 10^6 \frac{0.638}{1.5}} = 2.18\text{mm} \tag{6.61}$$

Table 6.11: Data on designed wingbox

Strut/no strut	**Material**	**Spar thickness** [mm]	**Skin thickness** [mm]
Strut	QI CFRP	10.0	27.0
	7075-T6 aluminum	8.0	20.0
No strut	QI CFRP	14.0	38.0
	7075-T6 aluminum	11.0	28.0

Verification and Validation

Firstly, the shear, moment and torque diagrams of a simple model of the wing was made using the same coordinate system. The plots created by the program were verified by comparing them to the expected shear, moment and torque diagrams made by hand. The plots were also verified by solving a practice problem from the Mechanics of Materials book [39] and replicated.

The shear flow due to the V_x (thrust) was assumed to be negligible. This turned out to be a very reasonable assumption to make as the $\frac{V_x}{I_{zz}}$ term is at least 53 times larger than the $\frac{V_z}{I_{xx}}$ term for any mentioned design option. Secondly, the program used to determine the strut force was not used as it determined the strut forces for a pinned wing. Following, all shear, moment and torque diagrams begin and end at zero indicating the correctness of the diagrams at free ends. The results from the wing analysis tool were compared to the predicted wing weights of a similar aircraft in MTOW, wing loading and taper ratio, with the same aspect ratio from a conceptual study of strut braced wings (SBW) [40] (presented below in Table 6.12)[2]. The difference of the weight is in the correct order of magnitude for both Aluminum and CFRP.

[2]The "rigid" (no optimization performed) wing weights were selected from the study for comparison

Table 6.12: Calculated (single) wing weights for both conventional and strut-braced at A=14

	A=14	Conv.	SBW	Dif (%)
Reference	Aluminium	5,100 kg	4,400 kg	13.7
Design	Aluminium	4,521 kg	3,796 kg	19.1
Reference	CFRP	4,400 kg	3,500 kg	20.4
Design	CFRP	3,565 kg	2,997 kg	19.0

6.4.3. Strut Design

The trade-off has been made between the drag produced by the strut and the required mass. The strut has been designed for buckling as it was shown to be the driving factor for landing. For instance, the axial stress margin of the material at maximum tension was over 100 MPa, while the buckling margin was barely above zero. The optimum thickness-to-chord ratio (TTCR) for a strut was found to be between 18 to 23% [29]. Setting a total skin thickness (including stringers) to 8mm, the mass varied from 79 kg for 18% to 64.5 kg for 23%. As the required mass varies only by kilograms, a airfoil with 21% TTCR was selected. The 7075-T6 aluminum was selected leading to a mass per strut of 69.2 kg with a spar thickness of 8 mm and optimal chord of 0.451 m. CFRP was also analyzed leading to an optimal chord of 0.526 m and a mass of over 75 kg for the 21% TTCR. After this a sensitivity analysis has been performed for different masses of the strut and their drag as shown in Table 6.13.

Table 6.13: Sensitivty analysis of the strut mass and drag coefficient

	Nominal Value	Weight					
		-30%	-20%	-10%	+10%	+20%	+30%
Minimum Strut Chord[mm]	451.0	523.0	520.0	501.0	491.0	447.0	439.0
Strut Drag Coefficient [10^{-3}]	0.775	+12.7%	+10.5%	+4.4%	-3.9%	-14.6%	-15.1%

6.4.4. Horizontal Tail Design

The horizontal tail has been sized in an identical manner as the wing, but without the strut reaction force. The loads of the tail are the tail lift, the tail weight and fuel stored in the tail. As the lift weight and fuel are simplified as one distributed force, the largest is taken to be the design load. This is determined using equation 6.62. The fuel stored in the tail is assumed to be pumped into the wing during landing. The critical loading case for the tail force is at landing with the cg at its most forward position. This means the tail needs to provide a downforce of 35.8 kN.

$$F_{design-tail-TO} = F_{tail-max} - \left(W_{tail} + W_{fuel-tail}\right) \cdot n \cdot g = 2.948 \cdot 10^4 \tag{6.62}$$

$$F_{design-tail-landing} = F_{tail-max} - \left(W_{tail} + W_{fuel-tail}\right) \cdot n \cdot g = -3.9738 \cdot 10^4 \tag{6.63}$$

Therefore, a design load of -40 kN is used to size the horizontal tail. The shear, moment and torque diagrams are presented below in Tables 6.16, 6.17 and 6.18.

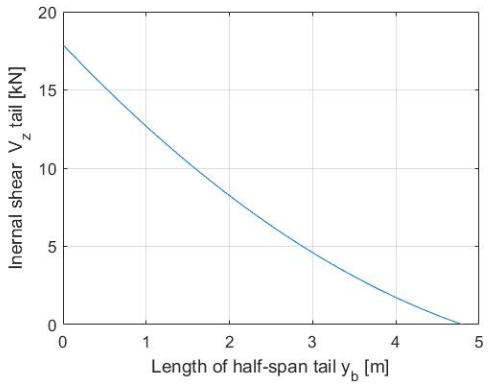

Figure 6.16: Internal Shear Diagram of Horizontal Tail in z_b

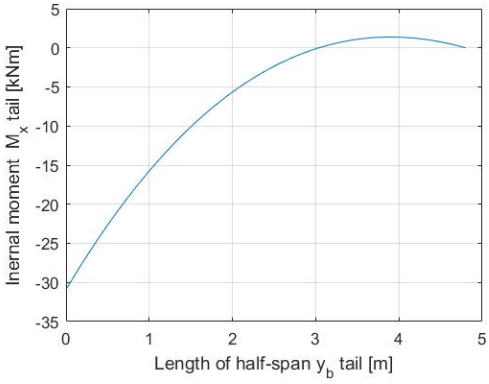

Figure 6.17: Internal Moment Diagram of Horizontal Tail about x_b axis

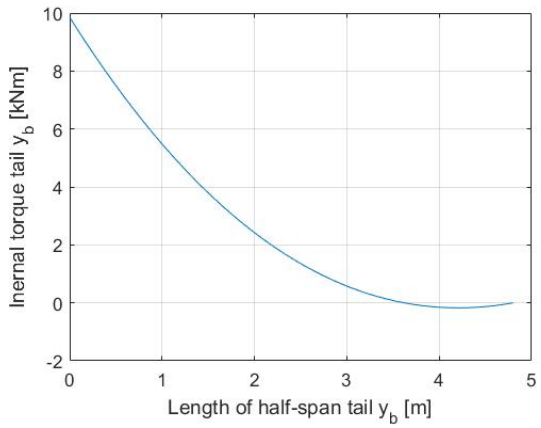

Figure 6.18: Internal Torque Diagram of Horizontal Tail in y_b

Table 6.14: Horizontal tail design trade-off table

Material	**Skin thickness** [mm]	**Spar thickness** [mm]
QI CFRP	1.0	6.0
7075-T6 aluminum	1.0	2.0

6.5. Material Characteristics

In this section, firstly, an updated table with material characteristics will be given. Secondly, a material selection for each of the designed parts will be made. thirdly, a table will be given with specific aircraft parts that will be made from other materials.

The updated table of material characteristics can be found in Table 6.15. These are the material characteristics as used in the calculations for the structural design. On top of this, for working with composites, a safety factor of 2.5 was applied. For working with metals, a safety factor of 1.5 was taken into account. The number of cycles has been calculated by multiplying the number of flights per day (8 flights) for 30 years of operation. This number was multiplied by a factor of 16 to correct for the structural interactions of the entire assembly, leading to a figure of about 1 million cycles. All data in Table 6.15 is taken from the CES Edupack database[3] unless stated otherwise.

Table 6.15: Material characteristics

Material	**Density** [kg/m^3]	**Material cost** [€]	**Yield strength** [MPa]	**Shear strength** [MPa]	**Young's modulus** [GPa]	**Fatigue strength** [MPa]	**Compressive strength** [MPa]
QI CFRP	1,610	52.50	649	649	48.0	422	668
2024-T6 aluminum	2,780	2.86	381	28	75.7	147	397
7075-T6 aluminum	2,830	3.60	530	370	76.0	168	530
Ti-6Al-4V titanium	4,430	20.40	1,080	550[4]	119.0	638	1,150

When designing the structure of the aircraft, the calculations for both aluminum and CFRP were made. The 2024-T6 aluminum was disregarded at the first design step as the fatigue strength to density ratio was significatly lower than the 7075-T6 while the cost savings are small. The largest strength to density CFRP was selected consisting of 70% fibers and 30% epoxy. Table 6.16 gives a trade off between both materials for each part that was designed. The last column gives the cost it takes to save one kilogram of weight when going from aluminum to CFRP. Note that this is a negative value for the strut because the strut made from aluminum is lighter than the strut made from CFRP.

[3] `http://www.grantadesign.com/education/edupack/edupack2017.htm` [Cited 29 May 2018]
[4] `http://asm.matweb.com/search/SpecificMaterial.asp?bassnum=mtp641` [cited 22 May 2018]

For the fuselage, the decrease in weight from aluminum to CFRP is about 4,500 kg. Although this increases the cost significantly, it is decided that this is worth the extra cost because it will decrease the DOC of the aircraft. The wingbox will also be made from CFRP. Although the additional cost per kg saved is higher than for the fuselage, a weight saving of 800 kg is still significant. The strut is lighter and cheaper in aluminum than it would be in CFRP so it is evident that aluminum will be used here. For the horizontal tail wingbox, 10 kg could be saved for an additional cost of 2,200 euro. This is not benificial for the overall cost of the aircraft. Therefore the horizontal tail wingbox will be produced out of aluminum.

Table 6.16: Material trade-off table

Part	**Material**	**Weight** [kg]	**Cost** [€]	**Saving Ratio** [Eur/kg]
Fuselage	QI CFRP	5,504	288,985	54.0
	7075-T6 Aluminum	10,178	36,741	
Wingbox	QI CFRP	2,997	157,930	180.5
	7075-T6 Aluminum	3,796	13,703	
Strut	QI CFRP	75	3,953	-370.4
	7075-T6 Aluminum	69	249	
Horizontal tail wingbox	QI CFRP	47	2,485	228
	7075-T6 Aluminum	57	205	

When working with composites, it has to be noted that there is the possibility to engineer them for specific loading cases. In the calculations performed in this report, a quasi isotropic CFRP is used throughout the whole aircraft. This is mainly done because of simplicity for the preliminary design and due to time constraints. However, the weight of the fuselage and wing can be further optimized by specifically engineering the composites for the respective load cases.

Besides the bigger parts of the aircraft discussed in Table 6.16, also other parts of the aircraft can be made out of different materials. Some very specific parts are made out of different materials than the rest of the aircraft. This can be seen in Table 6.17. The references used for this table are the Boeing 787 and the Airbus A350 because those are the two aircraft that make use of composites the most. Very heavy duty parts as for example the engine pylon are made of titanium, other parts like the leading edges of wings and tail planes are made out of aluminum. Also the struts that hold up the cabin floor will be made from aluminum because their primarily load case will be compression.

Table 6.17: Materials used for different parts of the aircraft

part	**CFRP**	**7075-T6 aluminum**	**Ti-6AI-4V titanium**
Fuselage			
Skin, stringers, frames	X		
Floor	X		
Floor struts		X	
Wing			
skin, spars, ribs, stringers	X		
Leading edge		X	
Struts		X	
Empennage			
Leading edges		X	
Horizontal tail wingbox		X	
Landing gear			X
Engine			
Pylon			X
Nacelle	X		
Leading edge nacelle		X	

6.6. Propulsion System Characteristics

As has been discussed in Chapter 4, it is chosen to implement ultra-high bypass ratio engines in the aircraft design. The engines will be positioned at 32.1% of the half span [1]. The design and sizing is done in two ways, first the engine is sized according to handbooks, which is explained in Subsection 6.6.1. However, due to flaws in this method the engine is scaled bases on thrust using the method of rubber engine sizing, of which an explanation can be found Subsection 6.6.2.

6.6.1. Engine Sizing

The engine sizes are determined by using different design methods, such as the ADSEE1-method [41] as taught in the course Aerospace Design and Systems Engineering Elements 1 at the TU Delft, a method described by Raymer [29] and a method developed by Jenkinson [8]. The results as obtained by the different methods are tabulated in Table 6.18. For details on the different methods such as the detailed formulas used, the reader is referred to the references as to be found in the bibliography. It can be observed that the methods all result in different values. The aforementioned methods all rely on statistical data from existing engines. The ADSEE1 method for example relies on engines as obtained from Torenbeek with all small bypass ratios [41].

Table 6.18: Engine sizing results

	ADSEE1	**Raymer**	**Jenkinson**
Nacelle length [m]	4.20	3.00	3.85
Maximum nacelle diameter [m]	1.67	2.70	3.36
Weight [kg]	2,789	1,330	-

Design Method Accuracy Assessment

In order to be able to assess the aforementioned design methods an accuracy assessment is performed in which existing engines are "designed" by application of known parameters and characteristics. Two engines are analyzed, namely the GEnx 1B70 and the LEAP 1A. The results of these engines as obtained from the ADSEE1 method and Raymer method along with the real values of the parameters are tabulated in Tables 6.19 and 6.20. It is clear that both the methods have their deficiencies. It can be concluded that the Raymer method is the most accurate for both engines. The only exception in this is the diameter of the GEnx 1B70 engine which is predicted the best by the ADSEE1 method. Because of the unreliability of the design methods, it is decided to perform a rubber engine sizing. In this method the engine to be designed is sized based on a reference engine.

Table 6.19: Design method accuracy assessment of the GEnx 1B70 engine

GEnx 1B70	**Real value**	**ADSEE1**	**Raymer**
Nacelle length [m]	4.93 [5]	6.30	4.60
Fan diameter [m]	2.82 [6]	2.60	3.80
Weight [kg]	6,147	8,131	5,331

Table 6.20: Design method accuracy assessment of the LEAP-1A engine

LEAP 1A	**Real value**	**ADSEE1**	**Raymer**
Nacelle length [m]	3.3 [7]	4.8	3.56
Maximum diameter [m]	2.5	1.9	2.9
Weight [kg]	2,990	4,190	2,381

[5] `http://rgl.faa.gov/Regulatory_and_Guidance_Library/rgMakeModel.nsf/0/31c884b43b7f7a7586257fda0075a93e/\protect\T1\textdollarFILE/E00078NE_Rev14.pdf` [cited 16 June 2018]

[6] `https://www.geaviation.com/sites/default/files/datasheet-genx.pdf` [cited 18 June 2018]

[7] `https://www.easa.europa.eu/sites/default/files/dfu/EASA%20E%20110%20TCDS%20Issue%202%20LEAP-1A_1C_20161103_1.0.pdf` [cited 16 June 2018]

6.6.2. Rubber Engine Sizing

In order to have an ultra-high bypass ratio engine, the fan and turbine should be connected via a gearbox to reduce the speed of the fan. Otherwise the fan tips will reach Mach 1 which would induce a lot of drag and noise. Pratt & Whitney has implemented this gearbox in the PW1000G series engine, hence this engine series has been used as reference for the rubber engine sizing. Furthermore, according to Pratt & Whitney the PW1000G series engine can be scaled for a thrust between 45 kN and 178 kN of thrust, while maintaining the same core size. This is done by altering the amount of stages of the compressor and turbine and by changing the speeds at which they are running. Therefore, the engine of the TU-ecoliner will be scaled by interpolation of two known data points using the PW1100G engine, which is currently an engine option for the Airbus A321neo and the PW1500G engine, which is the exclusive engine for the Bombardier CSeries [8]. This linear regression has been done as such, to scale the engine to the required thrust of the TU-ecoliner. The characteristics of both Pratt & Whitney engines and the TU-ecoliner engine which followed from the interpolation can be seen in Table 6.21.

Table 6.21: Engine characteristics Pratt & Whitney and TU-ecoliner

Parameter	PW1100G[42]	PW1500G[43]	TU-ecoliner
Maximum thrust [N]	145,810	102,566	106,500
Overall length (flange to flange) [m]	3.284	3.045	3.070
Weight [kg]	2,857.6	2,177.0	2,238.9
Bypass ratio	12.5	12.0	14.0
Diameter fan [m]	2.06	1.85	1.87
Diameter nose cowl [m]	2.224	2.006	2.030

However, the engine data from both Pratt & Whitney's are obtained from their type certification sheets and these do not include the total length of the engine and maximum diameter of the nacelle. In order to determine these dimensions for the TU-ecoliner, the total engine dimensions of the PW1100G were obtained from the "Airport Planning and Characteristics" of the Airbus A321neo and can be seen in Figures 6.19 and 6.20. The ratio of fan to maximum nacelle diameter and the ratio of overall length to total length of the PW1100G engine, which is equal to 1.26 and 0.645 respectively, are used. The maximum dimensions of the TU-ecoliner were obtained by multiplying these ratios with the values from Table 6.21, of which a maximum nacelle diameter of 2.36 m and total length of 4.76 m were obtained.

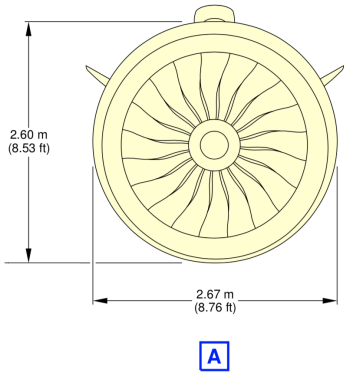

Figure 6.19: Frontview of the PW1000G engine [44]

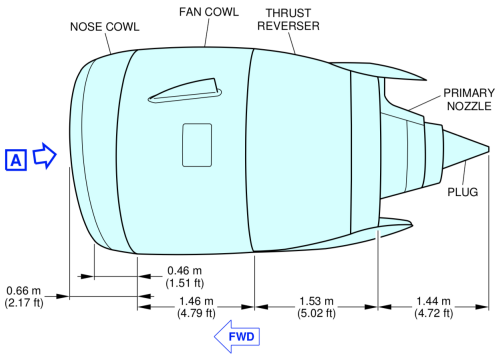

Figure 6.20: Sideview of the PW1000G engine [44]

A note that has to be made is that the TU-ecoliner could not be scaled for its higher bypass ratio, since no information on the core is shared by Pratt & Whitney, therefore there is some error in the determination of the fan and the maximum nacelle diameter.

[8] `https://www.pw.utc.com/Content/PurePowerPW1000G_Engine/pdf/B-1-1_PurePowerEngineFamily_SpecsChart.pdf` [cited 26 June 2018]

6.7. Stability and Control Characteristics

In order to assess the stability & control characteristics of the TU-ecoliner, a good first order estimate of the center of gravity during several loading cases has to be made. For this, it is required to know with sufficient accuracy how the internal cabin lay-out looks like, including seat arrangement and seat pitch. Also, the position of the cargo containers including their mass is of importance. Furthermore, the center of gravity for several aircraft components has to be located in order to get an idea of the center of gravity of the operational empty aircraft. For all this see Section 6.7.1.

From this data the wing position could be varied to see how this shifts the most forward and aft c.g., with which the longitudinal wing position and required horizontal stabilizer surface area could be determined taking into account stability and controllability requirements.

6.7.1. Center of Gravity

In this subsection the individual contributions for the total center of gravity will be discussed.

Operational Empty Weight

The starting point of the center of gravity determination, is the localization of the center of gravity of the unloaded aircraft, i.e. without fuel and payload. This has been done by considering all the separate components from the Class II Weight Estimation which can be found in Section 6.1 and their respective center of gravity.

The component weights have also been taken from the Class II Weight Estimation, where the average values from the used methods were considered [9]. There are two groups that deserve some more attention in this section, videlicet the landing gear group and the empennage group. Both groups consist of two separate components, the nose and main landing gear and the horizontal and vertical stabilizer, respectively, each having a different center of gravity. The weight of the nose landing gear has been assumed to be at 10% of the total landing gear weight, and the main landing gear at 90% accordingly. For the empennage, the horizontal stabilizer was assumed to contain a quarter of the total weight, hence the vertical stabilizer three quarters. Even though this was a rough approximation, data from reference aircraft supports this.

For the components' center of gravity relative to the nose of the aircraft, several other assumptions were made. Those assumptions do not relate to the center of gravity of the components themselves, as those were retrieved from [45], but rather from the longitudinal positioning of the components. A note has to be made that also relates to the purpose of this stability and control analysis, which is that the longitudinal position of some components have been fixed from the start, whilst the longitudinal wing position was regarded as a variable at first. The positioning of the landing gears was regarded as an iteration product, depending on the position of the most forward and most aft center of gravity. A total load carried by the nose landing gear of in between 6% and 15% was adhered to for ground turning performance, whilst not disregarding the angle in between the most aft center of gravity and the main landing gear for tip back constraints. The following assumptions have been made regarding the fixed longitudinal positioning of some major components:

- The horizontal stabilizer has been positioned such that the longitudinal position of the most aft tip (i.e. of the tip chord) coincided with the back of the fuselage. The longitudinal location of the center of gravity would then follow from geometry.
- The vertical stabilizer has been placed such that the end of its MAC (MAC_v) coincided with the back of the fuselage.
- For the engines, the longitudinal center of gravity position have been assumed to be in front of the leading edge of the wing, to be more exact at a distance of 30% of the nacelle length in front of the leading edge. As engine data about this c.g. position was hardly available, this position was used as it was considered that the last 30% of the engine length would be below the wing, and the engine c.g. is expected to be at less than 50% of the total engine length.
- The reasoning for the longitudinal c.g. position of the nacelle is analogous to the one for the engine, however the nacelle c.g. could was found to be at around 40% the nacelle length [45].
- For the fixed equipment, the c.g. was at first assumed to coincide with the fuselage center of gravity. Later on a scaling factor was applied to this, which was retrieved from a jet transport aircraft weight & balance analysis in Roskam [21]. This shifted the longitudinal c.g. position of all fixed equipment about 1 meter in front of the fuselage c.g.

[9] A Torenbeek and a Roskam method were used and averaged to obtain the final component weights.

In Table 6.22 all components are depicted with their respective weight, center of gravity and the moment they create w.r.t. the nose of the aircraft. These values represent the values after the final wing placement has been performed, and thus represent the final center of gravity locations for the designed aircraft.

Table 6.22: Longitudinal c.g. positions of components.

	Mass [kg]	$\mathbf{x_{cg}}$ [m]	**M** [kg·m]
Wing	7,657	20.39	156,125
Horizontal stabilizer	319	41.82	13,337
Vertical stabilizer	957	41.93	40,114
Fuselage	10,203	19.20	195,890
Nacelles	667	17.44	11,626
Nose landing gear	204	4.50	919
Main landing gear	1,837	21.40	39,314
Engines	6,385	17.77	113,428
Fixed equipment	9,916	18.75	185,918
Operational Empty Weight	38,143	20.10	766,680

Fuel

Section 7.2 will elaborate on the fuel tank positioning and will show how the fuel volume within the wing was obtained. This tool that could determine the wing (fuel) volume has been consulted to find the spanwise position at which half of the fuel is stored. Assuming a uniform fuel density yielded the spanwise c.g. position of the fuel. Assuming a chordwise c.g. position of the fuel that lies exactly in between the two spars (hence, in the middle of the fuel tank), the longitudinal position of the fuel center of gravity could conveniently be calculated, following from geometry. This yielded a $x_{cg_{fuel}}$ of 20.20 meters, or 0.47 of the MAC.

Payload

The location of the center of gravity of the payload of the aircraft depends on many variables. The main part of the payload is represented by the passengers and all of their luggage. It is assumed here that every passenger together with all of their luggage weighs 90 kg. Furthermore, it is assumed that the carry on luggage has the same center of gravity location as the passenger it belongs to. All other passenger luggage is carried in containers in the cargo compartment of the aircraft. The other type of payload the aircraft carries is belly cargo. The aircraft is designed to be at maximum take-off weight with a passenger load factor of 94% and a range of 1.800 km. This makes it unable to carry any additional cargo on these missions. Shorter range missions or lower passenger load factors means that there is a possibility of carrying additional belly cargo. This cargo is evenly distributed over the belly of the aircraft and has a center of gravity location halfway through the fuselage, which is made possible by the high wing configuration which ensures one continuous cargo bay throughout the fuselage.

6.7.2. Loading Diagram

To clearly show the c.g. of the aircraft for different loading cases a loading diagram has been constructed. In a loading diagram one can see what the aircraft loading consists of and in what order it is being loaded. This loading diagram has been based upon the maximum capacity of passengers of 240 in a single class configuration with a seat pitch of 28 inch. Normally in this condition there would be no weight left for cargo but a less than usual amount of fuel is loaded to leave some weight available for additional cargo to show the effect on the loading diagram. The loading diagram of the TU-ecoliner can be found in Figure 6.21.

The contribution of the cargo can be seen by the first dotted line going from the operational empty weight center of gravity to the bottom of the first large so-called 'potato'. The cargo is loaded through standard LD3-W45 containers of equal weight. These are loaded either back to front or front to rear. After this, the contribution of the passengers that are loaded in a certain order is added. First, all the window seats are filled. These are shown to be filled from the front to the rear and from rear to front. This can be seen by the forward and aft side of the potato respectively, where the two lines meet to form the closed potato and where the next potato starts from is when all window seat passengers are loaded. This process is then repeated twice, first for the middle seats and then for the aisle seats. Once this is finished you arrive at the maximum zero fuel weight (MZFW). Finally the fuel is added to get to the maximum take-off weight.

The loading diagram shows that the most forward center of gravity that is obtained is 0.25 MAC and the most aft center of gravity is 0.67 MAC. This means that the center of gravity range is 0.42 MAC or 1.29 m. The maximum take-off weight center of gravity is at 0.54 MAC. One could argue that the center of gravity range of the aircraft is slightly too much to the rear of the aircraft, when looking at the center of gravity location expressed in MAC values. This, however, is caused by the fact that the main wing leading edge is quite far forward at 18.75 m from the nose of the aircraft. Also, the wing has a high sweep angle of 32.9° and a relatively short mean aerodynamic chord length of 3.08 m due to the high aspect ratio of the wing. These three factors combined lead to the values of center of gravity location over mean aerodynamic chord having relatively high values but compared to the total aircraft the centers of gravity are at a proper location. They are also well inside of the bounds to ensure a stable and controllable aircraft with a reasonable tail volume.

The finished loading diagram shows the most forward and aft center of gravity the aircraft can encounter. Before these values are taken to generate the stability diagram of the aircraft a stability margin of 0.02 MAC is added to account for c.g. changes during operations such as people moving around in the aircraft. The loading diagram shown here, has been plotted for the final wing position, so after making the scissor plot and center of gravity range plot which will be explained in the next sections.

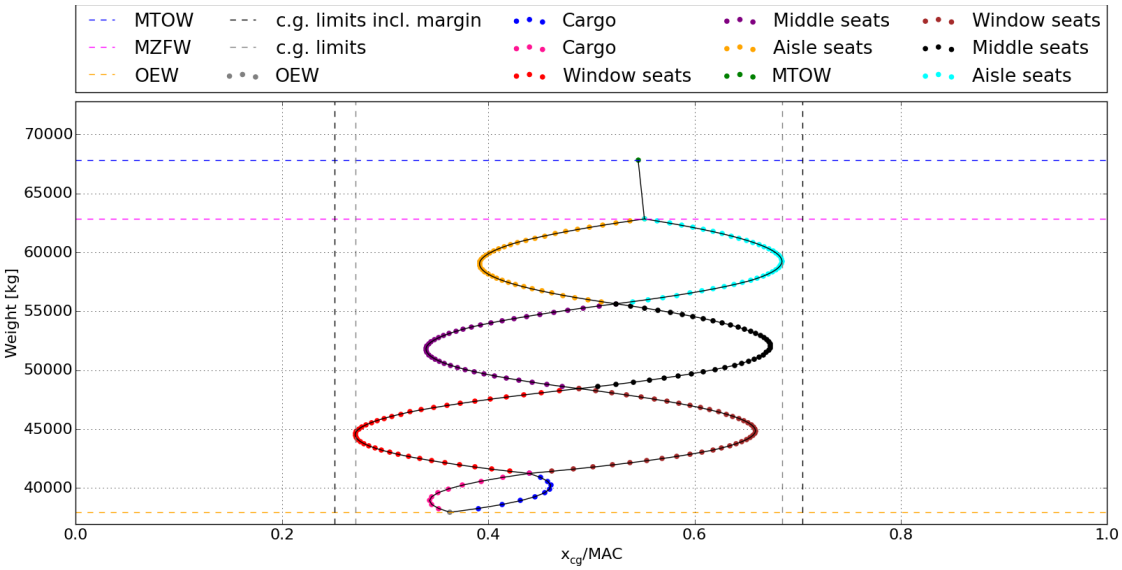

Figure 6.21: Loading diagram with a fuel weight of 5,000 kg and a cargo weight of 3,600 kg.

6.7.3. Scissor Plot

In Section 6.7.2 it can be seen how the c.g. would shift for a particular loading case. As mentioned in that section, the presented loading diagram is for the final wing positioning, an output of the stability & control analysis. How this was done, is shown in Section 6.7.4. A quintessential part of the analysis is the determination of the possible c.g. range, which has been done by generating a scissor plot. This scissor plot was established through the use of a so-called "controllability curve" and a "stability curve", for which the equations are shown below in Equation 6.64 and 6.65, respectively:

$$\frac{S_h}{S} = m\bar{x}_{cg} + q = \frac{1}{\frac{C_{L_h}}{C_{L_{A-h}}}\frac{l_h}{\bar{c}}\left(\frac{V_h}{V}\right)^2}\bar{x}_{cg} + \frac{\frac{C_{m_{ac}}}{C_{L_{A-h}}} - \bar{x}_{ac}}{\frac{C_{L_h}}{C_{L_{A-h}}}\frac{l_h}{\bar{c}}\left(\frac{V_h}{V}\right)^2} \tag{6.64}$$

$$\frac{S_h}{S} = n\bar{x}_{cg} + p = \frac{1}{\frac{C_{L_{\alpha_h}}}{C_{L_{\alpha_{A-h}}}}\left(1 - \frac{d\varepsilon}{d\alpha}\right)\frac{l_h}{\bar{c}}\left(\frac{V_h}{V}\right)^2}\bar{x}_{cg} - \frac{\bar{x}_{ac} - 0.05}{\frac{C_{L_{\alpha_h}}}{C_{L_{\alpha_{A-h}}}}\left(1 - \frac{d\varepsilon}{d\alpha}\right)\frac{l_h}{\bar{c}}\left(\frac{V_h}{V}\right)^2} \tag{6.65}$$

The derivations of these equations have been left out but can be found in [46]. For the reproducibility of the plots, the two following subsections will briefly elaborate on the parameters involved in each of the equations. Note that each of the equations presented have been retrieved from [46] [35], id. for some values that have been checked and affirmed by professors of the faculty Aerospace Engineering.

Controllability

The tail arm l_h has been calculated by taking the distance between the center of gravity of the wing and the horizontal stabilizer, which was an iterative process as the longitudinal wing position varied during the entire analysis. The speed ratio $\frac{V_h}{V}$ squared was taken as 0.85, considering the small vertical distance between the main wing and the horizontal stabilizer. That raised the expectation that the horizontal stabilizer would be partially in the wake of the main wing, lowering the incoming flow velocity. C_{L_h} was taken to be -0.8, as the tail is adjustable. The moment coefficients around the aerodynamic center ($C_{m_{ac}}$) have been calculated before in Section 6.2.6, just as $C_{L_{A-h}}$. Finally, $\bar{x}_{ac}$ have been calculated using Equation 6.66. $(\bar{x}_{ac})_w$ was determined graphically and found to be 0.35. Equation 6.67 and Equation 6.68 were used to correct for the fuselage contribution. Finally, the nacelle contribution was calculated as shown in Equation 6.69.

$$\bar{x}_{ac} = (\bar{x}_{ac})_{wf} + (\bar{x}_{ac})_n \tag{6.66}$$

$$(\bar{x}_{ac})_{f,1} = -\frac{1.8}{C_{L_{\alpha_{A-h}}}} \frac{b_f h_f l_{fn}}{S\bar{c}} \tag{6.67}$$

$$(\bar{x}_{ac})_{f,2} = \frac{0.273}{a+\lambda} \frac{b_f c_g (b-b_f)}{\bar{c}^2 (b+2.15 b_f)} \tan(\Lambda_{0.25}) \tag{6.68}$$

$$\Delta_n (\bar{x}_{ac})_n = \sum k_n \frac{b_n^2 \cdot l_n}{S\bar{c} \cdot C_{L_{\alpha_{A-h}}}} \tag{6.69}$$

Stability

For the stability curve the only newly introduced parameters were the downwash gradient $\frac{d\varepsilon}{d\alpha}$, $C_{L_{\alpha_h}}$ and $C_{L_{\alpha_{A-h}}}$. These were calculated using Equation 6.70, Equation 6.72 and Equation 6.74, respectively.

$$\frac{d\varepsilon}{d\alpha} = \frac{K_{\epsilon_\Lambda}}{K_{\epsilon_{\Lambda=0}}} \left(\frac{r}{r^2+m_{tv}^2} \frac{0.4876}{\sqrt{r^2+0.6319+m_{tv}^2}} + \left(1 + \left(\frac{r^2}{r^2+0.7915+5.0734 m_{tv}^2}\right)^{0.3113}\right) \left(1 - \sqrt{\frac{m_{tv}^2}{1+m_{tv}^2}}\right) \right) \frac{C_{L_{\alpha_w}}}{\pi A} \tag{6.70}$$

$$K_{\epsilon_\Lambda} = \frac{0.1124 + 0.1265\Lambda + 0.1766\Lambda^2}{r^2} + \frac{0.1024}{r} + 2 \tag{6.71}$$

$$C_{L_{\alpha_h}} = \frac{2\pi A_h}{2 + \sqrt{4 + \left(\frac{A_h \beta}{\eta}\right)^2 \left(1 + \frac{\tan^2 \Lambda_{0.5_{C_h}}}{\beta^2}\right)}} \tag{6.72}$$

$$\beta = \sqrt{1-M^2} \tag{6.73}$$

$$C_{L_{\alpha_{A-h}}} = C_{L_{\alpha_w}} \left(1 + 2.15 \frac{b_f}{b_w}\right) \frac{S_{net}}{S} + \frac{\pi}{2} \frac{b_f^2}{S} \tag{6.74}$$

From the scissor plot is plotted as can be seen in Figure 6.22. Note that there are two stability curves - one representing static stability and the other one including a static stability margin of 0.05 of the MAC, which functions as a safety margin. The latter will thence be used to size the empennage and longitudinally position the wing, on which the next section will elaborate further.

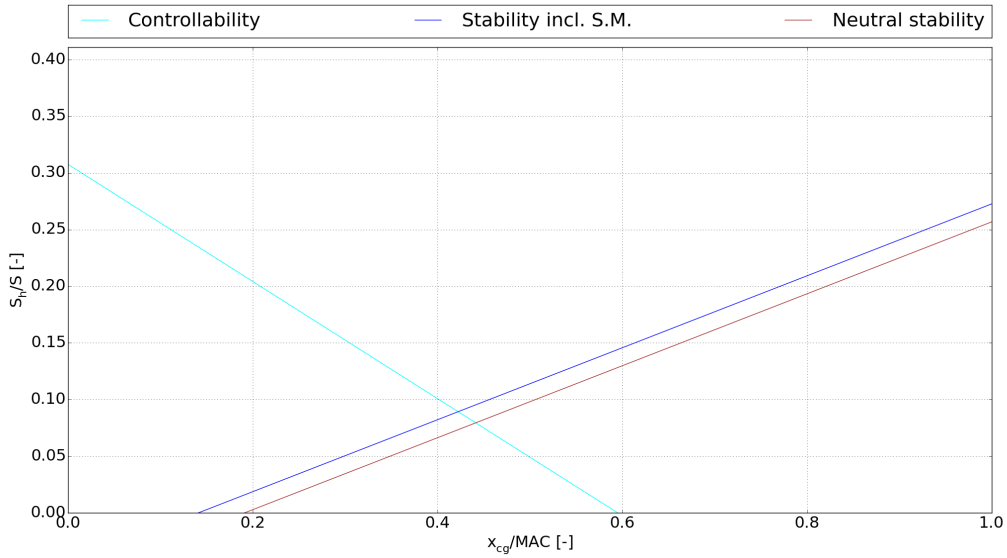

Figure 6.22: Scissor plot showing the controllability curve and two stability curves: one static stability curve and one including a margin of 0.05 MAC.

6.7.4. Empennage Sizing and Wing Placement

Using the center of gravity ranges for certain wing locations and the scissor plot, the location of the wing and the empennage size can be determined. First of all, the location of the wing is set in such a way that the center of gravity range of the aircraft falls within certain safety limits, for which $0.02 \cdot \text{MAC}$ has been added to the most forward and most aft c.g. It should be located on sections of the wing mean aerodynamic chord (MAC) to ensure the aircraft is stable and controllable during flight, this also limits the size of the empennage as the forces required by the horizontal stabilizer to balance the aircraft do not need to be as large if the center of gravity of the aircraft lies close to the aerodynamic center of the wing. Also the landing gear location is an important parameter in determining the wing location. Having the center of gravity of the aircraft too far in front of the main landing gear means that a very large tail is required to rotate the aircraft at take-off. Having the center of gravity too close to the main gear or even behind it means that the aircraft could easily tip-over backwards. A tip-back angle of 15° is held as a safe margin.

To size the horizontal tail two graphs were combined. One is the scissor plot and the other is the graph showing the ranges of the center of gravity location with a varying wing location. This can be seen in Figure 6.23 These two plots are overlapped in such a way that the center of gravity range coincided as closely as possible to the stable and controllable region in the scissor plot. This means that with a certain wing location the smallest amount of horizontal tail surface is required to ensure a stable and controllable aircraft. Taking these factors into account together with the landing gear location requirement and shifting the two graphs relative to each other led to a main wing location of 18.75 m from the nose of the aircraft or 42.5% of the fuselage length. Overlapping the center of gravity ranges plot with the scissor plot gave a horizontal tail surface over wing surface of 0.21 and a corresponding horizontal tail surface of 23.1 m^2.

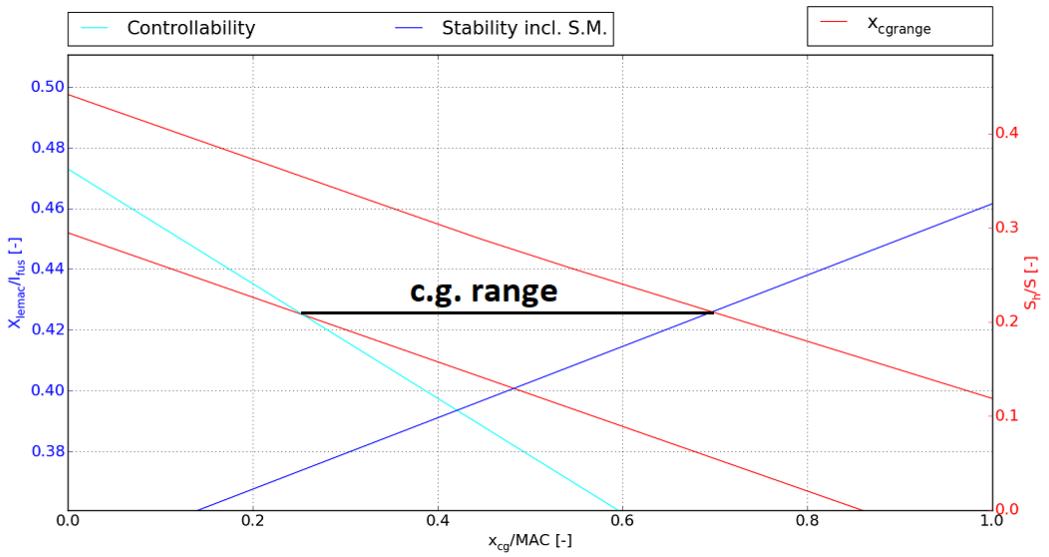

Figure 6.23: Match of scissor plot and c.g. range plot.

6.7.5. Sensitivity Analysis

Now that the empennage has been sized and the wing placement determined, a sensitivity analysis is performed as shown in Table 6.23. The change of the tail surface ratio and the position of the wing has been found for four different variables; the lift ratio, the lift slope, the maximum cg range, and the position of the cg. The results were written down for both 10% decrease and increase from the nominal values.

Table 6.23: Sensitivity analysis on the tail surface ratio and position of the wing with respect to cg variation and the lift and lift slope coefficient fractions

	Nominal Values	$C_{L_h}/C_{L_{A-h}}$		$C_{L_{\alpha_h}}/C_{L_{\alpha_{A-h}}}$		**x_{cg} shift** [MAC]		**x_{cg} range** [MAC]	
		-10%	+10%	-10%	+10%	-10%	+10%	-10%	+10%
S_h/S	0.21	+9.5%	-4.8%	+4.8%	-4.8%	+4.8%	-4.8%	-9.5%	+14.3%
X_{lemac}/l_{fus}	0.425	-0.47%	+0.71%	+0.24%	-0.47%	-4.7%	3.5%	+0.47%	-0.24%

6.7.6. Verification and Validation

Proper detailed verification and validation on the stability and control of the aircraft is difficult as there is hardly any data available for comparable aircraft and there is no 'answer sheet' for the aircraft that has been designed. Therefore, professors from the faculty of Aerospace Engineering have been consulted extensively to see whether the results from one program or section made sense before these values were used as input for another program or section. The programs themselves have been validated by using the data available from existing aircraft to see whether they gave reasonable results when using the program that was used. Furthermore the programs were verified by step-by-step manual calculations along the way to check that the programs themselves worked properly.

Table 6.24: Comparison of horizontal tail area-surface area ratio and tail volume coefficient between different aircraft.

	TU-ecoliner	**A319-100**	**A320-200**	**A321-200**	**A340-300**	**B757-200**	**B777-300**
$\frac{S_h}{S}$	0.210	0.253[10]	0.253[10]	0.253[10]	0.201[10]	0.270[11]	0.237[12]
$\frac{S_h \cdot l_h}{S \cdot \bar{c}}$	1.495	0.689[10]	0.799[10]	0.957[10]	0.791[10]	0.957[11]	0.891[12]
$\frac{l_h}{l_{fus}}$	0.497	0.345[10]	0.360[10]	0.364[10]	0.458[10]	0.404[11]	0.452[12]

[10] https://booksite.elsevier.com/9780340741528/appendices/data-a/table-1/table.htm [cited on 26 June 2018]
[11] https://booksite.elsevier.com/9780340741528/appendices/data-a/table-3/table.htm [cited on 26 June 2018]
[12] https://booksite.elsevier.com/9780340741528/appendices/data-a/table-4/table.htm [cited on 26 June 2018]

As can be seen in Table 6.24, data have been collected about the horizontal tail area-surface area ratio, the horizontal tail volume coefficient and the ratio of the tail arm and fuselage length for different transport jets for which this data was available. The data serves as a validation method to see whether the obtained results relate to other transport jets and if not, if and how this could be explained.

The obtained $\frac{S_h}{S}$ turned out to be lower than most reference aircraft. Also the horizontal tail volume coefficient is 50% higher than the second highest value, even though $\frac{S_h}{S}$ is lower for the TU-ecoliner. The conclusion from this is that $\bar{c}$, or the Mean Aerodynamic Chord, causes the coefficient to be so far off, which on its turn is due to the high aspect ratio in combination with the high aspect ratio wing. Lowering the aspect ratio to 9 resulted in a horizontal tail volume coefficient of 0.993, which is in line with the data from reference aircraft.

The major cause of the relatively low $\frac{S_h}{S}$ is also due to the high aspect ratio, of which the effect could be seen in Equation 6.70. Changing the aspect ratio from 14 to 9 increases the downwash gradient by 36%, which could be reasoned by the fact that lowering aspect ratio increases the chord near the tip[13]. Hence more air is pushed downwards resulting in a higher downwash gradient. Here the high aspect ratio as adopted on the TU-ecoliner shows one of its potentials: the horizontal stabilizer is considerably more effective and could thus be made smaller. From the created tool it turned out that with an aspect ratio of 9 the ratio $\frac{S_h}{S}$ would become 0.24, which is again in line with reference aircraft.

6.8. Empennage Design

The empennage encompasses two main control surfaces, the horizontal tail and the vertical tail, and is placed at the back of the aircraft. For the TU-ecoliner a conventional tail was specified. The conventional tail design allows the horizontal tail surface to stay out the most severe downwash flow from the main wing, while reducing weight and drag compared to T-tail [47] [29]. The sizing of the horizontal tail based on the stability and controllability of the aircraft has already been conducted in Subsection 6.7.4. A more detailed design of the horizontal tail will be presented next. Afterwards, the vertical tail will be sized and designed.

6.8.1. Horizontal Tail

The surface area for the horizontal tail was determined to be 23.1m^2 in Subsection 6.7.4. The optimal aspect ratio was determined to be 4. From statistical methods an aspect ratio of 5 was determined for this class of aircraft [47]. However, in order to prevent the engine exhaust flow from interfering with the horizontal tail, the aspect ratio was lowered. This results in a horizontal tail with a span 9.61 m, that stays clear of the engine exhaust. Moreover, the taper ratio was determined to be 0.33, based on a statistical relation from [47]. This results in a root chord of 3.61 m and tip chord 1.19 m. The mean aerodynamic chord for the horizontal tail equals 2.61 m.

6.8.2. Vertical Tail

The vertical tail surface area was determined to be 21.59 m^2, using a statistical relation from [47]. Moreover, the aspect ratio and taper of the vertical tail were determined using similar relations from [47]. The aspect ratio equals 1.8 and the taper ratio is set at 0.34. The overall tail height equals 6.23 m with a root chord of 5.17 m and tip chord of 1.76 m. This brings the mean aerodynamic chord to 3.74 m.

[13] In here it is assumed that the wing surface area remained the same

6.9. Internal Configuration

In Figure 6.24, the internal dimensions of the cabin and cargo bay are shown. It can be seen that the dimensions of the cabin permit to place six seats abreast using a seat width of 17 in (43 cm) leaving an aisle width of 24 in (61 cm). In longitudinal direction, the cabin is 34.4 m long and it contains 40 rows of seats, each with a seat pitch of 29 in (74 cm). With an aisle height of 2.19 m, their is no problem even for the tallest passengers. The cargo bay was dimensioned as seen in Figure 6.24 in order to fit the LD3-45W cargo container. The cargo bay is long enough to fit over 10 of these containers as stipulated in the requirements.

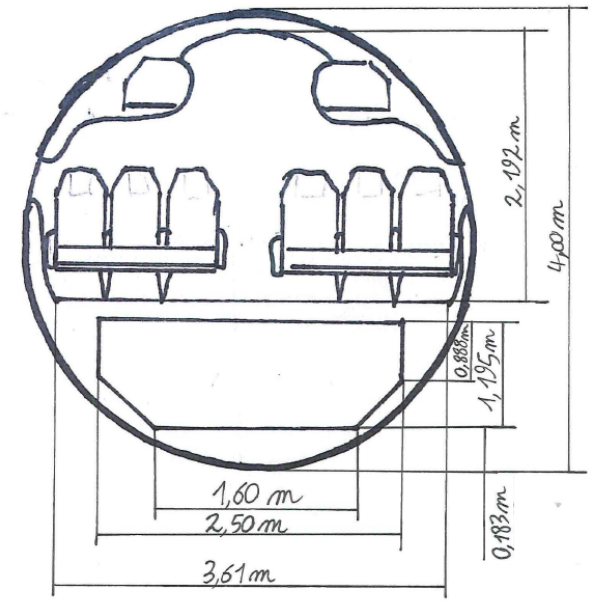

Figure 6.24: Internal dimensions of cabin and cargo bay

6.10. Summary of Design Characteristics

For each component of the TU-ecoliner, a table including a summary of important design characteristics is presented. Tables 6.25, 6.26, 6.27, 6.28 and 6.29 summarize the design of the aircraft in general, the fuselage, wing, empennage and engines and landing gear, respectively. Figures 6.25, 6.26 and 6.27 illustrate the TU-ecoliner's side, top and front views, respectively. Finally, in Table 6.30, a summary of the aerodynamic characteristics of the TU-ecoliner can be found.

Table 6.25: Summary of General Design Characteristics

Symbol	Value	Unit
TU-ecoliner		
Pilots	2	-
Cabin Crew	5	-
Passengers	240	-
OEW	37,934	kg
MTOW	67,834	kg
MLW	62,366	kg
$Fuel_{max}$ [1]	12,161	kg
$Fuel_{design}$	9,530	kg
$Payload_{max}$ [1]	21,600	kg
$Payload_{design}$	20,375	kg
V_{cruise}	0.79	Mach

Table 6.26: Summary of Fuselage Design Characteristics

Symbol	Value	Unit	Symbol	Value	Unit	Symbol	Value	Unit
Fuselage: Exterior			*Fuselage: Interior*			*Fuselage: Structure*		
d_{ext}	3.80	m	d_{int}	3.48	m	material	QI-CFRP	-
l_{fus}	44.85	m	h_{cabin}	2.00	m	t_{skin}	1.00	mm
$l_{cockpit}$	4.00	m	w_{cabin}	3.40	m	n_{string}	83	-
$l_{nosecone}$	6.00	m	l_{cabin}	33.70	m			
$l_{tailcone}$	14.80	m	w_{cargo}	2.50	m			
l_{tail}	6.40	m	h_{cargo}	1.18	m			
			l_{cargo}	15.30	m			

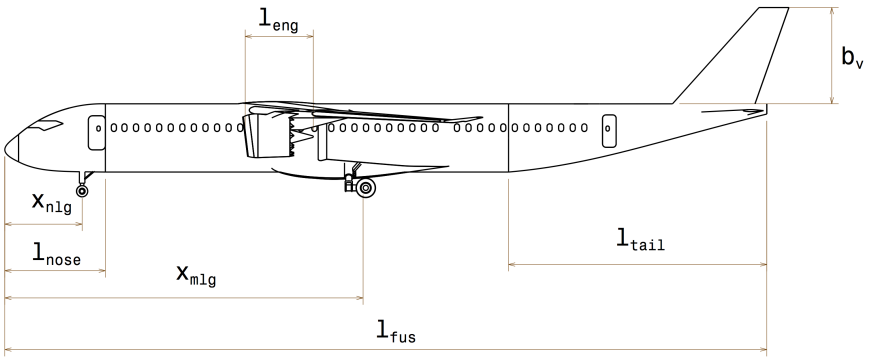

Figure 6.25: TU-ecoliner side profile

Table 6.27: Summary of Wing and Strut Design Characteristics

Symbol	Value	Unit	Symbol	Value	Unit	Symbol	Value	Unit
Wing: Planform			*Wing: Structure*			*Strut*		
S	110	m^2	airfoil	SC20-612	-	airfoil	NASA 16-021	-
A	14	-	material	QI CFRP	-	material	Al 7075-T6	-
b_w	39.24	m	t_{skin}	27	mm	l_{strut}	7.27	m
λ	0.29	-	x_{spar_1}	20	%c	t/c	21	%
$\Lambda_{\frac{c}{4}}$	31.3	°	x_{spar_2}	65	%c	c	451	mm
dihedral	-2	°	t_{spar}	10	mm			
c_r	4.34	m						
c_t	1.26	m						
MAC	3.08	m						
X_{LEMAC}	18.75	m						

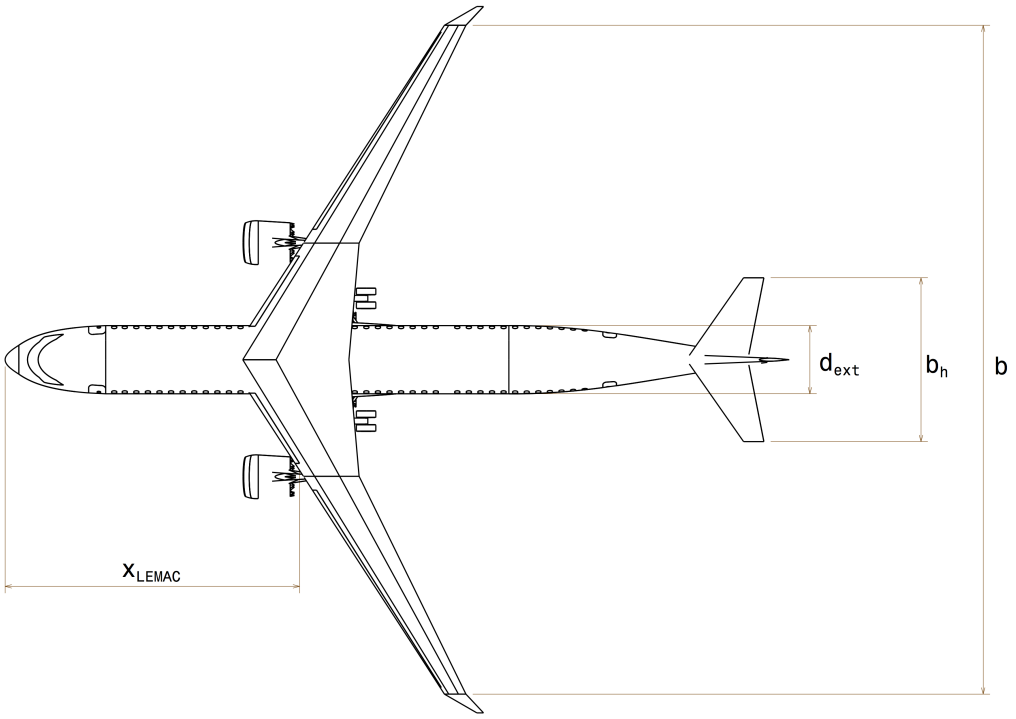

Figure 6.26: TU-ecoliner planform

Table 6.28: Summary of Empennage Design Characteristics

Symbol	Value	Unit	Symbol	Value	Unit
Horizontal Tail			*Vertical Tail*		
S_h	23.1	m^2	S_v	21.6	m^2
A_h	4	m	A_v	1.8	m
b_h	9.61	m	b_h	6.23	m
λ_h	0.33	-	λ_v	0.34	-
Λ_{LE}	55	°	Λ_{LE}	48	°
c_{r_h}	3.61	m	c_{rv}	5.17	m
c_{t_h}	1.19	m	c_{tv}	1.76	m
MAC_h	2.61	m	MAC_v	3.74	m
x_{LEMAC_h}	40.93	m	x_{LEMAC_v}	40.94	m
material	Al 7075-T6	-			
t_{skin_h}	1	mm			
t_{spar_h}	6	mm			

Table 6.29: Summary of Engine and Landing Gear Design Characteristics

Symbol	Value	Unit	Symbol	Value	Unit
Engine and Nacelle			*Landing Gear*		
T_{max}	106.50	kN	x_{nlg}	4.50	m
l_{eng}	3.07	m	x_{mlg}	21.40	m
W	2,238.91	kg	y_{mlg}	6.50	m
BypassRatio	14	-	h_{mlg}	1.50	m
d_{fan}	1.87	m	scrapeback angle	9.5	°
$d_{nosecowl}$	2.03	m	tipback angle	15	°
y_{eng}	12.60	m	tipoverangle	63	°

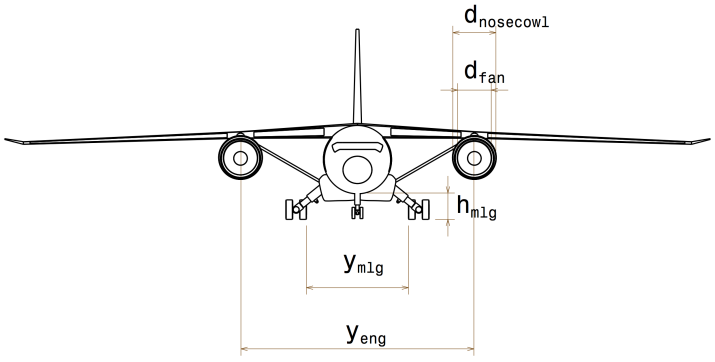

Figure 6.27: TU-ecoliner front view

Table 6.30: Summary of Aerodynamic Characteristics

Parameter	Clean cruise	Clean low speed	Landing flapped	Take-off flapped
$C_{L_{design}}$	0.66	-	-	-
α_{trim} [deg]	3.3	-	-	-
$C_{m_{ac}}$	-1.009	-	-	-
$C_{L_{max}}$	1.04	1.45	2.9	2.2
α_{stall} [deg]	9.4	17.0	18.0	16.9
C_{L_α} [rad^{-1}]	5.89	4.69	5.99	5.66
C_{D_0}	0.0131	0.0131	0.0974	0.0346

7

System Analysis

In this chapter, first the cabin environmental control was discussed in Section 7.1. After that, in Section 7.2, the fuel system is elaborated upon. Later, the hydraulic system is depicted in Section 7.3. Finally, in Section 7.4, the electrical system is discussed.

7.1. Cabin Environmental Control

To ensure a safe and comfortable cabin environment, certain consequences of flying at high altitudes need to be taken into account. First of all, it is impossible for humans to survive on ambient air at high altitudes. Therefore, a cabin pressurization system must be installed to ensure there is enough oxygen in the cabin for the passengers to breathe normally. Even though the cabin is made of CFRP, which is stiffer than the aluminum of previous generation aircraft, the cabin pressure altitude will not be reduced. A standard cabin altitude of 8,000 ft will be sustained on board of the aircraft. This is because the fuselage can then be made thinner which reduces the weight of the aircraft. Also, typical flights of the aircraft only last a few hours which means it makes less of a difference in comfort levels experienced by the passengers if the cabin pressure is slightly higher. In case the pressurization system fails there is an emergency oxygen tank on board with sufficient oxygen to give the pilots ample time to dive to a safe altitude. Next to the low ambient pressure at high altitudes, the outside air temperature at 39,000 ft is $-56.5°$ C. As the aircraft should also be able to operate in hot environments with temperatures reaching 50° C, the aircraft should also have an air conditioning system capable of supporting a moderate inside climate under these extreme outside conditions.

As will be further discussed in Subsection 7.4.2, the APU will be removed. That means that the APU will not be available to provide bleed air for the air conditioning. Therefore, while the aircraft is at the gate it must be connected to an external air conditioning air supply. In order to provide a reliable supply of fresh air to the cabin, an additional secondary auxiliary air conditioning connector will be included on the aircraft.

7.2. Fuel System

The fuel system is a vital system to any modern airliner. Therefore, a high level of redundancy has been implemented. A schematic overview of the fuel system is presented in Figure 7.1. The figure presents the overview of the three main fuel tanks that can be identified. These main fuel tanks are the left and right wing fuel tank and the trim tank located in the horizontal tail. The fuel tanks located in the wings will be subdivided into four smaller fuel tanks in order to manage the balance and stability of the aircraft. An overview of all nine fuel tanks is provided in Figure 7.2.

The TU-ecoliner will be able to carry a maximum fuel weight of 12,161 kg of Jet A-1 fuel. With a fuel density[1] of 810 kg/m^3, the total fuel volume to be carried on board equals 15,013 L. With the wing planform and airfoil as presented in Section 6.4.2, the total wing volume available for fuel storage has been calculated to equal 15,310 L. The two wing fuel tanks combined will house 14,500 L of fuel, while the remaining 513 L will be housed in the trim tank. Consequently, each main wing fuel tank will be able to carry 7,250 L of fuel.

[1] `https://www.exxonmobil.com/en/aviation/products-and-services/products/jet-a-jet-a-1` [cited 13 June 2018]

As can be seen from Figure 7.1, an intricate and redundant fuel system has been designed for the aircraft. The fuel system features three fuel distribution networks, the red, blue and purple systems. These provide a high level of redundancy and allow each of the engines to still be supplied with fuel if two of the fuel systems fail. The system has no single points of failure. Furthermore, it can be seen that, the fuel pumps, indicated with 'P' will be housed in the fuel tanks. These pumps will pressurize the entire system. The fuel valves, indicated with 'V', allow for full control of the fuel system. Moreover, the system features two refueling couplings, indicated with 'R1' and 'R3' in Figure 7.1, one underneath each wing. The system also features two fuel dumping nozzles, indicated by 'R2' and 'R4', in order to be able to dump fuel quickly in case of an aborted flight. This fuel jettison system allows the aircraft to attain its maximum landing weight quickly in case of emergency.

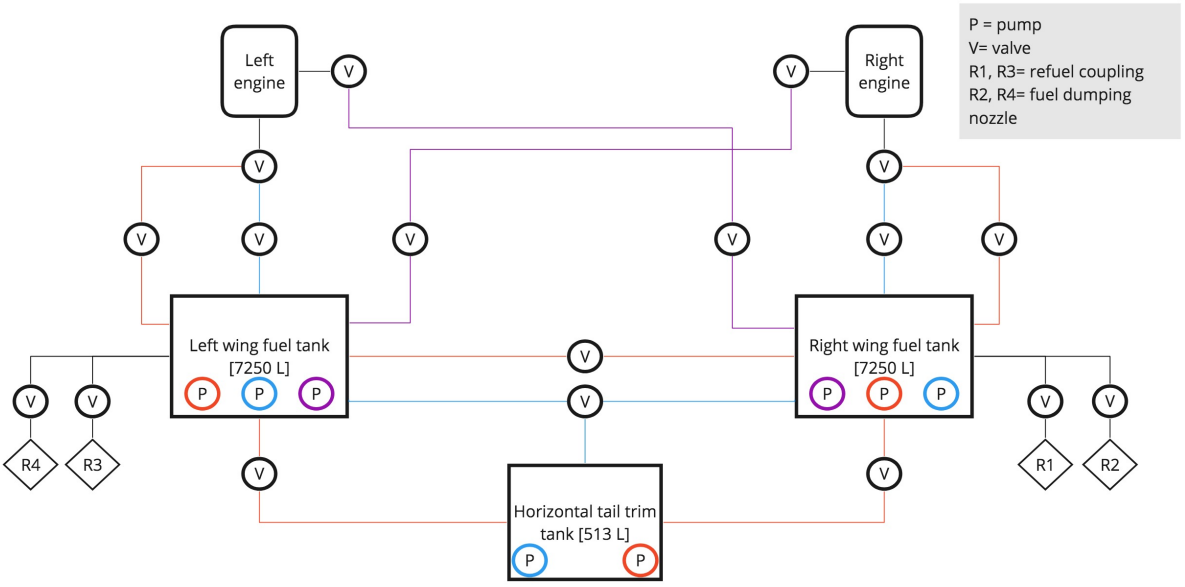

Figure 7.1: Fuel system layout

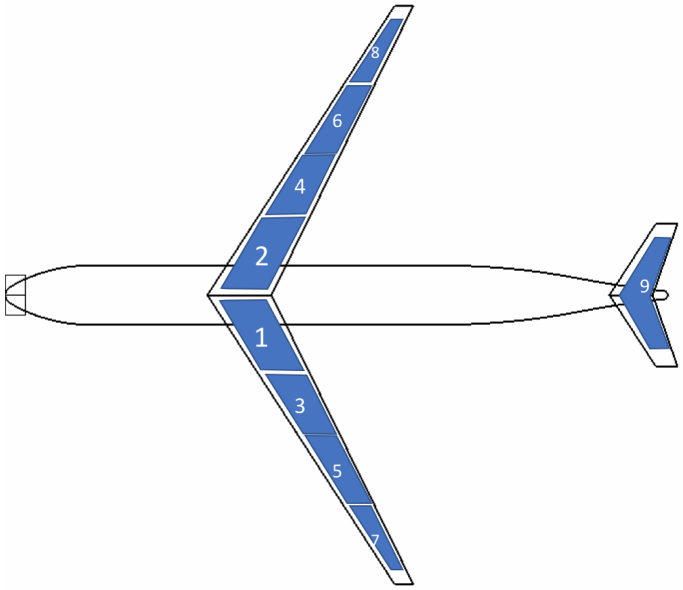

Figure 7.2: Overview of the fuel tank layout

7.3. Hydraulic System

The hydraulic system provides power to the main flight controls. As these controls are essential to the control and safety of the aircraft, a high level of redundancy is required. As such, the system has been designed to not have a single point of failure in the power supply of the most critical flight control. In order to provide such a level of redundancy, the hydraulic comprises three completely separate subsystems, the left, center and right system. Each system provides hydraulic power to specific flight controls, this is presented in Table 7.1. As can be seen from this table, the ailerons, elevators, flaps, main landing gears and nose landing gear are all powered by two different systems. The slats, spoilers and trim tab are considered less critical to the controllability of the aircraft and will therefore be powered by the center system only. This choice has been made in order to save weight from the overall system.

Figure 7.3 provides a schematic overview of the full hydraulic system and how its main components are integrated into the aircraft. In the figure, the left system is indicated with green, the center system is presented in blue and the right system is depicted in red. Since the center system covers all hydraulically powered systems throughout the aircraft, it spans along both the full fuselage and the wings. The left and right systems only span part of the aircraft.

The circles presented in Figure 7.3 represent the hydraulic motors. Since the aircraft is considered a more-electric aircraft, the hydraulic power will be generated using electrically powered hydraulic motors. How these motors are integrated into the electrical system is explained in Subsection 7.4. From Figure 7.3 it is evident the center system will be powered by two hydraulic motors located in the empennage. From the empennage hydraulic hoses will be carried throughout the fuselage floor, through the struts and along the leading edge of the wings. Since fewer systems rely upon hydraulic power supplied by the left and right systems, they will be powered by just one hydraulic motor. Both the left and right hydraulic motor will be located in the central box directly above the fuselage. The pressurized hydraulic fluid will be carried through hoses running along the rear spar of the wings and the roof of the fuselage. The separation of the center, left and right systems has been included in order to provide an additional level of redundancy.

During normal operation, the left wing systems will be powered by the left hydraulic system and the right wing systems will be powered by the right hydraulic system. The central hydraulic system will merely power the empennage and landing gear systems during normal operation. In addition to the hydraulic systems, also two electrical actuators provide extra redundancy levels.

Table 7.1: Hydraulic system division

		Left system	**Center system**	**Right system**	**Electrical actuators**
Aileron	Left	X	X		2
	Right		X	X	2
Rudder		X	X		2
Elevator	Left	X	X		2
	Right		X	X	2
Flaps	Left	X	X		2
	Right		X	X	2
Slats			X		2
Spoilers			X		2
Trim tab			X		2
Nose gear			X	X	2
Main gear	Left	X	X		2
	Right		X	X	2

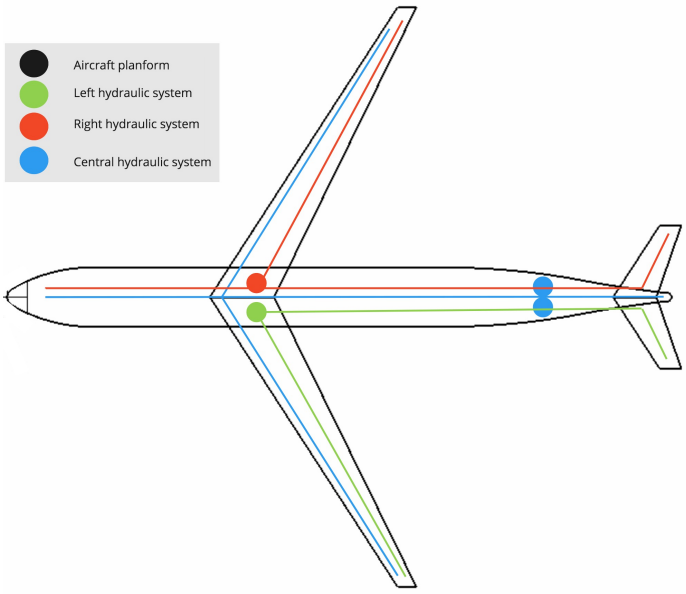

Figure 7.3: Schematic overview of the hydraulic system

7.4. Electrical System

The electrical system for the aircraft will be presented in three distinct parts. First, the general system layout will be discussed, including the electrical block diagram. Next, the removal of the APU will be explained and justified. Moreover, the new electric green taxiing system will be elaborated upon. Finally, a rough power estimate is presented.

7.4.1. Electrical Block Diagram

The electrical system provides electrical power to almost all subsystems, sensors and instruments of the aircraft. The system is vital to the operation of the aircraft, especially in the case of this more-electric aircraft. A schematic overview of the system is presented in Figure 7.4. The figure presents all power sources in purple and all non-critical electrical systems in green boxes.

As can be seen from the figure, there are a total of ten possible power sources that provide a constant reliable and redundant power supply. First, the system features four generators, two on each engine. The generators provide all electrical power during normal flight operation. In case all generators fail mid-flight, two back-up batteries are available to power the most critical systems. The two batteries will be placed separate from each other in order to obtain a higher level of redundancy. In case both the generators and batteries fail, a ram air turbine (RAT) is available to power a few vital systems.

After the aircraft has landed, a battery cart will be attached automatically to allow for electric taxiing. After the aircraft has arrived at the gate, auxiliary power will be attached to one or both of the auxiliary power ports located on the left side of the aircraft. Both a forward auxiliary power port, located close to the nose of the aircraft, and an aft auxiliary power port, located near the start of the tail cone, will be available to allow for a redundant ground power supply.

Power distribution will be handled by two main power distribution buses, the forward power distribution bus and the central power distribution bus. It was chosen to use two distribution buses to save weight that would be induced by the additional wiring that would be required with only one bus. The forward distribution bus will be located directly underneath the cockpit and mainly handles the flight control and flight data system. It also handles the cabin comfort systems and the cargo door actuator system. The central distribution bus will be located in the cargo compartment and mainly handles the electrical wing systems, the electric taxiing system, fuel system, hydraulic system and the environmental control systems.

In Figure 7.4 two electrical systems are presented, the red system and the blue system. The red system is the full primary electrical distribution network that will be active during normal operation. The blue system provides an additional level of redundancy for the connections between the power sources and the distribution buses. For the clarity of the diagram the blue system is not worked out completely. However, it may be assumed that the red lines connecting the black boxes feature a full secondary redundant connection as well. In order to save weight no additional redundancy system will be provided to the green non-critical systems.

7.4.2. Removal of the APU

From Figure 7.4 it is evident that the aircraft's electrical system does not feature an auxiliary power unit (APU). It was chosen to remove the APU in order to save weight and reduce ground emissions.

Studies have found that for an Airbus A320 removing the APU could shave up to 630 kg from the MTOW [48], not accounting for the saved fuel. The APU is used during three flight phases, namely ground operations, climb and descent. Taking into account an average turnaround time of about 30 minutes, 20 minutes climb and 28 minutes descent and an APU fuel usage of 2 kg per minute, an additional 150 kg of fuel is saved. However, during climb and descent, the engines will have to deliver additional power so they will consume more fuel. As aircraft already have an emergency battery unit [49], only additional ground power should be provided. With removing the APU one of the four redundancies (two engines, APU, ram air turbine, emergency batteries) of an aircraft is removed. To restore this, a second battery unit of 25.5 kg is added, doubling the capacity. These batteries are purely for emergency cases and are not intended to replace the APU. The engines are able to provide all the necessary power. Taking of all this into account, removing the APU saves 664.5 kg from an A320 like aircraft. Moreover, the APU produces 19% of all ground level emissions [48]. Removing it will save those, as well as noise normally produced by the APU.

In order to account for the required additional ground power, a second ground power connection point has been incorporated into the electrical system. This provides an additional level of redundancy and reduced load for the auxiliary power connectors. The APU is normally also responsible for providing air conditioning while the aircraft is stationed at the gate. This problem will also be resolved by an auxiliary ground system, as explained in 7.1.

7.4.3. Electric Green Taxiing System

The TU-ecoliner will feature an electric green taxiing system (EGTS). The EGTS system is a system in which taxiing is performed electrically, using electric motors on the landing gears. This means that the main engines will not be running, which can save a significant amount of fuel and emissions while also lowering the noise level on and around the airport. The EGTS system can save up to 21% of the ground level emissions of an aircraft [48]. Moreover, since the engines are inoperative during taxiing, no sound is produced so the noise level decreases significantly. Furthermore, no fuel is used for taxiing. An estimated 600 kg of fuel could be saved per aircraft per day, taking into account that an aircraft on short and medium distance routes taxis 2.5 hours per day[2]. Translated to a per flight basis, with an average of 20 minutes taxi time, 80 kg of fuel is saved. The EGTS system itself weighs only 300 kg, so for a minor weight penalty (220 kg net) better noise and emissions performance can be achieved.

An EGTS system has already been developed and tested by Safran and Honeywell[3] [4] [5], a next-generation battery powered version of this system will be implemented on the aircraft. The system will feature two electric motors, one on each of the inner wheels of the main landing gear. These motors will allow the aircraft to be accelerated to a speed of 20 knots. Moreover using EGTS, the aircraft will be able reverse away from the gate without a push-back tractor and reduce the chance of engine damage caused by foreign object debris. Finally, the electric motors will feature a kinetic energy recovery system, which will cause the motors to partially slow down the aircraft during landing and ground operations while generating electric energy to be stored in the aircraft batteries. This will allow for smaller brakes and lighter brakes to be implemented and it allows the kinetic energy to be reused.

[2] https://www.ainonline.com/aviation%2Dnews/air%2Dtransport/2013%2D06%2D18/honeywell%2Dsafran%2Ddemo%2Delectric%2Dtaxiing%2Dsystem%2Dairlines [cited 21 May 2018]

[3] https://www.safran-Dgroup.com/media/20120209_easyjet%2Dfirst%2Dairline%2Dtrial%2Delectric%2Dgreen%2Dtaxiing%2Dsystem%2Dsafran%2Dand%2Dhoneywell [cited 16 May 2018]

[4] https://www.flightglobal.com/news/articles/farnborough-honeywell-and-safran-halt-electric-tax-427400/ [cited 16 May 2018]

[5] https://www.ainonline.com/aviation-news/air%2Dtransport/2013%2D06%2D18/honeywell%2Dsafran%2Ddemo%2Delectric%2Dtaxiing%2Dsystem%2Dairlines [cited 17 May 2018]

As already mentioned in Section 5.4, the EGTS system will be provided with energy by means of an autonomous electric battery-filled cart that is to be attached during taxiing. This cart will be connected shortly after landing in order to provide the power for taxiing to the gate. At the gate, the cart will charge alongside the aircraft using external power supply from the airport mains. When the aircraft leaves, the cart again provides power for taxiing to the runway. Shortly before entering the runway the engines are started and warmed-up and the cart is disconnected. The cart then autonomously returns to a charging station on the airport, ready to be used for the next aircraft.

Using the fact that 80 kg of fuel will be saved per flight, the energy usage of the system and the battery cart capacity can be estimated. A kilogram of Jet-A fuel can roughly release 42.8 MJ[6]. Consequently, 80 kg of Jet-A fuel contains roughly 3.42 GJ. Assuming the 25% of the energy released will be used effectively, 856 MJ should be provided to the aircraft while taxiing. Assuming that the aircraft taxis around 20 minutes per flight, it can be determined that the system consumes about 713 kW of power.

Current state-of-the-art lithium-ion batteries have an energy storage capacity of about 175 Wh/kg[7] or 0.63 MJ/kg. Assuming that 85% of the energy saved in the battery can be effectively used, the effective energy capacity reduces to 0.536 MJ/kg. Consequently, a 1,598.5 kg battery is required for the EGTS. Since the cart will also have to return back to base and taxiing times might increase in case of heavy airport congestion, a safety factor of 1.2 will be implemented to the battery cart energy storage capacity. This brings the total battery weight for the cart to roughly 1,918.2 kg.

7.4.4. Power Estimation

As mentioned before, the aircraft to be designed will be a more-electric aircraft. This means that major systems will be powered by electric power instead of hydraulic or pneumatic power. For obvious reasons the electric power required by more-electric aircraft is significantly higher than for a regular aircraft. The Boeing 787 is a recent example of the trend that the electric power usage of civil aircraft keeps growing since electrical power systems continuously replace complex and heavy systems such as the bleed air systems[8]. Therefore, the Boeing 787-9 will be used as a baseline for this power estimation.

Three main contributors to the power budget have been identified, the environmental control system (ECS), the electric motor pumps and the wing anti-icing system. All of these systems used to be hydraulically or pneumatically powered but will be electric in this aircraft. In the Boeing 787-9, the ECS uses around 500 kW of power to pressurize and temperature control a fuselage with a volume of $1,324.3 m^3$[9] [50]. Scaling this to a fuselage volume of $366.3 m^3$, the estimated power consumption of the ECS equals 138.3 kW.

The electric motor pumps on the Boeing 787 consume about 400 kW of power in order to power the hydraulic and fuel systems [50]. Since our aircraft uses a similar hydraulic and fuel system set-up and has the same number of engines as the Boeing 787, the electric motor pumps are also expected to consume 400 kW of power.

The wing anti-icing system on the Boeing 787 is also performed electrically. The system uses around 100 kW of power [50]. Since the anti-icing system is Incorporated into the wing leading edge, the power consumption is scaled using the ratio of wing spans. The Boeing 787-9 has a wing span[10] of 60.17 m, while the TU-ecoliner has a wing span of 39.24 m. Therefore, the power consumed by the wing anti-icing system is estimated to be 65.22 kW.

[6] https://hypertextbook.com/facts/2003/EvelynGofman.shtml [cite 28 June 2018]
[7] http://batteryuniversity.com/index.php/learn/article/types_of_lithium_ion [cited 28 June 2018]
[8] http://aviationweek.com/electrical-power-systems/part-2-source-all-aircraft-power [cited 24 May 2018]
[9] https://www.globalair.com/aircraft-for-sale/Specifications?specid=1535 [cited 18 June 2018]
[10] https://www.boeing.com/commercial/787/by-design/#/787-9-characteristics [cited 28 June 2018]

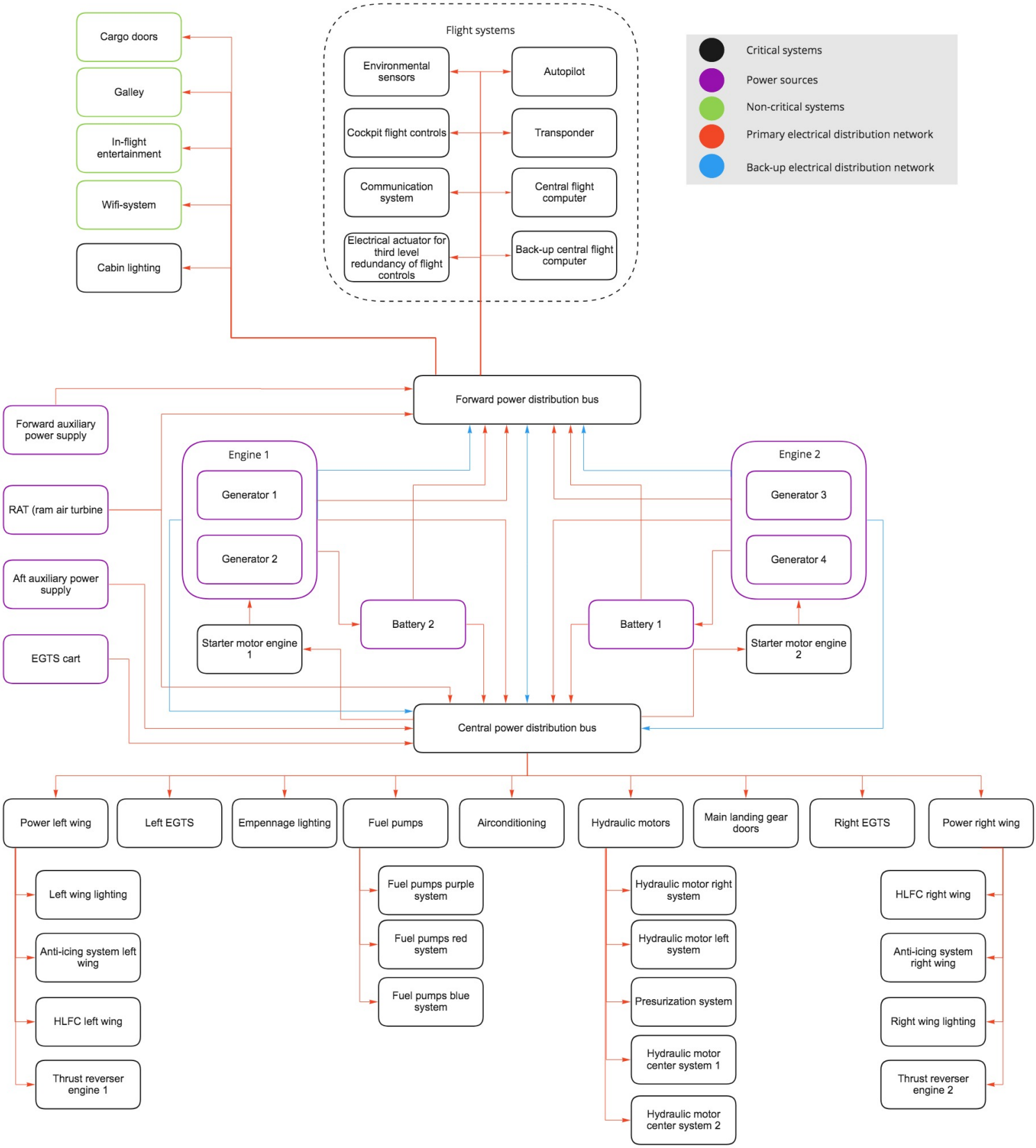

Figure 7.4: Schematic overview of the electrical system

8

Final Design Analysis

In this chapter, the final design analysis will be discussed. First, a performance analysis will be performed in Section 8.1. Next, the aircraft noise will be analyzed in Section 8.2 and the emissions will be analyzed in Section 8.3. In Section 8.4, the reliability, maintainability, availability and safety of the aircraft will be elaborated upon. The financial aspect of the project is discussed in Section 8.5. Section 8.6 presents the risk assessment. Finally, Section 8.7 presents the resource budget breakdown.

8.1. Performance Analysis

The following section will describe the performance of the TU-ecoliner. Subsection 8.1.1 will start with describing the take-off performance along with the landing performance in Subsection 8.1.2. Moreover, the second segment climb performance is analyzed in Subsection 8.1.4. Finally, the climbing performance of the aircraft is discussed in Subsection 8.1.5.

8.1.1. Take-off Performance

The take-off performance of the aircraft is assessed based on a method as described by Jenkinson [8]. The take-off analysis consists of three parts: ground roll, transition to climb and climb to screen height. The aircraft starts at rest and accelerates along the runway until the stall speed (V_S) is passed. At the lift-off speed (V_{LOF}), which is larger than the stall speed (V_S), the aircraft can lift off the ground and climb until the screen height of 35 ft, as prescribed by the CS-25 regulations [6] is reached. Each phase of the take-off will be analyzed in the following sub-subsections.

Ground roll

The forces on the aircraft during the ground roll are depicted in Figure 8.1.

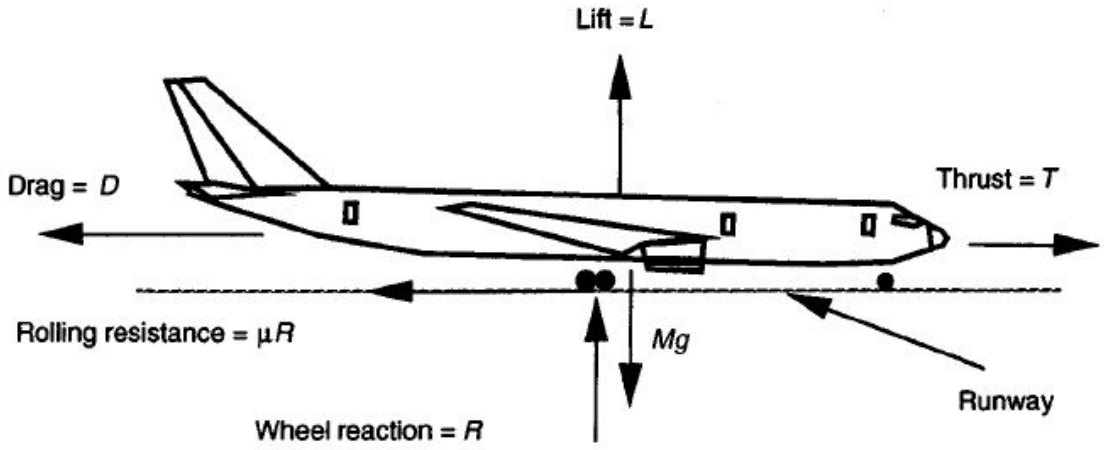

Figure 8.1: Forces acting on the aircraft during the take-off roll [8]

Solving these forces results in Equations 8.1 and 8.2. These can be combined, resulting in Equation 8.3.

$$T = D + MTOW(dV/dt) + \mu R \tag{8.1}$$

$$R = Mg - L \tag{8.2}$$

$$MTOW \cdot (dV/dt) = T - D - \mu(MTOW \cdot g - L) \tag{8.3}$$

In these equations MTOW is the aircraft maximum take-off mass, $\frac{dV}{dt}$ is the aircraft acceleration, μ is the runway coefficient of friction, R is the undercarriage reaction force (Mg – L) and g are the gravitational acceleration. The runway coefficient of friction during the ground roll is assumed to be 0.02 [8]. Using the aircraft's drag polar and the equations for lift and drag, equation 8.4 is obtained.

$$\frac{dV}{dt} = g\left[\frac{T}{MTOW} - \mu + \left(\frac{\rho}{2MTOW/S}\right)\left(-C_D - \mu C_L\right)\right] \tag{8.4}$$

The ground run is determined by the integral of $\left[\left(\frac{1}{2a}\right)dV^2\right]$ from 0 up to the lift of speed, V_{LOF}. Moreover, it is assumed that the C_L will be constant and the lift will be proportional to V^2. This is justified because the aircraft incidence angle will be constant during the majority of the ground run [8]. A mean value for the thrust at speed of 0.707·V is used since the variation of the take-off thrust with speed is approximately linear [8]. The variation of thrust with speed is taken into account using the equation 8.5 as obtained from [47]. In which F_n is the net thrust and F_g is the gross thrust. From these two constants, K_T and K_A can be defined.

$$\frac{F_n}{F_g} = 1 - 2 \cdot M\frac{1+\beta}{3+2\beta} \tag{8.5}$$

$$K_T = \frac{T}{MTOW} - \mu \tag{8.6}$$

$$K_A = \rho\frac{(-C_D - \mu C_L)}{2MTOW/S} \tag{8.7}$$

Substituting Equations 8.6 and 8.7 into Equation 8.4 and integrating between 0 and V_{LOF} results in Equation 8.8 for the ground roll distance.

$$s_{G_{takeoff}} = \frac{1}{2gK_A} \cdot ln\left(\frac{K_T + K_A \cdot V_{LOF}^2}{K_T}\right) \tag{8.8}$$

Transition to Climb

After the ground roll, the aircraft accelerates from V_{LOF} to V_2, the take-off climb speed. During the transition phase it is assumed that the aircraft flies at $0.9 \cdot C_{LMax}$ and that the average speed in this phase is determined using Equation 8.9. Where, V_{TRANS} is taken to be 1.15 times the stall speed in take-off configuration. Furthermore, it is assumed that the aircraft flies along an arc, as depicted in Figure 8.2.

$$V_{TRANS} = \frac{V_{LOF} + V_2}{2} \tag{8.9}$$

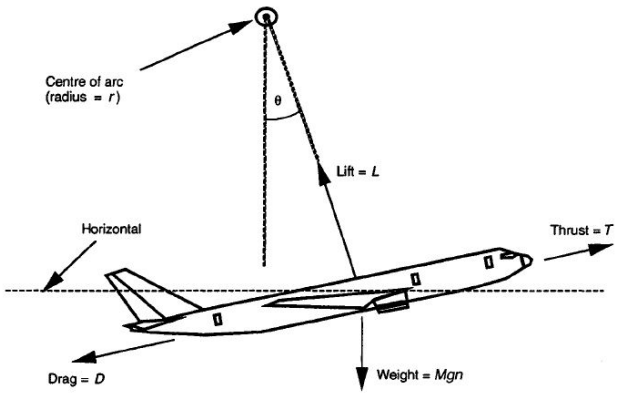

Figure 8.2: Forces acting on the aircraft during the transition phase of the take-off [8]

Taking the force equilibrium normal to the flight path results in Equation 8.10. Where r is the radius of the arc. In this manoeuvre a load factor 'n' can be defined by Equation 8.11. The load factor is taken to be 1.2. Substituting Equation 8.10 into Equation 8.11 results in Equation 8.12 for small angles ($\cos(\theta) = 1.0$). The ground distance reached during the transition phase is then given by Equation 8.13, in which γ is the final climb gradient.

$$L = MTOW \cdot g \cdot cos(\theta) + \frac{MTOW \cdot V_{TRANS}^2}{r} \tag{8.10}$$

$$n = \frac{L}{MTOW \cdot g} \tag{8.11}$$

$$r = \frac{V_{TRANS}^2}{g(n-1)} \tag{8.12}$$

$$s_T = r \cdot \gamma \tag{8.13}$$

A first order estimate of the lift coefficient during the climb phase is obtained using Equation 8.14 [8]. From this equation, the drag coefficient during climb can be determined using Equation 8.15, leading to the drag during the climb phase determined by Equation 8.16. The climb gradient γ is then obtained using Equation 8.17, in which the net thrust is determined using Equation 8.5.

$$C_{L_{climb}} = \frac{C_{L_{max_{take-off}}}}{1.2^2} \tag{8.14}$$

$$C_{D_{climb}} = C_{D_{0_{climb}}} + \frac{(C_{L_{climb}})^2}{(\pi \cdot A \cdot e)} \tag{8.15}$$

$$D_{climb} = C_{D_{climb}} \cdot \frac{1}{2} \cdot \rho \cdot V_2^2 \cdot S \tag{8.16}$$

$$\gamma = \frac{\text{Net thrust} - D_{climb}}{MTOW} \tag{8.17}$$

Climb

The final part of the take-off run of the aircraft is the climb to the screen height of 35ft, as prescribed by the CS-25 (CS-25.107) [6]. The distance reached from the end of the transition to the screen height is defined by the Equation 8.18. In which s_C is the ground distance to the screen height from the end of the transition, h_t is the height at the end of the transition given by: $\frac{r \cdot \theta \cdot \theta}{2}$ and γ_C being the climb angle. A typical climb angle during take-off is 4.5 ∘. However, it is possible that the screen height is already reached during the transition phase. The distance to the screen height is then computed using Equation 8.19. The total distance is finally multiplied by 1.15 to account for operational variabilities as prescribed by the CS-25 regulations (CS-25.113) [6].

$$s_C = \frac{screenheight - h_t}{tan(\gamma_C)} \tag{8.18}$$

$$S_s = [(r + screenheight)^2 - r^2]^{0.5} \tag{8.19}$$

Take-off Analysis Inputs and Results

As discussed in the preceding sub-subsections, different speeds are defined in the analysis of the take-off performance of the aircraft. These are summarized and tabulated in Table 8.1. The method, as described in the preceding sub-subsections, resulted in a take-off distance of 1,673 m. This is the take-off distance at sea-level conditions. The input data used in the take-off performance analysis are tabulated in Table 8.2.

Table 8.1: Speeds as defined in the take-off performance analysis

Speed	Determined from	Value [kts]
$V_{S_{to}}$ (stall speed)	-	131
V_{LOF} (Lift off speed)	$1.1 \cdot V_{S_{to}}$	144
V_2	$1.2 \cdot V_{S_{to}}$	157

Table 8.2: Input data used for take-off performance analysis

	Value
Maximum take-off mass [kg]	68,731
Wing area [m^2]	110
Aspect Ratio	14
$C_{L_{max-take-off}}$	2.2
$C_{L_{take-off}}$	1.1
$C_{L_{climb}}$	1.5
$C_{D_{0_{take-off}}}$	0.035
$C_{D_{0_{climb}}}$	0.030
$C_{D_{climb}}$	0.113
Oswald efficiency factor	0.727
Screen height take-off [6] [m]	11
Rolling coefficient [8]	0.02
Take-off climb angle [∘]	4.5
Take-off static thrust [kN]	213
Load factor during take-off	1.2

From the obtained results it is clear that the thrust of the engines can be reduced. Decreasing the thrust with 10% increases the take-off length to 1,851 m. However, due to time constraints there was no time to perform an additional iteration with respect to the engine thrust.

Verification & Validation

The Python program made to analyze the take-off performance is verified by implementing known aircraft data, followed by the assessment of the obtained results. The aircraft data is obtained from Jenkinson [8]. The driving aircraft parameters and the take-off performance analysis results are tabulated in Table 8.3. It clear that the simulation results in highly accurate results and is therefore verified.

Table 8.3: Take-off performance verification inputs and outputs

Speed	Aircraft data from Jenkinson	Results from simulation	Difference [%]
Maximum Take-off mass [kg]	230,000	-	-
Wing area [m^2]	376.4	-	-
$C_{L_{Max}}$ **take – off**	1.75	-	-
C_D **take – off**	$0.035 + 0.05\ C_L^2$	-	-
V_{stall} [m/s]	74.70	74.77	0.094
V_{LOF} [m/s]	82.20	82.25	0.06
Take-off distance [m]	2,150	2,162	0.56

The obtained take-off distance and speeds were validated by comparison with reference aircraft. The aircraft considered in the validation are the following: A319-100,A320-200, A321-200, A330-200, A330-300, A340-200, A340-300, 717-200, 727-200Adv, 737-200, 737-300, 737-400, 737-500, BAe RJ70, BAe RJ85, BAe RJ100, BAe RJ115, EMB-145, Fokker F70 and the Fokker F100 [1]. Figure 8.3 depicts the take-off length and MTOW of reference aircraft and the TU-ecoliner (the red dot). It is evident that the TU-ecoliner performs average compared to reference aircraft. With respect to the Airbus A321neo TU-ecoliner requires 35% less runway length for take-off, as the Airbus A321neo needs around 2300 m [2]

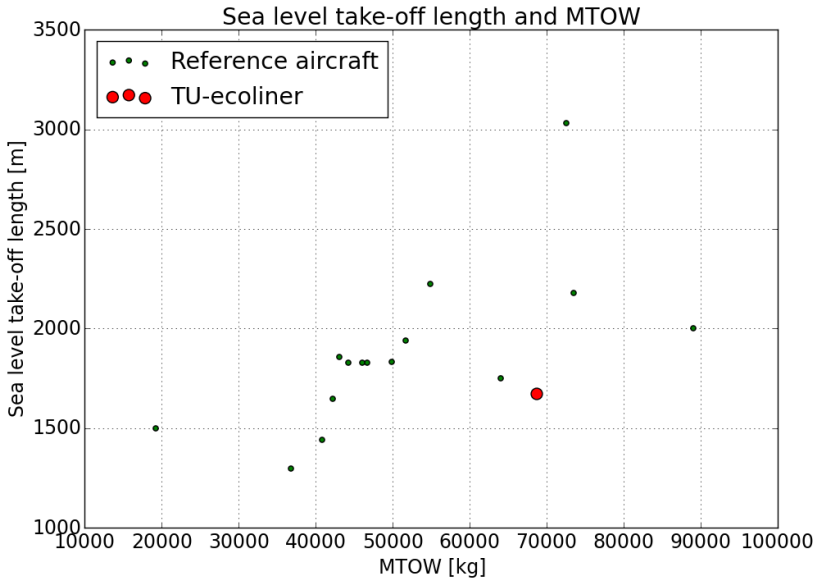

Figure 8.3: Take-off length of the designed aircraft and reference aircraft

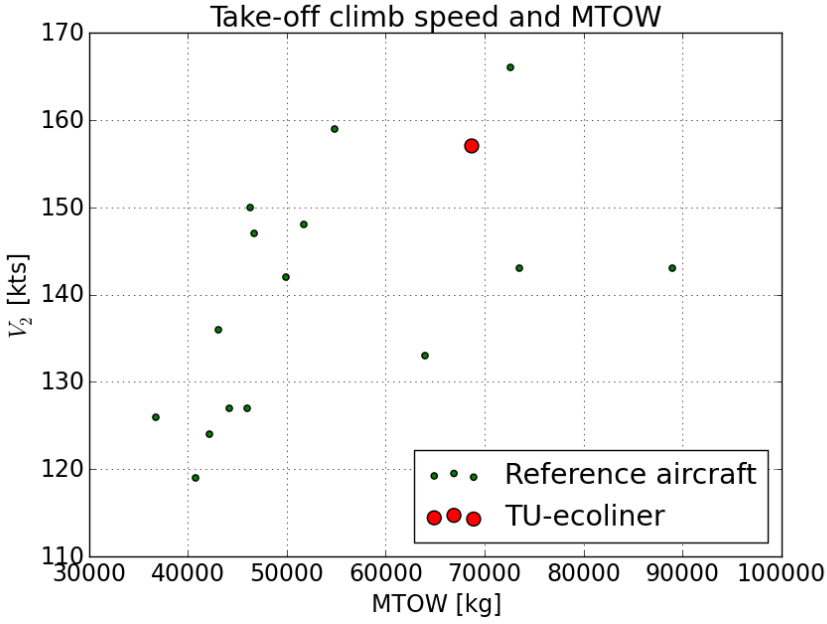

Figure 8.4: Take-off climb speed (V_2) of the designed aircraft and reference aircraft

[1] Aircraft data is obtained from `https://booksite.elsevier.com/9780340741528/appendices/data-a/default.htm` [cited 21 June 2018]

[2] `http://janes.ihs.com` [cited 23 June 2018]

With respect to the take-off climb speed, as depicted in Figure 8.4, it can be seen that the obtained result for the TU-ecoliner is comparable to reference aircraft but still on the higher side. This is mainly caused by the smaller wing area. Increasing the $C_{L_{max}}$ slightly can lower the take-off climb speed. However after investigating the accelerations during take-off, it was decided to aim at an average acceleration during take-off of around 0.25g. Furthermore, reference aircraft reach $C_{L_{max}}$ values for take-off of around 2.5 [3], which means that a $C_{L_{max}}$ of 2.2 is reasonable.

8.1.2. Landing Performance

The landing performance of the aircraft is also analyzed using a method described by Jenkinson [8]. In this method the landing is divided into three segments/phases: the approach, flare and the ground roll. The landing manoeuvre is depicted in Figure 8.5. The analysis of each phase will be discussed in the following sub-subsections.

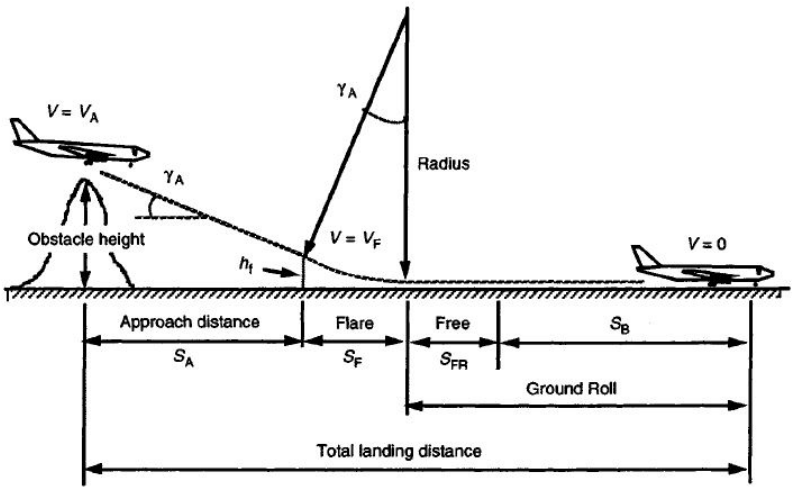

Figure 8.5: Landing performance [8]

Approach

The approach phase is defined to start at the screen height of 50 ft, as prescribed by the CS-25 [6]. It ends at the flare height h_F, as can be seen in Figure 8.5. The value of the flare height is given by Equation 8.20. In which γ_A is the approach gradient. In the simulation the approach gradient is taken to be 3°. The approach distance can then be calculated using Equation 8.21.

$$h_F = \frac{r \cdot \gamma_A \cdot \gamma_A}{2} \tag{8.20}$$

$$s_A = \frac{(screenheight - h_F)}{tan(\gamma_A)} \tag{8.21}$$

Flare

The next phase in the landing is the flare. During this phase the aircraft decelerates from the approach speed, V_A, to the touch-down speed, V_{TD}. The average speed during the flare, V_F, is determined using Equation 8.22. From Jenkinson [8], V_{TD} is taken to equal $1.15 \cdot V_{S_{landing}}$. The radius of the flare manoeuvre r_{FLARE} is given by Equation 8.23. The load factor is taken to be 1.2. Moreover, the distance covered during the flare is determined using equation 8.24.

$$V_F = \frac{V_A + V_{TD}}{2} \tag{8.22}$$

$$r_{FLARE} = \frac{V_F^2}{g(n-1)} \tag{8.23}$$

$$s_F = r \cdot \gamma_A \tag{8.24}$$

[3] `https://booksite.elsevier.com/9780340741528/appendices/data-a/default.htm` [cited 21 June 2018]

Ground Roll

Before the pilot applies the brakes and spoilers, the aircraft will roll for a few seconds after the touch-down. The distance covered during this free roll is determined using Equation 8.25. In which s_{FR} is the free roll distance, t is the time elapsed during this free roll and V_{TD} is the aforementioned touch-down speed. Since it takes approximately 2.0 seconds before the brakes and spoilers are applied, a value of 2.0 is taken for t [8].

$$s_{FR} = t \cdot V_{TD} \tag{8.25}$$

The braking distance of the aircraft is then calculated using Equation 8.26. Where, $K_T = -\mu$ and K_A is obtained using Equation 8.27. In which MLW is the maximum landing weight. The thrust and lift coefficient are evaluated at the average energy speed ($0.707*V_{TD}$). It is assumed that the thrust will be zero and that the coefficient of friction during braking is 0.45 [8]. Jenkinson suggests using a value of 0.3, however since regenerative braking is implemented in the aircraft design, a value of 0.45 is taken as the coefficient of friction. A value that is too high might result in brake and tire wear. Furthermore, this calculation does not take into account the application of thrust reverse.

$$s_B = \frac{1}{2gK_A} ln\left(\frac{K_T + K_A V_{TD}^2}{K_T}\right) \tag{8.26}$$

$$K_A = -\rho \cdot a \frac{2 \cdot MLW}{S} \tag{8.27}$$

The total landing distance that is obtained from this method is multiplied by 1.66 to account for variability in pilot and operational uncertainties during the landing manoeuvre [8].

Landing Analysis Inputs and Results

As discussed in the preceding sub-subsections, different speeds are defined in the analysis of the landing performance of the aircraft. These are summarized and tabulated in Table 8.5. The method resulted in a landing distance of 1,554 m at sea-level conditions. The input parameters used in the simulation are tabulated in Table 8.4.

Table 8.4: Input data used for the landing performance analysis

	Value
Maximum landing mass [kg]	62,366
$\mathbf{C_{L_{max_{landing}}}}$	2.9
$\mathbf{C_{D_{0_{landing}}}}$	0.0974
Oswald efficiency factor	0.727
Screen height landing [6] [m]	15.24
Rolling coefficient landing [8]	0.45
Landing approach angle [◦]	3
Load factor during landing	1.2

Table 8.5: Speeds as defined in the landing performance analysis

Speed	**Determined from**	**Value [kts]**
$\mathbf{V_{S_{land}}}$ **(stall speed)**	-	109
$\mathbf{V_A}$ **(Approach speed)**	$1.3 \cdot V_{S_{land}}$	141
$\mathbf{V_F}$ **(Average Flare speed)**	$(1.15 + 1.3) \cdot V_{S_{land}}/2$	133
$\mathbf{V_{TD}}$ **(Touch-down speed)**	$1.15 \cdot V_{S_{land}}$	125

Verification and Validation

The Python program developed to analyze the landing performance is verified by implementing known aircraft data, followed by an assessment of the obtained results. The aircraft data is obtained from Jenkinson [8]. The driving aircraft parameters and the landing performance analysis results are tabulated in Table 8.6. It can be clearly seen that the simulation results in very accurate results and is thus verified.

Table 8.6: Landing performance verification inputs and outputs

Speed	**Aircraft data from Jenkinson**	**Results from simulation**	**Difference** [%]
Maximum landing mass [kg]	184,000	-	-
Wing area $[m^2]$	376.4	-	-
$\mathbf{C_{L_{Max_{land}}}}$	2.5	-	-
$\mathbf{C_{D_{land}}}$	$0.055 + 0.05\ C_L^2$	-	-
$\mathbf{V_{stall_{land}}}$ $\left[\frac{m}{s}\right]$	55.96	55.95	-0.018
$\mathbf{V_{TD}}$ $\left[\frac{m}{s}\right]$	64.35	64.35	0
Landing distance [m]	1,916	1,915	-0.052

Furthermore, the obtained results are validated by comparison with reference aircraft. The same aircraft as discussed in the verification and validation part for the take-off performance are considered. Figure 8.6 depicts the landing length of the TU-ecoliner and reference aircraft. It is evident that the landing length of the TU-ecoliner is higher compared to competitors. The landing distance of the A321neo is around 1600 m, which is comparable to the TU-ecoliner [4]. However, it must be noted that the performed analysis does not account for thrust reversers.

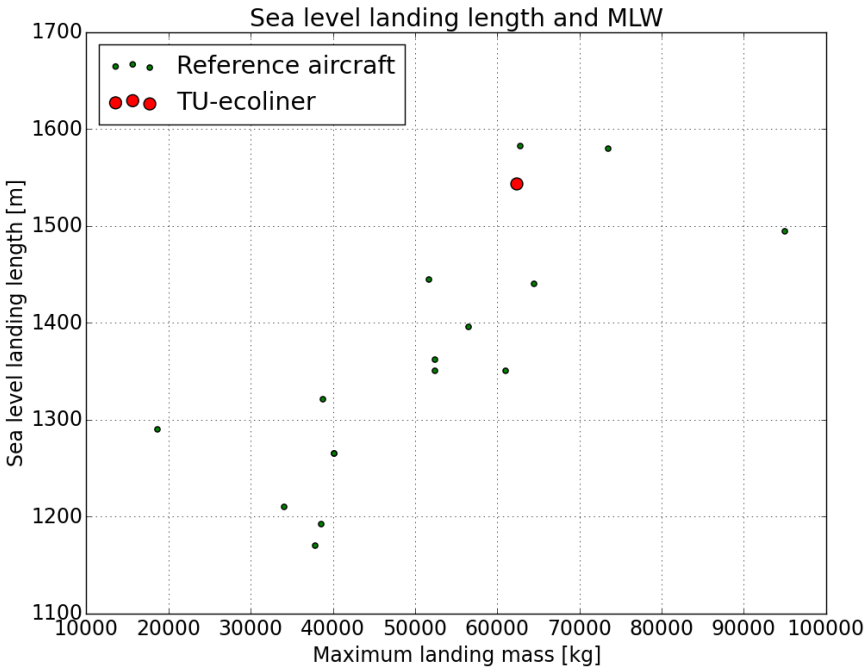

Figure 8.6: Landing length of the designed aircraft and reference aircraft

From Figure 8.7, it is evident that the obtained results for the approach speed are comparable to reference aircraft. The approach speed of the Airbus A321 is 138 kts [5], which means that the difference is small. The $C_{L_{max_{land}}}$ value of 2.9 is also reasonable compared to reference aircraft, which reach values of around 3.0 [5].

[4] `http://janes.ihs.com` [cited 23 June 2018]

[5] Aircraft data obtained from `https://booksite.elsevier.com/9780340741528/appendices/data-a/default.htm` [cited 23 June 2018]

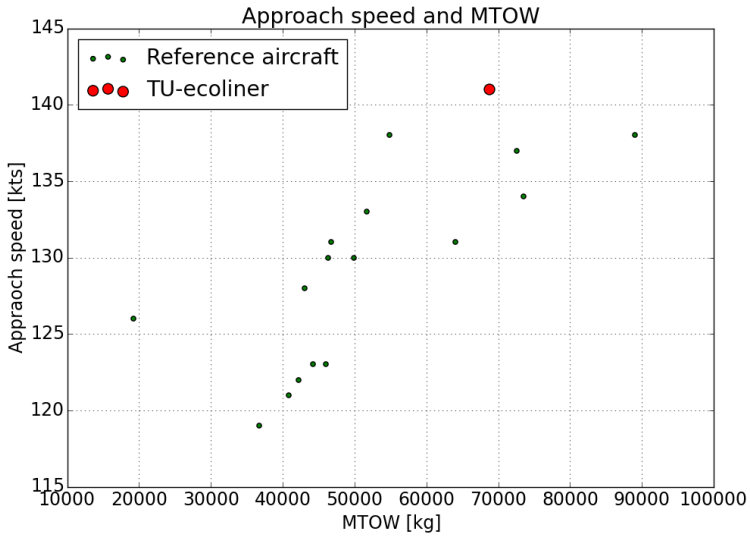

Figure 8.7: Approach speed, $V_{approach}$, of the designed aircraft and reference aircraft

8.1.3. Take-off and Landing Performance as Function of Altitude

The take-off and landing performance of the aircraft is analyzed for different altitudes by implementing the effect of altitude on thrust. In order to account for this effect, Equation 8.28 [6] is implemented into the simulation. The take-off and landing performance of the aircraft with respect to the airport altitude is depicted in Figure 8.8.

$$\frac{F_n}{F_g} = \frac{P_{altitude}}{P_{sea-level}} \cdot \sqrt{\frac{T_{sea-level}}{T_{altitude}}} \tag{8.28}$$

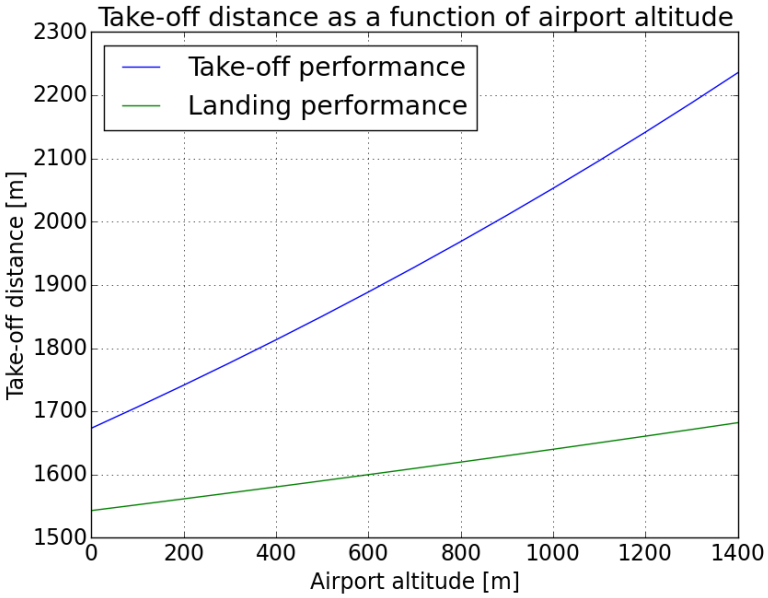

Figure 8.8: Take-off and landing performance as function of altitude

[6] `https://www.grc.nasa.gov/www/k-12/Missions/Jim/Project1ans.htm` [cited 18 June 2018]

Sensitivity Analysis

A sensitivity analysis has been performed for the take-off and landing performance (at sea level) for three dominant aircraft parameters, aircraft weight, zero-lift drag and maximum thrust. In this analysis the effect of an increase and decrease of 10% of each of the three aforementioned parameters was investigated. The change in the take-off and landing distance is presented as a percentage change with respect to the nominal value. The results are presented below in Table 8.7. From this analysis, it is clear that the weight of the aircraft has the largest influence on the take-off and landing performance of the aircraft.

Table 8.7: Sensitivity analysis of the take-off and landing distances with respect to the aircraft weight, maximum thrust and drag coefficient

	Nominal Value	**Weight** [kg]		**Zero-lift drag** [-] (for resp. conf.)		**Maximum Thrust** [kN]	
		-10.0%	10.0%	-10.0%	10.0%	-10.0%	10.0%
Take-off Distance [m]	1,673	-18.0 %	+21.0 %	-0.3 %	+0.36 %	+10.6 %	-8.5 %
Landing Distance [m]	1,543	-7.0 %	+7.0%	+0.2 %	-0.2 %	0.0 %	0.0 %

8.1.4. Second Segment Climb with One Engine Inoperative

The CS-25 regulations specify a minimum climb gradient in the case of one engine inoperative that has to be obtained by any aircraft to be certified under CS-25. For twin-engined aircraft a minimum climb gradient of 0.024 has to be obtained in the second segment of climb (CS-25.121 [6]).

The assessment of this requirement will be discussed here. First, the lift and drag coefficient during this phase of the flight have to be determined. In this analysis, the drag coefficient due to the failed engine is estimated using Equation 8.29 [8]. In which A_f is the diameter of the fan as obtained from the engine sizing in Subsection 6.6.2. Furthermore, the trim drag is estimated using Equation 8.30, in which $C_{D_{climb}}$ is the drag coefficient during the climb phase of the take-off run as discussed in Subsection 8.1.1. The total drag coefficient during the second segment climb with one engine inoperative is then obtained using Equation 8.31. From this, the total drag can be determined using Equation 8.32. Finally, the climb gradient during the second segment climb with one engine inoperative is obtained using Equation 8.33.

$$C_{D_{failedengine}} = \frac{0.3 \cdot A_f}{S} = \frac{0.3 \cdot 1.87}{110} = 0.0051 \tag{8.29}$$

$$C_{D_{trim}} = 0.05 \cdot C_{D_{climb}} \tag{8.30}$$

$$C_{D_{climb-OEI}} = C_{D_{climb}} + C_{D_{trim}} + C_{D_{failedengine}} \tag{8.31}$$

$$D_{climb_{OEI}} = C_{D_{climb-OEI}} \cdot \frac{1}{2} \cdot \rho \cdot V_2^2 \cdot S \tag{8.32}$$

$$\gamma_{OEI} = \frac{\frac{1}{2} \cdot Thrust_{net} - D_{climb_{OEI}}}{MTOW} \tag{8.33}$$

Input and Results

Using the prescribed methodology and the input parameters as tabulated in Table 8.8, a climb gradient of 0.059 is obtained. This means that the requirement is met.

Table 8.8: Input data used for second segment climb with one engine inoperative analysis

	Value
$\mathbf{C_{D_{failedengine}}}$	0.0051
$\mathbf{C_{D_{trim}}}$	0.0052
$\mathbf{C_{D_{climb-OEI}}}$	0.1130
$\mathbf{Thrust_{One-engine}}$ [N]	87,427

Verification and Validation

The Python program made to analyze the second segment climb with one engine inoperative performance is verified by implementing known aircraft data, followed by the assessment of the obtained results. The aircraft data is obtained from Jenkinson [8]. The aircraft data and program results are tabulated in Table 8.9. It can be clearly seen that the simulation results in very accurate results and is thus verified.

Table 8.9: Second segment climb with one engine inoperative verification inputs and outputs

Speed	**Aircraft data from Jenkinson**	**Results from simulation**	**Difference** [%]
Maximum take-off mass [kg]	230,000	-	-
Wing area $[m^2]$	376.4	-	-
$\mathbf{C_{L_{Max_{TO}}}}$	1.75	-	-
$\mathbf{C_L at V_2}$	1.215	1.215	0
$\mathbf{C_{D_{climb}}}$	$0.025 + 0.05\ C_L^2$	-	-
$\mathbf{C_{D_{failedengine}}}$	0.00199	0.00199	0
$\mathbf{C_{D_{trim}}}$	0.00494	0.00494	0
$\mathbf{D_{climb}}$ [N]	195,884	196,325	-0.23
$\gamma\mathbf{climb_{OEI}}$	0.0308	0.0306	0.60

8.1.5. Climbing Performance

An important aspect of the aircraft performance is the climbing performance. This will for example determine what rates of climb are achievable and how long it will take to climb to cruise altitude.

The forces acting on the aircraft during climb are presented in Figure 8.9. Summing forces parallel to the flight path results in Equation 8.34 and perpendicular to the flight path results in Equation 8.35. For the sake of simplicity the thrust vector points into the direction of the velocity.

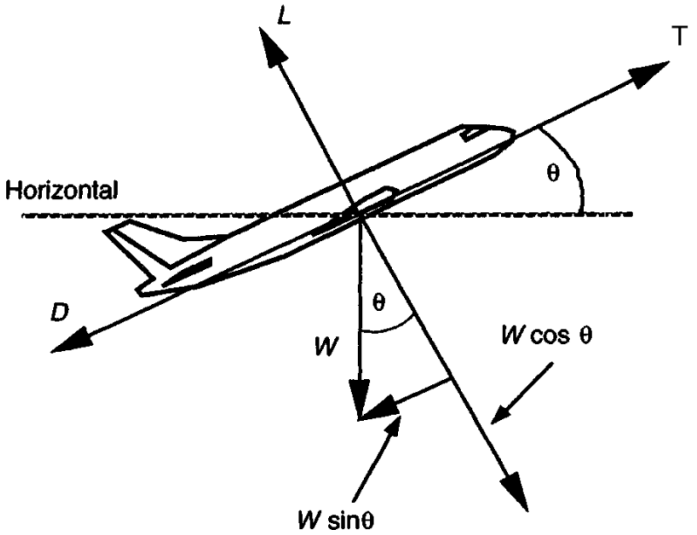

Figure 8.9: Forces acting on the aircraft during climb [8]

$$T - D - W\sin(\theta) = \frac{W}{g}\frac{dV}{dt} \tag{8.34}$$

$$L - W\cos(\theta) = \frac{W}{g}V\frac{d\theta}{dt} \tag{8.35}$$

Using the small angle approximation and assuming steady symmetric flight conditions, results in Equations 8.36 and 8.37. In real life however, the aircraft also accelerates during climb, this will be incorporated later.

$$T - D - W sin(\theta) = 0 \tag{8.36}$$

$$L = W \tag{8.37}$$

Multiplying Equation 8.36 with V for convenience, results in Equation 8.38. Where, TV is the power available, P_a, DV is the power required, P_r, and V$\sin(\theta)$ is the rate of climb, RC. So, rewriting Equation 8.38 to Equation 8.39 provides the relation for rate of climb in steady symmetric flight conditions.

$$TV - DV - WV \sin(\theta) = 0 \tag{8.38}$$

$$\frac{P_a - P_r}{W} = RC \tag{8.39}$$

In order to plot the power available and power required curves, the drag of the aircraft should be determined first. The drag is determined using Equation 8.40. Where, C_D is calculated using Equation 8.41 and C_L follows from Equation 8.42, where lift is assumed to equal weight from Equation 8.37.

$$D = C_D \frac{1}{2} \rho V^2 S \tag{8.40}$$

$$C_D = C_{D_0} + \frac{C_L^2}{\pi A e} \tag{8.41}$$

$$C_L = \frac{W}{\frac{1}{2}\rho V^2 S} \tag{8.42}$$

With the thrust of the aircraft known, the curves can now be plotted. However, since the thrust of a turbofan engine decreases with increasing speed and altitude [51], a correction has to be applied first. This correction is presented in Equation 8.43 [52], which accounts for the air density and Mach number. Where the K's are empirical constants given by Table 8.10, σ is the ratio between sea-level density and the density at the altitude, M is the Mach number, λ is the bypass ratio and n = 0.7 for the troposphere. It should be noted, however, that the relationship is developed for a bypass ratio of 8, while the TU-ecoliner has a bypass ratio of 14.

$$\frac{F_N}{F_{N_0}} = K_1 + K_2 \lambda + (K_3 + K_4 \lambda) M \sigma^n \tag{8.43}$$

Table 8.10: Thrust parameters for Equation 8.43

Mach no.	**K_1**	**K_2**	**K_3**	**K_4**
0.0-0.4	1.0	0.0	-0.595	-0.030
0.4-0.9	0.89	-0.014	-0.300	0.005

Plotting the power available and power required curves versus speed resulted in Figure 8.10 for sea-level conditions. The discontinuity in the curve is caused by the difference of constants in the empirical relation after a Mach number of 0.4.

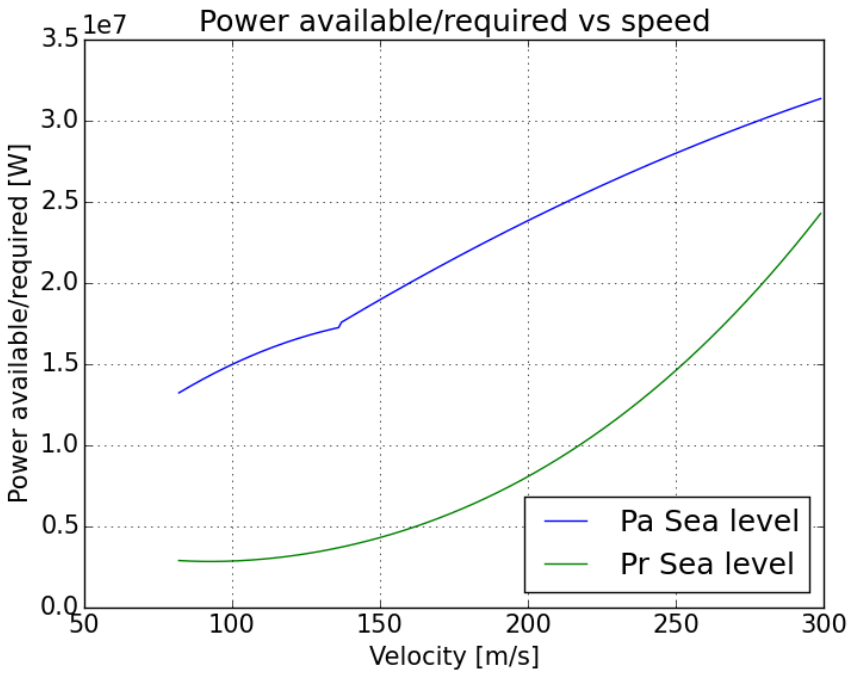

Figure 8.10: Power available and power required curves versus speed at sea-level

From Equation 8.39 it is known that the difference of the power available and power required divided by the weight is equal to the rate of climb. Applying this to all speeds and altitudes up to the cruising altitude with steps of 5,000 ft, resulted in Figure 8.11. This indicates that the maximum rate of climb at sea level is equal to 4,672 ft/min. However, this is the rate of climb at steady symmetric conditions, which is not valid in real life. Therefore, a correction has to be applied.

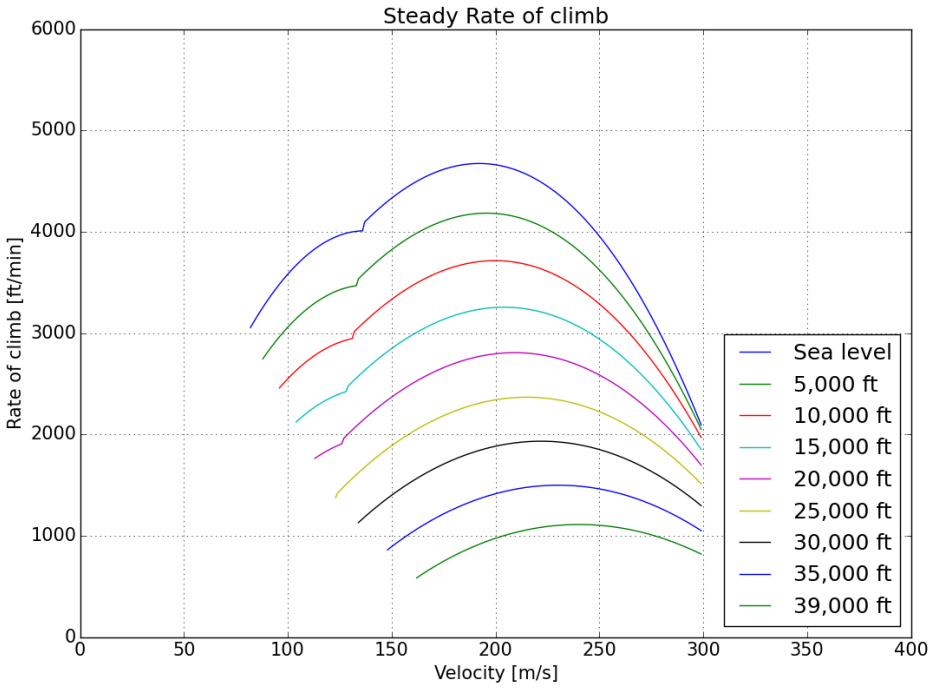

Figure 8.11: Steady rate of climb performance of the TU-ecoliner

In order to determine the unsteady rate of climb, Equation 8.34 is multiplied with V first. This results in Equation 8.44. Furthermore, using the fact that $\frac{dh}{dt} = V\sin\gamma = RC$, $TV = P_a$ and $DV = P_r$, and rearranging Equation 8.44 yields Equation 8.45. Using Equation 8.39 for steady conditions, the ratio between the rate of climb in steady and unsteady conditions is given by Equation 8.46. Where the subscript "s" is used to denote steady condition. This resulted in the rate of climb graph as presented in Figure 8.12. From this graph it can now be deduced that the maximum rate of climb at sea level equals 4,013 ft/min.

$$TV - DV - WV\sin(\theta) = \frac{W}{g}V\frac{dV}{dh}\frac{dh}{dt} \tag{8.44}$$

$$ROC\left[1 + \frac{V}{g}\frac{dV}{dh}\right] = \frac{P_a - P_r}{W} \tag{8.45}$$

$$\frac{ROC}{ROC_s} = \frac{1}{1 + \frac{V}{g}\frac{dV}{dH}} \tag{8.46}$$

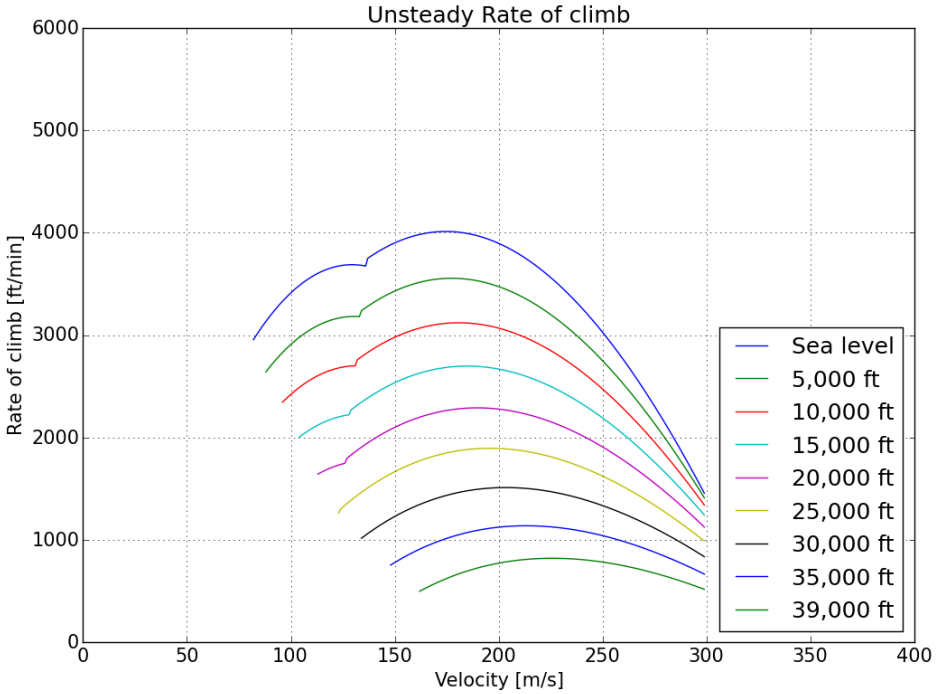

Figure 8.12: Unsteady rate of climb performance of the TU-ecoliner

Verification and Validation

The simulation developed for the rate of climb is verified by simplified calculations at a specific flight speed in Microsoft Excel. Since the simulation results in the rate of climb performance as a function of flight speed, a specific flight speed was chosen at sea level. Table 8.11 depicts the results of the calculations for a single point at 80.0 m/s and the results as obtained from the simulation. Additionally, the percentage difference between the simulation and point calculation is presented in Table 8.11. The difference between the obtained rates of climb is around 1%, which is mainly caused by rounding errors. Moreover, it can be seen that there is a small difference in the lift coefficient, which then translates in the drag coefficient.

Table 8.11: Rate of Climb verification

Parameter	Result from point calculation	Simulation	Difference %
$\mathbf{C_L}$	1.54	1.54	-0.036
$\mathbf{C_D}$	0.0897	0.0859	-4.271
D [N]	38679.96	37027.15	-4.273
$\mathbf{P_r}$ [W]	3,094,397	2,962,172	-4.273
Thrust [N]	162,171	162,171	0
$\mathbf{P_a}$ [W]	12,973,680	12,973,679	-7.70791E-06
$\mathbf{ROC_{steady}}$ [m/s]	14.9	15.05	1.333
$\mathbf{ROC_{steady}}$ [m/s]	14.4	14.59	1.338

The method applied here follows from the course Flight and Orbital Mechanics as taught at the Delft University of Technology [53]. The associated assumptions result in accurate results as has been assessed in the course slides. The difference between the simplified method and a method in which the equations of motion are not simplified is 0.52% [53]. However, it must be noted that this accuracy does not take into account the prediction of thrust variation that is implemented into the model used for the presented results.

Sensitivity Analysis

A sensitivity analysis has been performed to determine the sensitivity of the theoretical service ceiling and the maximum steady rate of climb with respect to critical aircraft parameters such as MTOW, zero-lift drag and maximum thrust. Each of the aforementioned parameters were increased or decreased by 10%. The results of the sensitivity analysis are tabulated in Table 8.12. It can be seen that the maximum thrust has the largest influence on the maximum rate of climb that is achieved and the theoretical service ceiling of the aircraft.

Table 8.12: Sensitivity of MTOW, zero-lift drag and maximum thrust at sea level on the maximum steady climb rate and theoretical ceiling height

	Nominal Value	**Weight** [kg]		**Zero-lift drag** [-]		**Maximum Thrust** [kN][7]	
		-10.0%	+10.0%	-10.0%	+10.0%	-10.0%	+10.0%
Maximum Rate of Climb [ft/min]	4,672	+12.5%	-10.3 %	+4.2 %	-3.7 %	-14.4%	+14.8%
Theoretical Ceiling [ft]	43,100	+7.0%	-6.3%	+1.9%	-1.6%	-6.3%	+5.6%

8.2. Noise

Reducing the noise of the aircraft compared to current state-of-the-art aircraft is one of the project objectives as discussed in Chapter 1. The analysis of the noise of the designed aircraft is the subject of this section. First an explanation of the noise requirements that have to be met by the aircraft is given, followed by the methodology that is followed to assess the noise and finally the results of the assessment will be discussed.

8.2.1. Noise Requirements

Noise requirements are stipulated by the aviation authorities in CS-36 [7]. Different noise requirements are defined in so-called chapters. Current state-of-the-art aircraft such as the Airbus A320neo are certified under chapter 4 of the noise regulations. The different noise chapters can be found in Figure 8.13. It can be seen that aircraft to be certified from 2017 onward have to comply with chapter 14 of the noise regulations. Chapter 14 is cumulatively (calculated from the total noise level measurements in approach, flyover and lateral) 7 EPNdB more stringent [54] compared to aircraft certified under the chapter 4 requirements. EPNdB stands for Effective Perceived Noise measured in decibels, which is a standard used internationally in measuring aircraft noise.

[7] Measured at sea level conditions.

Noise Certification

During noise certifications the noise emitted by the aircraft is assessed at three different points, namely at the approach, lateral and in a fly over as depicted in Figure 8.14.

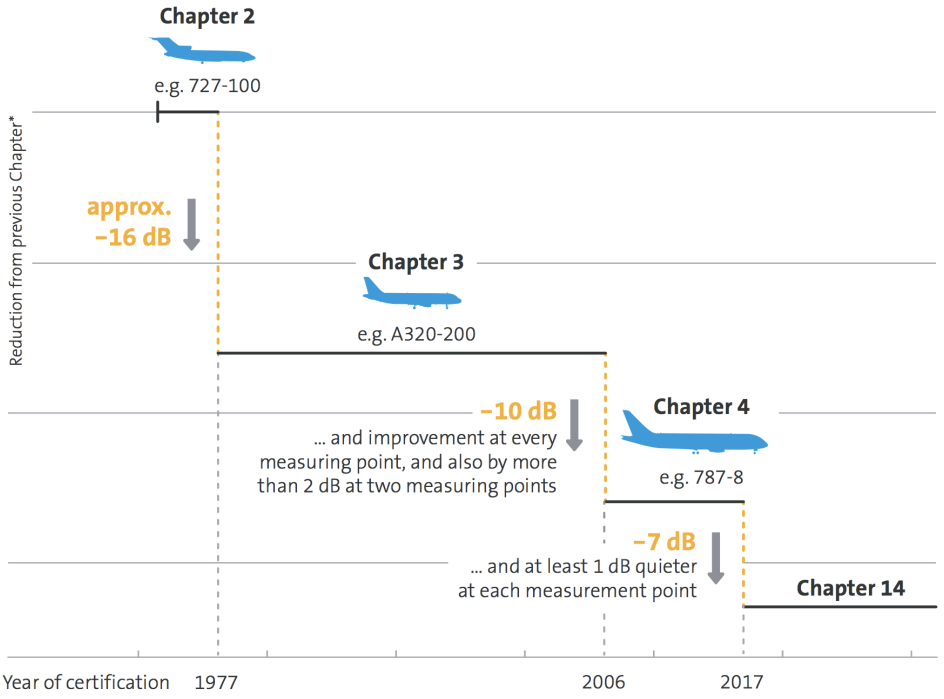

Figure 8.13: Different noise requirements along with their relative reduction[55]

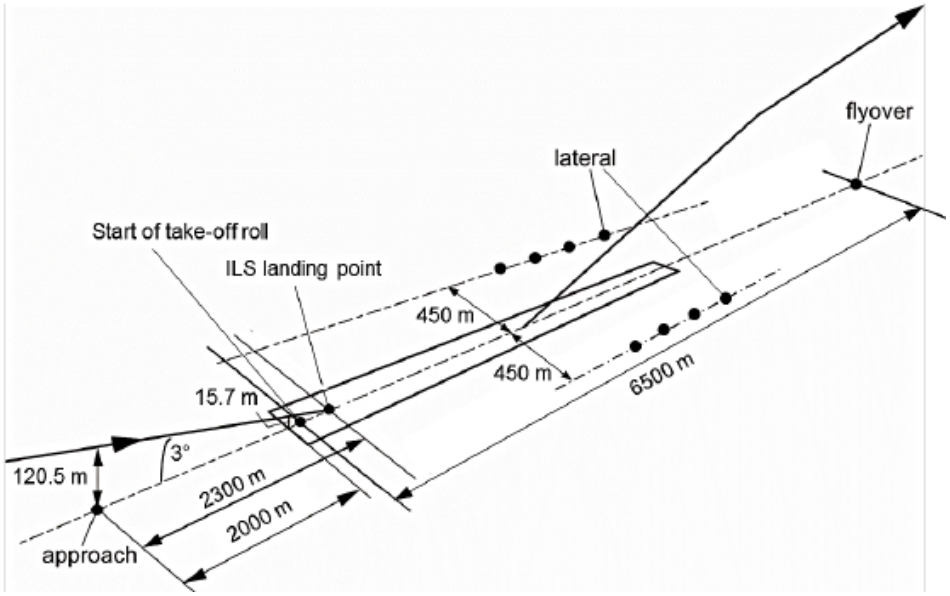

Figure 8.14: Position of measurement points during noise certification[54]

8.2.2. Assessment Methodology

The aircraft noise can be divided into two different groups: airframe noise and engine noise. These can be further divided as will be discussed in the following.

Airframe Noise Analysis

Airframe noise can be divided into the noise generated by: the clean wing, vertical & horizontal tail, slats, flaps, the landing gear and the landing gear strut. The airframe noise of the aircraft is analyzed using Fink's Airframe Noise Prediction Method[56], which is also used in NASA's Aircraft Noise Prediction Program (ANOPP). This ANOPP model is not available to students. Therefore, the empirical relations from Fink are programmed in Python and is indicated as "self-written code" from here on. The Fink method is based on measurements of several aircraft flyovers and assumes theoretical functions to predict airframe noise spectra for each component as a function of third-octave frequency, polar directivity angle and azimuthal directivity angle. Since noise from the airframe is not radially symmetric and also varies with aircraft azimuthal angle [57].

Each airframe noise component is calculated using Equation 8.47, this gives the pressure differential due to the components as a function of the frequency (f), polar directivity angle (θ) and azimuthal directivity angle (ϕ). Where the polar directivity angle and azimuthal directivity angle can be set towards a certain location, as can be seen in Figures 8.15 and 8.16. For this analysis $\theta = 90\,\text{deg}$ and $\phi = 0\,\text{deg}$. Furthermore, M is the flight Mach number, c is the ambient speed of sound and ρ is the ambient density. P, D and F are calculated using Equations 8.48 till 8.59.

$$p_e^2(f,\theta,\phi) = \frac{\rho_\infty c\, P\, D(\theta,\phi) F(S)}{4\pi r^2 (1 - M\cos\theta)^4} \tag{8.47}$$

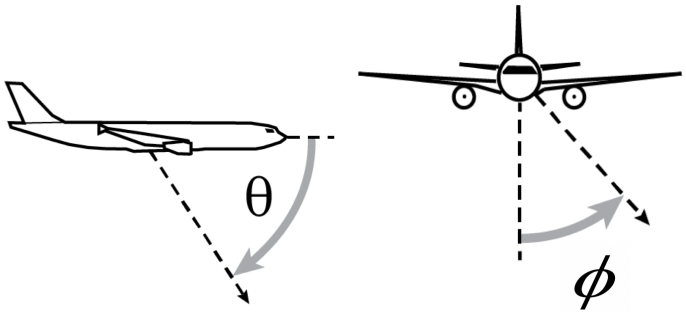

Figure 8.15: Polar directivity angle **Figure 8.16:** Azimuthal directivity angle

P is the power function given by Equation 8.48. Where K is an empirical constant and a relates the radiated acoustic power to the flow speed. The effect of airframe component geometry on the acoustic power is incorporated by G. The variables for each component can be found in Table 8.13.

$$P = K\, M^a\, G\left(\rho_\infty c^3 b_w^2\right) \tag{8.48}$$

Table 8.13: Input variables for Equation 8.48 and Equation 8.49

Airframe noise source	G	L	K	a
Clean wing	$0.37\frac{A_w}{b_w^2}\left(\frac{\rho_\infty M_\infty c_\infty A_w}{\mu_\infty b_w}\right)^{-0.2}$	Gb_w	$4.464\cdot10^{-5}$	5
Leading edge slats	Same as for wing			
Horizontal tail	$0.37\frac{A_h}{b_h^2}\left(\frac{\rho_\infty M_\infty c_\infty A_h}{\mu_\infty b_h}\right)^{-0.2}\left(\frac{b_h}{b_w}\right)^2$	Gb_h	$4.464\cdot10^{-5}$	5
Vertical tail	$0.37\frac{A_v}{b_v^2}\left(\frac{\rho_\infty M_\infty c_\infty A_v}{\mu_\infty b_v}\right)^{-0.2}\left(\frac{b_v}{b_w}\right)^2$	Gb_v	$4.464\cdot10^{-5}$	5
Trailing edge flaps	$\frac{A_f}{b_w^2}\sin^2(\delta_f)$	$\frac{A_f}{b_f}$	$2.787\cdot10^{-4}$	6
Landing gear	$n\left(\frac{d_{wheel}}{b_w}\right)^2$	d_{wheel}	$4.349\cdot10^{-4}$	6
Landing gear strut	$\left(\frac{d_{strut}}{b_w}\right)^2\left(\frac{l_{strut}}{d_{strut}}\right)$	d_{strut}	$2.753\cdot10^{-4}$	6

Equations 8.50 till 8.54 are all empirical spectral functions for each airframe component as a function of the Strauhal number S, which was calculated using Equation 8.49 and takes into account the length of the particular airframe noise source considered. Equation 8.50 was used for the clean wing as well as the horizontal and vertical stabilizer. Equation 8.51 for the slats, Equation 8.52 for the flaps, Equation 8.53 for the landing gears and Equation 8.54 for the landing gear strut.

$$S = \frac{f\,L(1 - M\cos\theta)}{Mc} \tag{8.49}$$

$$F_{cleanwing} = 0.613\,(10S)^4\left[(10S)^{1.5} + 0.5\right]^{-4} \tag{8.50}$$

$$F_{slats} = 0.613\,(10S)^4\left[(10S)^{1.5} + 0.5\right]^{-4} + 0.613\,(2.19S)^4\left[(2.19S)^{1.5} + 0.5\right]^{-4} \tag{8.51}$$

$$\begin{aligned} F_{flaps} &= 0.0480\,S \quad \text{for} \quad S < 2 \\ F_{flaps} &= 0.1406\,S^{-0.55} \text{ for} \quad 2 \le S \le 20 \\ F_{flaps} &= 216.49\,S^{-3} \quad \text{for} \quad S > 20 \end{aligned} \tag{8.52}$$

$$F_{lg} = 13.59\,S^2\left[S^2 + 12.5\right]^{-2.25} \tag{8.53}$$

$$F_{strut} = 5.325\left(30 + S^8\right)^{-1} \tag{8.54}$$

Lastly, the directivity function can be calculated calculated using Equations 8.55 till 8.59, where Equation 8.55 is used for the clean wing as well as the slats and horizontal stabilizer, Equation 8.56 is used for the vertical stabilizer. Equation 8.57 is used for the flaps, Equation 8.58 is used for the landing gears and lastly Equation 8.59 is used for the landing gear strut.

$$D_{cleanwing}(\theta,\phi) = 4\cos^2(\phi)\cos^2(\theta/2) \tag{8.55}$$

$$D_{verticaltail}(\theta,\phi) = 4\sin^2(\phi)\cos^2(\theta/2) \tag{8.56}$$

$$D_{flaps}(\theta,\phi) = 3\left(\sin\delta_f\cos\theta + \cos\delta_f\sin\theta\cos\phi\right)^2 \tag{8.57}$$

$$D_{lg}(\theta,\phi) = \frac{3}{2}\sin^2(\theta) \tag{8.58}$$

$$D_{strut}(\theta,\phi) = 3\sin^2(\phi)\sin^2(\theta) \tag{8.59}$$

Using all these equation resulted in a pressure differential at a certain frequency for each component. This pressure differential is translated to a Sound Pressure Level (SPL) using Equation 8.60, where P_{e_0} is the reference pressure of $2.0 \cdot 10^5$ N/m^2 [58].

$$SPL = 10log\frac{P_e^2}{P_{e_0}^2} \tag{8.60}$$

It should be noted that although the Fink airframe noise model is a suitable model for parametric prediction of noise radiated from the aircraft geometry, it predicts the primary airframe noise sources in a simplified manner. Other important airframe noise sources such as those from spoilers, the flap edge, cavities, fuel vents in the wing and the interaction of components that produce additional noise, are not incorporated in this model.

Engine Noise Analysis

The noise produced by an engine can be divided in contributions from different parts of the engine as depicted in Figure 8.17. However, only the jet and fan noise will be taken into account in the analysis since the largest contributions are from these two parts of the engine [57]. During the take-off assessment of the aircraft jet noise is predominant [57], while during landing the fan noise is predominant. The relation between airframe and engine noise during approach and take-off is depicted in Figures 8.18 and 8.19. It is clear that the noise during take-off (flyover measurement) is driven by the engine noise. Therefore, in order to be able to quantify and compare the noise levels of the designed aircraft and current state-of-the-art aircraft, the engine noise has to be estimated/quantified.

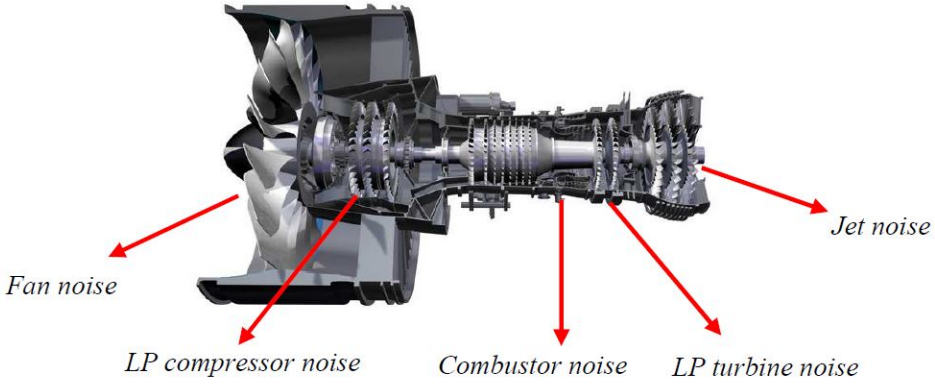

Figure 8.17: Contributions to engine noise [57]

The engine noise can be assessed in several ways. First a method as described in the PhD thesis of Lothar [9] was followed to quantify both the jet and fan noise. However, due to the lack in detail of the propulsion design this method could not be used to assess the engine noise. For this reason, the decision was made to analyze the engine noise based on research performed on the assessment of noise.

From Sahai [57] it was obtained that the acoustic power of the jet is proportional to the eighth power of the average exit speed of the engine, V^8_{exit}. From this Equation 8.61 is derived. The change in sound pressure level (SPL) between two engines based on their respective average exit speed can be assessed using Equation 8.62. This shows that an increase in the bypass ratio, which lowers the average exhaust velocity, results in a reduction of the noise generated.

$$SPL = 10 \cdot log(Acousticpower)^8 \tag{8.61}$$

$$SPL_2 = SPL_1 + 80 \cdot log\left(\frac{V_{exit_2}}{V_{exit_1}}\right) \tag{8.62}$$

In which SPL_2 is the sound pressure level of the new engine, while SPL_1 is the sound pressure level of the reference engine.

During the approach phase jet noise is not predominant due to the low engine thrust settings, while fan noise now becomes predominant. Figure 8.18 depicts the jet, fan and airframe noise of a short range aircraft that is simulated in [9]. It shows that during approach airframe and fan noise are comparable, while during take-off this is not the case and Equation 8.62 has to be used. However, due to lack of detail in the engine design, the engine noise during take-off could not be assessed within a reasonable time frame.

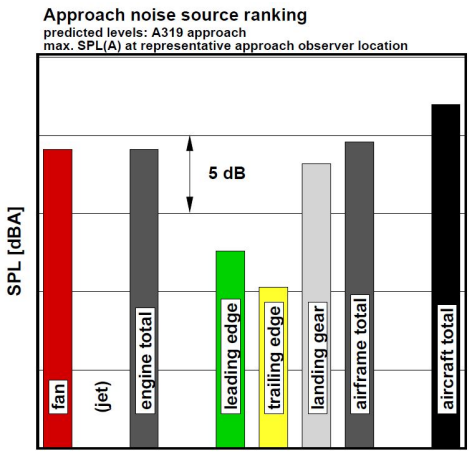

Figure 8.18: A319 Approach noise ranking [9]

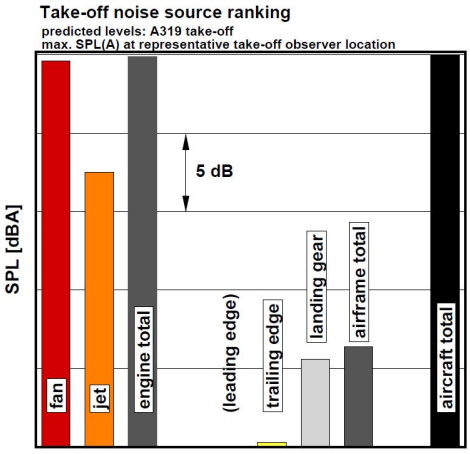

Figure 8.19: A319 Take-off noise ranking [9]

Noise Analysis Results

With the SPL levels of all the airframe components and the engines obtained, these could be summed using Equation 8.63[58]. For the analysis of the noise during approach, the decision has been made to assume that the engine noise is equal to the airframe noise. For take-off, the engine noise is calculated using Equation 8.62 and added to the airframe noise.

$$SPL_{total} = 10log\sum_{i=1}^{N} 10^{SPL_i/10} \tag{8.63}$$

Approach Conditions

Using the characteristics of the TU-ecoliner, as can be seen in Table 8.14, the SPL plot of the different components vs frequency were created and can be seen in Figure 8.20. From this plot, it can be observed that the vertical tail and the landing gear strut is not included. This is due the fact that the Azimuthal directivity angle is taken as 0, and according to Fink's model, noise of the vertical tail and strut is not emitted in that angle, as can also be deduced from Equations 8.56 and 8.59. Furthermore, from the plot it can be seen that the maximum SPL during approach is equal to 83 dB.

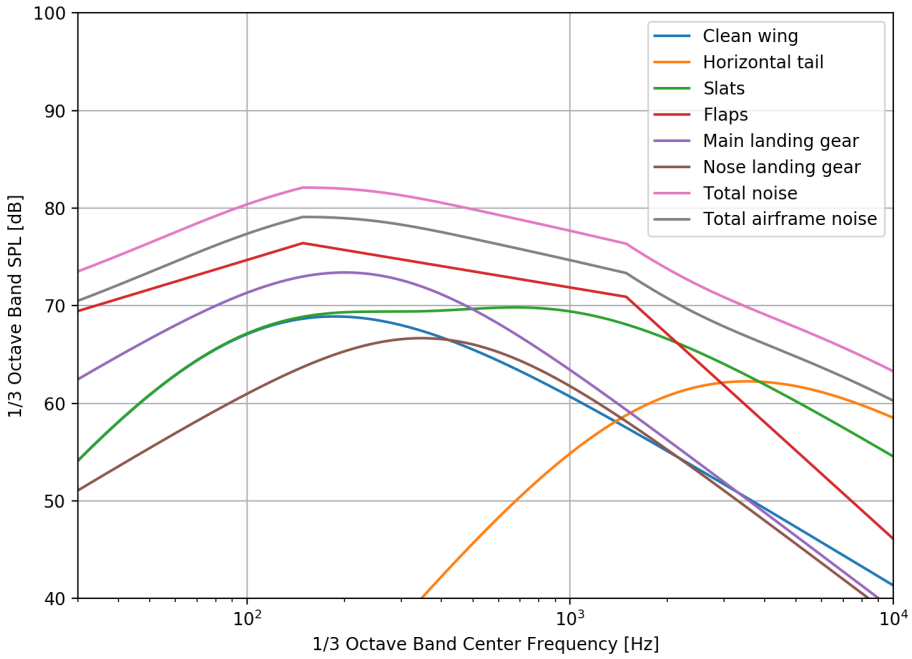

Figure 8.20: Noise of the TU-ecoliner in approach conditions

Since Fink's model does not represent the full aircraft noise as explained earlier. Figure 8.20 can not be compared to actual noise data from measurements of reference aircraft. Therefore, the decision has been made to input data from the Boeing 737 MAX 8 into the self-written program to obtain a rough estimation of the noise emitted by the TU-ecoliner compared to the Boeing 737 MAX 8. Inputting the aircraft characteristics, which can be seen in Table 8.14, resulted in the plot from Figure 8.21. From this plot it can be seen that for low frequencies the SPL level of the TU-ecoliner is lower, from around 160 Hz till around 900 Hz the TU-ecoliner is equally loud as the Boeing 737 MAX 8, whereas after 900 Hz the TU-ecoliner is louder. However there are some deficiencies in the self-written code, which will be elaborated upon in the verification and validation part.

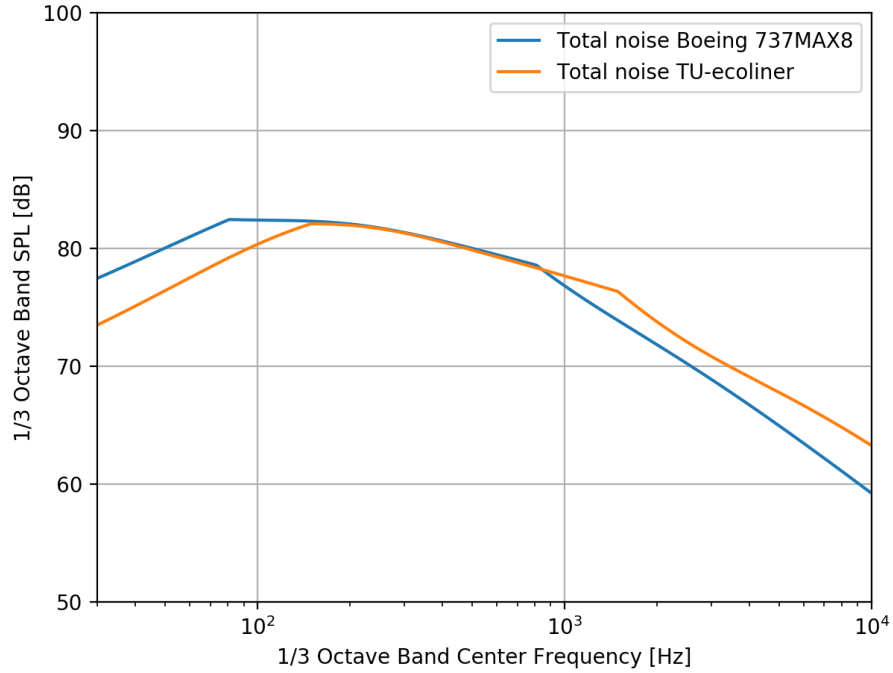

Figure 8.21: Comparison between Boeing 737 MAX 8 and TU-ecoliner in approach conditions

It should be noted that the SPL only takes into account the pressure difference due to the sound wave, while it is known that humans do not perceive noise similarly on all frequencies. The human hearing system perceives high frequencies louder than low frequencies. Therefore an A-weighted correction is applied, which makes a correction for sound pressure level according to the frequency. The A-weighted sound level is calculated using Equation 8.64, where the corrected band level is calculated using Equation 8.65 and the relative response is approximated using Equation 8.66[58]. To give an indication of what the A-weighting does to the SPL plot, a comparison between the normal SPL and A-weighted SPL plot of the TU-ecoliner can be seen in Figure 8.22. From this figure it can be seen that the SPL of the A-weighting is up to a frequency of 1,000 hz, lower than the normal SPL. The comparison between the A-weighted Sound Pressure Levels of the TU-ecoliner and the Boeing 737 MAX 8 can be seen in Figure 8.23. From the A-weighted SPL comparison between the Boeing 737 MAX 8 and the TU-ecoliner, it follows that the TU-ecoliner produces less noise until a frequency of around 900 Hz and hereafter produces more noise.

$$L_A = 10 \cdot \log\left(\sum 10^{\frac{L_A(i)}{10}}\right) \tag{8.64}$$

$$L_A(i) = SPL(i) + \Delta L_A(i) \tag{8.65}$$

$$\Delta L_A = -145.528 + 98.262 \cdot \log(f) - 19.509 \cdot (\log(f))^2 + 0.975 \cdot (\log(f))^3 \tag{8.66}$$

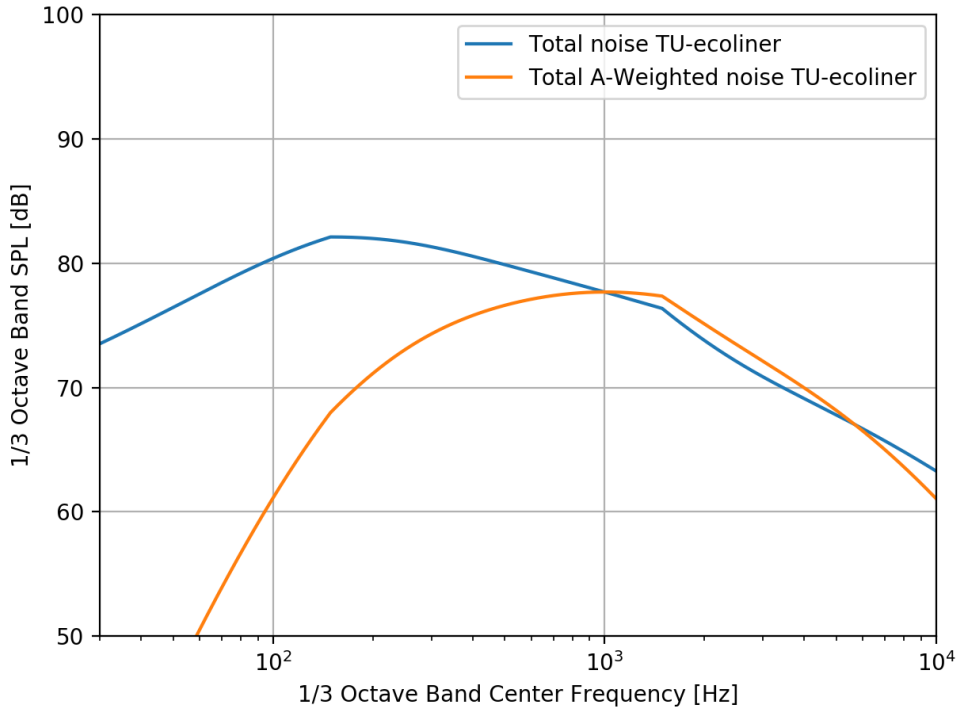

Figure 8.22: Comparison between the SPL and A-weighted SPL of the TU-ecoliner in approach conditions

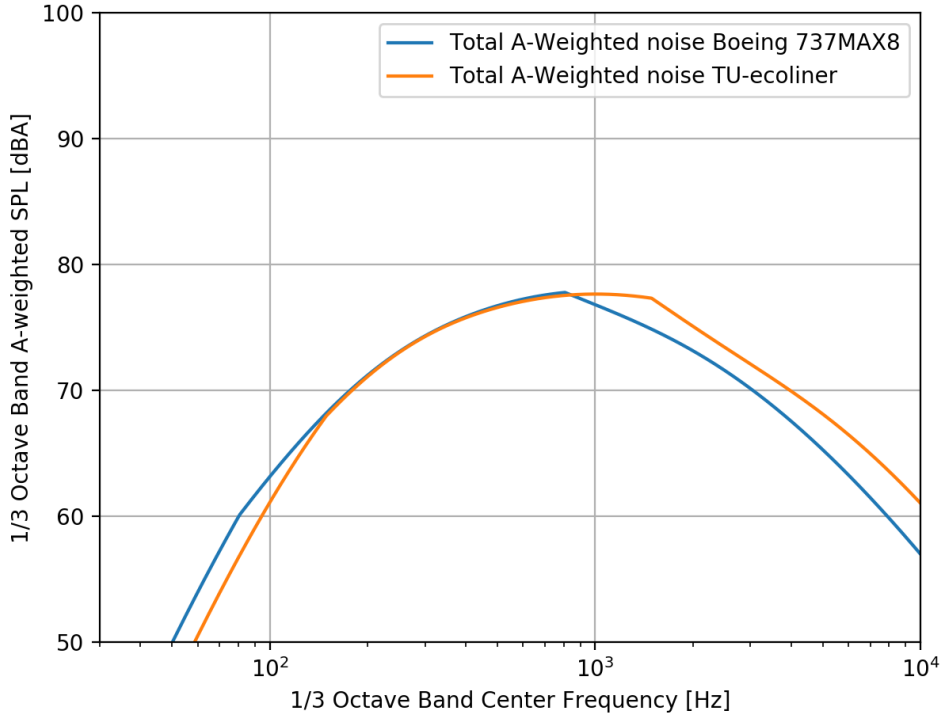

Figure 8.23: Comparison between Boeing 737MAX8 and TU-ecoliner in approach conditions

Verification and Validation

The airframe noise model is verified by comparing the results from the self-written code with a model written by United Technologies Research Center in [56]. In this technical report the airframe noise prediction method from Fink is applied to a Boeing 747 and compared to measured values, as can be seen in Figure 8.24. For this verification only the line which states "NASA ANOPP COMPONENT PREDICTION METHOD" is of importance.

In order to verify the self-written code, data from the Boeing 747 as can be seen in Table 8.14 was used as input in the code and yielded the graph as can be seen in Figure 8.25. From this comparison it can be seen that the 2 lines have some differences, this means that the self-written program has some deficiencies.

Furthermore, Fink's method itself does not correctly represent a real aircraft as mentioned earlier. This can also be seen in Figure 8.24, where the triangles and the dots in the graph indicate the SPL from measurements, and does not match the values of the ANOPP component prediction method. To have an indication of the offset of the self-written code, the maximum A-weighted SPL from the Boeing 737 MAX 8 is obtained from a database of Eurocontrol and is equal to 91.3 dBA[8], whereas the maximum A-weighted SPL from the self-written code is equal to approximately 78 dBA. This means that drawing a conclusion based on this analysis is questionable, therefore the decision has been made to assess the noise of the aircraft qualitatively based on the noise reduction technologies which will be implemented on the TU-ecoliner.

Table 8.14: Input data used for the noise modelling

Parameter	**TU-ecoliner**	**Boeing 737MAX8**[9]	**Boeing 747[56]**	**Unit**
Wing area (A_w)	110	127	510.97	m^2
Wing span (b_w)	39.24	35.9	59.65	m
Horizontal tail area (A_h)	23.1	32.78	136.57	m^2
Horizontal tail span (b_h)	9.6	14.35	22.17	m
Flap area (A_f)	22.6	38.1	78.69	m^2
Flap span (b_f)	23.21	21.5	34.36	m
Main landing gear wheel diameter (d_{mg})	1.14	1.13	1.17	m
Nose landing gear wheel diameter (d_{ng})	0.66	0.69	1.17	m
Flap angle (landing) (δ_f)	50	40	25	deg
Approach speed (V_{land})	72.54	71.51	104.95	m/s
Distance to observer (r)	60.69	60.69	152.4	m
Polar directivity angle (θ)	90	90	90	deg
Azimuthal directivity angle (ϕ)	0	0	0	deg

[8] `https://www.aircraftnoisemodel.org/` [cited 25 June 2018]
[9] `http://www.b737.org.uk/techspecsdetailed.htm` [cited 25 June 2018]

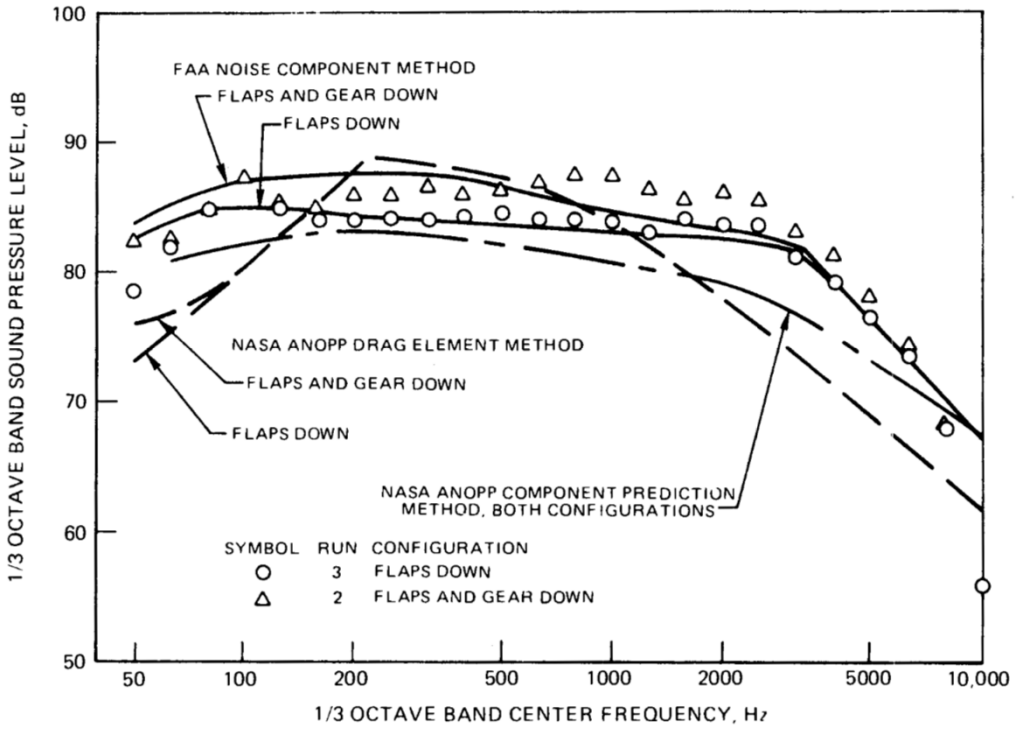

Figure 8.24: Boeing 747 noise estimation from reference [56]

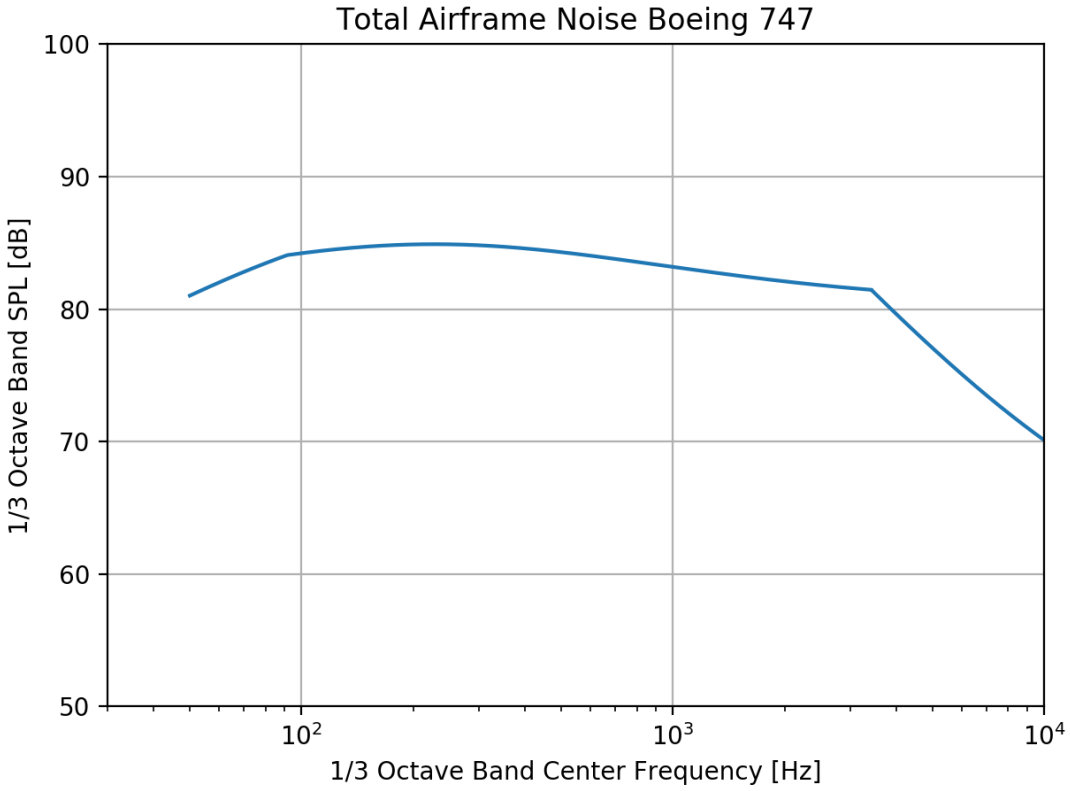

Figure 8.25: Boeing 747 noise estimation from self-written code

Qualitative noise assessment

The TU-ecoliner will be fitted with noise reduction technologies which are not accounted for in Fink's method. One of these noise reduction technology is the blowing and suction of air, this requires small strips to be attached to the flaps and landing gear to energize the flow before it reaches the extending surface. This adds a small amount of weight but has a relatively large positive effect on noise reduction. With this technology the broadband noise is expected to decrease by 3 to 5 dB[59].

Vortex generators (VG's) are also placed at the fuel tank pressure equalization vents[10] in order to disturb the flow there. These vents, when air flows over them, produce the same noise as blowing over the top of a bottle. Placing VG's there, eliminates this effect. This measure reduces the overall noise of an A320 like aircraft in landing by 4dB at a distance between 10 km and 17 km from the airport[11]. VG's are only 5 cm long[10] and therefore they hardly add any extra weight. They do, however, add some additional drag.

The landing gear is also a main contributor to the airframe noise, due to spurious noise sources and interaction of flows, therefore a fairing will be fitted around the landing gear as can be seen in Figure 8.27, this is expected to result in a noise reduction of approximately 3 dB[59].

Further noise reduction is achieved due to the usage of ultra-high bypass ratio geared turbofans. In conventional engines the tip of the fan rotors can reach supersonic speeds which induces a lot of drag and noise[12], according to [60] fan broadband noise is proportional to $u_{tip}^{5/2}$. Using a gearbox in the engine allows the fan to run at its optimal speed, hence reducing the noise. Secondly, due to the increased bypass ratio, the average exhaust velocity is decreased. This will lead to a reduction in jet noise[61], as can also be deduced from Equation 8.62.

Apart from the noise reduction due to the ultra-high bypass ratio geared turbofans, noise reduction technologies are also implemented in the engines. By applying metal foam liners in the area over the tips of the rotors, which is where most of the engine noise is generated, one can very efficiently damp the noise nearby where it is generated [62]. Implementation of this system is expected to result in a noise reduction of up to 5 dB[63]. The engines will also be equipped with chevrons, these mix the flow of air coming out of the engine with the surrounding air to reduce the exhaust velocity and thus reduce noise.

With these noise reduction technologies, the TU-ecoliner is expected to emit less noise compared to current state-of-the-art aircraft and comply with chapter 14 noise regulations of ICAO.

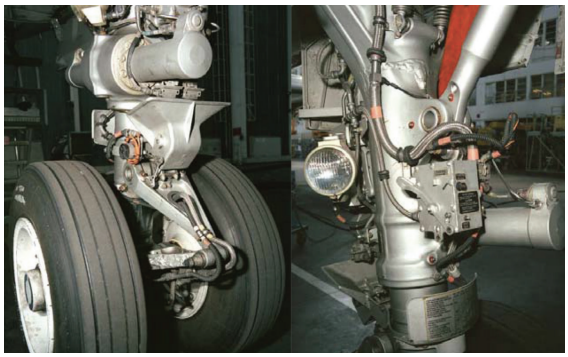

Figure 8.26: Conventional landing gear [64]

Figure 8.27: Landing gear with fairing [64]

[10] `http://www.greenaironline.com/news.php?viewStory=2116` [cited 24 May 2018]

[11] `https://www.lufthansagroup.com/en/responsibility/climate-and-environmental-responsibility/active-noise-abatement.html` [cited 24 May 2018]

[12] `https://www.southampton.ac.uk/engineering/research/projects/buzz_saw_noise_and_non_linear_acoustics.page` [cited 3 July 2018]

8.3. Emissions

The following section will discuss the emission analysis of the TU-ecoliner. The section starts with a description of the regulations and certification with respect to aircraft emissions in Subsection 8.3.1. Following on this, the assessment methodology will be discussed in Subsection 8.3.2. This section will be concluded with the assessment evaluation in Subsection 8.3.3 in which a sensitivity analysis is performed along with verification and validation.

8.3.1. Regulations & Certification

The combustion of jet fuel produces both particulate and gaseous pollutants. The International Civil Aviation Organization (ICAO) stipulates regulations for the LTO (landing-takeoff) cycle for NO_x, CO, unburned hydrocarbons (UHC) and smoke emissions [65]. The ICAO Annex 16: Enviromental Protection Volume 2 Aircraft engine emissions [65] specifies the regulatory framework for the certification of engine emissions.

The aforementioned ICAO regulations specify the thrust setting and the time in the operating mode during the LTO cycle. Based on the compressor pressure ratio of the engine the regulations specify the allowed emissions. During certification tests the emission rate (emission index multiplied by the fuel flow), gross emission of each gaseous pollutant over the LTO cycle (in grams) and the maximum smoke number.

8.3.2. Assessment Methodology

The following subsection will describe the methodology followed to assess the fuel consumption and CO_2 emissions of the TU-ecoliner.

Fuel Consumption

As a first step of deriving the emissions specific for the considered design, the fuel consumption was determined for different flight phases, namely in the take-off, cruise and approach/descend phase. A database from ICAO [13] was consulted, containing the fuel consumption of over 500 engines. As the maximum output thrust could also be obtained from this database, the fuel consumption could be converted into a thrust-specific fuel consumption (TSFC). With this a statistical analysis was run, which is shown in Figure 8.28 where the TSFC during take-off has been plotted as a function of the engine bypass ratio. In here only the engines with a similar thrust output, of in between 80 kN and 130 kN of thrust were considered [14].

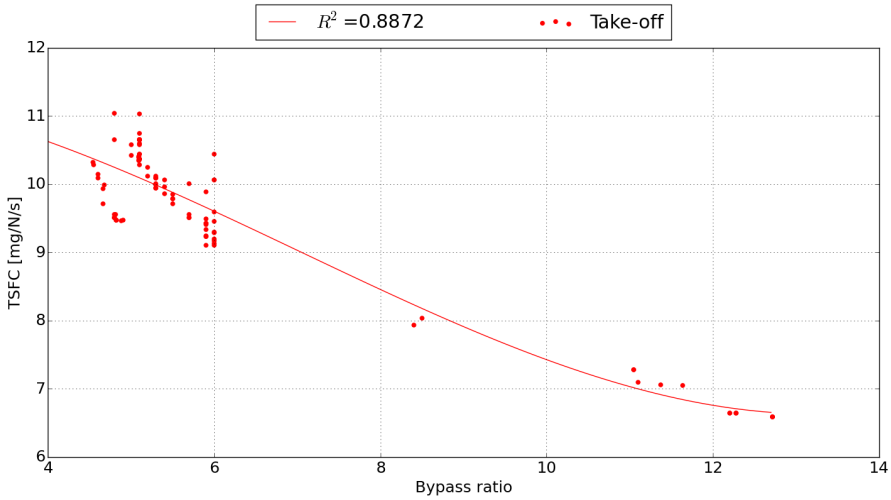

Figure 8.28: Thrust-specific fuel consumption versus bypass ratio for various engines with a similar thrust output.

Along with the data points a regression line representing a third-order polynomial[15] was plotted in order to represent the data. As it was decided to use an ultra-high bypass ratio turbofan with a bypass ratio (BP) of 14, the polynomial was used to extrapolate and obtain a predicted value for the TSFC. This yielded a TSFC of 6.692 mg/N/s for take-off, or a $c_{j_{TO}}$ of 1.425 kg/s for both engines.

[13] https://www.easa.europa.eu/easa-and-you/environment/icao-aircraft-engine-emissions-databank [cited 22 June 2018]
[14] The maximum thrust output for this design is $\frac{213}{2}$ = 106.5 kN.
[15] A third order polynomial resulted in the most realistic curve, with a r^2 of 0.8872

In order to verify the obtained TSFC during take-off, data from the same database has been used indicating the testing dates of all engines. This data has been analyzed to see whether there is a relationship between test date and the TSFC of the respective engine. Here it should be noted that the year of testing does not mean that the engine has been introduced in that same year, but it gives a good indication of the generation of the engine. In Figure 8.29 the bars indicate the *average* TSFC of the engines tested in that year, while the red error bars indicate the standard deviation of the data belonging to that cohort. Only the years in which more than ten engines were tested have been included, in order to ensure reliable data and prevent outliers from influencing the perceived data too much.

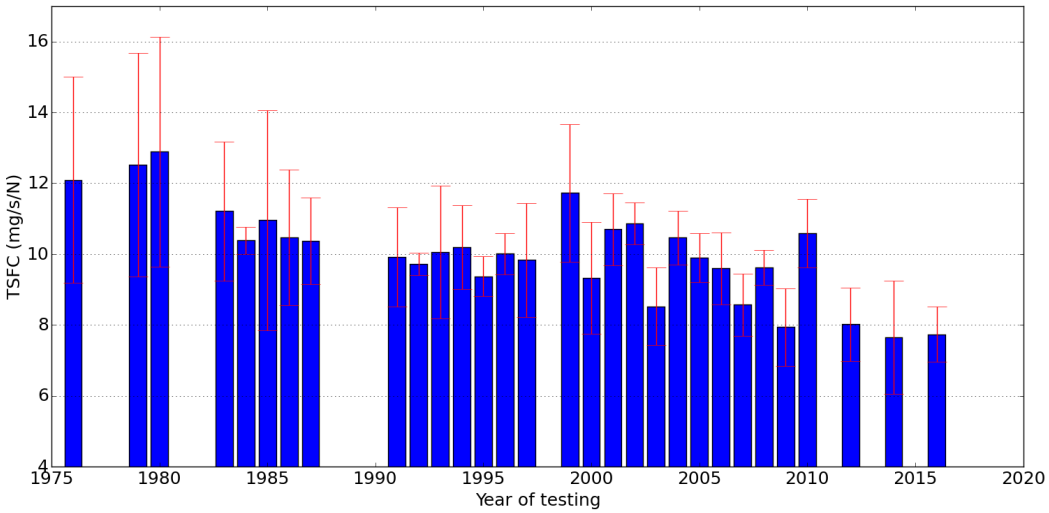

Figure 8.29: The development of the thrust specific fuel consumption over time.

A limitation of the data is that there is no cruise thrust and thrust setting during approach given for all different engines, which is mainly dependent on the aircraft on which the engines are integrated. A solution for this was found by looking at the ratio between specific fuel consumption in take-off and cruise and in take-off and approach. This is shown in Figure 8.30.

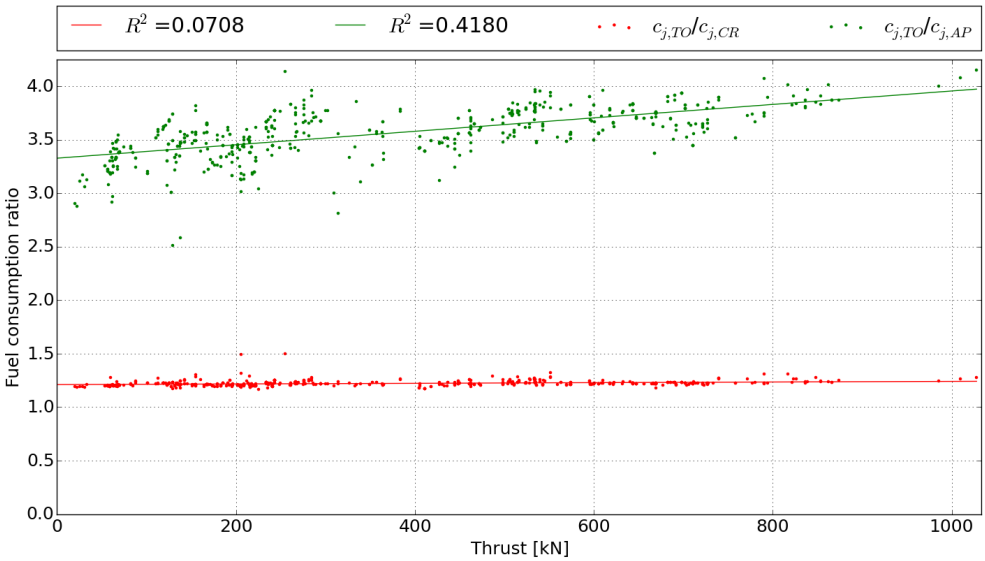

Figure 8.30: Fuel consumption ratios versus output thrust for various engines.

The linear regression lines that are plotted in Figure 8.30 were considered relevant and representative for the data as their p-value would be below 0.05, meaning a rejection of the null hypothesis that the slope is zero (and hence that there would not be a statistical relation between the two variables). For both regression lines, $p \ll 0.05$. The statistical analysis yielded $\frac{c_{j_{TO}}}{c_{j_{CR}}} = 1.217$ and $\frac{c_{j_{TO}}}{c_{j_{AP}}} = 3.460$, hence $c_{j_{CR}} = 1.171$ kg/s and $c_{j_{AP}} = 0.412$ kg/s for both engines. This leads to a reduction of around 17% in fuel consumption compared to the A321neo which is powered by two Leap A1 engines, and a reduction of about 1% compared to the PW1122G-JM which is the data point most to the right in Figure 8.28.

CO_2 *Emissions*

From the obtained engine fuel consumption the CO_2 emissions of the aircraft could be determined using Equation 8.67. The CO_2 emitted by the aircraft during a flight is determined using the fuel flow in the specific phase of the flight, the emission index (the kg CO_2 emitted per second) and the time spend during the flight phase.

$$CO_2 emissions = \sum c_j \cdot \text{Emission Index} \cdot \text{time in mode} \tag{8.67}$$

The emission index is determined using the energy density of the fuel used and the amount CO_2 that is emitted by the combustion of the fuel type. The fuel types that were considered in the analysis can be found in Table 8.15 along with the energy density and emissions of each fuel type.

Table 8.15: Summary of information on a variety of available biofuels

Fuel Type	**Aromaticity** (%)	**Area Density** [kg/ha]	**Energy Density** [MJ/kg]	**Volume Density (15 C)** [kg/m^3]	**Cost** [USD/kg]	**Emissions** [gCO2/MJ]
JP-8	18.8 [66]	-	42.8 [67]	775-840 [67]	0.55 [16]	73.1 [68]
Algae Oil	11 [66]	80,370 [69]	41 [70]	846 [70]	Open pond 3.24 [66]	35.2 [71]
					Closed Photobioreactor 6.85 [66]	86.5 [71]
Jatropha Oil	11 [66]	1,590 [69]	44.3 [68]	749 [67]	1.22 [72]	20-60 [71]
Camelina Oil	24.2 [66]	490 [69]	44.0 [68]	753 [67]	1.08 [73]	-10 - 60 [71]
Soybean Oil	2.6 [66]	375 [69]	37 [17]	917 [18]	0.79 [66]	30 -250 [71]

As the obtained fuel consumption turns out to be 17% lower than the A321neo, the CO_2 emissions per second went down inherently, from 4.23 kgCO_2/s to 3.52 kgCO_2/s. This would lead to a CO_2 emissions reduction of about 7 tons for each flight over the design range of 1,800 km. The emissions per km are left out for simplicity, as it does not bring new insights or different conclusions. Furthermore, it would require information about the flight speed of reference aircraft during all flight phases.

For a comparison between the emissions per revenue passenger km, the passenger capacity including the load factor for different ranges should be known. As this data is hardly obtainable, a deep analysis has been left out. However, for the obtained fuel consumption and by using kerosene as only fuel source, a value for the Boeing 747 gCO_2/passenger/km is found. Considering the combination of payload and range, this value is significantly lower than for comparable aircraft as can be seen in [74]. An analysis of this fashion is of importance however, as is illustrated by the following example. The PW1122G-JM engine turns out to be very favorable in terms of fuel consumption, being close to the one found for the aircraft under consideration. It is being used to power the Irkut MC-21 series, with a maximum passenger capacity varying from 132 to 212 passengers [19]. As the TU-ecoliner has a payload capacity of 240 passengers, averagely loaded with 226 passengers, the emissions per passenger km will turn out less than the Irkut series, even though the difference in fuel consumption is merely 1%.

[16] as defined in the HF-STK-AL-08 [3],

[17] `https://www.soya.be/soybean-oil-nutritional-values.php` [cited 30 May 2018]

[18] `https://www.sigmaaldrich.com/catalog/product/supelco/47122?lang=en&region=NL` [cited 30 May 2018]

[19] `https://www.aerospace-technology.com/projects/irkut-21-aircraft/` [Cited 22 June 2018]

Next to bringing down the fuel consumption, another way of reducing emissions that is considered viable within the next generation is by using alternative fuels that emit less than conventional fuel. With "emitting less" the net effect is met, i.e. taking into consideration the entire life cycle of the resource.

A promising new technique to reduce carbon emissions and thus slow global warming is the so called Solar Fuel. It incorporates a technology in which CO_2 is converted into hydrocarbons, which can be used as conventional fuel [75]. The advantage of this is that it is a so called 'drop-in fuel' which means the current engines need no changes to be able to use it [76]. The technique has not been used on large scale but it is promising nonetheless as it can be used after the aircraft has been taken into operation and it is thus feasible that it will be used in the lifetime of the aircraft.

A technique that has been under development for a longer time and that has been proven viable and effective already, is the combustion of biomass. There are plentiful different resources of biomass, all having their advantages and disadvantages. In order to narrow down the scope of this section, the focus will lie on Oil-To-Jet (OTJ) fuels, as those fuels interfere least with the food production, amongst other things [66][20]. More specific, the use of jatropha, camelina and algae have been looked into, also soybeans were taken into account as they have a very high efficiency which means they are considered even though it interferes with food production. Each of these fuels has been mixed into a blend with 60% and 80% kerosene. The results of this analysis are shown in Figure 8.31.

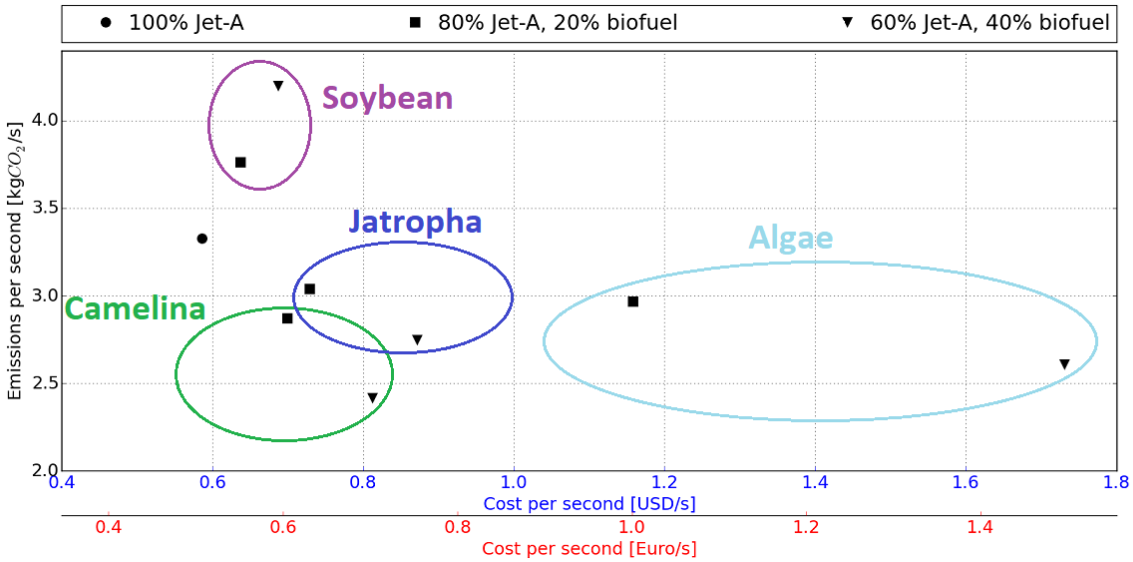

Figure 8.31: Fuel cost per second vs fuel consumption per second for different fuel blends.

Looking at the figure, it becomes apparent that a blend of conventional fuel and camelina shows a favorable combination of fuel cost and emissions compared to other blends. To get a feel for the numbers, a blend of kerosene with 40% of camelina would lead to a decrease in emissions of more than 8 tons compared to when only kerosene is used, leading to 21.7t CO_2 emitted in a flight of 1,806 km. However, an advantage of jatropha compared to camelina is that the area density is considerably higher as can be seen in Table 8.15. This is of importance as a high area density puts a lower demand on land usage, which is one of the major constraints for biofuel usage [66].

The biofuel analysis was a high level analysis attempted to get a first-order idea of the impact biofuel usage has on fuel cost and emissions. Due to the high uncertainty of in particular the yield of biomass and its related cost, the presented data have a high uncertainty.

[20] Also the aromatic compound of the resources have led to this choice, along with the yield per area unit.

8.3.3. Assessment Evaluation

In the following subsection the results of the sensitivity analysis performed on the fuel consumption analysis will be described along with the verification and validation of the obtained results.

Sensitivity Analysis

In order to assess the sensitivity of the obtained fuel consumption the order of the polynomial used in the analysis was altered. The results as discussed in the fuel consumption section were obtained using a polynomial with an order of 3. The results of the sensitivity analysis are tabulated in Table 8.16. It can be seen that with increasing order of the polynomial the specific fuel consumption slightly increases until the order of 4 is reached. At this point a large decrease in the fuel consumption is observed. This is where the deficiencies of statistics are really visible. The obtained regression line shows a large drop in the fuel consumption from a bypass ratio of 12, as can be seen in Figure 8.32. The dotted line depicts the prediction up to a bypass ratio of 14. This explains the large decrease in fuel consumption. The same logic applies to the fifth order of the polynomial, at which a large increase in the fuel consumption is visualized due to an increasing slope of the respective regression line as can be seen in Figure 8.33 where again the dotted line depicts the prediction up to a bypass ratio of 14.

Table 8.16: Specific fuel consumption as function of order of polynomial

Order of polynomial	**1**	**2**	**3**	**4**	**5**	**6**
Specific fuel consumption [kg/s]	1.236	1.306	1.425	0.768	2.704	1.361
Difference [%]	-13	-8.35	0	-46	90	-4.5

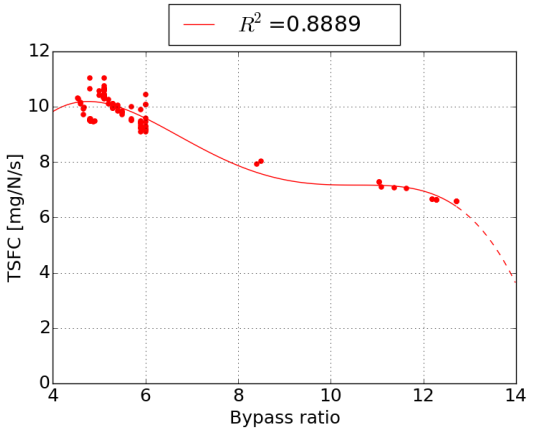

Figure 8.32: Regression line of a fourth order polynomial

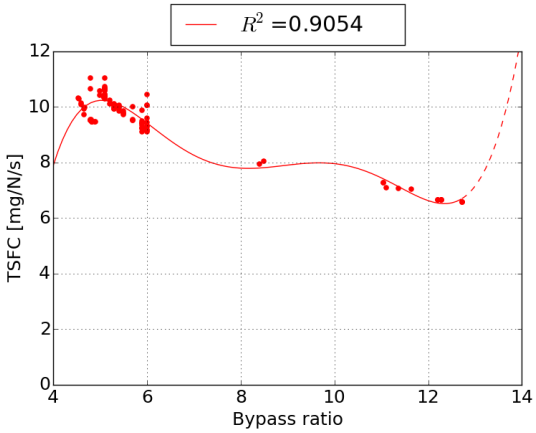

Figure 8.33: Regression line of a fifth order polynomial

Furthermore, a sensitivity analysis is performed on the change in emissions and cost associated with a change in the amount of biofuel used together with conventional fuel. For this, a fuel mixture of 99% conventional fuel and 1% biofuel is assessed. The results are tabulated in Table 8.17 and show the change in emissions and cost as a percentage compared to the case in which 100% conventional fuel is used. The results show that for some biofuels, such as algae, the application is a trade-off between cost and emissions. It can be seen that the use of jatropha is promising as it reduces both the emissions and cost.

Table 8.17: Change in emissions and cost associated with a 1% increase in biofuel

	Jatropha (+1%)	**Soybean (+1%)**	**Camelina (+1%)**	**Algae (+1%)**
Emissions [% change]	-0.432	0.656	-0.685	-0.538
Cost [% change]	1.217	0.435	0.966	4.88

Verification and Validation

In order to assess the obtained results for fuel consumption during the different flight phases, a comparison was made with reference aircraft. The results of this assessment are depicted in Figure 8.34. The specific

fuel consumption (SFC) during take-off is depicted in red, the SFC during cruise in green and the SFC during the approach phase is depicted in blue. The large dots represent the TU-ecoliner. It can be seen that the TU-ecoliner performs best compared to reference aircraft as the lowest SFC values for this thrust class are obtained. The obtained SFC values have the same order of magnitude compared to reference aircraft and perfectly fit in the trends as obtained from the reference aircraft data.

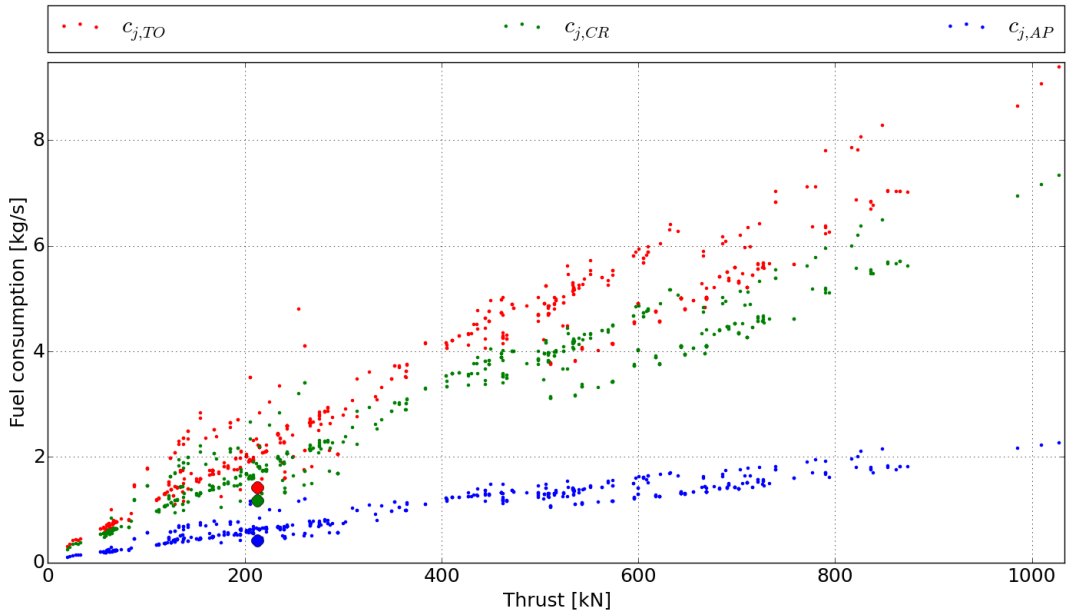

Figure 8.34: Fuel consumption of the TU-ecoliner compared to reference aircraft

Furthermore, the emission index has been verified, as this value together with the fuel consumption determined the CO_2 output of the program made for the assessment. The emission index was simply calculated by Equation 8.68, in which E represents the energy density (column 4 in Table 8.15) and I represents the emissions density (column 7 in Table 8.15).

$$\text{Emission index} = E \cdot I \tag{8.68}$$

This resulted in an emission index of 3.129 $kgCO_2/kg_{fuel}$, which is close to the values used in literature [21] [77].

8.4. RAMS Characteristics

In this section, first the reliability of the aircraft will be discussed. After that, the availability is touched upon. Later on, the maintainability will be elaborated. Finally, the Safety of the aircraft is discussed.

8.4.1. Reliability, Availability and Maintainability

Since the TU-ecoliner is similar to the current state-of-art aircraft in the inter-European market in many respects, the reliability of the aircraft is expected to be comparable to these aircraft. When taking the Airbus A321 as a baseline, reliability is predicted to be on par. However, the implementation of next-generation aircraft monitoring technologies will increase availability and reliability, while enhancing the maintainability of the aircraft. On the other hand, the extensive use of new technologies might lower the reliability.

For instance, the active hybrid laminar flow control (HLFC) system requires an extensive and complicated system in order to function. The fact that this system will be brand-new and has not been implemented on this scale before will mean that it will be more prone to begin-of-life failures. The additional level of complexity of the wing electronics induced by the system will possibly result in a reduction of the aircraft reliability. Moreover, the increased complexity and number of parts will lead to more maintenance and lower availability. However, the use of technology monitoring systems means that any faults or mishaps in the system are immediately noticed and passed on to the ground station where spare parts can be laid ready to

[21] `https://www.ipcc.ch/ipccreports/sres/aviation/110.htm` [cited 26 June 2018]

minimize downtime. Additionally, the HLFC-system will be designed in such a way that section of the system can be replaced individually. Hereby lowering the cost and time of repair for a single section of the HLFC.

When looking at the expected reliability of the engines, no significant changes compared to the Airbus A321neo are expected. Although the engine will incorporate several new technologies, which might reduce reliability, the addition of an extensive engine monitoring system means the overall reliability will increase. The monitoring system will allow operators to check up on the engines remotely and receive maintenance warnings and notifications. This valuable information will allow them to plan maintenance and repair activities with greater efficiency and order the required parts in time. Thereby enhancing the overall availability of the engine.

The strut is designed with high repair effectiveness in mind. Even though it must withstand the huge loads of the wing it is easily mountable and dis-mountable. This means that downtime is minimized when repairing and replacing the strut which is slightly more prone to damage as it is new for operators using conventional aircraft like the A321.

8.4.2. Maintenance

As with any aircraft, expected and unexpected maintenance task will have to be carried out. Expected, or scheduled, maintenance might include en-route service, terminating pre-flight checks, service checks and maintenance checks [78]. These maintenance can be properly prepared and scheduled and will, therefore, result in lower downtime and greater availability. Thanks to an extensive aircraft monitoring system, the aircraft's maintenance will be mostly expected or predictable. Therefore, the maintenance can be scheduled properly, reducing downtime and maintenance cost.

Next to the regular maintenance activities, the aircraft will have to undergo regular check-up in the form of A and C checks. These checks are standard practice in the aviation industry and are expected to still be relevant to the next-generation of aircraft. The intervals between which these need to be performed are presented in Table 8.18 [78]. Note that C-checks also include all A-checks.

Table 8.18: A- and C- check overview against flight hours

Check	300	600	900	1,200	1,500	1,800	2,100	2,400	2,700	3,000	3,300
1A	X	X	X	X	X	X	X	X	X	X	X
2A		X		X		X		X		X	
3A			X			X			X		
4A				X				X			
5A					X					X	
C										X	

8.4.3. System Failure

Before the safety of the system could be assessed and risks could be mitigated, the potential weaknesses of the system have to be identified. The identification of potential weaknesses are an outflow of a so-called "failure tree" or "fault tree", in which the different levels represent a cause-consequence relation. As an aircraft consists of endless components which all have a risk of failing, the choice was made to merely focus on the most severe events. In this way the tree gives a brief yet crucial overview of some possible causes of system failure. The fault tree is presented in Figure 8.35.

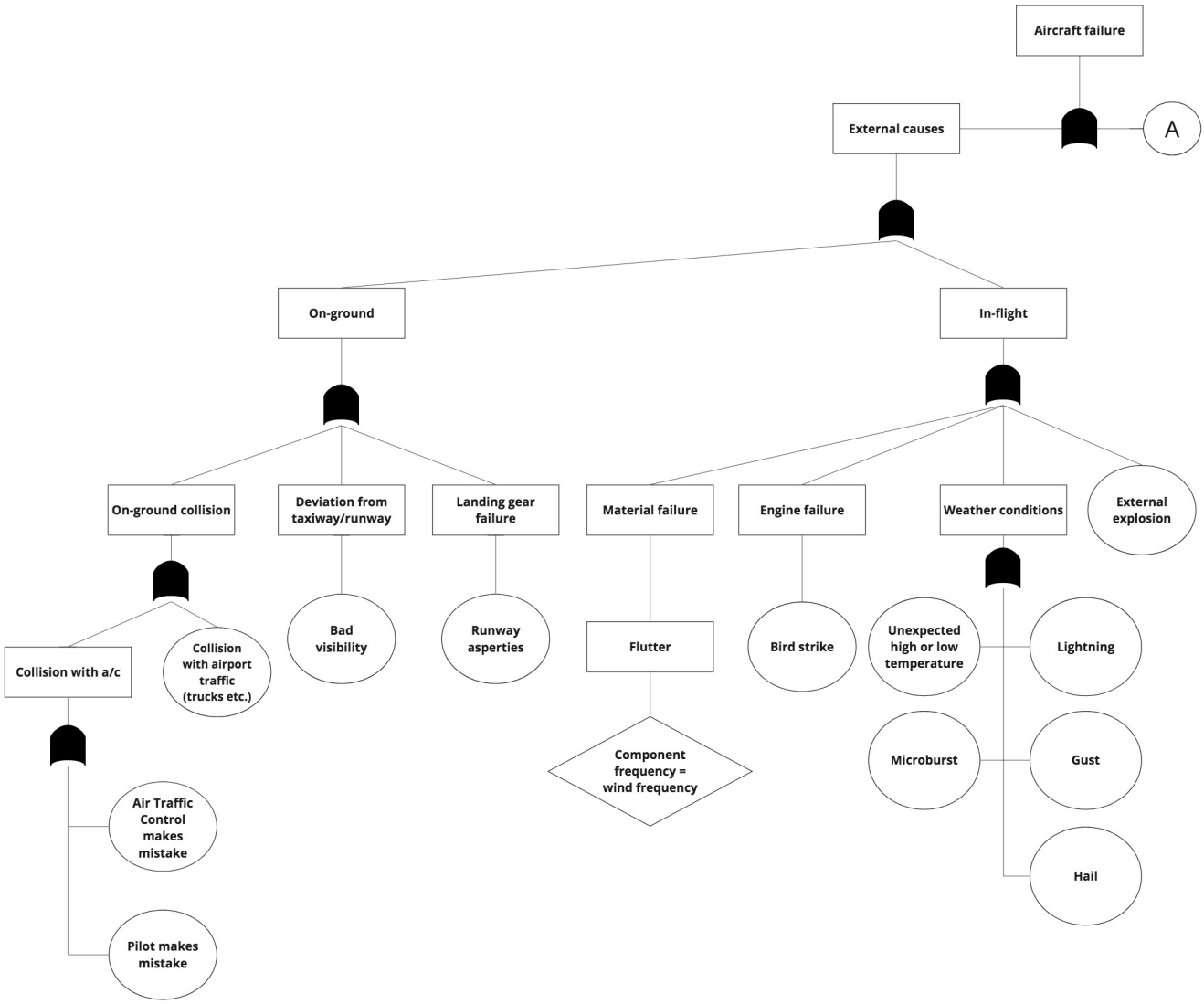
Aircraft failure
External causes
A
On-ground
In-flight
On-ground collision
Deviation from taxiway/runway
Landing gear failure
Material failure
Engine failure
Weather conditions
External explosion
Collision with a/c
Collision with airport traffic (trucks etc.)
Bad visibility
Runway asperties
Flutter
Bird strike
Unexpected high or low temperature
Lightning
Component frequency = wind frequency
Microburst
Gust
Hail
Air Traffic Control makes mistake
Pilot makes mistake

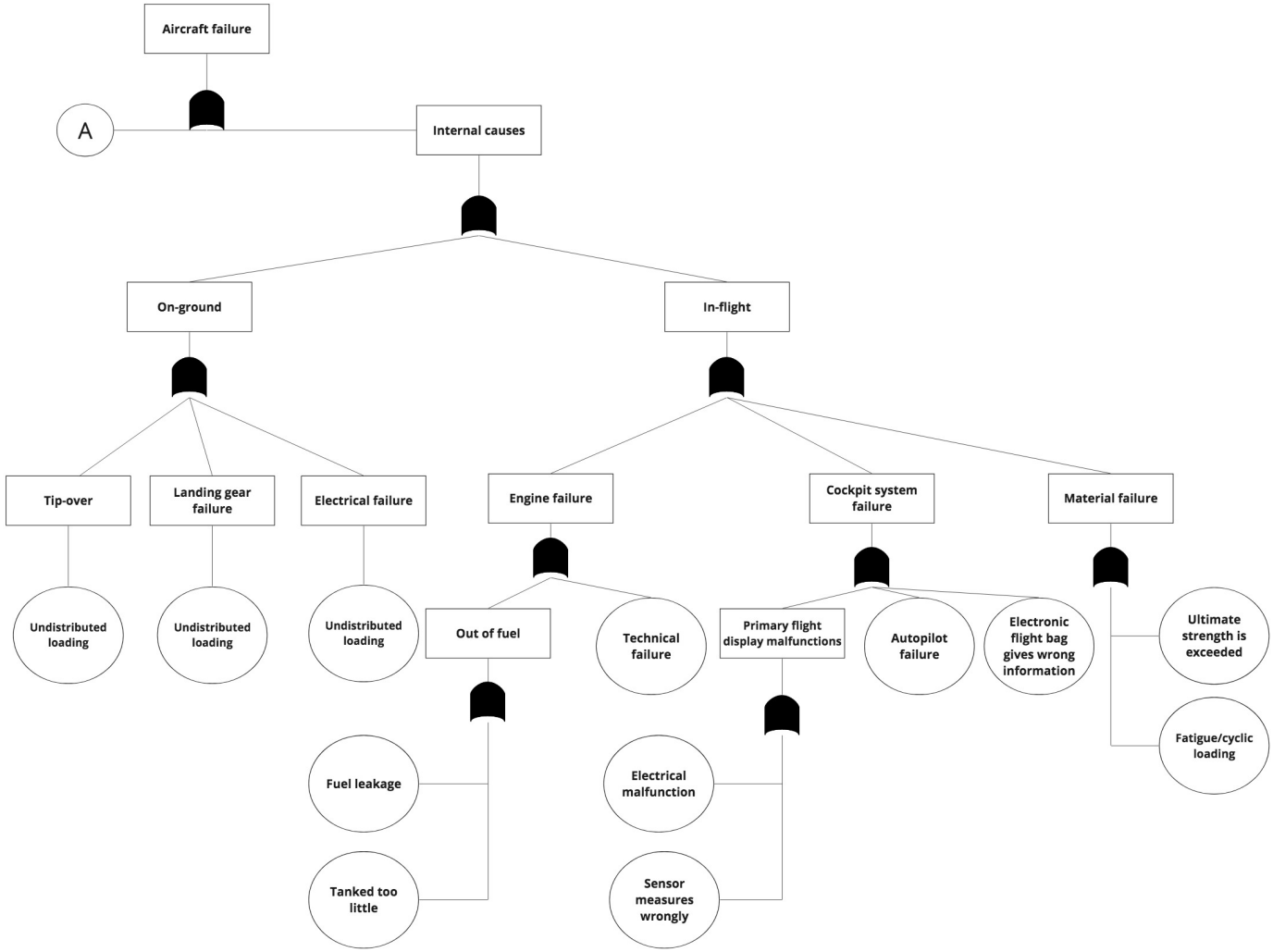

Figure 8.35: The fault tree for the TU-Ecoliner.

8.4.4. Safety

Safety will be guaranteed by two main design aspects, a solid redundancy philosophy and full compliance with CS-25 [6]. Each of these aspects will be touched upon briefly in this subsection.

List of Safety Critical Functions

In order to design for safety it is important to identify the systems and functions of the aircraft that might impact the safety when they fail. These systems or functions are compiled in the list of safety critical functions presented below. This list includes those systems or functions whose loss of performance might lead to one or more of the following consequences [79]:

- Death or serious injury to people
- Loss or severe damage to equipment
- Environmental harm

The items from this are also treated with special attention in the redundancy philosophy presented below. The list of safety critical functions includes the following items:

- Primary flight controls
- Main landing gear
- Nose landing gear
- High-lift devices
- Air-traffic control communication system
- Aircrew life-support system
- Cabin pressurization system
- Engines
- Fuel system
- Hydraulic system
- Primary flight instruments
- Brakes
- Emergency exits
- Emergency oxygen supply
- Wing structure
- Fuselage structure
- Anti-icing system
- Central flight computer
- Fly-by-wire system

Redundancy Philosophy

The redundancy philosophy has been applied in order to ensure that the aircraft will remain controllable when multiple systems fail. Four layers of redundancy will be applied to the primary flight controls. The layers of redundancy will be supplied by the hydraulic systems, while a further two layers will be provided by the electrical actuators.

Moreover, the fuel system has a triple layer redundancy built in. This system allows the engines to keep operating normally even when two fuel systems fail. The fuel pumps of these systems will also be driven by different electrical systems, allowing the fuel system to remain operational when a power system fails.

The hydraulic system also features two redundant systems to all vital aircraft subsystems. Additionally, the electrical system features several layers of redundancy as well. All these redundancy characteristics have been laid out in more detail in Subsections 7.2, 7.3 and 7.4.

The basic philosophy behind the redundancy is that all important aircraft systems feature at least a double level of redundancy. The vital flight controls will all feature four levels of redundancy and the engines feature three levels of redundancy. This philosophy will ensure that the aircraft is controllable and stable in all situations.

CS-25 Compliance

The requirements on safety as laid out by EASA in the CS-25 regulations document [6] have been met in order to provide a great level of safety. Not all individual requirements will be mentioned here, as they are beyond the scope of this report. However, the following paragraph will elaborate upon the requirements on emergency doors and evacuation devices.

In Figure 8.36[22], the position of the (emergency) doors and the evacutation devices are depicted. In this figure, only the left part of the aircraft is shown. It has to be noted that this layout is perfectly symmetrical about the centerline of the aircraft. A second note that has to be made is the fact that in this picture, there are two overwing exits on each side of the aircraft. Because the aircraft that was designed has a high wing, these will be underwing exits instead, but their position remains the same. The exits on the front (door 1), behind the wing (door 3) and at the back (door 4) are all type I doors according to the CS-25 stipulations[23]. The two underwing exits (forward and aft) are type III exits. The amount and dimensions of the emergency exits are chosen so that they are compliant with the corresponding CS-25 stipulations.

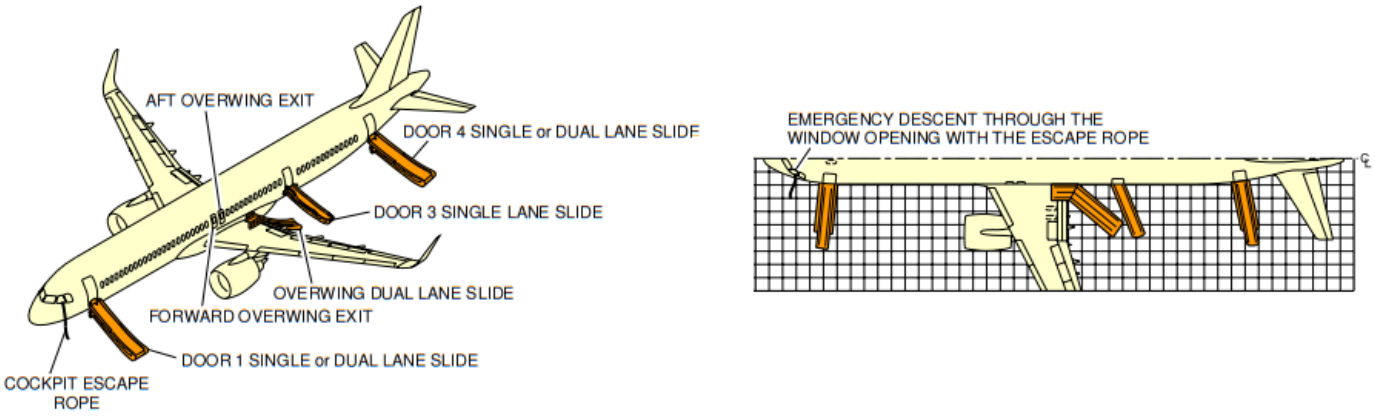

Figure 8.36: Layout of (emergency) doors and evacuation devices[22]

8.5. Cost Analysis

In order for the aircraft to compete with the current inter-European state-of-the-art, it must be cost-effective. In the following sections, the cost breakdown structure is explained. Hereafter, the development and production cost, market price, market share, direct operating cost will be estimated. Following from this, the return of investment is determined.

8.5.1. Cost Breakdown Structure

The total cost incurred on aircraft program, the life cycle cost, can be broken down into the development cost (research development, test, and evaluation), acquisition cost, operating cost, and disposal cost. The cost breakdown structure is given in Figure 8.37. The acquisition cost is the sum of the production cost and the manufacturer's profit. The acquisition cost, together with the development cost and the number of aircraft produced, determines the unit price per aircraft. The operating costs include among others the maintenance and fuel costs. In order to make the aircraft attractive for airlines to buy, the direct operating cost should be kept as low as possible.

[22] https://www.airbus.com/content/dam/corporate-topics/publications/backgrounders/techdata/aircraft_characteristics/Airbus-Commercial-Aircraft-AC-A321-Feb18.pdf [cited 14 June 2018]

[23] https://www.easa.europa.eu/sites/default/files/dfu/agency%2measures%2docs%2certification%2specifications%2CS%225%200%2CS%225%2Amdt%212%2Change%2Information.pdf [cited 14 June 2018]

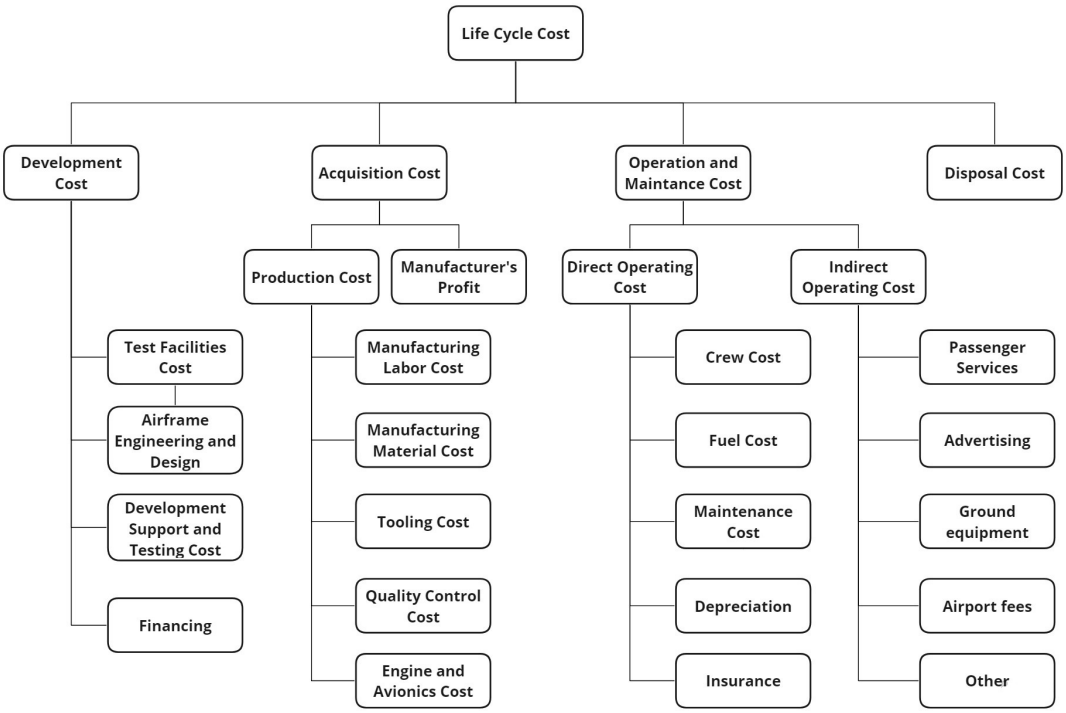

Figure 8.37: Breakdown of the Aircraft's Life Cycle Cost

8.5.2. Development and Production Cost

The combined development and production cost in US dollars of the aircraft are estimated using statistical cost estimating relationships of the RAND DAPCA IV model as suggested by Raymer [29]. As this is the cost invested by the manufacturer, it is referred to as the investment cost (C_{inv}). This cost model is given by Equation 8.69.

$$C_{inv} = H_E R_E + H_T R_T + H_M R_M + H_Q R_Q + C_D + C_F + C_M + C_e N_e + C_{avionics} \tag{8.69}$$

The factors this equation are the labor hours for production, hourly rates, development support costs, materials cost, engine cost and avionics cost. These are estimated using statistical equations that use empty weight and cruise speed as input. Raymer recommends to increase the hours and cost estimates by about 30% for advanced advanced designs. The estimated hours are based on aluminum aircraft, however the TU-ecoliner is build mainly from CFRP. Therefore, a fudge factor of 1.3 is applied to the estimated labor hours. Lastly, the costs are multiplied by a factor of 1.51 to take into account the inflation from 1999 to 2018. The components contributing to the development and production cost are presented in Table 8.19. The estimated investment cost is:

$$C_{inv} = 33,287,983,292 = 33.3\,\text{billion USD} \tag{8.70}$$

Table 8.19: Breakdown of the development and production cost

Cost component	**Symbol**	**Cost [USD]**
Engineering	$H_E R_E$	6,477,441,334
Tooling	$H_T R_T$	8,096,575,743
Manufacturing	$H_M R_M$	12,501,576,557
Quality control	$H_Q R_Q$	2,767,386,662
Development support	C_D	463,706,444
Flight test	C_F	188,224,288
Materials	C_M	2,761,314,196
Engine	$C_e N_e$	6,191,198
Avionics	$C_{avionics}$	25,566,866
Total	C_{inv}	33,287,983,292

8.5.3. Market Price

To estimate a reasonable purchase price of a single aircraft, statistical from reference aircraft are used. Sforza [47] proposes a relation between empty weight in pounds and total aircraft cost (TC) based on the price and weight data of 32 Boeing and Airbus aircraft, including the current state of the art such as the Airbus 321neo and the Boeing 787-10. This correlation is given by Equation 8.71. It gives the purchase price in millions of US dollars.

$$TC = 1.1 \cdot 425 \cdot erf\left[\frac{W_e - 10^4}{4.5 \cdot 10^5}\right] \tag{8.71}$$

The factor 1.1 is used to inflate the price from 2012 to 2018. The resulting purchase price is 85.2 million USD.

8.5.4. Market Share

To determine the market share of the aircraft, the market analysis (Chapter 2) was consulted, in conjunction with an estimated market share based on the current competition. Over the next 20 years, Boeing and Airbus estimate deliveries of 5,880 and 5,249 single aisle aircraft, respectively [5, 13], in Europe alone. Furthermore, considering 4% will be regional jets with less than 100 seats, and that larger members of the Boeing and Airbus single aisle category account for approximately 98% of family deliveries [15], it is conservatively estimated that around 5170 aircraft in the large single aisle category are forecast to be delivered.

Of the current single aisle aircraft produced by Airbus, 31% of total European orders are in the 230-240 seat category[24]. Assuming this value is representative of the market demand for aircraft in the 230-240 seat category, 1600 aircraft in the TU-ecoliner's segment are forecast over the next 20 years, or 80 aircraft per year.

With the A321neo's dominating the 240 seat market, and a 737MAX series equivalent due for entry in 2020[25], it is assumed that the 230-240 seat market will be composed of the A321neo, the 737MAX 10 (230 seats) and the TU-ecoliner. The market share estimates for these aircraft are 40% and 20% respectively [15]. Thus, an estimated market share of 40% is allocated to the TU-ecoliner in the 230-240 seat market.

Taking the time frame into account (and assuming constant demand), in 15 years when the TU-ecoliner enters service, it will have a 40% market share of the 80 aircraft (in the 230-240 seat segment) per year, for 5 years. This results in demand for 32 TU-ecoliner's per year, or 960 TU-ecoliners over 30 years, the intended model production period.

8.5.5. Direct Operating Cost

In this report, the variable costs considered as Direct Operating Cost are the fuel cost, maintenance cost, flight crew cost, depreciation, and insurance cost, as can be seen in the Cost Breakdown Structure. The DOC is defined as cost per block hour. The block time is the time between brake release at the departure airport to setting the breaks at the destination. A ground maneuvering time of 21 minutes is added to the flight time to determine the block time. A flight time of 145 minutes or 2.42 hours is taken for a typical mission of 1800 km. The block time of a mission is then:

$$t_b = t_f + 21/60. = 2.42 + 0.35 = 2.77 \text{ hr} \tag{8.72}$$

The maintenance cost were estimated using elaborate cost estimating relations used by Sforza [47], who uses the approach of developed by the Air Transportation Association of America and adjusted it for the current application. With these estimating relations, the labor cost and materials cost for airframe and engine maintenance can be determined using the empty weight in pounds, take-off thrust, engine cost, labor rates, and block time as input.

$$C_{maint} = C_{af,labor} + C_{af,material} + C_{eng,labor} + C_{eng,material} = 242.0 + 390.6 + 127.8 + 53.9 = 814 \text{ USD/hr} \tag{8.73}$$

[24] `http://www.airbus.com/aircraft/market/orders-deliveries.html` [cited 26 June 2018]
[25] `https://www.boeing.com/commercial/737max10/index.page` [cited 24 June 2018]

The fuel cost per hour during flight can be found by simply multiplying the fuel cost per second found in Figure 8.31 by 3600. The cost of fuel per flight is determined by multiplying this result by the flight time, because no fuel is burned during ground maneuvering due to the electric green taxiing system. The fuel cost per block hour can then be calculated by dividing this by the block time. This fuel cost assumes the jet fuel price of 1.69 dollar per gallon, which translates into a fuel cost per second of 0.61 UDS/s with an average fuel consumption of 1.12 kg/s as determined in Section 8.3.2.

$$C_{fuel} = \frac{0.61 \cdot 3600 \cdot 2.42}{2.77} = 1{,}919 \text{ USD/hr} \tag{8.74}$$

The flight crew cost per block hour is estimated using Equation 8.75 from [47], assuming a two-man crew, inflated from 2012 to 2018.

$$C_{crew} = 1.1\left(\frac{W_{to}}{1000} + 697\right) = 820 \text{ USD/hr} \tag{8.75}$$

The depreciation per year is estimated by assuming that the resale value is 10 % of the market price which is depreciated over the 30 years of aircraft lifetime. This value is divided by the total ammount of block hours per year in which it is assumed that the aircraft performs six flights per day.

$$C_{dep} = \frac{0.9TC/30}{2.77 \cdot 6 \cdot 365} = 411 \text{ USD/hr} \tag{8.76}$$

The insurance cost is assumed to add 1 % to the direct operating costs.

The same calculations have been done for two other aircraft that operate on the target routes. The input values that change are the cruise Mach number, empty weight, take-off weight, fuel consumption, unit price, and take-off thrust. All other variables, such as block time have been kept constant, in order to compare the DOC of the TU-ecoliner to other aircraft performing the same mission. The results are presented in Table 8.20. The DOC is divided by the ammount of seats available to determine the DOC per seat hour. It can be observed that the Airbus A321neo and Boeing 737MAX9 have similar DOC per seat hour. The TU-ecoliner has reduction in DOC per seat hour of 26 % compared to the Airbus A321neo .

Table 8.20: Comparison of the DOC with other aircraft

Cost in USD per block hour	Fuel	Crew	Maintenance	Depreciation	Insurance	Total DOC	DOC per seat hour
A321neo	2,909	845	1,053	557	53	5,419	22.58
B737MAX9	2,910	838	958	497	52	5,255	23.89
TU-ecoliner	1,918	820	814	411	39	4,004	16.69

8.5.6. Return on Investment

With the development and production cost, market price, and market share known, the Return of Investment of the aircraft program can be calculated for the manufacturer using the definition of ROI given by Equation 8.77. With the values for the development cost and number of aircraft sold determined in Section 8.5.2 and 8.5.4, a total profit of about 146 % of the initial investment in development and production will be made.

$$ROI = \frac{N_s \cdot TC - C_{inv}}{C_{inv}} = \frac{960 \cdot 85{,}222{,}886 - 33{,}287{,}983{,}292}{33{,}287{,}983{,}292} = 1.458 \tag{8.77}$$

8.6. Risk Assessment

The following section describes the technical risks that may occur during the design phase. It is important to identify these risks early in the design process to mitigate them during the design. Table 8.24 shows the risks associated with each department, where 1 stands for the Flight Performance & Propulsion group, 2 for Stability & Control group, 3 for the Structures group and 4 for the Aerodynamics group. The M stands for miscellaneous and can not be assigned to a department. The table includes the level of impact (I) and likelihood (L) of each risk. Impact is from negligible (1) to catastrophic (4). Likelihood is scored from nearly impossible (1) to very likely (6). An identifier based on the design concept number has been assigned to every risk. This results in the risk map shown in Table 8.22. For every risk a mitigation strategy is implemented. The risk map incorporating the mitigation strategies is presented in Table 8.23.

Table 8.21: Color chart

color	green	yellow	red

Table 8.22: Risk map of the technical risks before mitigation

Likelihood \ Impact	Negligible	Marginal	Critical	Catastrophic
Very likely			R.A.2	
Likely		R.4.1		R.M.4
Plausible		R.A.4	R.3.2, R.M.2	R.A.1, R.A.3, R.M.1
Unlikely			R.1.1, R.3.1	R.2.1, R.3.3
Very unlikely				
Nearly impossible				

Table 8.23: Risk map of the technical risks after mitigation

Likelihood \ Impact	Negligible	Marginal	Critical	Catastrophic
Very likely				
Likely				
Plausible	R.M.2	R.M.1		
Unlikely		R.A.4, R.3.2, R.4.1	R.A.2	R.A.1, R.A.3
Very unlikely		R.M.4	R.1.1, R.3.1	R.2.1, R.3.3
Nearly impossible				

Table 8.24: Risk analysis for design concepts

Department	ID	Cause	Event	Consequence	L	I	Mitigation
1,2,3,4	R.A.1	For simplification purposes, assumptions have to be made for calculations	Incorrect assumption	Calculation is incorrect/Aircraft has to be redesigned	4	4	Only make assumption if it is according to research/ Validate the assumption
1,2,3,4	R.A.2	Calculations are done through a programmed code	Code does not calculate the intended	Calculations are false	5	3	Perform verification/validation on the program
1,2,3,4	R.A.3	Aircraft has to comply with CS-25	Fails to meet CS-25 requirements	Aircraft fails certification	3	4	Take into account regulations when setting up requirements and keep track of them throughout the design process
1,2,3,4	R.A.4	Requirement is set up at the start of the project	Requirement is not met	Aircraft is not designed as intended	4	3	Keep track of requirements throughout design process
1	R.1.1	Engine design is a trade-off (e.g. between noise and emission)	The design has been optimized for a single aspect	User requirement will not be met on the other aspect	3	3	Keep into account requirements during design choices
2	R.2.1	Aircraft has to be designed for control & stability	The design has been optimized for a single aspect	The aircraft is controllable but not stable or vice versa	3	4	Find the balance between controllability and stability
3	R.3.1	Wings have to be integrated with the fuselage	During design the integration of wing with fuselage is not taken into account	Wings do not integrate with fuselage/Aircraft has to be redesigned	3	3	System engineer keeps overview on the components and integration of them
3	R.3.2	Implementation of CFRP on the strut	CFRP is weak in buckling	Excess of material is necessary resulting in weight and cost increase	4	3	Use a different material on the strut
3	R.3.3	Implementation of CFRP on the majority of the aircraft	Misalignment of the fibers during production	Structure will fail	3	4	Use safety factors during calculations
4	R.4.1	Aircraft wings are supported by a strut	Struts adds too much drag	The implementation of a strut is not feasible	5	2	Aerodynamically shape the strut to minimize the drag
	R.M.1	Implementation of electric actuators on primary flight controls	Use of electric actuators on primary flight controls have not been implemented yet	The electric actuators could show reliability issues after extensive use	4	4	Use them as a redundant system only, so that it is only used if the primary actuator system fails
	R.M.2	EGTS system is used for taxiing	The system fails during taxiing	Aircraft will hold up the taxiway	4	3	Use the engines to taxi when the EGTS system failed
	R.M.3	Implementation of Hybrid Laminar Flow Control system	System does not function properly due to contamination	Aircraft drag is increased	5	4	Deploy slats during landing and take-off to mitigate the contamination
	R.M.4	Removal of the APU	A redundant system is removed	During failure the redundant system cannot be used	5	4	Implement a different redundant system such as an extra pack of batteries

8.7. Resource Budget Breakdown

First of all, the mass distribution of the final design is presented below in two pie charts. Beneath the two charts Table 8.25 shows the comparison of the new masses of the aircraft wing and fuselage with respect to the masses from mid term report. It should be noted that the skin of the wing is overdesigned as the stringers have yet to be designed. The drag budget breakdown can be found in table 6.4.

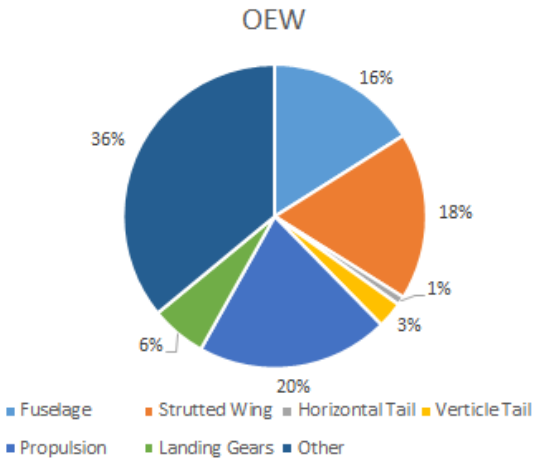

Figure 8.38: Mass distribution of the final design at OEW condition

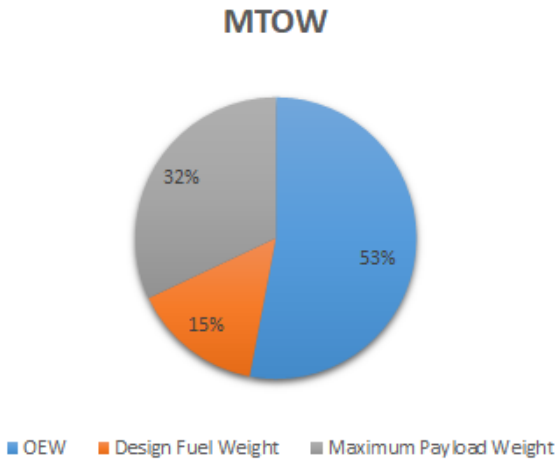

Figure 8.39: MTOW distribution of the final design at maximum payload condition

Table 8.25: Detailed Mass Distribution of designed components

Strutted Wing (both)						**Horizontal Tail**		**Landing Gear**	
Component	Skin	Stringers	Ribs	Spars	Strut	Wingbox	Other	Nose	Main
Mass (kg)	5,197	NA	86.6	708	138	114	205	204	1,837
Fuselage						**Propulsion**		**Other**	
Component	Skin	Stringers	Floor	Frames		Engines	Nacelles	12,375	
Mass (kg)	810	1,704	1,213	1,803		6,385	667		

9

Design Rationale

9.1. Requirement Compliance and Feasibility Analysis

A compliance matrix is presented below showing the requirements that have been satisfied for the design of this project. This is shown below in three tables, the first presenting the stakeholders' requirements in Table 9.1, second presenting the product (entire aircraft) requirements in Table 9.2, and lastly the system and subsystem requirements in Table 9.3[1].

Table 9.1: Compliance matrix of stakeholder requirements

Requirement	Check?	**Requirement**	Check?	**Requirement**	Check?
Stakeholder - Airlines					
HF-STK-AL-01	✓	HF-STK-AL-02	✓	HF-STK-AL-03	✓
HF-STK-AL-04	✓	HF-STK-AL-05	✓	HF-STK-AL-06	✓
HF-STK-AL-07	✓	HF-STK-AL-08	✓	HF-STK-AL-09	✓
HF-STK-AL-10	✓	HF-STK-AL-11	✓	HF-STK-AL-12	✓
HF-STK-AL-13	✓				
Stakeholder - Autorities					
HF-STK-AU-01	✓	HF-STK-AU-02	✓	HF-STK-AU-03	✓
Stakeholder - Airports					
HF-STK-AP-01	UN	HF-STK-AP-02	UN	HF-STK-AP-03	✓
Stakeholder - Passengers					
HF-STK-PS-01	UN	HF-STK-PS-02	UN	HF-STK-PS-03	✓

Table 9.2: Compliance matrix of product requirements

Requirement	Check?	**Requirement**	Check?	**Requirement**	Check?
Pre-flight operations system					
HF-PROD-PFOPS-01	✓	HF-PROD-PFOPS-02	✓	HF-PROD-PFOPS-03	✓
Ground Operations					
HF-PROD-GO-1	✓				
Flight					
HF-PROD-FLT-01	✓	HF-PROD-FLT-02	✓	HF-PROD-FLT-03	UN
HF-PROD-FLT-04	✓	HF-PROD-FLT-05	UN	HF-PROD-FLT-06	✓
HF-PROD-FLT-07	✓	HF-PROD-FLT-08	✓	HF-PROD-FLT-09	✓
HF-PROD-FLT-10	✓	HF-PROD-FLT-11	✓		

[1] ✓ :Requirement Passed, X: Requirement Failed, UN:Unknown

Table 9.3: Compliance matrix of system and subsystem requirements

Requirement	Check?	**Requirement**	Check?	**Requirement**	Check?
Wing					
HF-SYS-WING-01	✓	HF-SYS-WING-02	✓	HF-SYS-WING-03	✓
HF-SYS-WING-04	✓	HF-SYS-WING-05	✓		
HF-SYS-WING-BOX-1	✓	HF-SYS-WING-BOX-2	✓	HF-SYS-WING-BOX-3	✓
HF-SYS-WING-HLD-1	✓	HF-SYS-WING-HLD-2	✓	HF-SYS-WING-HLD-3	✓
HF-SYS-WING-AIL-1	✓	HF-SYS-WING-AIL-2	✓		
Propulsion					
HF-SYS-PROP-01	✓	HF-SYS-PROP-02	✓	HF-SYS-PROP-03	✓
HF-SYS-PROP-FUE-01	✓	HF-SYS-PROP-FUE-02	✓	HF-SYS-PROP-FUE-03	✓
HF-SYS-PROP-FUE-04	✓				
Landing Gear					
HF-SYS-LG-01	UN	HF-SYS-LG-02	✓	HF-SYS-LG-03	✓
HF-SYS-LG-04	✓	HF-SYS-LG-05	✓	HF-SYS-LG-06	✓
Fuselage					
HF-SYS-FUS-01	✓	HF-SYS-FUS-02	✓	HF-SYS-FUS-03	✓
HF-SYS-FUS-04	✓	HF-SYS-FUS-05	✓	HF-SYS-FUS-06	✓
HF-SYS-FUS-CL-01	✓	HF-SYS-FUS-CL-02	✓	HF-SYS-FUS-CL-03	✓
HF-SYS-FUS-FL-01	✓				
HF-SYS-FUS-ST-01	✓	HF-SYS-FUS-ST-02	✓	HF-SYS-FUS-ST-02	✓

As you may see in the compliance tables above, most of the requirements have been met. A requirement that has not been checked is the floor failure. The design of the floor is planned in detailed structural analysis in the post-DSE activities of the project (see Section 10.3).HF-STK-AP-01 and HF-STK-AP-02 are not clear due to the fact that specific list of airports and gates have not been determined. A list of gate dimensions and runway clearances for all desired airports from the airliner would be incorporated in the final design on the aircraft. HF-STK-PS-01 (passenger comfort) is not clear as the fuselage dimensions are set to a minimum. Customer testing is necessary to implement accurate comfort feedback with seat position and quality. HF-PROD-FLT-03 must be verified building a CFD analysis of the aircraft to evaluate the dynamic stability of the aircraft.HF-SYS-LG-01 must be verified by detailing the brake design and the brake system in the future DSE activities.

9.2. Sustainable Development Strategy

Nowadays, sustainable development is assuming a more central role in society. In 2015 the United Nations (UN) formulated 17 Sustainable Development Goals[2] (SDGs) in order to protect the planet from human actions and consumption.

In the "Brundtland Report", a report of the World Commission on Environment and Development, sustainable development is defined as follows:

"Development that meets the need of the present without compromising the ability of future generations to meet their own needs."[80]

Looking at the practical definition of sustainability, the concept touches upon different disciplines: technical or environmental, economic and social sustainability. This project will primarily focus on technical or environmental sustainability. Despite this, the economic and social aspects should not be disregarded.

When considering the aviation industry, it is evident that three SDGs are directly applicable: 'industry, innovation and infrastructure', 'responsible consumption and production' and 'climate action'. It is apparent that addressing the aviation sector is an important target in the process towards a more sustainable world. Especially considering the forecast growth of the industry [81]. At the current rate, aircraft CO_2 emissions are expected to grow by up to 300% by 2050[3]. Therefore, sustainable development is considered a high priority in this aircraft design process.

[2] `https://www.un.org/sustainabledevelopment/sustainable-development-goals/` [cited 3 May 2018]

[3] `https://www.icao.int/environmental-protection/GIACC/Giacc-4/CENV_GIACC4_IP1_IP2%20IP3.pdf` [cited 21 June 2018]

9.2.1. Sustainable Approach

In this section, first the environmental sustainability is discussed. After that, economic and social sustainability is touched upon.

Environmental Sustainability

The primary purpose of designing this aircraft is to see how far we can get in decreasing the environmental impact of an aircraft within a generation. This is a clear indication of the central role that sustainability plays in this project. It has been concreted by requirements such as ***HF-STK-AL-10***[4] and ***HF-STK-AL-12***[5] [3]. From now on the term "environmental impact" will cover both noise and emissions, unless specified otherwise. The emissions include all the emissions produced during production, operation and disposal of the aircraft. The sustainable framework is visible throughout the entire project approach [2].

To start off with, the range is specified so that approximately 90% of inter-European flights can be performed, thereby preventing that the aircraft range is over-designed. This will lead to a lower fuel consumption. The environmental impact of the aircraft is further reduced by a lower total fuel weight, keeping the aircraft weight lower, resulting in a lower thrust requirement for a particular thrust-over-weight ratio. A lower thrust requirement has a positive influence on the emissions of the aircraft [82]. All together, this will make the aircraft considerably more sustainable than its competitors.

The life cycle of the product consists of the selection of the materials, manufacturing, operational phase, optimization of lifetime and lastly end of life (EOL). The material shall be selected such that most of the aircraft is recyclable and non-hazardous. Alternative materials with lower environmental impacts (carbon footprint, recyclability, renewability, etc.) shall always be selected. The manufacturing phase will be strongly based on the LEAN manufacturing philosophy. Where, all steps will be optimized for minimum waste of energy and resources. Moreover, manufacturing will be centralized as much as possible in order to minimize the carbon footprint due to transportation. The lifetime shall be optimized by designing for easy and quick repairability with access to the regions that are either prone to failure or parts that must be checked regularly. The environmental impact and noise of the operational phase (along with the points mentioned in the preceding paragraphs) shall be minimized by selecting the most efficient off-the-shelf engines for the N+1 generation.

In the end-of-life phase, major emphasis will be put on the recycling of the aircraft. Currently, around 80% - 85% of an aircraft can be recycled [83]. These recycled parts have an estimated value of between $1,000,000 - $3,000,000, where the engines are the most valuable parts [10]. For the TU-ecoliner significant efforts will be made in order increase both the percentage of recycled materials and the value of these materials. The benefit of these efforts will be twofold. On the one hand, recycling of the aircraft materials will lower the overall impact on the environment, while providing a sustainable supply of high quality materials. On the other hand, increasing the value of recycled parts provides a strong and clear incentive for operators to renew their fleet in a timely and sustainable manner, focusing heavily on recycling. In order to achieve these goals, the design team will work in accordance with the BMP guidelines and the AFRA accreditation [10].

Economic and Social Sustainability

For social sustainability, the following definition is found:

"*Social sustainability is the enduring, harmonious quality of life of people affected and affecting a project, program, product, or process.*"[6]

For the TU-ecoliner this relates to all stakeholders of the project. These include, but are not limited to, passengers, aircraft operators, maintenance personnel, operating crews, engineers, near-airport residents and policy makers. These can be split up into three main groups of stakeholders, pre-operational stakeholders, externally influenced stakeholder and the operational stakeholder.

[4] The aircraft shall be at least 1 noise class lower compared to current inter-European state-of-the-art aircraft.

[5] The aircraft shall have an emissions reduction of at least 10% compared to current inter-European state-of-the-art aircraft.

[6] `https://clas-pages.uncc.edu/inss/blog/2013/08/15/social-sustainability-from-an-engineers-perspective/` [retrieved on 14-5-2018]

The pre-operational stakeholder group consists of all people involved in the design, testing and manufacturing of the aircraft. For this group social sustainability will mainly be realized by complying with the European Labour Law[7], which defines rights and obligations for both employers and employees. All designing, testing and manufacturing of the aircraft shall be carried out in compliance with this law. The company behind the TU-ecoliner will enforce this compliance within the own company but also within external companies and partners.

Externally influenced stakeholders encapsulate all people that are in any way affected by the aircraft but do not have a direct say in the way it is operated. These are the people living around airports or under the approach and departure routes. Social sustainability for these people means that their worries and complaints are taken seriously and that together with them a sustainable solution is found to ensure they live in harmony with the aircraft. Special emphasis has been put on reducing aircraft noise and emissions.

Operational stakeholders include the passengers, maintenance personnel, legislators and aircraft operating personnel. For these stakeholders, social sustainability is mainly achieved by designing and building a safe, maintainable and comfortable aircraft in accordance with international legislation.

For this aircraft, economic sustainability is achieved by ensuring that the entire supply chain, from the raw material supplier up to aircraft operators, can sustain a profitable operation. Besides this the project seeks to lower the direct operating cost in an effort to make flying more accessible.

[7] `http://ec.europa.eu/social/main.jsp?catId=157&langId=en` [cited 21 June 2018]

10 Outlook

In this chapter, the future of the project will be outlined. First, in Section 10.1, the manufacturing, assembly and integration plan will be discussed. After that, in Section 10.2, the project design and development logic is elaborated on. Finally, in Section 10.3 the planning for the post-DSE phase of the project is elaborated on.

10.1. Manufacturing, assembly and integration plan

In Figure 10.1 the manufacturing, assembly and integration (MAI) plan is depicted. It shows a time ordered outline of the activities required to construct the product from its constituent parts. The process of constructing an aircraft starts with manufacturing the small parts such as rivets, bolts, stringers or spars. Simultaneously, or in some cases maybe earlier, the parts and subsystems that are not made by the manufacturer itself need to be ordered. Some parts or subsystems take a while to be produced and thus delivered. When all parts of a certain assembly are there, the assembling can begin. First, subsub assemblies such as the wingbox, skin panels or flaps are made, which are then used to make the sub assemblies such as the fuselage sections, the wing sections or the landing gear. After that, these sub assemblies are combined into a final assembly of which the complete aircraft is the output. Next, the aircraft needs a layer of paint. The final step is also the most important step, namely flight testing. Without proper tests the safety cannot be guaranteed. After it passed the flight tests, the aircraft is ready to be delivered to the customer.

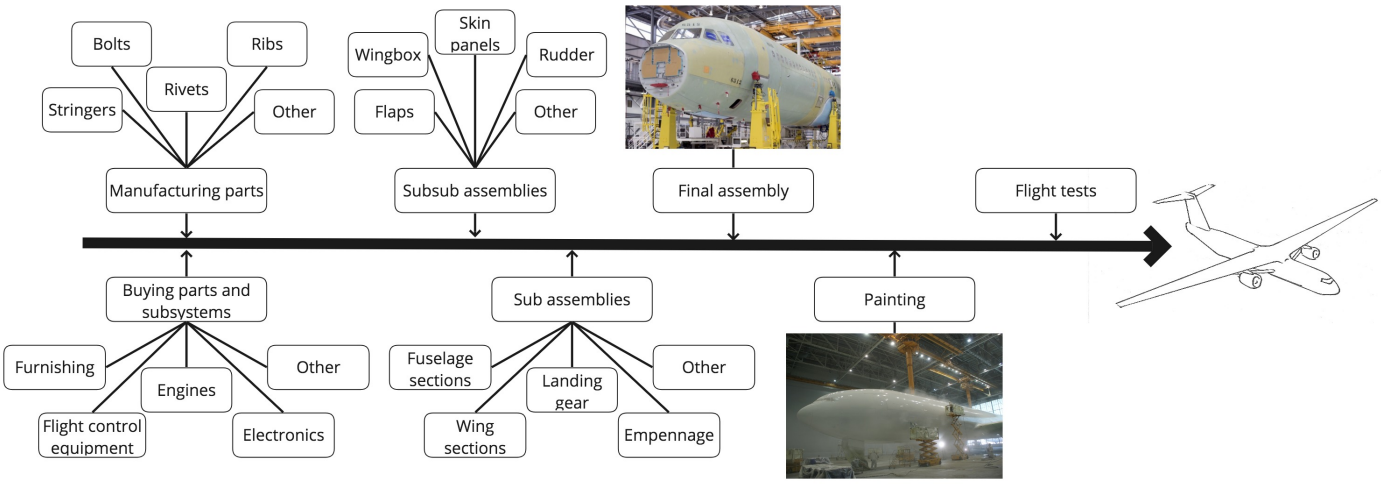

Figure 10.1: Manufacturing, Assembly and Integration Plan

10.2. Project Design and Development Logic

The project design and development logic is a flow chart that shows the logical order of activities as they are executed in the post-DSE phases of the project and can be seen in Figure 10.2. The green boxed are the top level of the diagram and provide the general guideline. They are structured in chronological order from left to right. It starts with design and goes through the whole process, until the first aircraft is delivered to the customer. The yellow boxes provide the second level of detail and are given per green box in chronological order. It provides more detail on what is meant with the bigger tasks in the green boxes. For example, the Design starts with iterating the preliminary design. Then the detailed design is made and also the tooling and production process is laid out. The arrows connecting the boxes indicate wether the tasks are performed in series or in parallel. The tasks given in the project design and development logic will be further detailed in the project Gantt chart which will be elaborated on in Section 10.3.

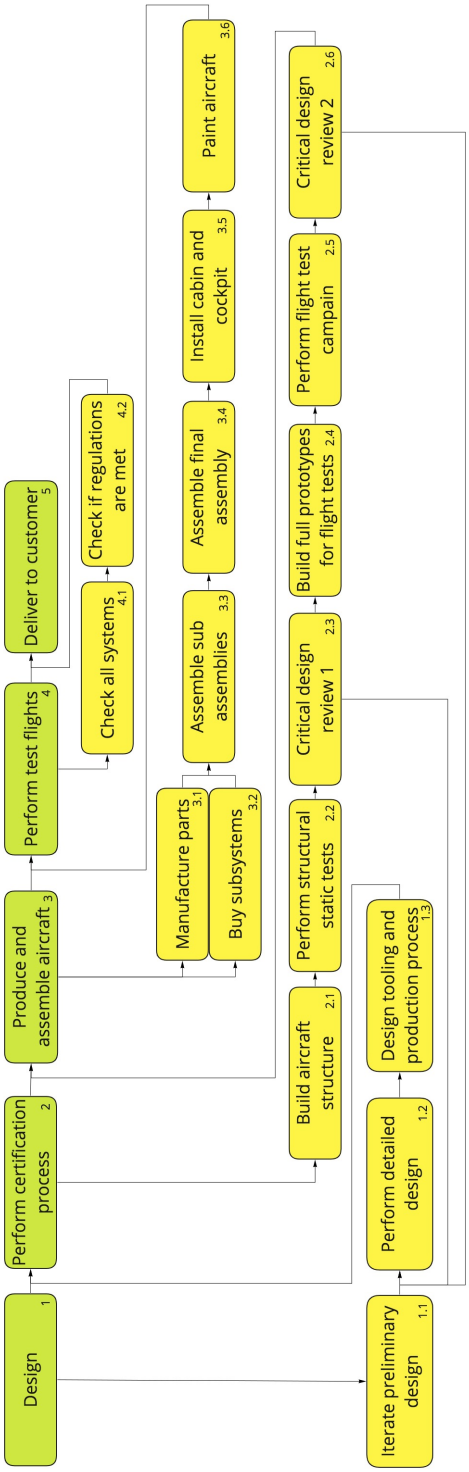

Figure 10.2: Project design and development logic diagram

10.3. Post-DSE Planning

In Figures 10.3 and 10.4, the project Gantt chart can be seen. This gives the post-DSE activities presented in the project design and development logic in more detail. They are also assigned a duration. The tasks for the test flight campaign were taken from the airbus test flight program[1]. The planning is made such that the first aircraft is delivered within 15 years as given in the requirements. As the planning is now, there is one year of contingency for delays along the road.

WBS	Task Name
1	**Design**
1.1	Iterate preliminary design
1.1.1	Configuration frozen
1.2	**Detailed design**
1.2.1	Wing design
1.2.2	Tail design
1.2.3	Fuselage design
1.2.4	Propulsion design
1.2.5	Landing gear design
1.2.6	Equipment and subsystem design
1.2.7	Control surface design
1.2.8	Detailed design complete
1.3	**Design of tooling and production process**
1.3.1	Design of assembly fixtures
1.3.2	Scheduling of production of parts
1.3.3	Scheduling of assembly of parts
1.4	Ready for building
2	**Certification process**
2.1	Build aircraft structure
2.2	**Structural static tests**
2.2.1	Flight test installation calibration test
2.2.2	Fuselage pressure test
2.2.3	Maximum wing bending at limit load
2.2.4	Ailerons and spoilers funtcioning test during max wing bend
2.2.5	Fatigue tests and flight cycles simulatin
2.3	Critical design review 1
2.4	**Build prototype for flight tests**
2.4.1	Build full prototypes
2.4.2	Calibration of gauges
2.4.3	Cabin pressurization testing
2.4.4	Navigation system testing
2.4.5	Prototypes ready for flight tests
2.5	**Flight test campain**
2.5.1	**Perform flight tests under normal circumstances**
2.5.1.1	General handling qualities assessment
2.5.1.2	Airfield noise emissions assessment
2.5.1.3	Systems operation assessment
2.5.2	**Perform flight tests under extreme weather conditions**
2.5.2.1	General handling qualities assessment
2.5.2.2	Airfield noise emissions assessment
2.5.2.3	Systems operation assessment
2.5.3	**Perform flight tests in failure scenarios**
2.5.3.1	General handling qualities assessment
2.5.3.2	Airfield noise emissions assessment
2.5.3.3	Systems operation assessment
2.5.4	**Further certification flight testing**
2.5.4.1	Water ingestion trails testing
2.5.4.2	Low speed take-off testing
2.5.4.3	Flutter testing
2.5.4.4	Rejected take-off and landing testing
2.5.4.5	Wake vortex trails testing
2.6	Critical design review 2
2.7	Release drawings for production

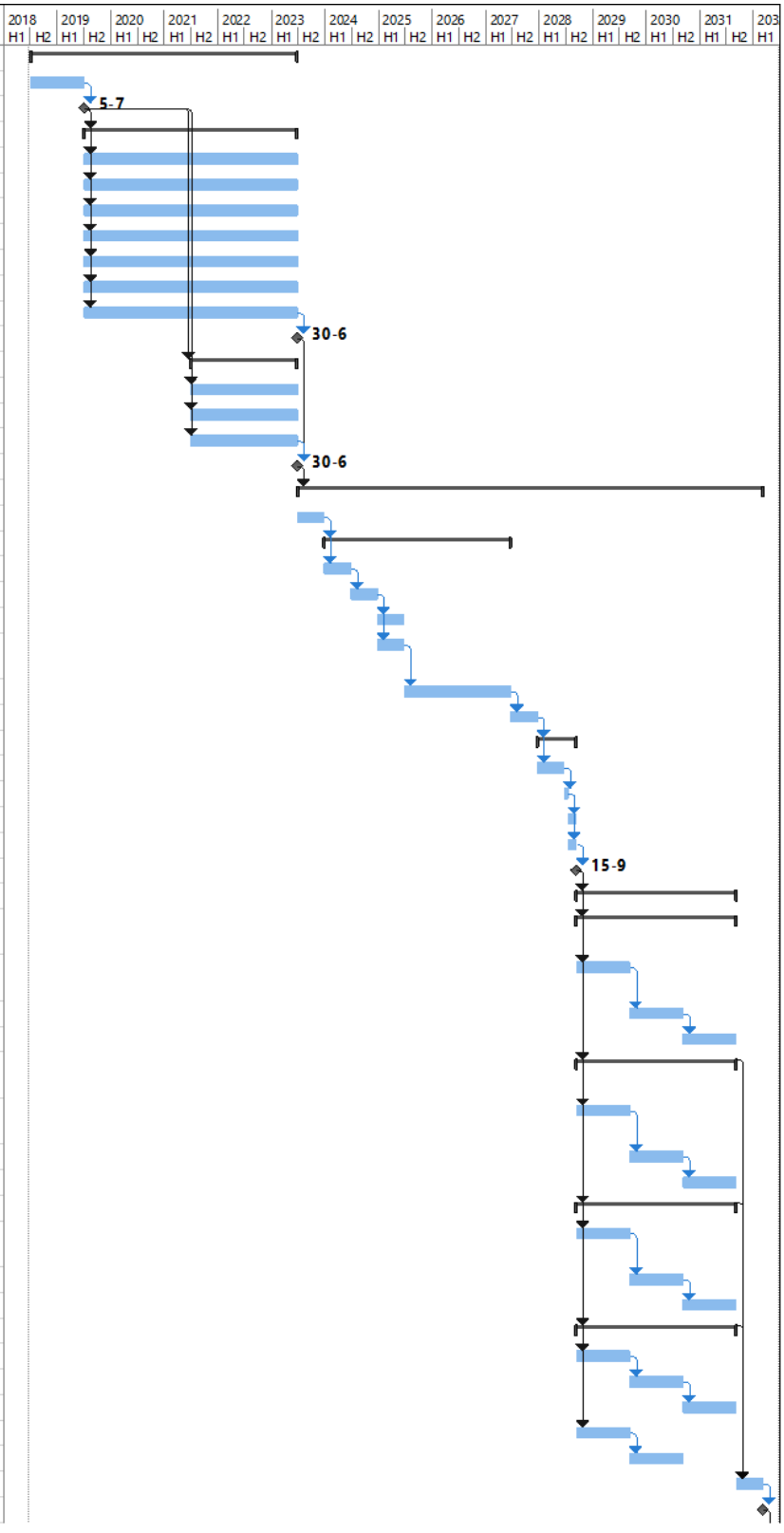

Figure 10.3: Project Gantt chart part 1

[1] http://www.airbus.com/aircraft/how-is-an-aircraft-built/test-programme-and-certification.html [cited 22 June 2018]

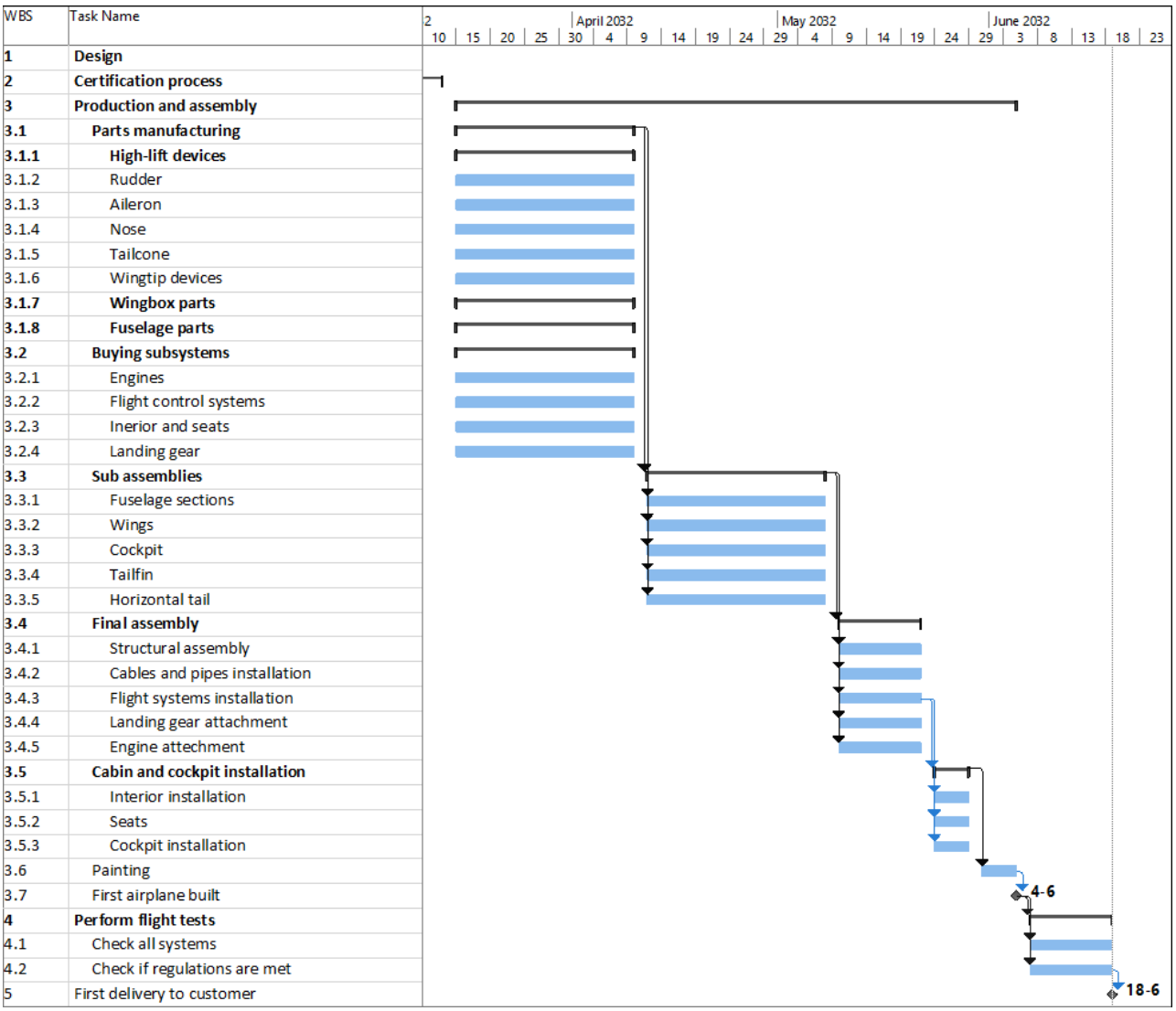

Figure 10.4: Project Gantt chart part 2

11

Conclusion and Recommendations

11.1. Conclusion

The aviation sector accounts for approximately 2% of global CO_2 emissions. Paired with industry's current annual growth rate of approximately 5.3%, the forecast emissions are of serious concern. Currently, an area of avoidable and unnecessary emissions lie in the operation of overdesigned aircraft on short range routes, such as the A321neo flying inter-European routes. These are aircraft capable of flying over twice the typical 2,000 km range. Thus, to address the environmental challenges facing the civil aviation sector, it was decided to optimize an aircraft of comparable capacity to the A321neo, for the shorter, inter-European range.

The TU-ecoliner has been developed with an emphasis on seeing "*How far can we get?*". With the initial goals of reducing emissions, noise and direct operating costs, the design of the aircraft focuses on achieving savings in these areas as much as possible. Designing for a smaller range essentially requires smaller wings, reducing wing weight and fuel required, all of which have a direct, positive impact on operating cost and emissions. Ultimately, as a result of an extensive market analysis, thorough concept trade-off and an in depth detailed design, the TU-ecoliner, compared to the A321neo, boasts 17% reductions in CO_2 emissions, while reducing DOC by 24%, and meeting ICAO Chapter 14 noise regulations.

The TU-ecoliner's improvements in efficiency come from the implementation of several key technologies and concepts. The high, strutted wing configuration allows for the wing to reach the high aspect ratio of 14. The result is a smaller, more efficient wing, with an overall 19% lighter structure, compared to a traditional cantilever wing. Two geared, ultra-high bypass ratio turbo fans power the aircraft. Implementing a gearbox allows the turbofan to reach the ultra-high bypass ratio of 14, which effectively reduces the average exhaust velocity, in turn reducing jet noise and lowering specific fuel consumption by 17%. Furthermore, the gearbox allows the turbine and fan to run at their respective optimal speeds. As such, less compressor and turbine stages are required, reducing overall weight while increasing propulsive efficiency. Finally, the adoption of state of the art technologies and operations with respect to developing a more electric aircraft have been implemented. This includes an EGTS which completely eliminates emissions and noise on the ground, the removal of the APU, and adoption of electric actuators, all contributing to further reductions in weight.

Each of these improvements in performance results in an aircraft optimized for the typical inter-European range. The TU-ecoliner is capable of transporting 240 passengers on over 90% of all European routes, and able to service 10% more airports than the current competition, while producing less emissions, meeting noise restrictions, all at a lower cost.

11.2. Recommendations

The TU-ecoliner presents a genuinely convincing response to the environmental challenges facing the civil aviation sector, while maintaining a commercially attractive profile. However, further refinement of the design is of course possible. As the future of aviation will be especially concerned with emissions, noise, and a gradual shift to fully electric aircraft, additional iterations of the design to further optimize for the design range can be done with a focus on these key aspects. Areas such as the propulsion and wing profile present opportunities where further detailed design would have a significant impact on realizing the TU-ecoliner's potential performance advantages. Further detailing these systems will allow for more accurate noise and emissions assessments. Furthermore, an emphasis on detailing the operational aspects of the aircraft will establish the TU-ecoliner as a truly viable option for the future of clean flying.

Bibliography

[1] Adib E., Aldrige H., Jacobson B., El Uamari H., Burger K., Beyens M., van der Toorn M., Kovacik P., and van der Duim T. "Midterm Report: How Far Can We Get". *Delft University of Technology*, pages Delft,The Netherlands, 2018.

[2] Adib E., Aldrige H., Jacobson B., El Uamari H., Burger K., Beyens M., van der Toorn M., Kovacik P., and van der Duim T. "Project Plan: How Far Can We Get". *Delft University of Technology*, pages Delft,The Netherlands, 2018.

[3] Adib E., Jacobson B., El Uamari H., Burger K., Aldrige H., Beyens M., van der Toorn M., Kovacik P., and van der Duim T. "Baseline Report: 'How Far Can We Get?'". *Delft University of Technology*, pages Delft,The Netherlands, 2018.

[4] International Civil Aviation Organization. "ICAO Environmental Report 2016", 2016.

[5] Airbus. "Global Market Forecast", 2018. URL: http://www.airbus.com/content/dam/corporate-topics/publications/backgrounders/Airbus_Global_Market_Forecast_2017-2036_Growing_Horizons_full_book.pdf [cited 1 May 2018].

[6] European Aviation Safety Agency. "Certification Specifications and Acceptable Means of Compliance for Large Aeroplanes CS-25", 2018. URL: https://www.easa.europa.eu/sites/default/files/dfu/CS-25%20Amendment%2021%20v1.pdf [cited 2 May 2018].

[7] European Aviation Safety Agency. "Certification Specifications and Acceptable Means of Compliance and Guidance Material for Aircraft Noise CS-36", 2016. URL: https://www.easa.europa.eu/sites/default/files/dfu/Annex%20to%20ED%20Decision%202016-002-R.pdf [cited 2 May 2018].

[8] Jenkinson L.R., Rhodes D., and Simpkin P. *"Civil Jet Aircraft Design"*. Arnold, first edition, 1999.

[9] Bertsch E.L. *"Noise Prediction within Conceptual Aircraft Design"*. PhD thesis, German Aerospace Institute, August 2012.

[10] Dwulet L. "AFRA – Leading the Way in Safe and Sustainable Aircraft End-Of-Life Management". In *On Board a Sustainable Future*, pages 196 – 198. ICAO, 2016.

[11] Burzlaff M. "Aircraft Fuel Consumption - Estimation and Visualization". *Hamburg, Germany*, page 62, 2017.

[12] OAG. "Busiest Routes 2018", 2018. URL: https://www.oag.com/hubfs/Free_Reports/Busiest%20Routes/OAG%20Busiest%20Routes%202018-A4.pdf?hsCtaTracking=5cf02a77-684e-42e5-aa7f-d56bbc799a4e%7Cd12dd304-c189-4484-9bf0-590a339253db [cited 8 May 2018].

[13] Boeing. "Current Market Outlook", 2018. URL: http://www.boeing.com/resources/boeingdotcom/commercial/market/current-market-outlook-2017/assets/downloads/2017-cmo-6-19.pdf [cited 1 May 2018].

[14] Bombardier Commerical Aircraft. "Market Forecast", 2017. URL: https://ir.bombardier.com/var/data/gallery/document/01/87/55/05/15/BCA-2017-2036-Market-Forecast-EN.pdf [cited 25 June 2018].

[15] Avolon. "World Fleet Forecast", 2018. URL: http://avolon.aero/wp/wp-content/uploads/2017/10/Avolon_White-paper_Digital-27.10.17.pdf [cited 25 June 2018].

[16] Airbus. "Airbus Family Figures", 2018. URL: http://www.airbus.com/content/dam/corporate-topics/publications/backgrounders/Airbus-Family-Figures-booklet.pdf [cited 1 May 2018].

[17] Melkert J.A. "Project Guide Design Synthesis Exercise 'How Far Can We Get?'", April 2018.

[18] International Civil Aviation Organization. "Annex 16 to the Convention on International Civil Aviation, Volume I Aircraft Noise", 2014. URL: http://dgca.gov.in/intradgca/intra/icao%20annexes/an16_v1_cons.pdf [cited 2 May 2018].

[19] International Civil Aviation Organization. "Annex 16 to the Convention on International Civil Aviation, Volume II Aircraft Engine Emissions", 2008. URL: https://law.resource.org/pub/us/cfr/ibr/004/icao.annex.16.v2.2008.pdf [cited 2 May 2018].

[20] Ahmadpour N., Robert J., and Lindgaard G. "Aircraft passenger comfort experience: Underlying factors and differentiation from discomfort". Elsevier, August 2015.

[21] Roskam J. *"Airplane Design Part V: Component Weight Estimation"*. DARcorporation, 1999.

[22] Torenbeek E. *"Synthesis of Subsonic Airplane Design"*. Kluwer Academic Publishers and Delft University Press, 1982.

[23] Roskam J. *"Airplane Design Part IV: Layout of Landing Gear and Systems"*. DARcorporation, 1986.

[24] Bos A.H.W. *"Multidisciplinary Design Optimization of a Second-Generation Supersonic Transport Aircraft using a Hybrid Genetic / Gradient-Guided Algorithm"*. Delft University of Technology, 1996.

[25] Elham A. "Aerospace Design and Systems Engineering Elements II AE2111-II aircraft part: Aircraft Aerodynamic Analysis - fundamentals". Lecture slides, September 2016. Published by Delft University of Technology.

[26] Anderson J.D. *"Fundamentals of Aerodynamics"*. McGraw Hill Education, fifth edition, 2011.

[27] Sforza P.F. *"Commercial Airplane Design Principles"*. University of Florida, Butterworth-Heinemann is an imprint of Elsevier, first edition edition, 2014. ISBN: 978-0-12-419953-8.

[28] Elham A. "Aerospace Design and Systems Engineering Elements II AE2111-II aircraft part: Aircraft Aerodynamic Analysis - Lift". Lecture slides, September 2016. Published by Delft University of Technology.

[29] Raymer D.P. *"Aircraft Design: A Conceptual Approach"*. AIAA Education Series, third edition edition, 1999. ISBN: 1-56347-281-0.

[30] Krishnan K.S.G., Bertram O., and Seibel O. "Review of Hybrid Laminar Flow Control Systems". *Progress in Aerospace Sciences*, 93:24–52, August 2017. URL: https://doi.org/10.1016/j.paerosci.2017.05.005 [cited 16 May 2018].

[31] Braslow A.L. "A History of Suction-Type Laminar-Flow Control with Empahsis on Flight Research". *Monographs in Aerospace History*, 1(12), 1999.

[32] Elham A. "Aerospace Design and Systems Engineering Elements II AE2111-II aircraft part: Aircraft Aerodynamic Analysis - Drag". Lecture slides, September 2016. Published by Delft University of Technology.

[33] Obert E. *"Aerodynamic Design of Transport Aircraft"*. IOS Press, 2009. Delft University of Technology.

[34] Sforza P.F. *"Commercial Airplane Design Principles"*. University of Florida, Butterworth-Heinemann is an imprint of Elsevier, first edition edition, 2014. ISBN: 978-0-12-419953-8.

[35] Oliviero F. "Systems Engineering and Aerospace Design AE3211-I Requirement Analysis and Design principles for A/C stability & control (Part 2)". Lecture slides, April 2018. Published by Delft University of Technology.

[36] Melkert J.A. and Vos R. "Aerospace Design and Systems Engineering Elements I: Landing Gear and Empennage Design", 2018. URL: https://www.brightspace.tudelft.nl [cited 24 May 2018].

[37] Melkert J.A. and Rans C.D. "Structural Analysis & Design: Buckling", 2018. URL: https://www.brightspace.tudelft.nl [cited 21 June 2018].

[38] Niu M.C.Y. *"Airframe Structural Design"*. Conmilit Press Ltd., 1988.

[39] Hibbeler R.C. *"Mechanics of Materials"*. Pearson, eighth edition, 2011.

[40] Chiozzotto G.P. "Conceptual Design Method for the Wing Weight: Estimation of Strut-Braced Wing Aircraft". Technical report, German Aerospace Center (DLR), 2015.

[41] Melkert J.A. and Vos R. "Wing and Propulsion System Design", 2018. URL: `https://www.brightspace.tudelft.nl` [cited 24 May 2018].

[42] EASA. "TYPE-CERTIFICATE DATA SHEET PW1100G-JM Series Engines". Technical report, European Aviation Safety Agency, 10 August 2017.

[43] EASA. "TYPE-CERTIFICATE DATA SHEET PW1500G Series Engines". Technical report, European Aviation Safety Agency, 27 Februari 2017.

[44] Airbus. "Airbus A320 Aircraft Characteristics - Airport And Maintenance Planning", 2018. URL: `https://www.airbus.com/content/dam/corporate-topics/publications/backgrounders/techdata/aircraft_characteristics/Airbus-Commercial-Aircraft-AC-A320-Feb18.pdf` [cited 24 May 2018].

[45] Oliviero F. "Systems Engineering and Aerospace Design AE3211-I Aircraft Weight & Balance". Lecture slides, March 2018. Published by Delft University of Technology.

[46] Oliviero F. "Systems Engineering and Aerospace Design AE3211-I Requirement Analysis and Design principles for A/C stability & control (Part 1)". Lecture slides, April 2018. Published by Delft University of Technology.

[47] Sforza P.M. *"Commercial Airplane Design Principles"*. Butterworth-Heinemann, first edition, 2014. ISBN: 978-0-12-419953-8.

[48] Scholz D. "An Optional APU for Passenger Aircraft". URL: `http://www.fzt.haw-hamburg.de/pers/Scholz/Airport2030/Airport2030_PRE_CEAS_15-09-07_Scholz.pdf` [cited 17 May 2018].

[49] U.S. Department of Transportation. "AMT Airframe Handbook Volume 1 Chapter 9". URL: `https://www.faa.gov/regulations_policies/handbooks_manuals/aircraft/amt_airframe_handbook/media/ama_Ch09.pdf` [cited 18 May 2018].

[50] Moir I., Seabridge A., and Jukes M. *"Civil Avionics Systems, Second Edition"*. John Wiley & Sons, 2013.

[51] Young T.M. *"Performance of the Jet Transport Airplane: Analysis Methods, Flight Operations, and Regulations"*. John Wiley & Sons, December 2017.

[52] Howe D. *"Aircraft conceptual design synthesis"*. Professional Engineering Publishing, 2000.

[53] Voskuijl M. "Flight and Orbital Mechanics - Climb and Descent". Lecture slides, March 2018. URL: `http://brightspace.tudelft.nl` [cited 22 June 2018].

[54] Michel U. "Correlation of Aircraft Certification Noise Levels EPNL with Controlling Physical Parameters". In *19th AIAA/CEAS Aeroacoustics Conference*, page 13, 2013.

[55] BDL Bundesverband Der Deutschen Luftverkehrswirtschaft. "Aircraft Noise Report", 2015. URL: `https://www.bdl.aero/download/2013/aircraftnoisereport2015.pdf` [cited 18 June 2018].

[56] Fink M.R. "Airframe Noise Prediction Method". Technical report, United Technologies Research Center, 1977.

[57] Sahai A.K. "Consideration of Aircraft Noise Annoyance during Conceptual Aircraft Design". *20th AIAA/CEAS Aeroacoustics Conference*, 2014.

[58] Ruijgrok G.J.J. *"Elements of Aviation Acoustics"*. Delft University Press, 1993.

[59] Yong L., Xunnian W., and Dejiu Z. "Control strategies for aircraft airframe noise reduction". Technical report, State Key Laboratory of Aerodynamics, China Aerodynamics Research & Development Centre, 2012.

[60] Enghardt L. "Improvement of Fan Broadband Noise Prediction: Experimental Investigation and Computational Modeling". CEAS Broadband noise workshop, 2008. Bilbao.

[61] Berton J.J., Envia E., and Burley C.L. "An Analytical Assessment of NASA's N+1 Subsonic Fixed Wing Project Noise Goal", 2009.

[62] Huff D. L. "Noise Reduction Technologies for Turbofan Engines". Technical report, NASA, 2007.

[63] Jones M.G., Parrott T. L., Sutliff D. L., and Hughes C. E. "Assessment of Soft Vane and Metal Foam Engine Noise Reduction Concepts", 2009.

[64] Leylekian L., Lebrun M., and Lempereur P. "An Overview of Aircraft Noise Reduction Technologies", 2014.

[65] International Civil Aviation Organization. "Annex 16: Enviromental Protection Volume 2 Aircraft Engine Emissions", 2008. URL: https://law.resource.org/pub/us/cfr/ibr/004/icao.annex.16.v2.2008.pdf [cited 22 June 2018].

[66] Cheng W. et al. "Review of Biojet Fuel Conversion Technologies". Technical report, National Renewable Energy Laboratory, 2016.

[67] Kinder J.D. and Rahmes T. "Evaluation of Bio-Derived Synthetic Paraffinic Kerosene (Bio-SPK)". Technical report, The Boeing Company: Sustainable Biofuels Research & Technology Program, 2009.

[68] Hileman J.J., Stratton R.W., and Donohoo P.E. "Energy Content and Alternative Jet Fuel Viability". *Journal of Propulsion and Power*, 26(6), December 2010.

[69] Heselton K.E. "Boiler Operator's Handbook".

[70] Schlagermann P., Göttlicher G., Dillschneider R., Sastre R.R., and Posten C. "Composition of Algal Oil and Its Potential as Biofuel". *Journal of Combustion*, 2012:14, 2012.

[71] Maniatis K., Heuvel E.V.D., and Kalligeros S., editors. *"Building the future Cost of Biofuel"*. European Commission, February 2017.

[72] L.K. Teong O.B., Cynthia. "Feasibility of Jatropha Oil for Biodiesel:Economic Analysis", 2011.

[73] Foulke T., Geiger M., and Hess B. "Is Biodiesel from Camelina right for you?". URL: https://www.sare.org/content/download/71599/1019535/file/B1249.pdf [cited 25 June 2018], August 2013.

[74] Miyoshi C. and Mason K.J. "The Carbon Emissions of Selected Airlines and Aircraft Types in Three Geographic Markets". URL: https://dspace.lib.cranfield.ac.uk/bitstream/handle/1826/3825/Carbon_emissions_of_selected_airlines_and_aircraft_types_in_three_geographic_markets-2009.pdf;jsessionid=590F688AD7AAABCC6BBCF75A3AB1EA67?sequence=1 [cited 22 June 2018], May 2009.

[75] "Directly Converting CO2 into a Gasoline Fuel", May 2017. URL: https://www.nature.com/articles/ncomms15174 [cited 18 June 2018].

[76] The Economist. "The Difference Engine: The Sunbeam Solution", Feb 2011. URL: https://www.economist.com/babbage/2011/02/11/the-difference-engine-the-sunbeam-solution [cited 21 June 2018].

[77] ICAO Secretariat. "Aviation's Contribution to Climate Change". Technical report, ICAO, 2010.

[78] Verhagen W. "AE4468 Airline Maintenance Operations". Lecture slides, February 2017. Delft University of Technology.

[79] Sommerville I. "Sofware Engineering 10th Edition". Book website, 2018. http://iansommerville.com/software-engineering-book/web/critical-systems/ [cited 26 June 2018].

[80] World Commission for Environment and Development. "Our Common Future", 1987. URL: http://www.un-documents.net/our-common-future.pdf [cited 1 May 2018].

[81] EEA EASA and Eurocontrol. "European Aviation Environmental Report 2016", 2016. URL: https://ec.europa.eu/transport/sites/transport/files/european-aviation-environmental-report-2016-72dpi.pdf [cited 1 May 2018].

[82] Koudis G.S., Hu S.J., Majumdara A., Jones R., and Stettler M.E.J. "Airport Emissions Reductions from Reduced Thrust Take-off Operations". Elsevier, May 2017.

[83] Dezombre J. and Oudjehani K. "The Future of Sustainable, End-of-Life Aircraft Management". In *On Board a Sustainable Future*, pages 199 – 200. ICAO, 2016.


TU Delft